Assessing the uses of ^{230}Th, ^{232}Th and ^{231}Pa as proxies in the past and modern ocean

Feifei Deng

Thesis submitted to the University of Oxford
for the degree of Doctor of Philosophy in Earth Sciences



Department of Earth Sciences & Wolfson College

Trinity Term 2014

Supervisors: Prof. Gideon M. Henderson & Dr. Alex L. Thomas

海納百川，有容乃大。

-林則徐

Assessing the uses of ^{230}Th, ^{232}Th and ^{231}Pa as proxies in the past and modern ocean

Thesis submitted for the degree of Doctor of Philosophy

Feifei Deng

Department of Earth Sciences & Wolfson College

Trinity Term 2014

ABSTRACT

Thorium-230 and protactinium-231 have been widely used as proxies of oceanic processes in both modern and past marine environment. Their application as such proxies is, however, limited by sparse data from the modern ocean with which to characterize their distribution and behavior. This thesis aims to provide such data and to assess their uses as oceanic proxies for ocean circulation, sediment dissolution, and modern dust input. Twelve profiles of dissolved ^{230}Th, ^{231}Pa and ^{232}Th obtained on a meridional GEOTRACES section in the Southwest Atlantic confirm the expected transport and fractionation of ^{231}Pa from ^{230}Th by deep ocean circulation out of the modern Atlantic. There is however neither a water mass dependence nor progressive change as water masses age, which challenges the use of sedimentary ^{231}Pa/^{230}Th to assess past flow in the South Atlantic. Decreases of ^{230}Th and ^{231}Pa observed in near-bottom water indicate enhanced sea-floor removal in regions where nepheloid layers are present. In a second study of sedimentary nuclides concentration, high-resolution $^{230}Th_{xs}$ profiles from sediment in Southeast Atlantic exhibit increasing $^{230}Th_{xs}$ concentrations from core-top to a depth of ~3 cm followed by relatively constant values at greater depth, suggestive of sediment dissolution in the upper sediment core. This observation suggests the use of $^{230}Th_{xs}$ to quantify sediment dissolution. Combined with sediment composition measurements, $^{230}Th_{xs}$ also provides an assessment of which constituents are dissolving from the sediment. $(^{231}Pa/^{230}Th)_{xs}$ ratios do not appear to be affected by sediment dissolution. A third study, in the tropical Atlantic Ocean, combines water-column measurements of ^{230}Th, ^{232}Th with coeval aerosol measurements, and allows assessment and improvement of the use of ^{232}Th to quantify dust input to the surface ocean. ^{232}Th-derived dust flux increases from 0.43 g/m^2/yr at low latitude in the South Atlantic to 10.70 g/m^2/yr at higher latitude in the North Atlantic, and broadly agree with a model of dust input. The data presented in this thesis have expanded the dataset of ^{230}Th, ^{232}Th and ^{231}Pa in the Atlantic Ocean, and provide an insight into future uses of these nuclides as oceanic proxies.

Assessing the uses of ^{230}Th, ^{232}Th and ^{231}Pa as proxies in the past and modern ocean

Thesis submitted for the degree of Doctor of Philosophy

Feifei Deng

Department of Earth Sciences & Wolfson College

Trinity Term 2014

EXTENDED ABSTRACT

Recent decades have seen an increasing interest in the use of ^{230}Th, ^{232}Th, and ^{231}Pa as proxies of oceanic processes, such as the rate of ocean circulation, biological productivity and dust deposition, in both modern and past marine environment. Their application as oceanic proxies is however limited by a lack of modern data with which to understand their distribution and behavior in various ocean settings. This thesis aims to provide such data, and to better understanding the use of these nuclides as proxies of past ocean circulation, of sediment dissolution, and of dust input to the modern ocean.

Sedimentary records of ^{231}Pa/^{230}Th have been used in a number of previous studies to reconstruct the past rate of ocean circulation. The principal underlying this proxy is the constant production of ^{230}Th and ^{231}Pa by α-decay of uniformly distributed U in the ocean and the fractionation of these nuclides during removal. Once produced in seawater, highly particle-reactive ^{230}Th is readily adsorbed onto particles and removed from seawater at its site of formation, while less particle-reactive ^{231}Pa can be advected by deep ocean circulation to areas of higher productivity to be subsequently removed. Therefore, ^{231}Pa/^{230}Th is expected to increase along deep-water flow paths and to vary with the rate of deep-ocean circulation. However, factors such as particle flux and composition also play a part in the oceanic and sedimentary distribution of ^{231}Pa and ^{230}Th. To make use of ^{231}Pa/^{230}Th as a paleo-circulation tracer requires a thorough understanding of the controls on the distribution of the two nuclides in seawater. Despite a growing knowledge of water-column ^{231}Pa and ^{230}Th concentrations, rather little is known about the distribution of the nuclides in the South Atlantic Ocean. This basin has recently been the focus

of down-core $^{231}Pa/^{230}Th$ records, but is characterized by a more complex pattern of deep-water circulation than the North Atlantic, with multiple water masses flowing in different directions.

To investigate the controls of these nuclides along the flow paths of deep waters in the South Atlantic, measurements of dissolved ^{230}Th, ^{231}Pa and ^{232}Th were made for twelve full-depth profiles along a Southwest Atlantic section during GEOTRACES cruise GA02S. Sampling captures all the main Atlantic deep water masses along their meridional flow paths and allows insight into the control on ^{230}Th and ^{231}Pa in a setting where waters are flowing in opposing directions, with direct relevance to understanding the use of $^{231}Pa/^{230}Th$ as an ocean-circulation proxy. Water-column ^{230}Th profiles exhibit a nearly linear increase with water depth, which can be explained by reversible scavenging models. ^{231}Pa increases from the surface to ~1200-1500 m, but is invariant or decreases with greater depth, deviating from the behaviour expected for reversible scavenging. Dissolved $^{231}Pa/^{230}Th$ ratios display a mid-water-column maximum at ~1000-2000 m which is broadly coincident with Upper Circumpolar Deep Water. Below 2000m, nuclide distributions and ratios exhibit no dependence on water mass, nor any indication of progressive change within a water mass, challenging the use of $^{231}Pa/^{230}Th$ as a past circulation tracer in the South Atlantic. Horizontal transport of ^{230}Th and ^{231}Pa by ocean circulation were calculated, indicating a net southward export out of the Atlantic of 19% of the ^{231}Pa and 3% of the ^{230}Th produced in that ocean. This removal is all from the North Atlantic while, in the South Atlantic, removal to sediment equals production. Simple one-dimensional modeling can simulate ^{230}Th profiles but not the mid-water-column maximum observed in ^{231}Pa profiles, suggesting an additional source of ^{231}Pa (perhaps lateral transport from the margin) or removal at depth due to bottom scavenging. Near seafloor minima in concentrations indicates bottom scavenging of ^{230}Th and ^{231}Pa, which is enhanced in the presence of nepheloid layers, particularly for ^{231}Pa. Near-bottom scavenging rates were estimated for both nuclides, suggesting that this additional scavenging fractionates ^{230}Th and ^{231}Pa and, in the presence of nepheloid layers, may lead to a small increase in sedimentary $^{231}Pa/^{230}Th$ ratios. Th-232 maxima were observed at the equator and in the area between 32°S and 45°S, indicating high dust input from the African and possibly South American continents. ^{232}Th concentrations were therefore paired with ^{230}Th-derived residence times in the upper 250 m of the water column to test the application of Th as a tracer of dust deposition.

The robustness of using sedimentary record of $^{231}Pa/^{230}Th$ as a proxy for past rates of ocean circulation (or particle flux) also depends on how well this record is preserved in the sediment. Dissolution of marine sediment at the seafloor takes place in all ocean basins. This process controls the release of chemicals from sediment back to seawater, and affects the composition of marine particulates and the preservation of all paleo-proxies in sediment. Assessing the rate and extent of this dissolution is therefore for many reasons. With a constant and well-known flux to the seafloor, $^{230}Th_{xs}$ has been employed to assess processes at the seafloor, such as sediment redistribution, and exhibits previously un-explored potential to assess sediment dissolution at the seafloor. To test the use of $^{230}Th_x$ as a tool to quantify sediment dissolution, high-resolution $^{230}Th_{xs}$ measurements were obtained from intact core-top sediment samples spanning a range of water depths on the slope of the Cape Basin (UK-GEOTRACES cruise D357) and the South Atlantic Mid-Ocean Ridge (Meteor cruise M34/3). Sedimentary $^{230}Th_{xs}$ concentrations increase with depth in the upper ~3 cm of sediment and are constant below this depth, which can be best explained as a result of sediment dissolution in the upper centimetres of the sediment. Based on these observations, I attempted to use core-top $^{230}Th_{xs}$ measurements to quantify the rate of sediment dissolution at the seafloor and assess the magnitude of this process in various ocean settings. $^{230}Th_{xs}$-derived dissolution rates vary from 0.11 to 0.24 g/cm^2/kyr, exhibiting a strong increase in rate with depth. Combining $^{230}Th_{xs}$ with sediment composition measurements provides an assessment of which constituents are dissolving from the sediment. In the core with the most unambiguous dissolution, situated a kilometer below the modern carbonate saturation horizon, there is surprising lack of observed carbonate dissolution, while opal does appear to be dissolving. Results also suggest dissolution of the detrital fraction of sediments, indicating that $^{230}Th_{xs}$ may enable quantification of submarine weathering fluxes. Measurements of $^{231}Pa_{xs}$ conducted on the same sediments enables the assessment of the impact of sediment dissolution on $(^{231}Pa/^{230}Th)_{xs}$ ratios. Despite significant dissolution observed by $^{230}Th_{xs}$ profiles, sedimentary $(^{231}Pa/^{230}Th)_{xs}$ is largely unaffected, indicating the robustness of sedimentary $(^{231}Pa/^{230}Th)_{xs}$ ratios to dissolution.

Recent studies have proposed the use of ^{232}Th as a tool to estimate dust input to the surface ocean. This approach is based on the assumption that the predominant source of ^{232}Th to the surface of the open ocean is dust input, and is facilitated by the use of ^{230}Th to estimate the removal rate of ^{232}Th from seawater. However, the new approach has yet to be fully constrained and tested. To assess the use of ^{232}Th to quantify dust input, water-column ^{230}Th and ^{232}Th were

measured for five sites in the tropical Atlantic Ocean between 7°S and 19°N during the UK-GEOTRACES cruise GA06 (D361). Dissolved ^{230}Th profiles exhibit a broadly linear increase with water depth in the upper water column, which can be explained by the reversible scavenging model. Dissolved ^{232}Th profiles exhibit more variability between sites in the surface water followed by relatively constant values at depth. The distinct difference between ^{230}Th and ^{232}Th profiles reflects their different sources to the ocean, ^{230}Th being supplied by constant decay of uniformly-distributed ^{234}U, whereas ^{232}Th is supplied by dissolution from atmospheric dust. This observation supports the use of ^{232}Th to estimate dust flux. Mixed layer depth was chosen as the optimal integration depth to yield ^{232}Th flux that represents dust flux to the surface ocean. With aerosol measurements of both total and soluble fractions of Th, dust Th solubility were obtained, and allowed a better estimate of dust flux from ^{232}Th flux using respective Th solubility for each site. ^{232}Th-derived dust flux increases northward from 0.46 g/m^2/yr at 7°S to 3.43 g/m^2/yr at 19°N. A comparison between these ^{232}Th-derived dust fluxes and those from a widely used model was made. Results agree with each other in the general northward increasing trend, but disagree in the absolute values, with higher dust flux estimated by the model than from the ^{232}Th observations. With a relative solubility ratio of Fe and Th at 0.16, Fe flux was also estimated from ^{232}Th flux, lying in a range between 0.35 and 2.26 mg/m^2/yr.

The data presented in this thesis have greatly expanded the dataset of ^{230}Th, ^{232}Th and ^{231}Pa in the Atlantic Ocean, leading to a better understanding of these nuclides in seawater and sediment, and provide an insight into future uses of these nuclides as proxies in the past and modern ocean.

ACKNOWLEDGEMENTS

This work would not be complete without support and aid from numerous people. I would especially like to thank my supervisor, Gideon Henderson, for his constant advice, guidance, support, encouragement, and understanding throughout the research and the writing of this thesis. I am grateful to all the wonderful research experience he has provided, be it collecting sample at sea or presenting my work at major conferences in other parts of the world. He has been, and always will be, a source of inspiration to expand my knowledge beyond my area of research and think about big questions in oceanography.

I would like to thank my co-supervisor Alex Thomas in particular for teaching me about Pa and Th analysis in the clean lab and analytical techniques by ICP-MS. I am grateful to his great patience in answering my every single question, and problem-shooting of ICP-MS even at mid-night and during holidays. Working with him in the lab has been one of the best experiences throughout my years in Oxford. He is appreciated equally as much for intellectually stimulating discussion throughout this thesis work.

I extend my thanks to the crew and scientific staff of the RRS James Cook (Cruise JC057, D357) and RRS Discovery (D361). I would especially like to thank the chief scientists of these cruises, Micha Rijkenberg, Gideon Henderson and Eric Achterberg, for providing sampling opportunities and making cruise data accessible for interpreting this work; and Maeve Lohan for collecting D361 samples used in this thesis. Appreciation also goes to Will Homoky and Lukas Jonkers for providing digested sediment samples for this thesis.

I would like to thank all the post-graduate students and post-doctoral researchers in the Climotope research group for their kind help in the lab and useful critique of my work. Special thanks must go to Alan Hsieh who has provided thought-provoking and constructive suggestions to my work. I would also like to thank Nick Belshaw, Phil Holdship, Andrew Mason and Steve Wyatt for their assistance in the lab and on Mass Spectrometry. I have also benefitted from discussion with several other people; Alex Baker, Thomas Browning, Heather Bouman, Rosie Chance, and Yves Plancherel.

I must also thank Prof. Robert Anderson and Dr. Don Porcelli for examining for this thesis. They provided constructive comments of my work and thought-provoking discussions during the viva, and for that I am very grateful.

Throughout my adventurous journey in Oxford, I have been fortunate to meet so many lovely people. Thank you, Slair Gelain, Samson Yuen and Kwok-ho Cheung, for giving the 20-something me extraordinary experience I would never have elsewhere. Thank you, Geraldine Adiku, Marcus Carlsen Haeggrot, and Ben Mullaney, for being the best housemates ever! Thank you, Siyu Liu, Chao Liu, Kun Ma, Qiong Zhang, and Xinyuan Zheng, for sharing so much laughter together! I am mostly grateful to China Oxford Scholarship Fund (COSF) for its generous financial support from 2010 to 2012. I would also like to thank all the friends from the COSF community for constantly motivating me to keep going, keep giving and keep engaging!

I could not have achieved any of this work without the support of my parents who have given me unconditional love and constant encouragement throughout. Thank you so much! *謝謝爸爸媽媽！*

This work was funded by GEOTRACES grants.

Contents

page

Abstract i
Extended abstract ii
Acknowledgements vi
Table of contents viii
List of figures xii
List of tables xv
List of abbreviations xvi

Chapter 1 Introduction

1.1 Thorium-230 and protactinium-231 in the ocean 2
1.2 $^{231}Pa/^{230}Th$ as a proxy for the rate of deep ocean circulation 6
1.3 Sedimentary $^{230}Th_{xs}$ as a constant flux proxy 12
1.4 Thorium-232 in the ocean 14
1.5 Goals and outline of the thesis 17

Chapter 2 Methods

2.1 Introduction 19
2.2 Sampling 21
2.2.1 Seawater samples 21
2.2.2 Sediment samples 24
2.3 Clean lab overview 25
2.3.1 Laboratory conditions 25

2.3.2 Reagents 26
2.3.3 Cleaning procedures 26
2. 4 Spikes 27
2.4.1 Isotope dilution mass spectrometry 27
2.4.2 ^{229}Th -^{236}U spike 29
2.4.3 ^{233}Pa spike 30
2.5 Sample weighing and pre-treatment 32
2.5.1 Procedures for seawater samples 32
2.5.2 Procedures for sediment samples 33
2.6 Elemental separation 34
2.6.1 Procedures for seawater samples 34
2.6.2 Procedures for sediment samples 35
2.7 Mass spectrometry 36
2.7.1 Machine and standard 36
2.7.2 Measurement of Pa and Th isotopes for seawater samples 39
2.7.3 Measurement of U-series isotopes for sediment samples 41
2.7.4 ^{233}Pa spike calibration 42
2.8 Data processing 43
2.9 Blanks and Uncertainties 44

Chapter 3 Controls on seawater ^{231}Pa, ^{230}Th and ^{232}Th concentrations along the flow paths of deep waters in the Southwest Atlantic

3.1 Introduction 48
3.2 Sampling strategies and settings 51
3.3 Analytical techniques 54
3.4 Results 55

3.5 Discussion 58

3.5.1 Meridional transport of ^{230}Th and ^{231}Pa 58

3.5.2 Quantifying seafloor removal rates of ^{230}Th and ^{231}Pa 61

3.5.3 ^{232}Th-derived dust flux deposition 68

3.5.4 Controls on ^{230}Th, ^{231}Pa, and ^{231}Pa/^{230}Th in the water column 71

3.6 Conclusions 74

Chapter 4 Assessing the use of $^{230}Th_{xs}$ to quantify sediment dissolution and its effect on sedimentary $(^{231}Pa/^{230}Th)_{xs}$

4.1 Introduction 78

4.2 Principles underlying the use of ^{230}Th as an indicator of sediment dissolution 80

4.3 Locations and samples 82

4.4 Analytical techniques 86

4.4.1 U-series analyses 86

4.4.2 Sediment composition 87

4.4.3 Salt-correction 88

4.5 Results 89

4.5.1 ^{232}Th and ^{238}U 89

4.5.2 $^{230}Th_{xs}$ 92

4.5.3 $^{231}Pa_{xs}$ and $(^{231}Pa/^{230}Th)_{xs}$ 95

4.5.4 Sediment composition 96

4.6 Discussion 97

4.6.1 $^{230}Th_{xs}$ as an indicator of sediment dissolution 97

4.6.2 Quantifying sediment dissolution rate with $^{230}Th_{xs}$ 98

4.6.3 Dissolution of sedimentary components and water-depth dependence 101

4.6.4 Influence of sediment dissolution on sedimentary $(^{231}Pa/^{230}Th)_{xs}$ 105

4.7 Conclusions 106

Chapter 5 Assessing the use of water-column ^{232}Th-^{230}Th to assess dust deposition to the ocean with coupled water and aerosol measurements in the tropical Atlantic

5.1 Introduction 110

5.2 Sampling strategies and settings 112

5.3 Analytical techniques 116

5.3.1 Thorium and protactinium isotopes analysis 116

5.3.2 Aerosol Th and Fe solubilities 117

5.4 Results 118

5.4.1 Water-column ^{230}Th, ^{232}Th and ^{231}Pa 118

5.4.2 Aerosol Th and Fe solubilities 122

5.5 Discussion 123

5.5.1 Th residence times and optimal depth of integration for dust flux assessment 123

5.5.2 Assessing Th solubility and ^{232}Th-derived dust flux 129

5.5.3 Comparison with dust model 133

5.5.4 Using Th to assess inputs of Fe to seawater 135

5.6 Conclusions 136

Chapter 6 Conclusions and outlook

6.1 Water-column ^{230}Th, ^{231}Pa and ^{232}Th in the Southwest Atlantic 139

6.2 ^{230}Th, ^{232}Th and ^{231}Pa in surface sediment of Southeast Atlantic 140

6.3 Water-column ^{230}Th and ^{232}Th in the tropical Atlantic Ocean 142

Bibliography 144

Appendix: Data tables and figures 156

List of figures

Page

1.1 Decay chains of the uranium series 3
1.2 A summary of water-column ^{230}Th and ^{231}Pa compiled from early measurements 4
1.3 Schematic of scavenging models 5
1.4 A schematic of the principal underlying the use of ^{231}Pa/^{230}Th as a deep ocean circulation tracer 8
1.5 Sediment records of ^{231}Pa/^{230}Th ratios in a high-accumulation-rate core retrieved from Bermuda rise in the deep western subtropical Atlantic 10
1.6 Th-232 concentrations in surface waters along an Atlantic transect from 32^{o}N to 37^{o}S 16
2.1 Sampling locations of seawater and sediment samples used in this thesis 22
2.2 Seawater sample collection 23
2.3 Fume hood used for sample acidification aboard RRS James Cook 24
2.4 Schematic of the Nu instruments MC-ICP-MS 36
3.1 Map of sampling stations during GEOTRACES cruise JC057 51
3.2 Vertical distributions of salinity; potential temperature; dissolved phosphate concentration and beam attenuation coefficient along the GEOTRACES GA02S section 53
3.3 Distributions of water column ^{230}Th; ^{231}Pa; ^{231}Pa/ ^{230}Th ratios and ^{232}Th along the transect in the southwest Atlantic Ocean 57
3.4 Horizontal transport and removal to sediment of ^{230}Th and ^{231}Pa in the Atlantic Ocean 60
3.5 Examples of linear extrapolation of vertical profiles of ^{230}Th and ^{231}Pa from Stations JC057-6 and JC057-18 63
3.6 Beam attenuation coefficient; and additional near-seafloor removal rates of ^{230}Th; ^{231}Pa and ^{231}Pa/^{230}Th 66
3.7 Comparison of ^{230}Th-^{232}Th-derived dust flux and modeled dust deposition 70

3.8 Water-column profile of ^{230}Th, ^{231}Pa, ^{231}Pa/^{230}Th averaged from measurements in this study 72
4.1 Schematic of principles underlying the use of ^{230}Th as an indicator of sediment dissolution 82
4.2 South Atlantic area showing sediment sample locations 83
4.3 Sediment cores retrieved from the continental margin of Cape Basin in the Eastern South Atlantic 84
4.4 Section figures of a) oxygen concentrations; b) omega values derived from measurements of alkalinity (ALK) and dissolved inorganic carbon (DIC) 85
4.5 Lithogenic fractions in the Cape Basin sediment estimated by concentrations of Al and of ^{232}Th 90
4.6 Vertical profiles of authigenic U measured in the Cape Basin Margin cores and the South Atlantic Mid-Ocean Ridge core 92
4.7 Vertical profiles of sediment $^{230}Th_{xs}$; $^{231}Pa_{xs}$; and (c) $(^{231}Pa/^{230}Th)_{xs}$ ratios measured in the Cape Basin Margin cores and the South Atlantic Mid-Ocean Ridge core 94
4.8 Vertical profiles of sediment content measured for sediment on the Cape Basin Margin in weight percentage (wt%) 96
4.9 Dissolved sediment fraction, core-top $^{230}Th_{xs}$ flux and dissolution rate calculated from $(^{230}Th)_{xs}$ concentration 100
4.10 Vertical profiles of $^{230}Th_{xs}$-normalized fluxes of sediment content for sediment on the Cape Basin Margin 102
4.11 $^{230}Th_{xs}$-normalized fluxes of sediment content, and their relative percentages to the Total for the core-top sediment and the lower sediment in Cape Basin Margin 103
5.1 Sampling settings of GEOTRACES cruise GA06 (D361) 113
5.2 Airmass trajectories, over the 4 d before occupation, at certain points in the tropical Atlantic Ocean along the cruise track of D361 114
5.3 Vertical profiles of full-depth water-column ^{230}Th, ^{232}Th, and ^{231}Pa; and shallow-depth water-column ^{230}Th, ^{232}Th, and ^{231}Pa 120
5.4 Distribution of water-column ^{231}Pa/^{230}Th ratios along the transect in the tropical Atlantic Ocean 122

5.5 Relationship between Th and Fe solubilities (%) and their respective total concentrations in aerosol samples. 123
5.6 Full-depth and shallow-depth ^{230}Th residence time and ^{232}Th flux calculated from water-column ^{230}Th and ^{232}Th concentrations integrated at all water depths..... 125
5.7 Relationship between Th solubility obtained from aerosol analysis and ^{232}Th-derived dust flux.. 132
5.8 Th-232-derived dust flux in this study and modelled dust flux by Mahowald et al. (2005) 134
5.9 Relationship between Fe solubility and Th solubility obtained from aerosol analysis along the transect in the tropical Atlantic. 136

List of tables

page

2.1 Atomic abundances and concentrations of the two mixed ^{229}Th-^{236}U spikes: Oxford Water Spike and Oxford Carbonate Spike 29

2.2 The general assembly for the collector array in the Nu instruments MC-ICP-MS 37

2.3 Two-step run configuration for measuring protactinium in seawater samples 40

2.4 Two-step run configuration for measuring thorium in seawater samples 40

2.5 Run configuration for measuring uranium in sediment samples 41

2.6 Two-step run configuration for measuring thorium in sediment samples 42

2.7 Run configuration for ^{233}Pa spike calibration 43

3.1 Meridional mass transport and ^{230}Th and ^{231}Pa concentrations in WOCE section water layers 60

3.2 Additional seafloor removal rates of ^{230}Th and ^{231}Pa. 67

3.3 Results of ^{230}Th-derived residence time and ^{232}Th-derived dust flux 71

4.1 Locations and water depths of sediment samples in this study 83

4.2 Calculated estimates of dissolved sediment fraction, core-top $^{230}Th_{xs}$ flux and sediment dissolution rate 100

5.1 Details of aerosol sample collection on D361 cruise 115

5.2 Th-230 residence time and ^{232}Th flux within the mixed layer 129

5.3 Th-232-derived dust flux in this study and modelled dust flux. 131

List of abbreviations

A	Activity of the nuclide
AABW	Antarctic Bottom Water
AAIW	Antarctic Intermediate Water
β	Production rate
CTD	Conductivity, Temperature, Depth
dpm	Disintegrations per minute
HNLC	High-Nutrient Low-Chlorophyll
ICP-AES	Inductively coupled plasma atomic emission spectroscopy
ICP-MS	Inductively coupled plasma mass spectrometry
IDMS	Isotope dilution mass spectrometry
ITCZ	InterTropical Convergence
LGM	Last Glacial Maximum
MC-ICP-MS	Multi Collector Inductively Coupled Plasma Mass Spectrometry
MOC	Meridional Overturning Circulation
NACW	North Atlantic Central Water
NADW	North Atlantic Deep Water
OM	Organic matter
TC	Total carbon
TIC	Total inorganic carbon
TIMS	Thermal ionization mass spectrometry
TOC	Total organic carbon
2se	2 standard errors

Chapter 1

Introduction

This thesis considers the use of naturally occurring radioisotopes - ^{230}Th, ^{232}Th and ^{231}Pa - as tools to assess processes in the modern and past oceans. I start this introductory chapter with an overview of the ocean chemistry of the nuclides, before discussing their possible use as a proxy for past ocean circulation, as a constant flux indicator in sediments, and as a measure of modern dust input to the surface ocean.

1.1 Thorium-230 and protactinium-231 in the ocean

Naturally occurring ^{230}Th (half-life 75.58 kyr; Cheng et al., 2013) and ^{231}Pa (half-life 32.76 kyr; Robert et al., 1969) are produced in seawater through the α-decay of dissolved ^{234}U and ^{235}U, respectively (Figure 1.1). Uranium forms soluble uranyl-carbonate species in oxidizing aqueous conditions and therefore behaves conservatively in seawater. Its mean residence time in the open ocean is ~4×10^5 yr (Cochran, 1992), a time scale much longer than the time required for the complete mixing of ocean water masses (~1×10^3 yr; Broecker and Peng, 1982). The concentration of uranium in seawater is therefore reasonably constant in both space and time, varying only with salinity (Cochran, 1992). Consequently, the decay of ^{234}U and ^{235}U provides an *in situ* source for ^{230}Th and ^{231}Pa in the ocean with a well-known constant production rate throughout the water column, and can be calculated as:

$$\beta_{^{230}\mathrm{Th}} = A_{^{234}\mathrm{U}} \times \lambda_{^{230}\mathrm{Th}} \quad (1.1)$$

$$\beta_{^{231}\mathrm{Pa}} = A_{^{235}\mathrm{U}} \times \lambda_{^{231}\mathrm{Pa}} \quad (1.2)$$

where $A_{^{234}\mathrm{U}}$ and $A_{^{235}\mathrm{U}}$ are activities of ^{234}U and ^{235}U in seawater, dpm/1000 l; $\lambda_{^{230}\mathrm{Th}}$ and $\lambda_{^{231}\mathrm{Pa}}$ are the decay constants for ^{230}Th and ^{231}Pa, yr^{-1}.

Using 2835 dpm/1000 l and 118 dpm/1000 l for seawater activities of ^{234}U and ^{235}U (Henderson and Anderson, 2003), equations (1.1) and (1.2) give production rates of ^{230}Th and ^{231}Pa of 0.026 dpm/1000 l/yr and 0.0025 dpm/1000 l/yr, respectively.

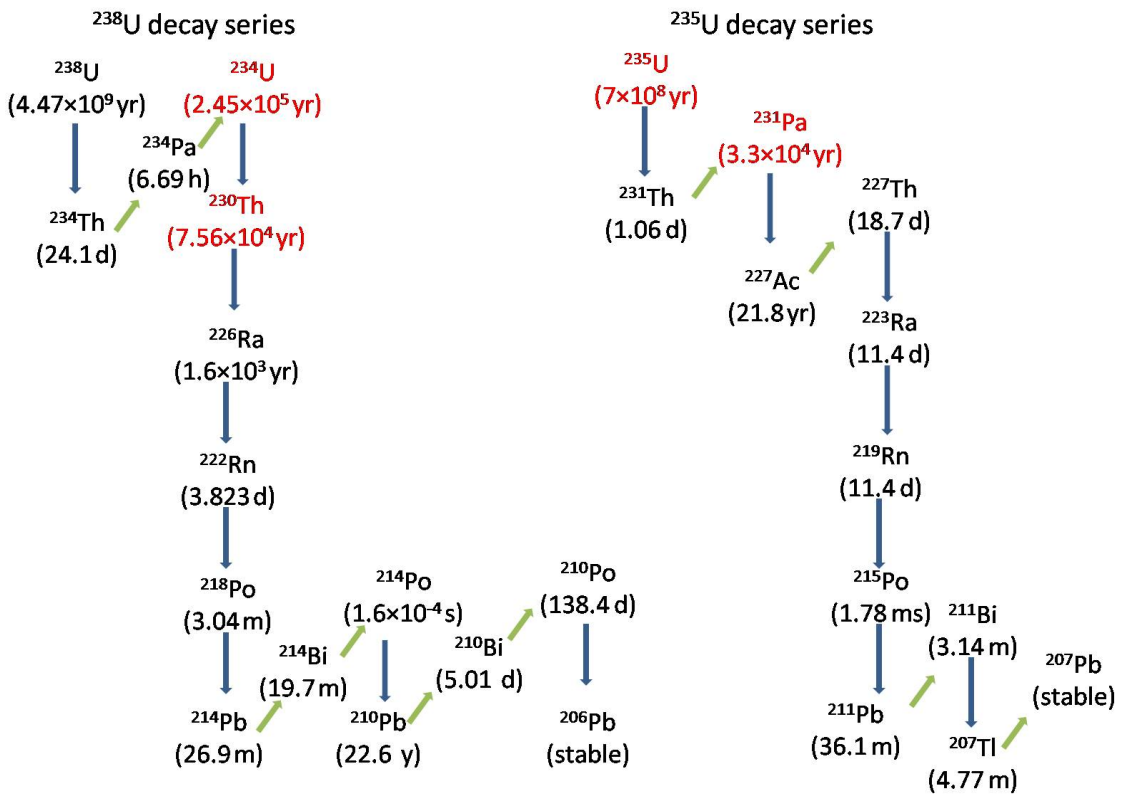


Figure 1.1: Decay chains of the uranium series. Below each radionuclide is its half-life. Blue arrow indicates α-decay, and green arrow indicates β-decay.

Unlike their soluble uranium parents, ^{230}Th and ^{231}Pa are highly insoluble in seawater. After their production in the water column, ^{230}Th and ^{231}Pa tend to be adsorbed onto marine particles and removed from seawater as particles sink to the sediment; a process termed scavenging (Goldberg, 1954). The residence time of ^{230}Th is much shorter than its U parent, at ca. 20 years (Henderson and Anderson, 2003). ^{231}Pa is slightly less insoluble than ^{230}Th, and is removed less readily from seawater, with a residence time of ~120 yr (Henderson and Anderson, 2003).

Early studies determined water-column profiles of ^{230}Th (e.g. Nozaki et al., 1981; Bacon and Anderson, 1982) (Figure 1.2). These studies observed a nearly linear increase of ^{230}Th concentrations with water depth down to the seafloor in both dissolved and particulate forms. I*n*-

situ production and particle removal cannot readily explain such profiles. Such unidirectional scavenging models (Figure 1.3a), used in earlier studies on radionuclide scavenging (e.g. Craig et al, 1973; Krishnaswami et al., 1976) predict a linear increase of particulate ^{230}Th with depth, but failed to explain the same trend observed for dissolved ^{230}Th. To better explain the water-column distribution of ^{230}Th, Bacon and Anderson (1982) suggested a reversible scavenging model, which allows the exchange of ^{230}Th between dissolved and particulate phases so that the initial uptake of dissolved ^{230}Th can be reversed. Shown in Figure 1.3b is a schematic of this reversible scavenging model adapted from a later study by Clegg and Whitfield (1991) with details of exchange processes involved. Using the reversible scavenging model, increases of ^{230}Th with water depth in both particulate and dissolved forms can be successfully predicted.

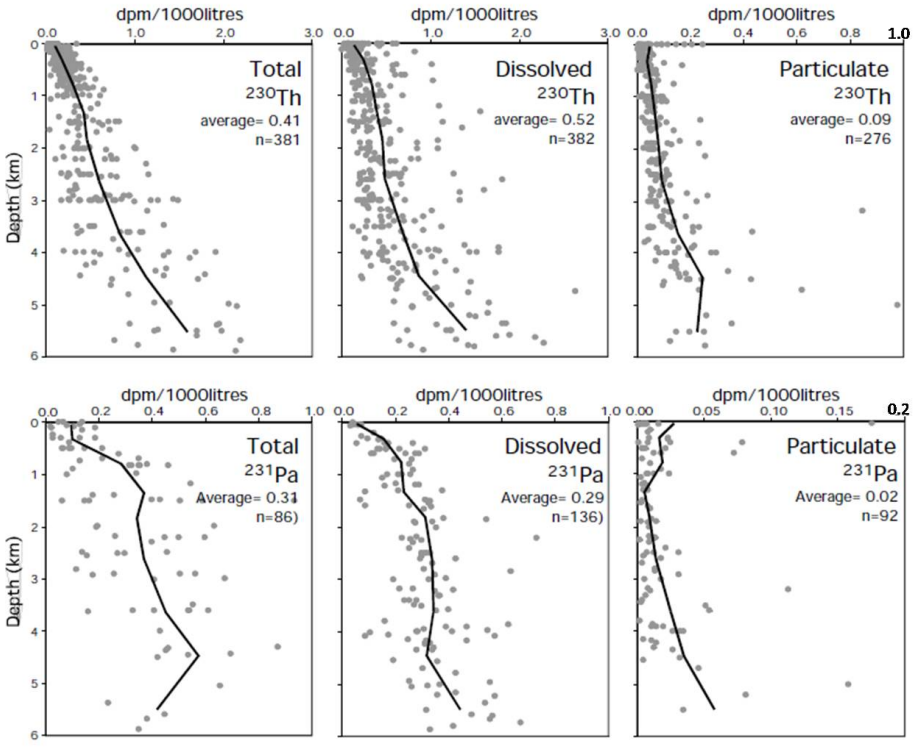


Figure 1.2: A summary of water-column ^{230}Th and ^{231}Pa compiled from early measurements (Henderson and Anderson, 2003).

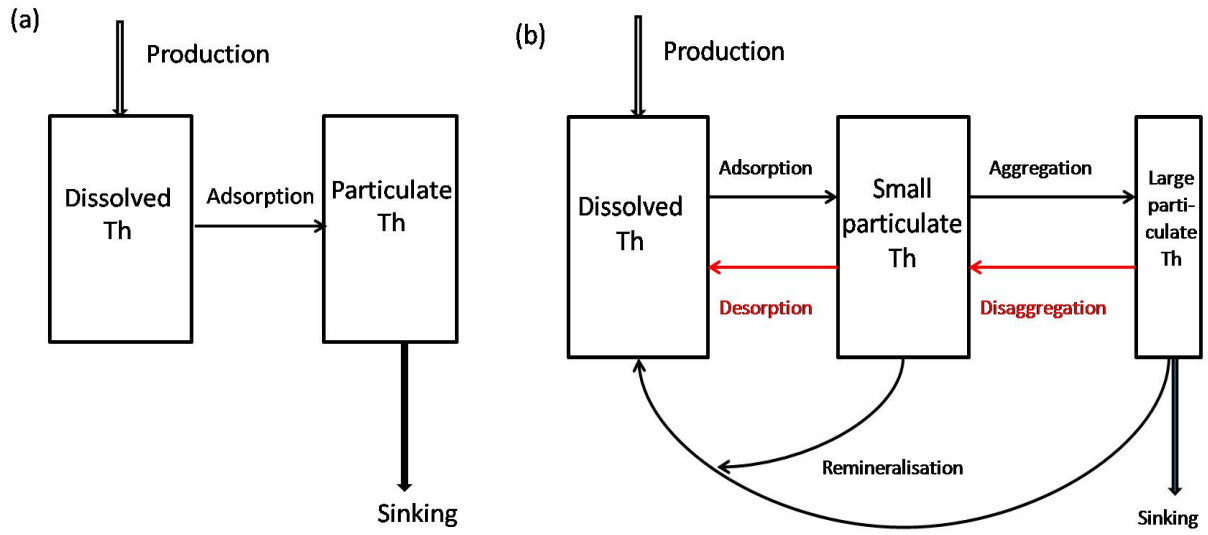


Figure 1.3: Schematic of scavenging models. (a) unidirectional scavenging model. Dissolved Th is supplied by the decay of its uranium parent, adsorbed onto particles, and removed from seawater as particles sink; (b) reversible scavenging model. Dissolved Th is introduced by production through the α-decay of uranium, and exchanges with the small particulate reservoir by adsorption and desorption. Small particulate Th is exchanged with a large particulate fraction by aggregation and disaggregation, and removed from the water column by sinking. Remineralization returns both small and large particulate Th to the dissolved phase.

Early studies of water-column profiles of ^{231}Pa (e.g. Anderson et al., 1983a; Nozaki and Nakanishi, 1985; Nozaki and Yamada, 1987) exhibit a trend similar to ^{230}Th in the upper water column, increasing nearly linearly with water depth, until a mid-depth maximum is reached (Figure 1.2). This feature can also be explained by the exchangeable scavenging. In deep water, however, ^{231}Pa profiles deviate significantly from the linear relationship observed in the upper water column, staying relatively constant or decrease towards the bottom.

In the last decade a significant increase in precision of water-column profiles of ^{231}Pa and ^{230}Th, with a wider coverage of the world's ocean has become available, facilitated by the development of new sampling and analytical techniques (e.g. Deng et al., 2014; Hayes et al., 2013b; Scholten et al., 2008; Thomas et al., 2006; Venchiarutti et al., 2011). With higher-resolution sampling, more water-column structures of ^{230}Th profiles can be observed, frequently

showing deviations from the linear increase with depth predicted by the reversible scavenging model. Early measured profiles of ^{231}Pa, on the other hand, have been supported by these more recent data. Processes that might cause the depletion of both ^{230}Th and ^{231}Pa in deep water have been suggested, such as advection of recently ventilated deep-waters (e.g. Moran et al., 2002); boundary scavenging (e.g. Anderson et al., 1983b); upwelling of waters (e.g. Rutgers van der Loeff and Berger, 1993); or bottom scavenging (e.g. Okuba et al., 2012). To better understand these features observed for water-column ^{230}Th and ^{231}Pa, more measurements of water-column ^{230}Th and ^{231}Pa covering a wider geographical area and a longer time scale are required.

1.2 ^{231}Pa/^{230}Th as a proxy for the rate of deep ocean circulation

The circulation of the ocean is usually divided into two parts, an explicitly wind-driven circulation that dominates in the upper few hundred meters, and deep circulation that dominates below. Deep ocean circulation, extends to the seafloor and is initiated by warm waters, flowing from the equator poleward at the surface to be cooled and to sink to depth at high latitudes.

Deep ocean circulation carries heat, salinity, CO_2, and other properties as it travels, making it an important factor in the earth's climate system especially in at least two aspects, 1) modulating the heat transported from the tropics to high latitudes; 2) partitioning CO_2 between the ocean and the atmosphere. Deep ocean circulation is therefore of significant importance to our understanding of climate, motivating studies of its pattern in the past ocean environment to provide insight into present and future climate change.

To study past deep ocean circulation, proxies, such as records of carbon isotope composition ($\delta^{13}C$) (Curry et al., 1988) and the cadmium content (Cd/Ca) of benthic foraminifera (Boyle and Keigwin, 1982), have been employed. These two proxies are linked to processes controlling the nutrient and carbon dioxide content of deep water, which provide important information to reconstruct the distribution of water masses in the past (Boyle, 1988). These proxies, however, provide little information about the flow rates of deep-water masses (Henderson and Anderson, 2003). A proxy to provides assessment of the water flow rates is also required. One such proxy, proposed by previous studies, is the ratio of ^{231}Pa /^{230}Th.

A schematic showing the principal underlying the use of $^{231}Pa/^{230}Th$ as a proxy to study deep ocean circulation is given in Figure 1.4. Pa-231 and ^{230}Th are produced in the ocean through the α-decay of their uniformly distributed uranium parents, their rates of production throughout the water column, as calculated by equations (1.1) and (1.2), is thus fixed at a ratio determined by the activities of their parents in the ocean, i.e., $^{231}Pa/ ^{230}Th = 0.093$ (activity ratio). Being highly particle-reactive with short residence times in seawater, ^{230}Th and ^{231}Pa are expected to be removed from seawater with a fixed activity ratio equal to their production ratio of 0.093. However, the difference in solubility of ^{230}Th (residence time 20 years) and ^{231}Pa (residence time 120 yrs) allows for ^{231}Pa advection by deep ocean circulation away from its site of formation prior to removal from the water column. Consequently, under regions where water are recently ventilated and are advecting, less ^{231}Pa is removed to the underlying sediment than produced in the water column, while the flux of ^{230}Th to the sediments approximately balances its rate of production in the water column. This results in a sedimentary $^{231}Pa/^{230}Th$ ratio lower than the production ratio of 0.093 at sites of vigorous deep-ocean circulation. As the water mass subsequently flows, the $^{231}Pa/^{230}Th$ ratio increases until ^{231}Pa formation is balanced again by

removal. Therefore, if rates of deep-water flow change, sedimentary $^{231}Pa/^{230}Th$ are expected to vary accordingly to reflect this change. At lower rates of deep water flow, for instance, less ^{231}Pa is exported out of its site of formation, and is recorded in the sediment by higher $^{231}Pa/^{230}Th$ ratios.

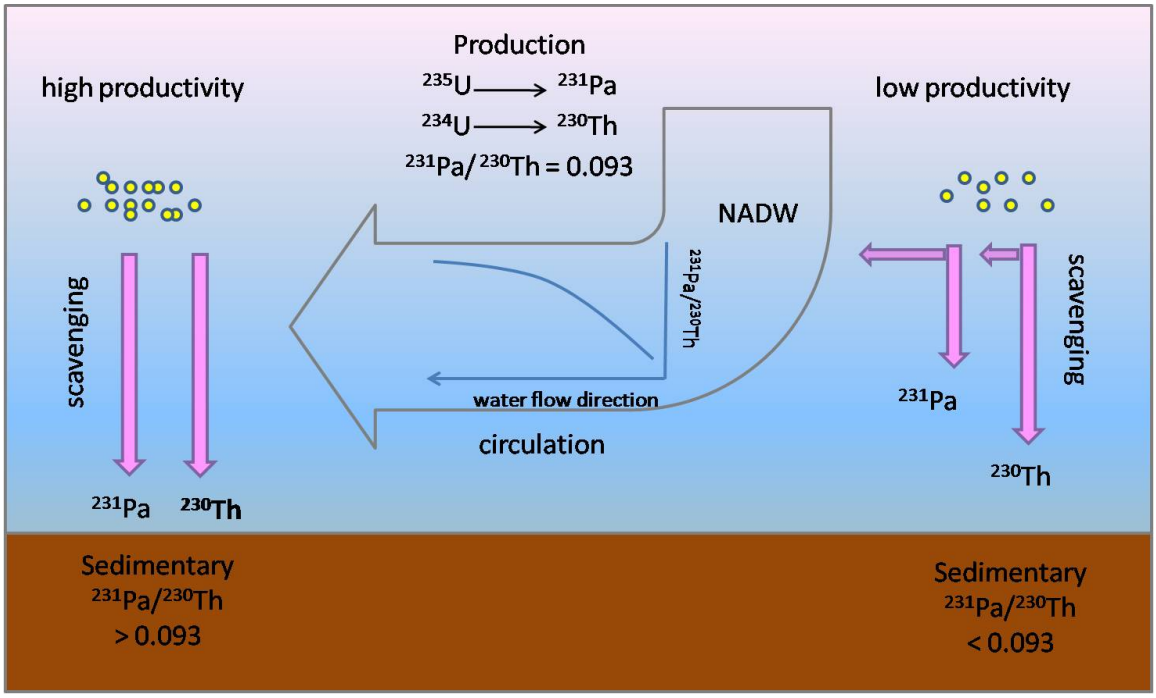
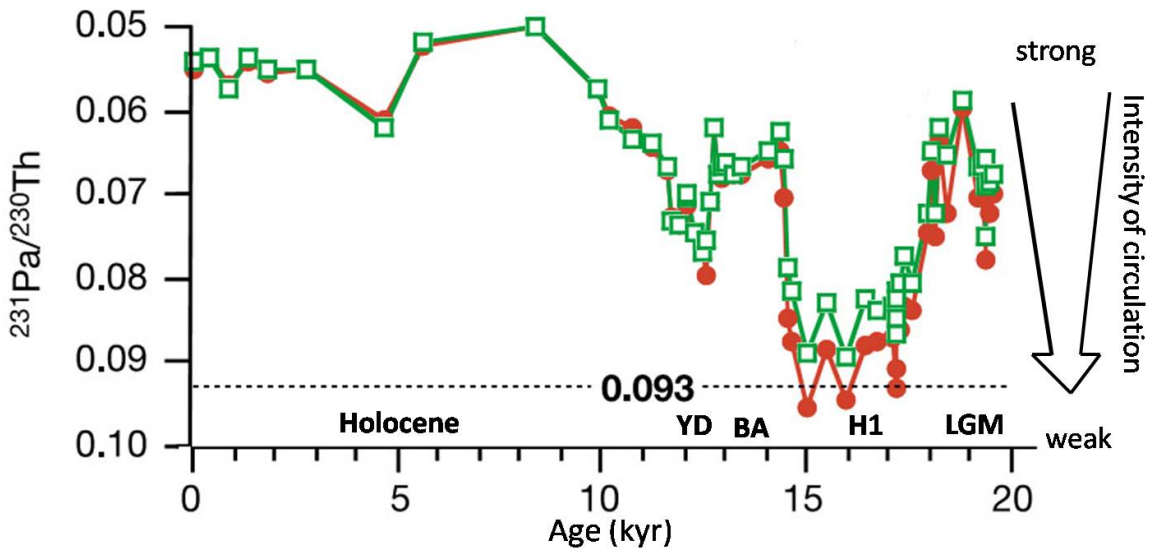


Figure 1.4: A schematic of the principal underlying the use of $^{231}Pa/^{230}Th$ as a deep ocean circulation tracer (Adapted from Henderson et al., 2002).

Based on this principal, a pioneering study by Yu et al. (1996) applied sedimentary $^{231}Pa/^{230}Th$ ratios to indicate little change in rates of ocean thermohaline circulation in the Atlantic between the Last Glacial Maximum (LGM) and the Holocene. In that study, Holocene sediments from the Atlantic were characterized by $^{231}Pa/^{230}Th$ ratios below the production ratio in the water column (0.093), whereas in the Southern Ocean sedimentary $^{231}Pa/^{230}Th$ were above 0.093. This pattern of ^{231}Pa depletion in Atlantic sediments and ^{231}Pa enrichment in Southern Ocean sediments was ascribed to southward ^{231}Pa export from the Atlantic by the Atlantic overturning circulation, while ^{230}Th was removed to sediment largely where it was formed. The same pattern was observed

in LGM sediment. Based on this observation, Yu et al. (1996) concluded that the net interbasin transfer of ^{231}Pa, and thus deep ocean circulation export to the Southern Ocean, were similar between the LGM and Holocene. Using the mean ^{231}Pa/ ^{230}Th ratios in Holocene sediments north of 50°S in the Atlantic, Yu et al. (1996) estimated that about 45% of the ^{231}Pa produced in the modern Atlantic water column was advected into the Southern Ocean, while only 15% of the ^{230}Th was exported.

A later study by McManus et al. (2004) applied this principle to link variations in past rates of deep-ocean circulation to abrupt glacial-deglacial climate changes by measuring sediment records of ^{231}Pa/^{230}Th in a core retrieved from the Bermuda rise in the deep western subtropical Atlantic. This study reported an abrupt increase of sedimentary ^{231}Pa/ ^{230}Th towards the production ratio of 0.093, starting at 17.5 kyr ago and continuing until 15 kyr ago (Figure 1.5). This result suggested a nearly total shutdown of the Meridional Overturning Circulation (MOC) that lasted more than 2000 yr during Heinrich event H1. Similarly, an abrupt increase in ^{231}Pa/^{230}Th at 12.7 kyr ago coincided well with the beginning of the Younger Dryas, suggesting a reduction of the Atlantic MOC during this period, although not to the same level as during H1. Abrupt resumption of Atlantic MOC was indicated by decreases in ^{231}Pa/^{230}Th ratios and can be associated with warm period such as Bølling-Allerød.



Figurer 1.5: Sediment records of ^{231}Pa/^{230}Th ratios in a high-accumulation-rate core retrieved from Bermuda rise in the deep western subtropical Atlantic (33°42'N, 57°35'W, 4.55 km). Red circles and green squares indicate ^{231}Pa/^{230}Th ratios corrected for the supported ^{230}Th and ^{231}Pa estimated from ^{238}U activity and ^{232}Th activity, respectively. Labels above the lower axis indicate climatic interval: Holocene, warm; YD, Younger Dryas, cooling; BA, Bølling-Allerød, warm; H1, Heinrich event 1, iceberg discharge; LGM, last glacial maximum. Higher values of ^{231}Pa/^{230}Th indicate less export of ^{231}Pa from the Atlantic, and thus lower rates of deep ocean circulation. A ratio of ^{231}Pa/^{230}Th equal to its production ratio in the water column (0.093) indicates a total cessation of deep ocean circulation (Adapted from McManus et al. (2004)). Note the inverted scale on the y-axis.

A series of studies have subsequently applied sediment records of ^{231}Pa/^{230}Th in the North Atlantic (e.g. Gherardi et al., 2009; Hall et al., 2006) to infer the linkage between Atlantic meridional overturning circulation and climate changes. However, controls other than deep-ocean circulation on the distribution of ^{231}Pa/^{230}Th in the ocean have also been suggested. Early work by Anderson et al. (1983b) had reported lower dissolved ^{231}Pa and ^{230}Th concentrations and ratios in the Panama and Guatemala Basins than in the open ocean. That study demonstrated that the scavenging of ^{230}Th and ^{231}Pa is intensified in these basins relative to the open ocean, and showed that particulate matter in these ocean-margin environment adsorb ^{230}Th and ^{231}Pa without detectable preference for one or the other. Ocean margins was therefore suggested to act as sinks for ^{230}Th and ^{231}Pa produced in the open ocean, and this enhanced scavenging occurring in these

regions is termed 'boundary scavenging'. Studies have suggested that this boundary scavenging might be caused by increased concentrations and fluxes of particulate matter compared to the open ocean, or by the presence at the margins of particulate phases which, by virtue of their unique chemical properties, are more efficient scavengers of trace metals than particles in the open ocean (Anderson et al., 1983b). A later study by Chase et al. (2002) examined the relative affinity of Th and Pa for sorption from seawater onto particles of variable compositions, i.e. opal, carbonate, lithogenic particles and organic carbon. That study showed that ^{230}Th is scavenged strongly by carbonate and lithogenics, while ^{231}Pa is scavenged strongly by opal. Both particle flux and composition are therefore important factors influencing the removal of ^{231}Pa and ^{230}Th from seawater, and thus their distribution in the ocean. Based on these observations, sediment records of ^{231}Pa/^{230}Th have been suggested to indicate variations in paleoproducitivity. Bradtmiller et al. (2007), for instance, examined seven cores from the equatorial and south Atlantic, and showed that down-core records of ^{231}Pa/^{230}Th are highly correlated with downcore opal records. Variations in sedimentary ^{231}Pa/^{230}Th ratios were interpreted as past changes in diatom productivity, rather than deep ocean circulation. Therefore, to better apply ^{231}Pa/^{230}Th to interpret past ocean environment, controls on the distribution of ^{231}Pa and ^{230}Th in the ocean, including those related to deep-ocean circulation, and to particle flux and composition, need to be further studied. Such investigation forms a significant part of this thesis, and is a particular focus of Chapter 3.

1.3 Sedimentary $^{230}Th_{xs}$ as a constant flux proxy

Once produced in seawater, ^{230}Th is rapidly removed from the water column to the seafloor in a way which can be explained by reversible scavenging models. This makes the ^{230}Th flux to the seafloor dependent only on the depth of the overlying water and on the concentration of ^{234}U in that water. Th-230 in the sediment consists of three fractions: 1) lithogenic ^{230}Th, the fraction that is locked in the mineral lattices of erosional debris, and transits rapidly through the water column without significant interaction with seawater; 2) scavenged ^{230}Th, the fraction that is derived directly from water-column ^{234}U decay; 3) authigenic ^{230}Th, the fraction that is produced from the decay of authigenic U in the sediment that is either adsorbed on oxides or precipitated in anoxic and suboxic sediments after diffusion from bottom waters (Barnes and Cochran, 1990; Klinkhammer and Palmer, 1991). Measured ^{230}Th therefore can be corrected for the presence of lithogenic and authigenic fractions of ^{230}Th to obtain $^{230}Th_{xs}$, the actual ^{230}Th flux to the seafloor derived directly from the overlying water column.

Assuming ^{230}Th flux to the seafloor equals its production rate in the overlying water column, $^{230}Th_{xs}$ can be used as a vertical flux proxy. The flux of other components from the water column into marine sediments can be assessed by measuring their concentration relative to that of $^{230}Th_{xs}$, given by (Bacon, 1984),

$$F_i = f_i \times \beta_{^{230}Th} \times z \,/\, ^{230}Th_{xs} \quad (1.3)$$

where F_i is the flux of component i in the sediment, g/m^2/yr; f_i is the weight fraction of component i in the sediment, %; z is the water depth, m; $^{230}Th_{xs}$ is the activity of scavenged ^{230}Th in sediment, dpm/g.

This approach gives an estimate for the instantaneous flux for that component at the time of its burial. It has been used, for instance, to assess carbonate fluxes to the seafloor in the equatorial Atlantic during the last 24,000 years (Francois et al., 1990) and to assess fluxes of windblown dust from the Sahara during the Holocene (Adkins et al., 2006).

Based on the same assumption, Suman and Bacon (1989) defined a focusing factor (Ψ) that quantifies syndepositional sediment redistribution:

$$\Psi = (\int_{z_1}^{z_2} {}^{230}Th_{xs}\rho_b \, dz) / \beta_{^{230}Th}(t_2 - t_1) \quad (1.4)$$

where z is the depth in the core, ρ_b is the dry bulk density of the sediment, and t_1 and t_2 are the ages of horizons z_1 and z_2.

$\Psi = 1$ indicates that sediments were unaffected by syndepositional redistribution; $\Psi > 1$ indicates sediment focusing, in which case lateral additional of ^{230}Th and associated sediment results in ^{230}Th accumulation rates higher than the production rate in the overlying water column; and $\Psi < 1$ indicates sediment winnowing, in which case lateral removal of ^{230}Th and associated sediment results in ^{230}Th accumulation rates lower than the production rate.

By assuming that particles accumulate on the seafloor with broadly constant syndepositional redistribution between stratigraphic age-control points, the accumulation of $^{230}Th_{xs}$ in marine sediments has also been used as a tool to determine relative variations in total

sedimentation rate between tie-points. This approach has been used, for instance, to determine the durations of short geomagnetic events (e.g. Knudsen et al., 2007; Bourne et al., 2012a).

All these applications are based on the assumption that ^{230}Th flux to seafloor is always equal to its production rate in the overlying water column. This assumption has been justified by a series of sediment-trap studies and model studies. Yu et al. (2011) analysed sampled obtained with deep-sea moored sediment traps deployed at 15 sites ranging from oligotrophic central gyres to ocean margins, and compiled these with existing sediment-trap data from the literature. That study showed that the flux of ^{230}Th measured in low flux regions amounts to 90 ± 6% of the production rate after correction trapping efficiency, and therefore confirmed that the flux of ^{230}Th scavenged to the seafloor remains close to its production rate from the decay of ^{234}U in the overlying water column. A model study by Henderson et al. (1999) also confirmed the assumption by GCM modelling to yield maps of the ^{230}Th flux to the sediment which indicates ~60-70% of the ocean floor receives a ^{230}Th flux within 30% of that expected from water column production. Larger deviations may arise, however, in the presence of boundary scavenging and deep ocean circulation (Francois et al., 2004).

This thesis makes use of ^{230}Th normalisation in a novel way to constrain post-depositional dissolution of sediment near to the sediment-water interface. This work is presented in Chapter 4.

1.4 Thorium-232 in the ocean

Another long-lived thorium isotope, ^{232}Th (half-life 1.40×10^{10} yr; Holden, 1990) also has great potential to understand certain processes in the ocean. Unlike ^{230}Th, ^{232}Th in the ocean is derived

from aeolian- or river-introduced detrital particles. Andersson et al. (1995) studied ^{232}Th along with ^{230}Th and uranium isotopes in fresh and brackish waters form the Baltic Sea and in the Kalixalven River. The study showed that the riverine ^{232}Th concentrations, governed by the discharge of the river, decreased in the low salinity region (<5‰), reaching a value close to that of seawater at a salinity of 7.5‰. Studies such as that, and the behavior of the short-lived thorium nuclides such as ^{230}Th, suggest that almost all of the riverine ^{232}Th is deposited in the low-salinity region of the estuary before it reaches the sea and that ^{232}Th found in the open ocean must be rather recently added to seawater. In the remote open ocean, ^{232}Th is therefore expected to be dominated by addition in wind-blown dust. After being introduced to the ocean, ^{232}Th is removed from the seawater in a way similar to ^{230}Th, i.e. adsorption onto sinking particles, and can also be explained by the reversible scavenging model, despite the fact that they are introduced to the ocean by different mechanisms.

The concentration of ^{232}Th in seawater shows substantial variations. An early study by Chen et al. (1986) reported a constant ^{232}Th concentration with water depth in the North Atlantic. Later studies, however, reported water-column profiles of ^{232}Th showing high concentrations at the surface, a mid-depth minimum and an increase towards the bottom (e.g. Cochran et al., 1987; Huh and Bacon, 1985). Roy-Barman et al. (1996) examined the source and fate of ^{232}Th in the central Pacific Ocean, and explained the absence of a surface maximum in the ^{232}Th profiles as a result of the low dust flux in the area. A more recent study by Hsieh et al. (2011) measured ^{232}Th in the Atlantic Ocean, showing high ^{232}Th concentrations in the surface water, which coincided well with the presence of Sahara dust plume in the studied area (Figure 1.6). Based on this observation, that study derived an approach to monitor the input of atmospheric dust to the ocean with ^{232}Th, which was adapted by a subsequent study by Hayes et al. (2013a) to estimate dust flux in the North

Pacific Ocean. These studies have demonstrated the potential for thorium isotopes to quantify dust deposition to the open ocean, but have also pointed out limitations on our present understanding of thorium chemistry in the ocean. A notable example is that the fraction of aerosol ^{232}Th that dissolves is poorly known, with direct implications for reconstruction of dust inputs. A better understanding of the source and fate of ^{232}Th in the ocean is required not only to better explain the variation of water-column profiles of ^{232}Th but also to provide robust evidence for its use to assess dust input to the ocean. An ability to better assess dust input would be useful given the significant impact that dust exerts on climate by supplying the surface of the open ocean with elements such as Fe that are essential for marine primary productivity. This thesis investigates the use of ^{232}Th as a tool to constrain dust input with work presented in Chapter 3 and, particularly, in Chapter 5.

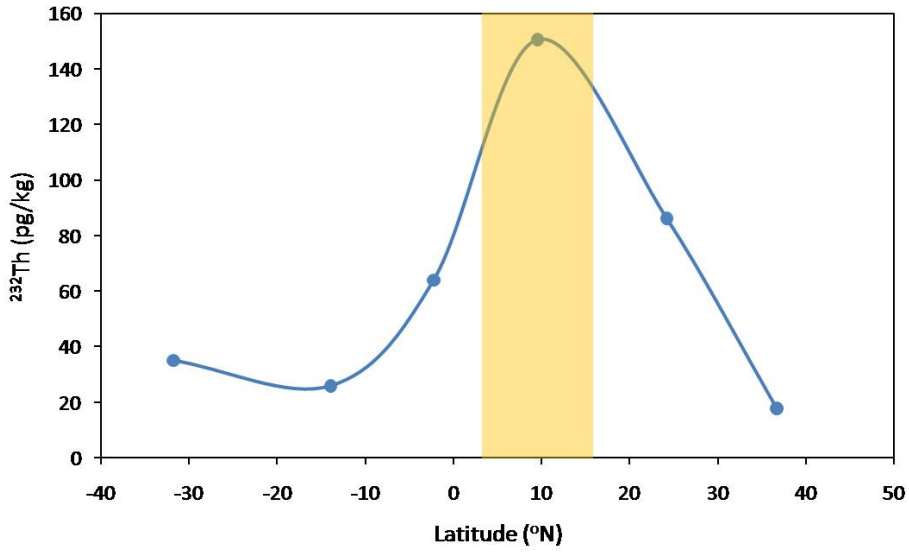


Figure 1.6: Th-232 concentrations in surface waters (~25 m) along an Atlantic transect from 32°N to 37°S. Yellow band indicates the high dust zone of the Saharan dust plume. (Adapted from Hsieh et al., 2011)

1.5 Goals and outline of the thesis

The goal of this thesis is to provide observational data of ^{230}Th, ^{231}Pa and ^{232}Th in ocean settings and to assess the robustness of using ^{230}Th, ^{231}Pa and ^{232}Th as proxies in the past and modern ocean. This includes examining the distribution these isotopes in seawater and sediment, and investigating processes that determine their oceanic distribution. With a better understanding of these isotopes, based on observation in the modern ocean, this thesis attempts to develop the uses of these isotopes to quantify oceanic processes.

The thesis consists of six chapters. This chapter has briefly introduced ^{230}Th, ^{231}Pa and ^{232}Th in the ocean setting, their sources and sinks, and some of their potential uses to study oceanic processes. Chapter 2 describes the method adopted to obtain the thorium and protactinium isotope data used in this thesis, which includes strategies for seawater and sediment sample collection, chemical analysis and mass spectrometry techniques. Chapter 3 examines controls of water-column distribution of ^{230}Th, ^{231}Pa and ^{232}Th in the Southwest Atlantic Ocean to provide an insight into the robustness of using ^{231}Pa/^{230}Th as a proxy to study rates of deep ocean circulation. Motivated by the prospect of applying sediment records of ^{231}Pa/^{230}Th to reconstruct past ocean environment, Chapter 4 assesses the preservation of water-column ^{231}Pa/^{230}Th records in the sediment, i.e. the impact of sediment dissolution on sedimentary ^{231}Pa/^{230}Th, and suggests a ^{230}Th-based approach to quantify sediment dissolution. Chapter 5 focuses on the distribution of water-column ^{232}Th in the tropical-subtropical Atlantic spanning an area under the influence of Saharan dust plume, to achieve a better understanding of the sources and fate of ^{232}Th in the ocean and to improve the Th-based approach to estimate dust input to the ocean proposed by previous studies.

Chapter 6 summarizes important conclusions from previous chapters and proposes future studies to compliment the study of thorium and protactinium isotopes in the ocean.

Chapter 2

Methods

2.1 Introduction

Early measurements of Th and Pa isotopes were performed by α-spectrometry, which entails complicated and time-consuming procedures for the separation and purification of each element before the measurement (e.g. Anderson and Fleer, 1982; Buesseler et al., 1992). This method requires large sample volumes of up to 200 liters for the measurement these isotopes in seawater and results in low precision (typically 5-10%) (e.g. Nozaki. et al., 1981; Nozaki and Nakanishi, 1985). With later development in mass spectrometry, well-established isotope dilution method was used in conjunction with thermal ionization mass spectrometry (TIMS) to determine Th and Pa isotopes in seawater samples (e.g. Edmonds et al., 1998; Moran et al., 1997, 1995; Vogler et al.,

1998). This method provides better sensitivity and precision than α-counting techniques for the measurement of low-concentration elements (typically 2-3%), and therefore dramatically reduces sample sizes to a few liters of seawater. TIMS techniques, however, are limited due to problems associated with ^{232}Th filament blanks and lower ionization efficiency for high Th loads. Sample preparation is also labor intensive. More recent development in inductively coupled plasma mass spectrometry (ICP-MS) provides an alternative technique for obtaining high-precision isotopic measurements for Th and Pa isotopes (e.g. Choi et al., 2001; Shen et al., 2002), and has advantages over TIMS in such aspects as superior ionization, fast analysis, multi-element capabilities, and simple sample preparation. Measurement of ^{231}Pa by ICP-MS is however still challenging due to its lower concentration than Th and U and the difficulty of preparing a suitable protactinium isotope for isotope dilution. This thesis adapted the techniques established in the University of Oxford by Thomas et al. (2006) using ICP-MS. The adapted method reduced the sample size to 5 liters of seawater (10 liters for surface) and produced data with higher precision. In this chapter, these techniques are described, including sampling strategies for seawater and sediment collection, element separation by anion exchange chromatography and isotope dilution method in conjunction with ICP-MS.

2.2 Sampling

2.2.1 Seawater samples

Seawater samples used in this thesis were collected from two GEOTRACES cruises, Netherlands-GEOTRACES cruise JC057 aboard RRS James Cook and UK-GEOTRACES cruise D361 aboard RRS Discovery. Cruise JC057 sailed from Punta Arenas, Chile (02-03-2011) to Las Palmas, Spain (06-04-2011). Full-depth seawater samples were collected by the author from 12 stations along the Southwest Atlantic transect (GEOTRACES section GA02) (Figure 2.1). Cruise D361 sailed from Tenerife, Canary Islands (Spain) (07-02-2011) to Tenerife (UK) (10-03-2011). Seawater samples were collected from five stations, in the sub-tropical Atlantic (GEOTRACES section GA06) by Dr. Maeve Lohan (Figure 2.1). Details of both cruises were described in their respective cruise report downloadable from the British Oceanographic Data Center (BODC) website.

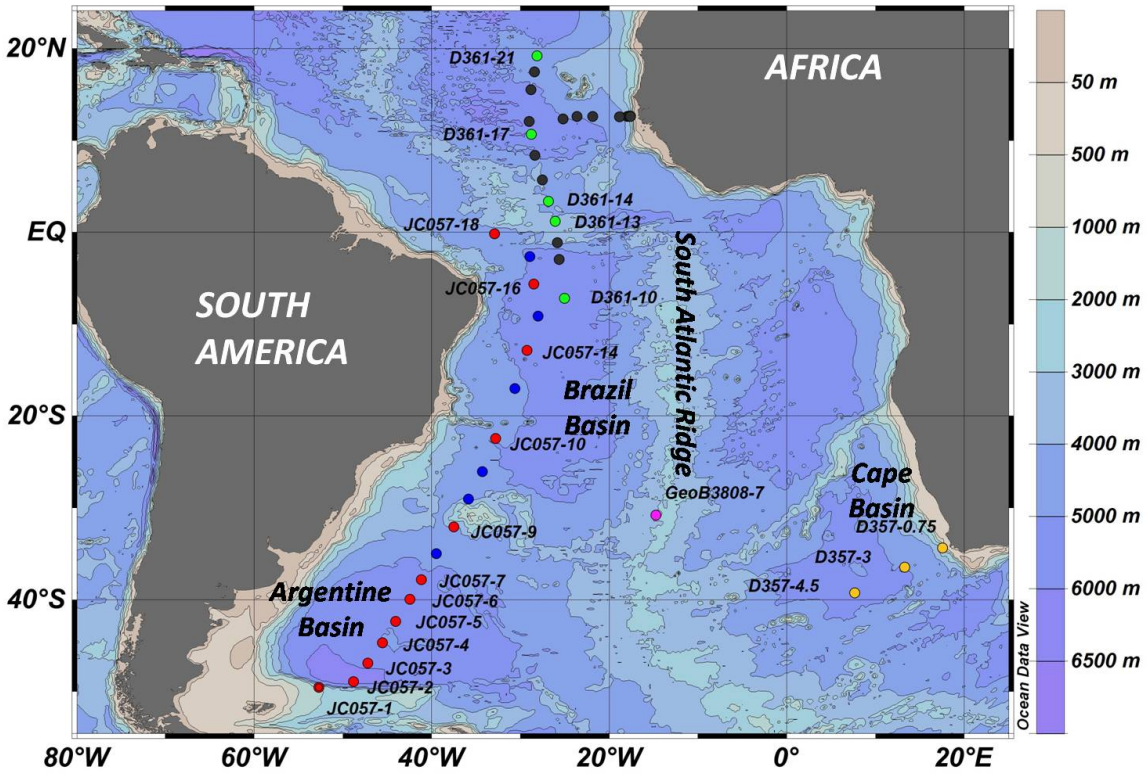


Figure 2.1: Sampling locations of seawater and sediment samples used in this thesis. Seawater samples were collected during Netherlands-GEOTRACES cruise JC057 (cruise track indicated by red and blue dots), and UK-GEOTRACES cruise D361 (cruise track indicated by green and black dots). Red and green dots indicate locations where seawater samples were collected during these cruises. Sediment samples were recovered from the Cape Basin during UK-GEOTRACES cruise D357, indicated by yellow dots, and from the South Atlantic Mid-Ocean Ridge during Meteor cruise M34/3, indicated by the pink dot.

Seawater samples were collected from 25 L Ocean Test Equipment (OTE) sampler bottles mounted on a stainless steel CTD (Conductivity, Temperature, Depth) rosette. Once the CTD rosette was recovered on deck, seawater samples of 5 L for all samples (except for the surface where 10 L was taken) were drawn directly from Niskin bottles after filtration through 0.45µm AcroPak Supor® hydrophilic polyethersulfone (PES) filter held in a polypropylene filter holder with a polycarbonate filling bell (Figure 2.2). The first few liters of seawater were used to thoroughly rinse the filter and sampling tube, and thus not collected into the sample bottle. Filtered seawater was collected directly into an acid-cleaned sample bottle made from high density

polyethylene plastic. This procedure minimizes the sample contact with the air, and hence contamination. Seawater samples were immediately acidified with 6-14 mL SEASTAR™'s BASELINE® HCl (w/w 32-35%) to pH <1.7 in a fume hood aboard the ship (Figure 2.3). Acidified samples were sealed with a screw top and parafilm to prevent contamination and evaporation, packed in two zip-lock bags and stored in the container at room temperature until arrival at home laboratory. This sampling strategy follows protocols suggested by GEOTRACES intercalibration work (Anderson et al., 2012).



Figure 2.2: Seawater sample collection. Seawater samples were colleced into acid-cleaned sample bottles directly from Niskin bottles mounted on a stainless CTD rosette after filtration through 0.45µm AcroPak Supor® filter.



Figure 2.3: Fume hood used for sample acidification aboard RRS James Cook. Seawater samples were acidified immediately after sampling to pH<1.7 in the fume hood to reduce potential contamination from the ship.

2.2.2 Sediment samples

Sediment samples used in this thesis were collected from the continental margin of Cape Basin during the UK-GEOTRACES cruise D357 in 2011, and from the South Atlantic Mid-Ocean Ridge during Meteor cruise M34/3 in 1996 (Figure 2.1). Details of both cruises were described in their respective cruise report downloadable from the British Oceanographic Data Center (BODC) website and the Center for Marine Environmental Sciences, University of Bremen website, respectively.

Two types of coring apparatus were used to recover sediments on D357, the Bowers Connelly Mega Core and the Box Core. The mega core was deployed using 8 core tubes at Cape Basin station D357-3 at a water depth of 4887 m. The box core was used for Cape Basin station D357-4.5 at 5269 m, and station D357-0.75 from the Cape Shelf slope at 1183 m. All the

recovered cores showed no signs of physical disturbance. For the sampling of sediment from the South Atlantic Mid-Ocean Ridge core GeoB3808-7 at 3213 m, a multicorer equipped with 8 large tubes of 10 cm and 4 smaller tubes of 6 cm diameter was used. Immediately after the recovery, sediment cores were sliced into 1 cm or 2 cm slices on the ship. Each slice was bagged separately, and stored in a refrigerator (4^{o}C) until arrival at home laboratory.

2.3 Clean lab overview

2.3.1 Laboratory conditions

Manipulation of all seawater and sediment samples subsequent to collection was performed in the clean-lab over-pressured with class 1000 hepa-filtered air at the University of Oxford. Handling of large volume seawater samples of 5-10 L, including sample weighing, acidification, spiking and co-precipitation, was performed on a clean-lab bench. All chemistry was performed in a laminar flow fume hood, over-pressured with class 100 filtered air. Preparation of ^{233}Pa spike was performed in a separate clean lab for the handling of radioactive material. This prevents the potential cross contamination between spike solution and the sample. At all times latex gloves and Tyvek clean suits were worn and clean lab clogs were worn to reduce contamination of the lab.

2.3.2 Reagents

Deionized water used throughout the work is 18 MΩ·cm high-purity water (Milli-Q water system, Millipore, Bedford, MA, USA). Distilled acids are sub-boiling distilled in quartz stills, from regent grade (RG) prepared in the clean lab at Oxford.

$NH_3 \cdot H_2O$ used for iron co-precipitation is isothermally distilled from reagent grade AnalaR Normapur® ammonia solution (28-32%).

Fe carrier was prepared from ~130 g of regent grade AnalaR Normapur® $FeCl_3 \cdot 6H_2O$ (~27 g of Fe) dissolved in 6N HCl, and purified by liquid-liquid extraction in isopropyl ether described in Thomas (2006). The resulting solution was dried down and dissolved in 270 ml of 2N HCl to make an approximately 100 mg/ml.

2.3.3 Cleaning procedures

High density polyethylene plastic sample bottles were soaked in 5% HCl (RG; Fisher Scientific) for at least 48 h, rinsed three times with 18 MΩ·cm Mill-Q water, capped, parafilmed and double-bagged before being sent to the ship for sample collection during the cruise.

All Teflonware (Savillex Corp.) was cleaned thoroughly before use, following the clean-lab cleaning protocols. Each vial was filled with half full of 2N HCl (RG), capped tightly and refluxed overnight on a hotplate at 100°C, and rinsed three times with 1 MΩ·cm water. Reversed aqua regia (15N HNO_3 (RG) and 10N HCl (RG) in a volume ratio of 3:1) was used instead of 2N HCl for vials used for sediment sample to remove organic matter residue. All Teflonware was then

cleaned in Teflon jars by heating on a hotplate at 100°C in 7.5N HNO_3 (RG) for at least 6 h, rinsing 3 times with 1MΩ·cm water, heating in 1MΩ·cm water for another 6 h, and rinsing again three times with Milli-Q water. Finally, each vial was filled with ~1 to 2 mL of 6N distilled HCl, capped tightly and refluxed on a hotplate at 100°C for at least 6 h, and rinsed three times with Milli-Q water before use.

Bottles used for storing acids were cleaned by soaking in the acid they were to be used to store on a hotplate overnight. All other plastics were soaked in 10% HNO_3 (RG) for at least 24 h and rinsed with Milli-Q water before use.

Dowex AG1-X8 resin (100-200 mesh) was cleaned with Milli-Q water, 6N distilled HCl, and Milli-Q water. Silica gel 60 (70-230 mesh) was cleaned with Milli-Q water, 7.5N distilled HNO_3, and Milli-Q water. This procedure with repeated at least five times before the resin is used.

2. 4 Spikes

2.4.1 Isotope dilution mass spectrometry

Isotope dilution mass spectrometry (IDMS) is an analytical method based on addition of a known amount of isotope (spike) to a sample with known isotopic composition of the analyte element but unknown element content. This spike contains the analyte element in a different isotopic composition: ideally enriched in the rarest natural isotope. After equilibration of the spike isotope with the natural element in the sample, sample gained a new isotopic ratio being between the isotopic ratio of the sample and that of the spike. The altered isotopic ratio is then measured by

mass spectrometry. The measured isotope ratio of isotope A to isotope B, R_m, can be calculated as follows:

$$R_m = \frac{A_x C_x W_x + A_s C_s W_s}{B_x C_x W_x + B_s C_s W_s} \qquad (2.1)$$

where A_x and B_x are the atom fractions of isotopes A and B in the sample; A_s and B_s are the atom fractions of isotopes A and B in the spike; C_x and C_s are the concentrations of the element in the sample and spike, respectively; and W_x and W_s are the weights of the sample and spike, respectively.

The concentration of the element in the sample can then be calculated:

$$C_x = (\frac{C_s W_s}{W_x})(\frac{A_s - R_m B_s}{R_m B_x - A_x}) \qquad (2.2)$$

The advantage of IDMS is that the chemical separation of an element needs not be quantitative. Once equilibration is achieved, the isotopic ratio defines the elemental concentration and this ratio will not change with element loss. Equilibration of the spike isotope and the natural isotope(s) is therefore critical in IDMS. In such scenarios as incomplete dissolution of the sample, selectively loss of the spike or sample isotopes before equilibration, or contamination in the dissolution process, the measured isotopic ratio(s) will not reflect the accurate ratio of added spike atoms to sample atoms for that element.

2.4.2 ^{229}Th -^{236}U spike

Mixed spikes containing ^{236}U and ^{229}Th of different concentrations were used for the IDMS of seawater sample (Oxford Water Spike) and sediment samples (Oxford Carbonate Spike). Because U and Th are measured in the same samples, a mixed spike reduces both the labor and the weighing errors involved in spiking samples. The compositions of both Oxford Water Spike and Oxford Carbonate Spike are listed in Table 2.1.

Calibration of the ^{229}Th-^{236}U spikes were conducted and described by Robinson et al. (2003). U-236 concentration is known from calibration against a certified gravemetric standard CRM-145, supplied by the New Brunswick Laboratory (see section 2.7.1). Th-229 concentration is known by calibration against a uraninite, Harwell- Uraninite-HU-1, which is in secular equilibrium with respect to ^{238}U/^{234}U and is within 1.3‰ of secular equilibrium for ^{238}U/^{230}Th (Cheng et al., 2000).

	Oxford Water Spike			Oxford Carbonate Spike		
	Atom %	Conc. g/g	2s.e. permil	Atom %	Conc. g/g	2s.e. permil
^{229}Th	0.32752	5.13×10^{-13}	15.7	0.99598	2.42×10^{-10}	2.4
^{230}Th	0.00075			0.00006		
^{232}Th	0.67182			0.00396		
^{234}U	7.23×10^{-11}			3.86×10^{-11}		
^{235}U	4.23×10^{-5}			4.21×10^{-5}		
^{236}U	0.99972	5.77×10^{-8}	1.4	0.99973	9.09×10^{-8}	0.8
^{238}U	0.00024			0.00023		

Table 2.1: Atomic abundances and concentrations of the two mixed ^{229}Th-^{236}U spikes: Oxford Water Spike and Oxford Carbonate Spike.

2.4.3 ^{233}Pa spike

Pa-233 (half-life 26.975 days; Usman and MacMahon, 2000) is used as a spike for the measurement of ^{231}Pa with IDMS, and prepared by "milking" from a ^{237}Np solution. The milking procedure was adapted from Regelous et al. (2004). The ^{237}Np solution, was stored in ~3 mL of 7.5N HNO_3+0.05N HF. ^{237}Np solution was fumed with 4 drops of concentrated $HClO_4$ to remove F^-, which is reactive with both Np and Pa. 10 mL of 7.5N HNO_3 were added to the solution, evaporated to a single drop, and redissolved in 2 mL of 7.5N HNO_3. This solution was loaded onto a polypropylene column containing 5.5 mL of pre-cleaned silica gel 60 (70-230 mesh) (see section 2.3.3), which had been washed with 20 mL of 7.5N HNO_3, 20 mL Milli-Q, and 20 mL of 7.5N HNO_3. The eluate was collected in a Teflon beaker (Np beaker). The column was then rinsed with 4×35 mL of 7.5N HNO_3. All the eluates were collected in separate Teflon beakers and combined after being dried down to small volumes. The Pa fraction was then eluted with 20 ml of 7.5N HNO_3 + 0.05N HF. The Pa fraction was checked with a hand monitor for α+β activity. If high α+β activity (^{233}Pa yield) was detected in the column, Pa was eluted with a mixed acid of higher HF concentration, i.e., 20 ml of 7.5N HNO_3 + 0.10N HF. After this elution, most of Pa should be eluted and can be checked with the hand monitor, showing lower α+β activity. The remaining Pa was eluted with another 20 ml of 7.5N HNO_3 + 0.10N HF. All Pa eluate was collected in a separate Teflon beaker (Pa beaker). The collected Pa solution was then evaporated to near dryness with 4 drops of concentrated $HClO_4$ and ~2 mL of concentrated HF, fumed with 2×10 mL of 7.5N HNO_3, and redissolved in 2 mL of 7.5N HNO_3. This Pa solution was then loaded onto a new column, and a second column pass was repeated to purify Pa from Np.

After collecting the second Pa fraction, the solution was evaporated to near dryness with 4 drops of concentrated $HClO_4$ and ~2 mL of concentrated HF, fumed with 2×10 mL of 7.5N HNO_3, and redissolved in 10 mL of 7.5N HNO_3. An aliquot of the Pa fraction was diluted with water, and the approximate Np/Pa ratio was determined by mass spectrometry. A separation factor of Pa from Np of > 10^6, corresponding to a $^{237}Np/^{233}Pa$ ratio of <30, was required in order that the effect of Np decay on the ^{233}Pa concentration of the spike solution over several half-lives was insignificant (Regelous et al., 2004). Generally, two column passes can meet this requirement. The purified ^{233}Pa spike was diluted to a concentration of ~300 fg/g with Mill-Q water to make up approximately 20 mL of 3N HNO_3, and stored with 50 uL of concentrated HF added in a parafilmed Teflon bottle. The combined Np solution was evaporated to near dryness with 4 drops of $HClO_4$, and stored for the next milking.

Two calibrations of ^{233}Pa spike were performed; one immediately after ^{233}Pa spike was milked, the other after all the ^{233}Pa had decayed to ^{233}U (several half-lives). To prepare the spike solution for calibrations, a diluted ^{229}Th-^{236}U Water Spike, containing ~ (4.37 ± 0.01) $\times 10^{-11}$ g/g ^{236}U and ~ (3.88 ± 0.04) × 10^{-16} g/g ^{229}Th, was added to an aliquot of ^{233}Pa spike solution. This solution was evaporated to near dryness, fumed with 2×100 μL of concentrated HNO_3, and redissolved in 42 uL of 7.5N HNO_3. The solution was then diluted with 958 μL Milli-Q to make 2×500 μL solution enough for two calibrations on mass spectrometer.

2.5 Sample weighing and pre-treatment

2.5.1 Procedures for seawater samples

Seawater samples were returned to the laboratory in Oxford for the analysis U-series isotopes. Seawater samples were weighed to ±5 g. Samples from cruise D361 were not acidified aboard the ship, and were thus acidified with distilled HCl to pH <1.7 after weighing. These samples were shaken and left for at least 48 hours to allow Pa and Th to desorb from the walls of the sample bottle.

A mixed ^{229}Th-^{236}U spike (Oxford Water Spike) and a ^{233}Pa spike made by milking from ^{237}Np were added to each sample (see sections 2.4.2 and 2.4.3). 50 mg of pre-cleaned Fe as a chloride solution (see section 2.3.2) was also added to each water sample. Samples were then left overnight to achieve sample-spike equilibration.

Isothermally distilled $NH_3 \cdot H_2O$ (see section 2.3.2) was then added to each sample to raise pH to ~8.5 to form insoluble Fe-oxyhydroxides to co-precipitate the actinides. Samples were shaken and left for up to two days for the Fe precipitate to settle. During its settling, samples were vigorously shaken several times to resuspend Fe precipitate to enhance the scavenging of the actinides in the seawater samples. Sample bottles were tilted in order for the precipitate to collect at one corner of the bottom of the bottle. The overlying water was then siphoned off with as little as possible precipitate being disturbed. The precipitate was then centrifuged to remove the remaining liquid and rinsed with Milli-Q H_2O several times to remove water-soluble salts. The precipitate was then dissolved with 2 mL Milli-Q water and 2 mL of 7.5N HNO_3, transferred to a

Teflon beaker, and evaporated to a small volume. Sample solution was refluxed with reversed aqua regia (3 ml of 15N HNO_3 and 1 mL 10N HCl for each sample) on a hotplate at 120^{o}C overnight to remove organic matter in the sample. Sample solution was then dried to a small volume, and fumed with 2 × 2 mL of 15N HNO_3 to remove any remaining HCl from the last step. After being evaporated to a small volume, sample solution was redissolved in 4 mL of 7.5N and refluxed overnight on a hotplate at 120^{o}C, after which it was ready for element separation.

2.5.2 Procedures for sediment samples

Sediment samples were digested prior to element separation. Cape Basin sediment samples (D357) were digested by Will Homoky in the laboratory at National Oceanography Center Southampton. Mid-Atlantic Ridge sediment (GeoB3808-7) was digested by Lukas Jonkers.

Aliquots of freeze-dried sediment samples was taken from bags spanning the top 0.5 to 24 cm of each core, grounded to a fine powder and homogenized with a ceramic mortar. Samples were then subject to total digestion using HCl, HNO_3, $HClO_4$ and HF acids. An aliquot of each digested sediment sample solution (~10 ml) in 8N HNO_3, containing approximately 0.05-0.1 g of sediment, was sent to the laboratory in Oxford. Sample solutions were weighed and spiked with a mixed ^{229}Th-^{236}U spike (Oxford Carbonate Spike) and a ^{233}Pa tracer solution (see sections 2.4.2 and 2.4.3). Sample solutions were then evaporated to a small volume on a hotplate at 100^{o}C followed by refluxing overnight with 4 mL of 7.5N HNO_3 at 100^{o}C, and was ready for element separation.

2.6 Elemental separation

2.6.1 Procedures for seawater samples

Pa, Th, and U in seawater samples were separated by anion exchange chromatography adapting the procedure described in Thomas et al. (2006). 10 mL Biorad column filled with 2 mL of pre-cleaned Dowex AG1-X8 anion-exchange resin (100-200 mesh) was washed with 10 mL Milli-Q water, 10 mL 6M HCl, 10 mL Milli-Q water, and preconditioned with 10 mL of 7.5N HNO_3. Each sample, dissolved in 4 ml of 7.5N HNO_3, was then loaded and washed into the column with a further 4 ml of 7.5N HNO_3. This washes off Fe and some U. The column was then converted to Cl^- with 1.5 mL of 6N HCl. Elution of Pa and Th was conducted with 7 mL of 6N HCl + 0.05N HF and collected in a Teflon beaker. The remaining U is eluted with 6 mL of Mill-Q water and collected in a separate Teflon beaker (U beaker). The Pa-Th split was evaporated to near dryness, redissolved in 2 mL of 7.5N HNO_3. The column chemistry was repeated to further remove U and to separate Th from Pa by elution of Th with 7 mL of 6N HCl followed by elution of Pa with 7 mL of 6N HCl + 0.05N HF. Th and Pa splits were evaporated to a single drop, fumed with 2 × 100 μL of 15N HNO_3, dissolved in 21 uL of 7.5N HNO_3 to remove HCl, and then diluted to 2% HNO_3 with Milli-Q water immediately prior to analysis.

2.6.2 Procedures for sediment samples

Separation of Pa, Th, and U in sediment samples was adapted from the anion exchange chromatography adopted for seawater samples. Unlike seawater samples, sediment samples have much higher Th concentrations, but lower U concentrations. Pa, Th, and U fractions are therefore eluted and collected separately during the first column pass. A second column pass is required for Pa fraction to purify Pa from Th.

Each sediment sample solution, dissolved in 4 mL of 7.5N HNO_3, was loaded onto an acid-washed and preconditioned 10 mL Biorad column filled with 2 mL of pre-cleaned Dowex AG1-X8 anion-exchange resin (100-200 mesh), as with seawater samples. A further 4 ml of 7.5 N HNO_3 was washed into the column to wash off Fe and some U. The column was then converted to Cl^- with 1.5 mL of 6N HCl. The Th fraction was eluted with 7 mL of 6N HCl and collected in a Teflon beaker (Th beaker). The Pa fraction, which is retained by the resin, was eluted into a separate Teflon beaker (Pa beaker) with 7 mL of 6N HCl + 0.05N HF. The remaining U is eluted with 6 mL of H_2O and collected in another Teflon beaker (U beaker).

The Pa fraction was then evaporated to near dryness, fumed with 2 × 100 μL of 15N HNO_3, and redissolved in 2 mL of 7.5 N HNO_3. A second column chemistry was repeated. The remaining Th was eluted with 7 mL of 6N HCl and discarded. The Pa fraction was eluted with 7 mL of 6N HCl + 0.05N HF and collected in the Pa beaker.

Pa, Th, and U splits were dried to a single drop, fumed with 2 × 100 μL of 15N HNO_3, and redissolved in 21 uL of 7.5N HNO_3 to remove HCl, and then diluted to 2% HNO_3 with Milli-Q immediately prior to analysis on mass spectrometry.

2.7 Mass spectrometry

2.7.1 Machine and standard

U-series isotopes were measured using a Nu Instruments Multi-collector inductively coupled mass spectrometer (MC-ICP-MS) at the University of Oxford. This mass spectrometer is a double focusing magnetic sector instrument with variable dispersion ion optics and a fixed array of 12 Faraday collectors (Belshaw et al., 1998). The layout of the instrument is shown in Figure 2.4. The general assembly for the Faraday detector array with three ion counting channels is shown in Table 2.2.

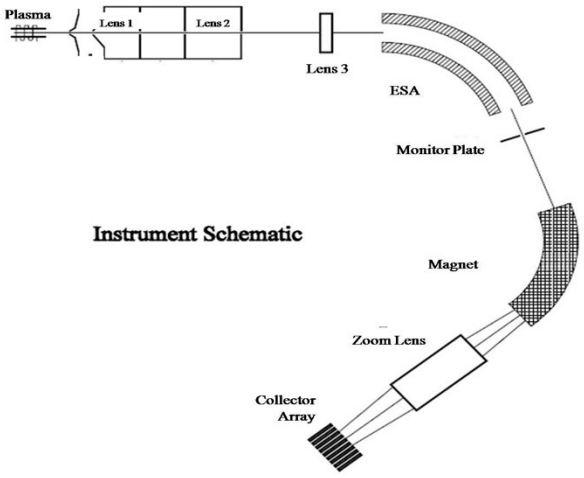


Figure 2.4: Schematic of the Nu instruments MC-ICP-MS. A lens stack (Lens 1, 2) was placed behind the cones to focus the beam. A further set of ion lenses (Lens 3) converts the shape of the beam to match the entrance aperture of the mass spectrometer. The major component of the 'double focusing' mass spectrometer is the arrangement of an electrostatic analyser (ESA) followed by a magnetic sector. The various beams, which are separated by mass by the magnet, are focused onto the collector array. Between the magnet and this array are placed two zoom lens arrays to alter the dispersion of the instrument and so moves the necessity for moveable collectors.

F_0	F_1	F_2	F_3	F_4	F_5	F_6	F_7	F_8	IC_0	F_9	IC_1	F_10	IC_2	F_11
F (+8)	F (+6)	F (+4)	F (+3)	F (+2)	F (+1)	AX - IAL	F (-1)	F (-2)	IC (-3)	F (-4)	IC (-5)	F (-6)	IC (-7)	F (-8)

Table 2.2: The general assembly for the collector array in the Nu instruments MC-ICP-MS. There are 12 Faraday collectors in total. We have adopted the convention to label the Faraday collectors from zero to eleven, with the lower numbers towards the outer (high mass) side of the instrument. Three ion counting channels (IC_0, IC_1 and IC_2) lie on the low mass side of the instrument between last four Faraday collectors (8 to 11). Faraday collector number 6 is on the instrument center line and is therefore the axial collector which defines the mass scale for the instrument. In this thesis, the collectors were referred to using the names listed in the bottom row. F indicates Faraday collector and IC indicates ion counting channel.

To obtain accurate and precise measurement on the double focusing MC-ICP-MS, especially for the measurement of low-concentration elements, four important aspects have to be taken into account: 1) mass fractionation, 2) Faraday/ion-counter gain, 3) isobaric interferences, and 4) abundance sensitivity.

It is known that heavier isotopes are transmitted more efficiently than lighter isotopes in ICP-MS. This physical effect is called mass fractionation, and causes a measurable mass bias in the obtained isotope ratios that needs to be corrected. Mass bias can be corrected for using isotopic reference materials of the element to be analyzed (external correction), other elements close in mass added to the sample (internal correction), or by measuring additional isotopes in combination with multiple linear regression (internal correction). In this thesis, an externally correction was made by bracketing each sample with a CRM-145 uranium standard.

Ion counter gain is the difference in the measurement of the same beam between an ion counter and a Faraday collector. In this thesis, gain was measured externally along with mass bias before and after each complete set of sample runs by measuring $^{238}U/^{235}U$ in a CRM-145 standard with ^{235}U beam in each ion counter and then a Faraday collector.

Isobaric interferences can result from elemental interferences, molecular ion interferences that can arise from the sample or residual gases in the mass spectrometer, and multiply-charged ions. These molecules formed have the same mass as an isotope of interest, and thus can add to the beam size measured and need to be accounted for. In this thesis, the most significant molecular interference is the formation of ^{232}ThH to contribution to the mass 233 beam. The magnitude of Th-hydride formation was assessed by monitoring the mass 233 beam on a pure ^{232}Th solution in IC(-3) with ^{232}Th in F(-4). Thomas (2006) measured ThH over time and showed that Th-hydration formation is time dependent, decreasing exponentially over time. This reduction of Th-hydration formation is likely to be caused by the removal of water vapor as the machine runs over a longer period (Crain and Alvarado, 1994). It is therefore essential to make this measurement throughout the sample run.

Abundance sensitivity is a measure of the contribution of the peak "tail" of a major isotope to an adjacent mass. It becomes a significant contribution to measurements when measuring small concentrations in the same solution as an isotope of relatively much greater concentration and slightly greater mass. For such measurements, an assessment of the abundance sensitivity must be made. In this thesis, abundance sensitivity was assessed by measuring the intensity at ½ amu either side of the mass of interest followed by the extrapolation to the desired abundance sensitivity. CRM-145 standard was used to assess the contribution of abundance sensitivity before and after each analysis.

Plasma noise and machine memory are also two factors that need to be taken into account for the measurement of low-concentration elements on MC-ICP-MS. Plasma noise between two steps was normalized using a large beam measured in Faraday collectors in each step. In this thesis, machine memory was minimized by ensuring that no concentrated solutions were run

immediately before sample measurements, that clean cones were used and by washing with washes of 2% and 10% HNO_3. Similar washes were carried out between each sample for 8-10 minutes. Machine memory that could not be removed by repeated washing was monitored by measuring each isotope in 2% HNO_3.

Most of the corrections described above were made by using a CRM-145 uranium standard with known isotopic ratios. CRM-145 standard is a gravemetric uranium standard made from a high purity metal, available from the New Brunswick Laboratory, NJ, USA. It has a natural $^{238}U/^{235}U$ ratio of 137.88 and $^{235}U/^{234}U$ close to natural at 137.19.

2.7.2 Measurement of Pa and Th isotopes for seawater samples

Concentrations of ^{231}Pa are very low in seawater. Samples are therefore run as concentrated as possible to maximize the beam sizes of ^{231}Pa and ^{233}Pa, i.e. all of the available ^{231}Pa is run in a solution of 700 μL. Measurement of the 231/233 mass ratio is performed using a two-step procedure with mass 233 and mass 231 measured sequentially in IC(-3) (Table 2.3). CRM-145 was added so that plasma noise could be corrected for intensity variation by normalizing the ^{238}U measured in each step. Machine memory for mass 231 and 233 was monitored by measuring each isotope in 2% HNO_3. Ion counter gain is assessed along with mass bias by bracketing samples with measurements of CRM-145 uranium standard, setting ^{235}U sequentially into an ion counter and then a Faraday collector. An assessment of abundance sensitivity on mass 231 and 233 as well as molecular interference from ^{232}Th, is made by monitoring ^{232}Th in each sample and bracketing every sample (or every two samples) with a measurement of a ^{232}Th solution.

F_0	F_1	F_2	F_3	F_4	F_5	F_6	F_7	F_8	IC_0	F_9	IC_1	F_10	IC_2	F_11
F (+8)	F (+6)	F (+4)	F (+3)	F (+2)	F (+1)	AX-IAL	F (-1)	F (-2)	IC (-3)	F (-4)	IC (-5)	F (-6)	IC (-7)	F (-8)
				238			235		233	232				
		238			235			232	231					

Table 2.3: Two-step run configuration for measuring protactinium in seawater samples.

Concentration of ^{230}Th is also very low in seawater, all the Th from each sample is measured in as small a volume as possible. Thorium was measured in a two-step dynamic routine with mass 229 and mass 230 measured sequentially in IC(-3) (Table 2.4). Intensity variations between steps were corrected for by normalizing the ^{235}U measured in each step. CRM-145 U standard was added to the sample solution to facilitate this correction. Although both ^{229}Th and ^{230}Th are measured in the same ion counter and does not require correction for ion counter gain, ^{232}Th is of interest in the study and a gain correction for the 232/229 mass ratio is required. Each sample is therefore bracketed with CRM-145 uranium standards to measure the ion counter gain and mass bias. A single step measurement of the gain is used with ^{234}U measured in the ion counter. Machine memory was monitored by measuring each isotope in 2% HNO_3 before each sample.

F_0	F_1	F_2	F_3	F_4	F_5	F_6	F_7	F_8	IC_0	F_9	IC_1	F_10	IC_2	F_11
F (+8)	F (+6)	F (+4)	F (+3)	F (+2)	F (+1)	AX-IAL	F (-1)	F (-2)	IC (-3)	F (-4)	IC (-5)	F (-6)	IC (-7)	F (-8)
	238		235			232			229					
				235			232		230					

Table 2.4: Two-step run configuration for measuring thorium in seawater samples.

2.7.3 Measurement of U-series isotopes for sediment samples

Protactinium concentrations are relatively low in sediment samples. As with seawater samples, sediment samples are therefore run as concentrated as possible following the protocol used for the measurement of protactinium in seawater (see section 2.7.2).

The high concentrations of ^{238}U and ^{232}Th in sediment samples require the U and Th fractions to be diluted before it is run on the MC-ICP-MS. Small and diluted aliquots of the U and Th fractions were used for a rapid concentration check of ^{238}U and ^{232}Th to optimize their intensities to match a mixed solution of Th and CRM-145 standard at ~5 V for ^{232}Th and ~2.5V for ^{238}U in the final measurement.

Uranium was measured statically with ^{238}U, ^{236}U, and ^{235}U focused in Faraday collectors, F(+1), F(-1) and F(-2), and ^{234}U in an ion counter, IC(-3) (Table 2.5). Samples were bracketed by CRM-145 standards to correct for mass bias, abundance sensitivity, and ion counter gain. A CRM-145 standard was run between samples as a dummy sample to assess the reproducibility of the measurements.

F_0	F_1	F_2	F_3	F_4	F_5	F_6	F_7	F_8	IC_0	F_9	IC_1	F_10	IC_2	F_11
F (+8)	F (+6)	F (+4)	F (+3)	F (+2)	F (+1)	AX-IAL	F (-1)	F (-2)	IC (-3)	F (-4)	IC (-5)	F (-6)	IC (-7)	F (-8)
					238		236	235	234					

Table 2.5: Run configuration for measuring uranium in sediment samples.

Thorium was measured in a two-step dynamic routine with mass 230 and mass 229 measured sequentially in IC(-3), correcting for intensity variation by normalizing the ^{235}U

measured in each step (Table 2.6). In cases where the sample ^{235}U signal in the diluted Th fractions was below 5mV, CRM-145 standard was added to the Th solution to increase the beam size to ~10mV to facilitate this correction. Although both ^{229}Th and ^{230}Th are measured in the same ion counter and does not require correction for ion counter gain, a gain correction for the 232/229 mass ratio is required. Each sample was therefore bracketed with CRM-145 uranium standards to correct for the ion counter gain using the standardized $^{235}U/^{234}U$ ratio of CRM-145 measured with ^{234}U in the ion counter in a single step. Machine memory was monitored by measuring each isotope in 2% HNO_3.

F_0	F_1	F_2	F_3	F_4	F_5	F_6	F_7	F_8	IC_0	F_9	IC_1	F_10	IC_2	F_11
F (+8)	F (+6)	F (+4)	F (+3)	F (+2)	F (+1)	AX-IAL	F (-1)	F (-2)	IC (-3)	F (-4)	IC (-5)	F (-6)	IC (-7)	F (-8)
				235			232		230					
238			235			232			229					

Table 2.6: Two-step run configuration for measuring thorium in sediment samples.

2.7.4 ^{233}Pa spike calibration

Pa-233 spike calibration was performed by measuring 233/231 and 236/233 mass ratios. 233/231 mass ratios were measured following the procedure for the measurement of protactinium in seawater (see section 2.7.2). 236/233 mass ratios were measured in a single step with ^{236}U beam focused in IC(-3) (Table 2.7). As with Pa measurement in seawater, mass discrimination and ion-counter gain were assessed by bracketing each sample analysis with measurement of the CRM-145 standard. Measurements were also made 0.5 amu either side of masses of interest to allow accurate

correction for the effect of abundance sensitivity on small ^{231}Pa and ^{230}Th beams, and a correction for ^{232}ThH interference on mass 233 was made from assessments of the hydride formation rate from a ^{232}Th standard. Machine memory was monitored by measuring each isotope in 2% HNO_3.

F_0	F_1	F_2	F_3	F_4	F_5	F_6	F_7	F_8	IC_0	F_9	IC_1	F_10	IC_2	F_11
F (+8)	F (+6)	F (+4)	F (+3)	F (+2)	F (+1)	AX-IAL	F (-1)	F (-2)	IC (-3)	F (-4)	IC (-5)	F (-6)	IC (-7)	F (-8)
				238			235		233					
		238			235				231					
							238		236	235				

Table 2.7: Run configuration for ^{233}Pa spike calibration.

2.8 Data processing

Raw data obtained from ICP-MS measurement were processed with a program, Donkey, developed by Andrew Mason at University of Oxford to make corrections for ICP-MS measurement. These corrections include ion counter gain, plasma noise, machine memory, non-linearity, abundance sensitivity, ion interference and mass fractionation. Uncertainties from these corrections were propagated by Donkey and reported as 2 standard errors (2 s.e.), i.e. twice the standard deviation on the ratio divided by the square root of the number of runs. Corrected ICP-MS data were then processed in Excel^{TM} spreadsheets to obtain the final concentrations for thorium, protactinium and uranium, during which blanks were subtracted for each sample.

2.9 Blanks and Uncertainties

Total procedural blanks were determined by performing a complete chemical procedure on ~100 ml of Milli-Q water with each batch of samples, and are summarized in Appendix Table 2.1. Blanks for ^{231}Pa, ^{230}Th and ^{232}Th in seawater samples are 0.5 ± 1.1 fg, 0.3 ± 1.0 fg and 22.8 ± 23.2 pg, respectively (uncertainties are 2 standard deviations). Blank contributions account for 0.6-56%, 0.1-4%, and 1-29% of the dissolved ^{231}Pa, ^{230}Th and ^{232}Th respectively. High values are for surface samples due to their low concentrations. Blanks for ^{231}Pa, ^{230}Th, ^{232}Th and ^{238}U in sediment samples are 0.77 ± 1.39 fg, 1.36 ± 3.36 fg, and 128.5 ± 95.2 pg, 132.8 ± 109.3 pg, respectively, and are always less than 1 % of the mass in analysed samples. Sources contributing to blanks might be Fe carrier solution, resin, and ^{229}Th-^{236}U and ^{233}Pa spikes.

Typical uncertainties of ^{231}Pa, ^{230}Th and ^{232}Th for seawater samples are ±0.03 dpm/1000 l, ±0.05 dpm/1000 l, and ±0.001 dpm/1000 l, respectively. For sediment samples, average total uncertainties for ^{230}Th, ^{232}Th and ^{231}Pa and ^{238}U are ±0.129 dpm/g, ±0.010 dpm/g, ±0.024 dpm/g, and ±0.003 dpm/g, respectively. Most uncertainties come from blank correction and measurements on MC-ICP-MS (with the largest uncertainty coming from memory measurement).

Chapter 3

Controls on seawater ^{231}Pa, ^{230}Th and ^{232}Th concentrations along the flow paths of deep waters in the Southwest Atlantic

A reformatted version of this chapter was published as: Deng, F., Thomas, A.L., Rijkenberg, M.J.A., Henderson, G.M., 2014. Controls on seawater ^{231}Pa, ^{230}Th and ^{232}Th concentrations along the flow paths of deep waters in the Southwest Atlantic. Earth and Planetary Science Letters 390, 93-102. doi:10.1016/j.epsl.2013.12.038. It is reproduced here in thesis format.

Abstract

Measurements of dissolved ^{230}Th, ^{231}Pa and ^{232}Th were made for twelve full-depth profiles along a Southwest Atlantic section during GEOTRACES cruise GA02S. Sampling captures all the main Atlantic deep water masses along their meridional flow paths and allows insight into the control on Th and Pa in a setting where waters are flowing in opposing directions, with direct relevance to understanding the use of ^{231}Pa/^{230}Th as an ocean-circulation proxy. Water-column ^{230}Th increases linearly with depth, in line with expected reversible scavenging models. ^{231}Pa increases from the surface to ~1200-1500 m, but is invariant or decreases with greater depth, deviating from the behaviour expected for reversible scavenging. Dissolved ^{231}Pa/^{230}Th ratios display a mid-water-column maximum at ~1000-2000 m which is broadly coincident with Upper Circumpolar Deep Water. Below 2000m, nuclide distributions and ratios exhibit no dependence on water mass, nor any indication of progressive change within a water mass, challenging the use of ^{231}Pa/^{230}Th as a past circulation tracer in the South Atlantic. Calculation of horizontal transport of ^{230}Th and ^{231}Pa by ocean circulation indicates a net southward export out of the Atlantic of 19% of the ^{231}Pa and 3% of the ^{230}Th produced in that ocean. This removal is all from the North Atlantic while, in the South Atlantic, removal to sediment equals production. Simple one-dimensional modeling can simulate ^{230}Th profiles but not the mid-water-column maximum observed in ^{231}Pa profiles, suggesting an additional source of ^{231}Pa (perhaps lateral transport from the margin) or removal at depth due to bottom scavenging. Near seafloor minima in concentrations indicates bottom scavenging of ^{230}Th and ^{231}Pa, which is enhanced in the presence of nepheloid layers, particularly for ^{231}Pa. This additional scavenging fractionates ^{230}Th and ^{231}Pa and, in the presence of nepheloid layers, may lead to an increase in sedimentary ^{231}Pa/^{230}Th ratios. ^{232}Th concentrations

were paired with ^{230}Th-derived residence times in the upper 250 m of the water column to test the application of Th as a tracer of dust deposition. Maxima in ^{232}Th indicate high dust input from the African and possibly South American continents.

3.1 Introduction

Deep ocean circulation is central to our understanding of climate change and the global carbon cycle because it transports heat and carries a significant amount of CO_2 deep into the ocean, keeping it from returning to the atmosphere. Studies of past deep ocean circulation apply nutrient-like tracers, such as carbon isotopes ($\delta^{13}C$) (Curry et al., 1988) or Cd/Ca (Boyle, 1988) in benthic foraminifera, to assess the distribution of water masses. These tracers, however, provide little information about the rate of deep water flow, which ultimately controls heat transport and CO_2 storage. To provide such rate information, sedimentary ^{231}Pa/^{230}Th ratios have been investigated and applied in the North Atlantic (Gherardi et al., 2009; McManus et al., 2004; Yu et al., 1996) and elsewhere (Hoffmann et al., 2013; Negre et al., 2010; Thomas et al., 2007).

Pa-231 (half-life 32.76 kyr) and ^{230}Th (half-life 75.58 kyr) are naturally occurring radionuclides in the ocean, produced through α-decay of dissolved ^{235}U and ^{234}U respectively. Since uranium concentration in seawater is reasonably constant in both space and time, ^{231}Pa and ^{230}Th are produced at a constant ratio (of 0.093, expressed as an activity ratio). Once produced, these two particle-reactive nuclides are adsorbed onto particles and removed from seawater as the particles settle to the sediment. Highly particle-reactive ^{230}Th (residence time 20-40 yr, Henderson and Anderson, 2003) is rapidly removed to sediment, while less particle-reactive ^{231}Pa (residence time 100-120 yr) can be transported by advection or mixing to areas of high-scavenging before it is removed. During advection of deep-water away from its site of formation, the lower particle reactivity of ^{231}Pa is expected to lead to a progressively increasing concentration along the flow path as the water ages. If the resulting increase in ^{231}Pa/^{230}Th is captured and preserved in

underlying sediments, they will record a history of past flow rates of the deep water. If the rate of deep-water flow varies, ^{231}Pa/^{230}Th is expected to vary accordingly, with lower sedimentary ^{231}Pa/^{230}Th ratios indicating faster water flow. The ^{231}Pa/^{230}Th ratio is therefore considered a potential proxy with which to reconstruct the rates of past ocean circulation.

Yu et al. (1996) first suggested the use of ^{231}Pa/^{230}Th as a paleo-circulation proxy, mapping out the ^{231}Pa/^{230}Th ratio in Holocene and LGM (Last Glacial Maximum) sediment in the Atlantic Ocean to infer similar rates of modern and last-glacial thermohaline circulation. Subsequently, McManus et al. (2004) applied ^{231}Pa/^{230}Th to a sediment core in the subtropical North Atlantic to suggest the collapse and rapid resumption of Atlantic meridional circulation associated with millennial scale climate events of the last 20kyr, an approach pursued in subsequent North Atlantic studies (Gherardi et al., 2009; Hall et al., 2006). These studies indicated linkage between Atlantic meridional circulation and abrupt climate change.

Other studies, however, have suggested that the oceanic distribution of ^{230}Th and ^{231}Pa is controlled largely by particle flux, particle composition, and boundary processes, rather than ocean circulation. Chase et al. (2003), for instance, reported down-core ^{231}Pa/^{230}Th records from the Pacific sector of the Southern Ocean and interpreted variations in ^{231}Pa/^{230}Th as due to changing opal productivity rather than rates of ocean circulation. Bradtmiller et al. (2007) provided a similar interpretation for ^{231}Pa/^{230}Th records for cores in the Equatorial Atlantic, although Lippold et al. (2012) observed a lack of correlation between opal and ^{231}Pa/^{230}Th in a compilation of Holocene ^{231}Pa/^{230}Th and biogenic silica measurements in the Atlantic sediment. To make use of ^{231}Pa/^{230}Th as a paleo-circulation tracer clearly requires a thorough understanding of the processes controlling the water-column distributions of these nuclides so that the competing impact of other factors, such as opal productivity, can be understood.

The South Atlantic Ocean has been the focus of recent sediment down-core ^{231}Pa/^{230}Th records (Negre et al., 2010), and is characterized by a pattern of deep-water circulation, with multiple water masses flowing in different directions. This modern pattern is somewhat similar to that suggested by water-mass proxies (e.g. Lynch-Stieglitz et al., 2007) for the whole Atlantic during the last glacial period, with deep northerly flowing waters underlying mid-water-depth southerly flow. The modern South Atlantic therefore provides an opportunity to assess the controls on ^{230}Th and ^{231}Pa in a region of relatively complex modern deep-water flow, with relevance to a critical period of past earth history.

Measurements of water-column ^{230}Th and ^{231}Pa provide important understanding of the ocean behavior of these nuclides, but have not been widespread in the South Atlantic. A range of such measurements in the North Atlantic (e.g. Cochran et al., 1987; Mangini et al., 1983; Moran et al., 1997; etc.) have greatly improved our understanding of the oceanic distribution of ^{230}Th and ^{231}Pa in that basin, but data in the South Atlantic are less complete, although measurements have been made in a number of previous studies (Hsieh et al., 2011; Luo et al, 2010; Moran et al., 2002; Rutgers van der Loeff and Berger, 1993; Scholten et al., 2008). In this study, we present dissolved ^{230}Th and ^{231}Pa data for twelve full-depth profiles in the Southwest Atlantic collected during GEOTRACES cruise GA02S. Based on these water-column profiles, we assess the extent to which water-mass advection and particle cycling have an influence on the distribution of ^{230}Th and ^{231}Pa when flow is present in two directions. These data significantly expand the data coverage for the South Atlantic Ocean and the global extent of water-column ^{230}Th and ^{231}Pa. We also report water-column ^{232}Th data from this section to assess its use as a dust input tracer, as recently suggested in the Atlantic (Hsieh et al., 2011) and Pacific (Hayes et al., 2013a) oceans.

3.2 Sampling strategies and settings

Samples were collected during GEOTRACES cruise GA02S in March 2011 on board the RRS James Cook (cruise 74JC057) (Figure 3.1). Seawater samples of 5-10 l were drawn from Niskin bottles mounted on a CTD rosette into acid-cleaned polyethylene bottles after filtration through 0.45μm AcroPak Supor® filters, following protocols suggested by GEOTRACES intercalibration work (Anderson et al., 2012). They were immediately acidified to pH~1.7 with concentrated HCl.

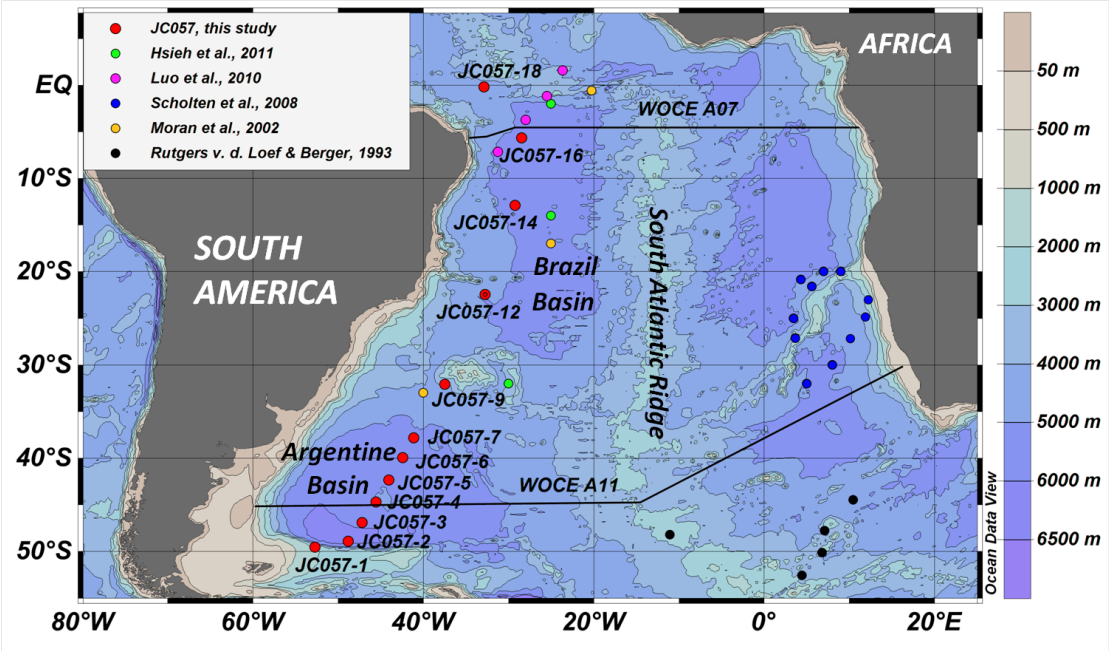


Figure 3.1: Map of sampling stations during GEOTRACES cruise JC057. Locations sampled for this study are indicated by red dots and labeled. Also noted are locations of previous measurements of water-column ^{231}Pa and ^{230}Th in the South Atlantic from references listed in the key. Black lines define the WOCE sections A07 and A11 used in Section 5.1 of the text to assess meridional transport of ^{230}Th and ^{231}Pa.

Temperature, salinity, phosphate, and other hydrographic parameters were measured at each sampling station and are used for water mass identification (Figure 3.2). The region features

four main water masses beneath the surface mixed layer. A low-salinity water mass, Antarctic Intermediate Water (AAIW), is found at a depth of about 500 m near 50°S, deepens to 1200 m at 35°S, and has a net northward flow. This water has a southern origin from the surface of the circumpolar region, and is formed particularly in the northern Drake Passage and the Falkland Current loop (Stramma and England, 1999). Below AAIW, Upper Circumpolar Deep Water (UCDW) is seen at ~1000-1500 m and can be identified by a phosphate maximum (Figure 3.2c), which reflects the properties of the parental deep water from the Indian and Pacific Ocean. The deepest water mass, characterized by low temperatures, is Antarctic Bottom Water (AABW), which flows northward, having formed over the Antarctic slope in regions such as the Weddell and Ross Sea (Morozov et al., 2010). Separating these southern-sourced waters is a southward flowing thick layer of relatively saline, low-phosphate water: North Atlantic Deep Water (NADW). It occurs at depths of ~1200-4000 m near the equator, with its thickness decreasing to a range from about 2400 to 3200 m at ~35°S, where it changes its propagation direction to be largely zonal toward the east (Larqué et al., 1997).

To characterize the optical property of the water, beam attenuation coefficients were obtained using a Wetlab C-Star Deep Red transmissiometer of 0.25 m path length centered at 660 nm along the transect (Figure 3.2d). High values of beam attenuation coefficient were found within 500 m of the seafloor, particularly at 35-50°S, suggesting the occurrence of nepheloid layers containing resuspended particulate matter in that area.

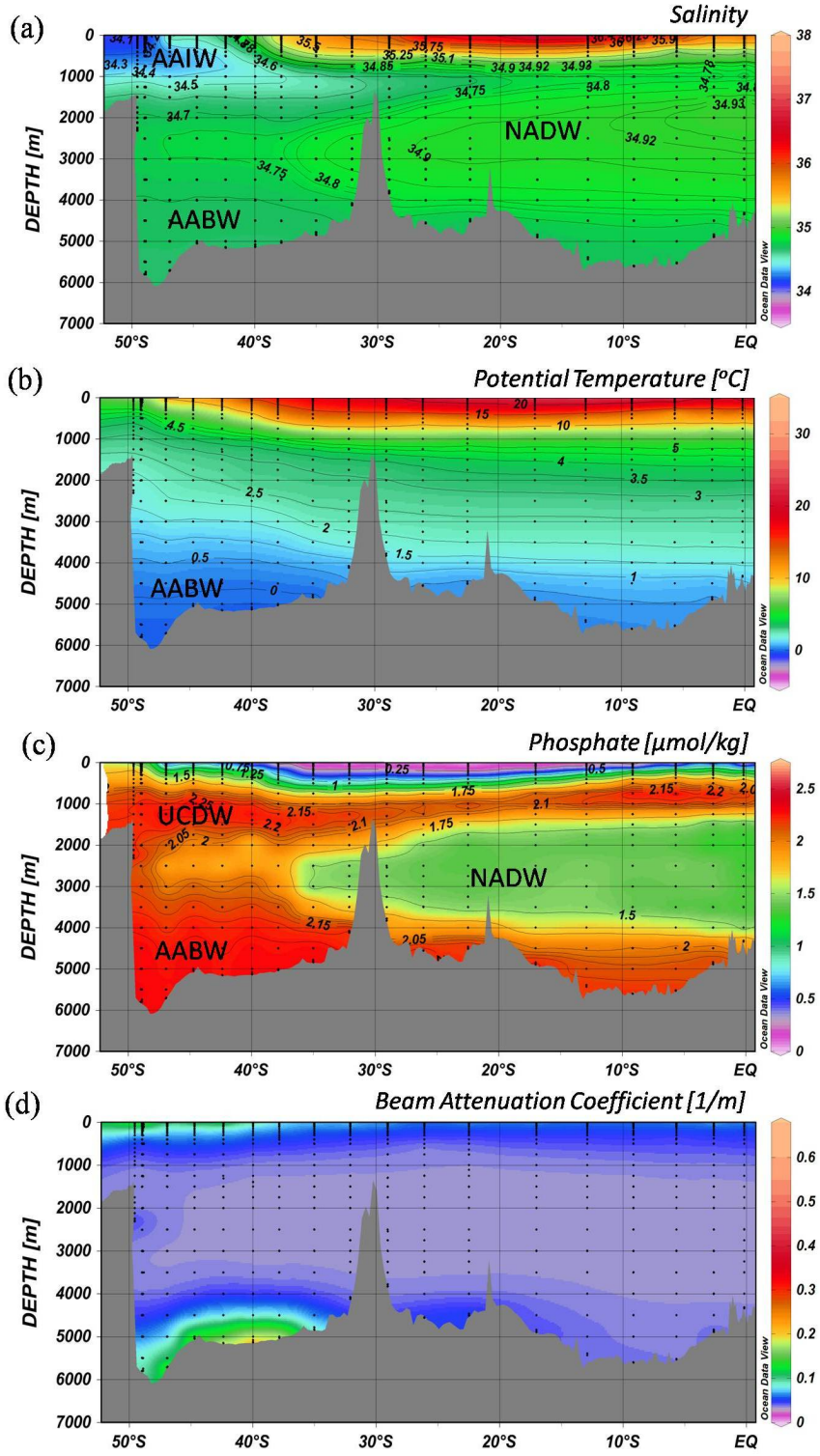


Figure 3.2: Vertical distributions of (a) salinity; (b) potential temperature; (c) dissolved phosphate concentration and (d) beam attenuation coefficient along the GEOTRACES GA02S section.

3.3 Analytical techniques

Acidified samples were returned to the laboratory in Oxford and weighed. A mixed ^{229}Th-^{236}U spike and a ^{233}Pa spike were added to each sample. ^{233}Pa spike was made by milking from ^{237}Np (following Regelous et al., 2004) and was calibrated against a known ^{236}U solution after complete decay of ^{233}Pa to ^{233}U (i.e. several months after spike production). 50 mg of pure Fe as a chloride solution was also added to each water sample. Samples were then left overnight to allow for spike equilibrium after which the pH was raised to ~8.5 using distilled NH_4OH to co-precipitate the actinides with insoluble Fe-oxyhydroxides. The precipitate was centrifuged and rinsed, and Th, Pa and U were separated using anion exchange chromatography following Thomas et al. (2006).

After chemical separation, Pa and Th were measured on Nu instruments MC-ICP-MS (Multi Collector Inductively Coupled Plasma Mass Spectrometry) at the University of Oxford. Mass discrimination and ion-counter gain were assessed by bracketing each sample analysis with measurement of the CRM-145 U. Use of a U standard for this purpose minimizes memory problems that might be caused by use of a Th or Pa standard (Thomas et al., 2006). Measurements were also made 0.5 amu either side of masses of interest to allow accurate correction for the effect of abundance sensitivity on small ^{231}Pa and ^{230}Th beams, and a correction for ^{232}ThH interference on mass 233 is made from assessments of the hydride formation rate from a ^{232}Th standard.

Chemistry blanks were determined by performing a complete chemical procedure on ~100 ml of Milli-Q water with each batch of samples. Based on nine blank measurements, blanks for dissolved ^{231}Pa, ^{230}Th and ^{232}Th are 0.4±0.2 fg, 0.2±0.2 fg and 19.8±8.1 pg, respectively (uncertainties are 2 standard deviations). Blank contributions account for 0.6-28%, 0.1-3%, and 1-

29% of the dissolved ^{231}Pa, ^{230}Th and ^{232}Th respectively (with the higher values being for surface samples due to their low concentrations).

All measured ^{230}Th and ^{231}Pa concentrations were corrected for, 1) ingrowth from radioactive parents in seawater since the time of collection, and 2) detrital, U-supported ^{230}Th and ^{231}Pa concentrations. These corrections are detailed in Appendix Table 3.1.

All uncertainties in this manuscript are 2 standard errors (2se) including the contribution from sample weighing, spike calibration, impurities in the spikes, blank corrections, and mass spectrometric measurement. Average total uncertainties for ^{231}Pa, ^{230}Th and ^{232}Th are ±0.03 dpm/1000 l, ±0.02 dpm/1000 l, and ±0.0004 dpm/1000 l, respectively.

3.4 Results

Measured and corrected activities of ^{231}Pa, ^{230}Th and ^{232}Th are provided in Appendix Table 3.1. Although analysis was conducted in terms of fg/kg, results are converted to dpm/1000 l for ease of comparison with previous work. This conversion assumes that the density of seawater was uniformly 1.025 g/cm^3 and half-lives for ^{231}Pa, ^{230}Th and ^{232}Th of 32,760 yr, 75,584 yr and 1.40×10^{10} yr respectively (Cheng et al., 2013; Robert et al., 1969; Holden, 1990). Results are plotted in cross sections in Figure 3.3, and as individual profiles in Appendix Figure 3.1.

Th-230 concentrations in the water column range between 0.004 and 1.27 dpm/1000 l and increase broadly linearly with depth (Figure 3.3a) in line with commonly expected reversible scavenging models for ^{230}Th (e.g. Bacon and Anderson, 1982). In waters within 500 m of the seafloor, however, particularly in the Argentine Basin, ^{230}Th concentrations decrease slightly

toward the bottom. Horizontally, there is little ^{230}Th gradient in waters more than 500 m above the seafloor, except somewhat lower values at depth in the far south of the section.

Pa-231 concentrations in the water column range between 0.01 and 0.36 dpm/1000 l and display an increase with depth from the surface to ~1200-1500 m (Figure 3b). Below this depth, ^{231}Pa concentrations remain relatively constant until close to the bottom (~500 m from the seafloor) where a slight decrease in ^{231}Pa is observed. This distribution agrees with previous observations and may be explained as a result of horizontal water mixing as well as reversible scavenging process (Moran et al., 2002). There is no clear latitudinal pattern in the distribution of ^{231}Pa although lower concentrations are observed in deep water at the equator.

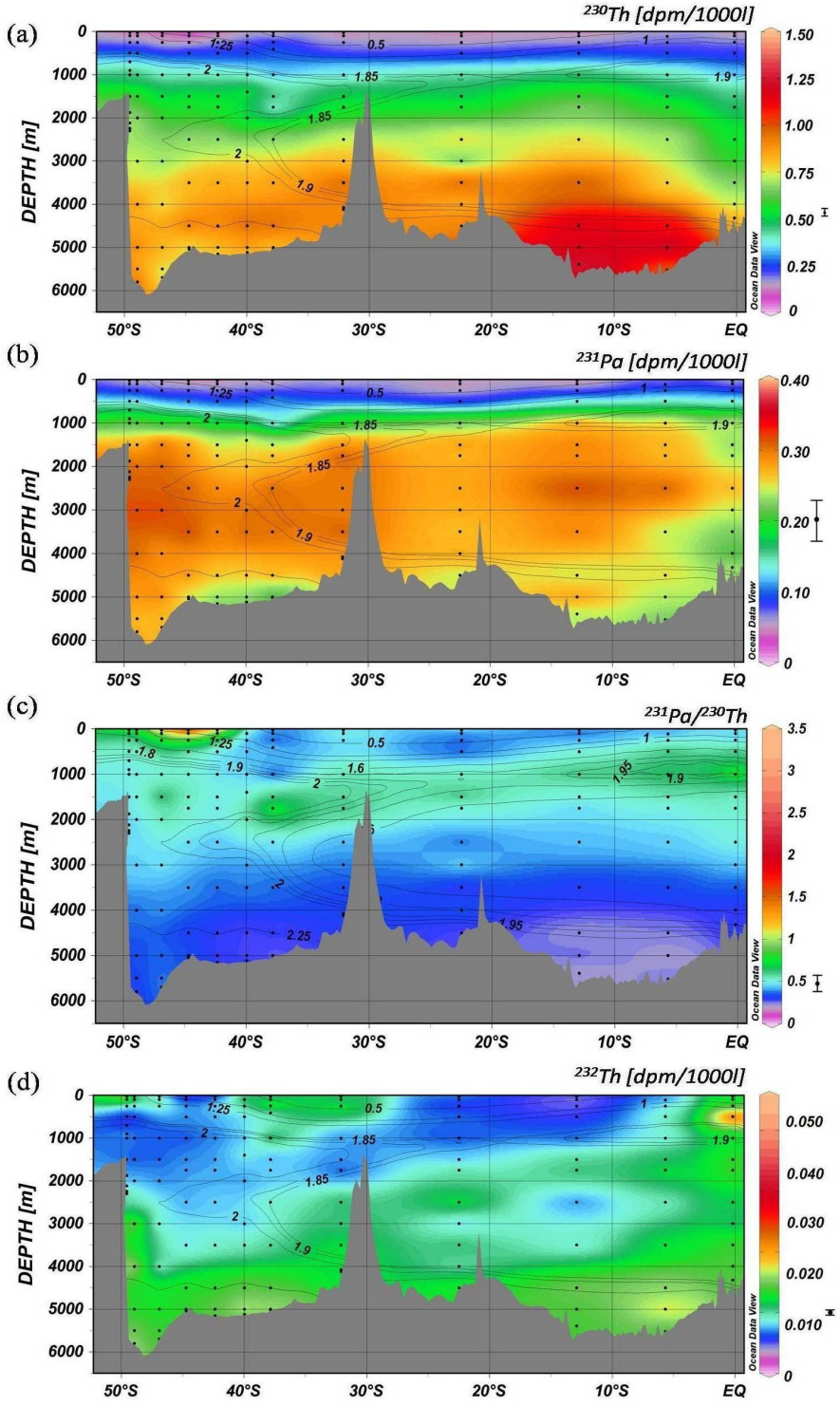


Figure 3.3: Distributions of water column (a) ^{230}Th; (b) ^{231}Pa; (c) ^{231}Pa/ ^{230}Th ratios and (d) ^{232}Th along the transect in the southwest Atlantic Ocean. Black contours are dissolved phosphate (see Figure 3.2c) and provide an indication of the location of the various water masses. Average concentrations and average 2 standard error are given next to scale bars.

Dissolved ^{231}Pa/^{230}Th ratios range between 0.18 and 3.37, all exceeding the production ratio of 0.093. In surface waters, ^{231}Pa/^{230}Th ratios are generally low, except at stations south of 40^{o}S. Below the surface, highest ratios occur in mid-water column with peak values at ~1500-2000 m in the south but at shallower depths (~1000 m) at the equator (Figure 3.3c). This depth is broadly similar to that of UCDW. Below 2000 m, ^{231}Pa/^{230}Th ratios decrease towards the bottom, and there is no significant gradient in ^{231}Pa/^{230}Th ratios with latitude. No dependence on water mass is observed below 2000 m, nor any indication of progressive change within a water mass.

Th-232 concentrations range between 0.001 and 0.054 dpm/1000 l. ^{232}Th concentrations generally increase with depth throughout the water column (Figure 3.3d). Significant variation is observed in near-surface waters, with higher ^{232}Th concentrations at the equator, the region around 30-40^{o}S, and the most southern station at 50^{o}S. Below 1000 m, little horizontal pattern is observed, although ^{232}Th concentrations north of 6^{o}S are higher than those to the south. In near-bottom water, decreased ^{232}Th is seen, as observed for ^{230}Th and ^{231}Pa, but less widespread and only clear at around 40-45^{o}S and 5-13^{o}S.

3.5 Discussion

3.5.1 Meridional transport of ^{230}Th and ^{231}Pa

The application of ^{231}Pa/^{230}Th as a tracer of past deep ocean circulation is based on fractionation between the two nuclides caused by the difference in their meridional transport in the ocean.

Transport of ^{230}Th and ^{231}Pa by meridional circulation in the modern Atlantic is therefore an important process to quantify. Yu et al. (1996) estimated a net southward transport of 11% of the ^{230}Th and 51% of the ^{231}Pa formed in the North Atlantic southward across 25^{o}N. Their calculation assumed a North Atlantic volume of 77×10^{15} m^3, with a northward flow of 19.26 Sv in the upper 1050 m balanced by a nearly equivalent southward flow below 1050 m. This calculation was based on low resolution measurements of dissolved ^{230}Th and ^{231}Pa in the North Atlantic Ocean (Cochran et al., 1987), assuming that the mean values of these data were representative of ^{230}Th and ^{231}Pa in the Atlantic Ocean. Using the new data presented here, we can reassess transport of ^{230}Th and ^{231}Pa out of the North Atlantic, and extend the approach to assess net advection of ^{230}Th and ^{231}Pa from the whole Atlantic.

To assess export from the North Atlantic, we use WOCE line A07 at 4.5^{o}S (Figure 3.1), where a southward flow of 25 Sv in NADW layer is compensated by similar northward flows of surface, intermediate and bottom water masses (Vanicek and Siedler, 2002). We assess the nuclide concentration of the various water masses using our data from Station JC057-18 at 0.19^{o}S (Table 3.1). This calculation indicates a net southward transport of ^{230}Th of 6.55×10^{6} dpm/s and of ^{231}Pa of 3.58×10^{6} dpm/s, equivalent to 6% of ^{230}Th and 33% of ^{231}Pa produced to the north of 4.5^{o}S (see Figure 3.4). This calculation therefore suggests a somewhat lower horizontal export of ^{230}Th and ^{231}Pa from the North Atlantic at 4.5^{o}N than Yu et al. (1996) assessed at 25^{o}N. This is consistent with observations of increasing deep-water ^{230}Th and ^{231}Pa concentration as water flows southward.

WOCE section	Water Layer	Upper Boundary (m)	Lower Boundary (m)	Meridional mass transport (Sv)	^{230}Th (dpm/1000l)	^{231}Pa (dpm/1000l)
A07 (4.5°S)	Surface	surface	250	15	0.15	0.07
	Intermediate	250	750	5	0.23	0.15
	Deep	750	3500	-24	0.49	0.24
	Bottom	3500	bottom	3	0.76	0.22
A11 (45°S)	Surface	surface	150	11	0.04	0.03
	Intermediate	150	1250	2	0.28	0.13
	Deep	1250	3000	-19	0.62	0.30
	Bottom	3000	bottom	5	0.83	0.28

Table 3.1: Meridional mass transport and ^{230}Th and ^{231}Pa concentrations in WOCE section water layers. Positive meridional mass transports are northward.

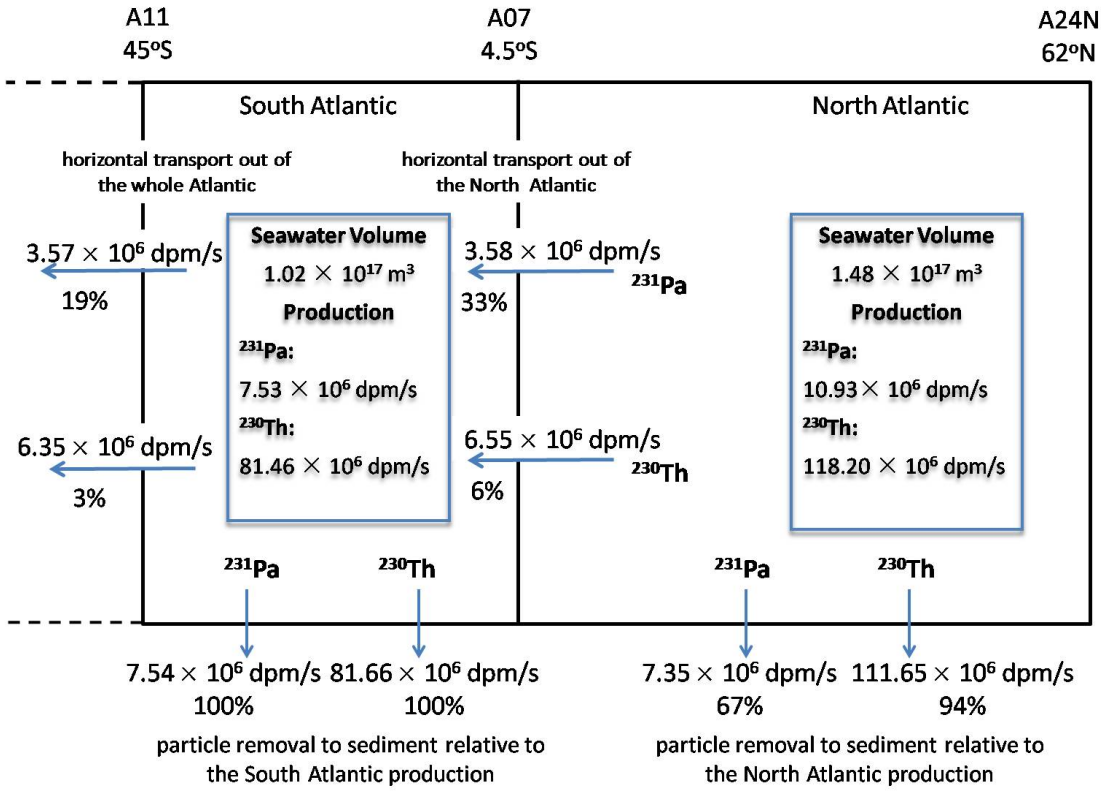


Figure 3.4: Horizontal transport and removal to sediment of ^{230}Th and ^{231}Pa in the Atlantic Ocean. WOCE lines A07 at 4.5°S and A11 at 45°S are used to estimate the export of both nuclides from the North Atlantic and the whole Atlantic, respectively. ^{230}Th and ^{231}Pa scavenged into sediment are given relative to their production in the North and South Atlantic. Production rates of ^{230}Th and ^{231}Pa are 0.026 dpm/m^3/yr and 0.0025 dpm/m^3/yr, respectively.

To assess export from the whole Atlantic, we use the WOCE A11 line, broadly at 45°S (Figure 3.1). At this latitude, surface and intermediate waters have northward flow of 11 Sv and 2 Sv respectively, underlain by southward flowing NADW of 19 Sv and northward flowing bottom water of 5 Sv (Vanicek and Siedler, 2002). Using ^{230}Th and ^{231}Pa concentrations from Station JC057-4 at 44.71°S (Table 3.1) indicates, in absolute terms, approximately the same export of ^{230}Th and ^{231}Pa out of the South Atlantic as is input by horizontal transport from the North Atlantic (Figure 3.4). This requires that scavenging in the South Atlantic removes ^{230}Th and ^{231}Pa produced in this region, but not significantly more. As a fraction of the total produced in the water column, the export of ^{230}Th and ^{231}Pa from the whole Atlantic is therefore lower (at 3% and 19% respectively) than from the North Atlantic only.

The fraction of ^{231}Pa transported by meridional circulation is about six times more than that of ^{230}Th from both the North and the whole Atlantic. This confirms that meridional transport has a smaller influence on ^{230}Th than ^{231}Pa, and supports the view that significant fractionation of ^{231}Pa from ^{230}Th is caused by deep ocean circulation at the basin scale in the North Atlantic. No such fractionation is observed at a basin scale for the South Atlantic, however. It is important to note that such estimation is only a simple calculation, and a 3-D model calculation is needed in further study.

3.5.2 Quantifying seafloor removal rates of ^{230}Th and ^{231}Pa

Th-230 and ^{231}Pa decrease towards the seafloor in the deepest 500 m at most stations of this study (Figure 3.3). This observation might be explained by either lateral advection of AABW with low nuclide content, or by additional nuclide scavenging at the seafloor (or close to it). Lateral

advection of newly-formed deep water has been suggested in previous studies as a cause of near-bottom ^{230}Th depletion (e.g. Rutgers van der Loeff and Berger, 1993). In our data, however, the pattern of samples exhibiting near-bottom depletion does not look similar to the distribution of recently-formed AABW (Figure 3.3). It is therefore more likely that near-bottom depletion reflects a removal process at or near the seafloor. Such enhanced near-bottom scavenging of ^{230}Th has previously been observed in the North Pacific Ocean (Okubo et al., 2012). In this study, we quantify the near-bottom removal rate of ^{230}Th and ^{231}Pa from our observations, and assess possible fractionation of ^{231}Pa/^{230}Th caused by this removal. If this removal causes significant fractionation, it may overprint the record of past circulation (or productivity) that sedimentary ^{231}Pa/^{230}Th are hoped to provide.

We assess removal of ^{230}Th and ^{231}Pa based on deviations in their near-bottom concentrations from expected behaviour. Water-column ^{230}Th concentration commonly displays a linear increase with depth as described by reversible scavenging models (Nozaki et al., 1987). On the other hand, ^{231}Pa has a longer residence time, somewhat similar to the residence times of deep water in an ocean basin. Deep-water advection thus exerts an impact on ^{231}Pa, reshaping its vertical profile, and ^{231}Pa concentrations are commonly rather constant with depth in the deep ocean.

For both nuclides, we first use a simple fit to data deeper than 1500 m and more than 500 m above the seafloor to define a linear trend in the absence of near-bottom removal. Extrapolation of this linear fit to the depth of the seafloor provides an expected nuclide concentration in the absence of near-bottom scavenging. The difference between the extrapolated value and that observed near the seafloor indicates the amount of the nuclide missing due to near-bottom scavenging (Figure 3.5).

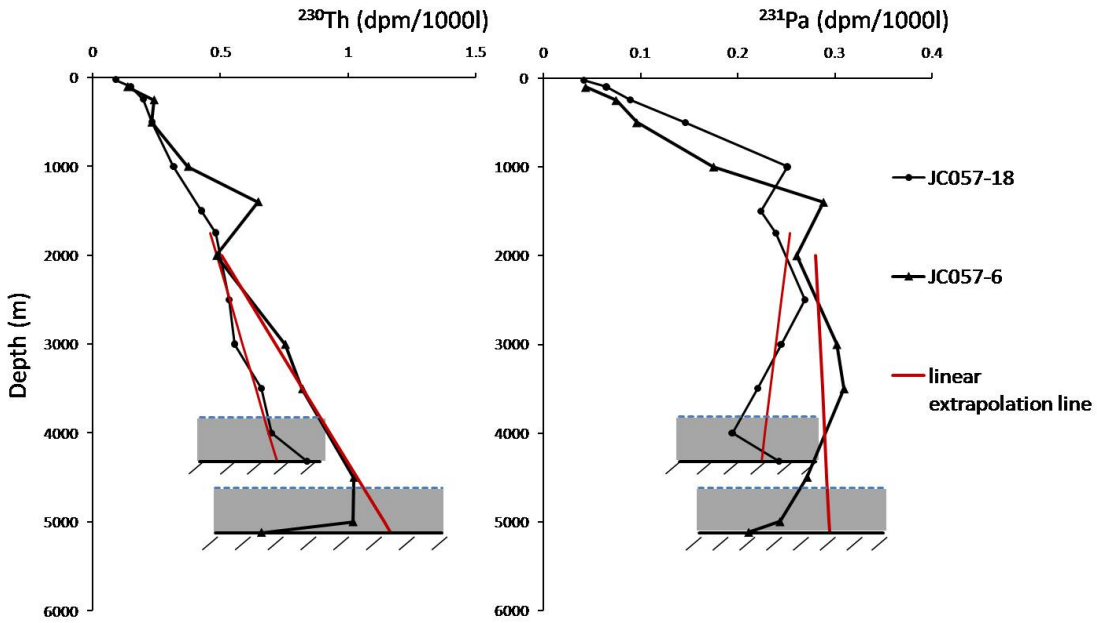


Figure 3.5: Examples of linear extrapolation of vertical profiles of ^{230}Th and ^{231}Pa from Stations JC057-6 and JC057-18. Black lines indicate observed water-column ^{230}Th and ^{231}Pa. Red lines show the linear extrapolation of ^{230}Th and ^{231}Pa using a linear fit between >1500m and <500m above the seafloor. Grey shading indicates a water layer of 500m, where additional bottom scavenging is observed at some stations. Additional near-bottom scavenging of both nuclides occurs at JC057-6, while JC057-18 is not affected by this process.

The net removal rate of a dissolved nuclide to particulate form can be calculated by applying the equation (Coale and Bruland, 1985):

$$\frac{\partial A_n^d}{\partial t} = A_U \lambda_n - A_n^d \lambda_n - J_n \qquad (3.1)$$

where A_n^d is the dissolved activity of the nuclide, A_U is the activity of its parent nuclide, λ_n is the decay constant of the daughter nuclide, and J_n is the net removal rate (i.e. adsorption minus desorption) of the nuclide from the dissolved phase to particulate phase.

Under steady-state conditions, the removal rate of the nuclide is

$$J_n = A_U \lambda_n - A_n^d \lambda_n \qquad (3.2)$$

Additional seafloor removal rates of the nuclide, ΔJ_n, can be calculated from the comparison of extrapolated concentrations with observed near-bottom concentrations using the following equation:

$$\Delta J_n = (A_{n,e} - A_{n,o}) \times \lambda_n \qquad (3.3)$$

where $A_{n,e}$ and $A_{n,o}$ are the observed and extrapolated activities of the nuclide.

This approach to calculating near-bottom scavenging compares scavenging fluxes to the total production of nuclide in the water-column. Pa-231 and particularly ^{230}Th are already removed rapidly by scavenging in the water column, so that more than 99.9% of the nuclide produced is scavenged even in the absence of near-bottom removal. There is therefore little nuclide remaining in seawater to be scavenged near the seafloor. The impact of near-bottom scavenging on observed seawater nuclide concentrations can be quite large (up to a 50% reduction is observed here), but the change that it causes to the total flux of ^{230}Th or ^{231}Pa to the sediment in this one-dimensional calculation is slight and always less than 0.1%. The notable decrease in seawater nuclide concentration caused by near-bottom scavenging will, however, lead to enhanced mixing of ^{230}Th and ^{231}Pa to that site from regions of higher concentration. Our 1D calculations of the impact of near-bottom scavenging on nuclide fluxes therefore represent a minimum value. Assessing the true value for any given site would require assessment of mixing and transport more widely and cannot be done without a 3D modelling approach.

Additional near-bottom removal rates are calculated in this study by averaging measurements within 500m of the seafloor and comparing these with extrapolated values in the 1D model described above (Figure 3.6). The average near-bottom removal, relative to production in the water-column, is 0.001% for ^{230}Th, and 0.003% for ^{231}Pa (Table 3.2). Near-bottom removal of ^{230}Th occurs at all stations except one (at the equator), while removal of ^{231}Pa is small north of ≈30^{o}S, but substantial between 35^{o}S and 45^{o}S (Figure 3.6). This zone of notable ^{231}Pa removal coincides with particularly high ^{230}Th removal, and with high values for beam attenuation (Figure 3.6a). Anderson et al. (1983b) suggested that the presence of a near-bottom nepheloid layer might be responsible for intensified near-bottom removal in the Panama and Guatemala Basins. In our study, the high beam attenuation (Figure 3.6a) suggests the occurrence of a nepheloid layer at 35-45^{o}S, and the coincidence of additional nuclide scavenging with this attenuation, that these nepheloid layers are responsible for the additional scavenging. Such scavenging indicates that the resuspended particles in nepheloid layers are somehow not fully equilibrated with the overlying seawater, perhaps due to a change in the chemistry of their surfaces, or to remobilisation of old sediment in which ^{230}Th and ^{231}Pa have decayed.

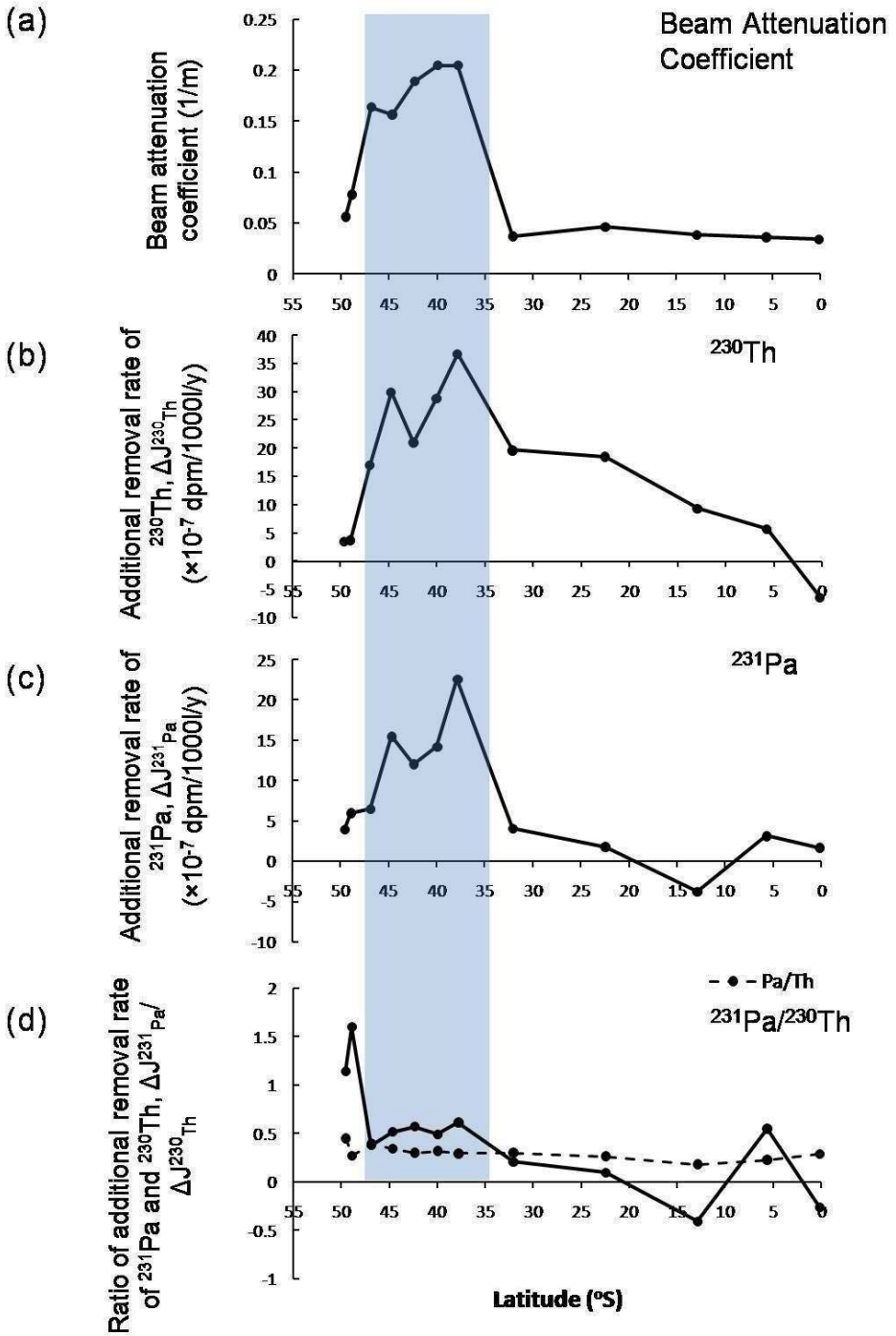


Figure 3.6: (a) Beam attenuation coefficient; and additional near-seafloor removal rates of (b) ^{230}Th; (c) ^{231}Pa and (d) ^{231}Pa/^{230}Th. Note that removal of ^{230}Th and ^{231}Pa is high in the area, marked by the vertical grey bar, in which beam attenuation is also high. Outside this area, ^{231}Pa removal is low, and probably within error of zero, but ^{230}Th removal is still seen at most stations. Panel d also shows, by the dashed line, the average ^{231}Pa/^{230}Th in water within 500 m (60 m for JC057-1) of the sea floor.

In the presence of a nepheloid layer, where bottom scavenging is most prevalent, near-bottom scavenging preferentially removes ^{231}Pa relative to ^{230}Th, compared with the ratio of these nuclides in seawater. This fractionation moves additional ^{231}Pa to the sediment and will enhance transport of ^{231}Pa to the site by mixing in the water column. The effect will be to increase the ^{231}Pa/^{230}Th ratio of sediment, but the magnitude of this effect cannot be simply calculated without consideration of 3D mixing and scavenging. Away from areas where nepheloid layers are present, near-bottom scavenging of ^{230}Th significantly outweighs that of ^{231}Pa. Although this might lead to a decrease in sedimentary ^{231}Pa/^{230}Th at these sites, water-column scavenging of ^{230}Th is already highly efficient so that near-bottom scavenging is not anticipated to make a substantial difference to sediment ^{231}Pa/^{230}Th.

Station number	Beam attenuation coefficient (1/m)	Additional removal rate of ^{230}Th ($\times10^{-7}$ dpm/1000l/y)	^{230}Th removal (%)	Additional removal rate of ^{231}Pa ($\times10^{-7}$ dpm/1000l/y)	^{231}Pa removal (%)	Ratio of additional removal rate of ^{231}Pa and ^{230}Th
1	0.056	3.46	0.00004	3.95	0.0004	1.14
2	0.078	3.74	0.00013	5.99	0.0022	1.6
3	0.164	17.03	0.00059	6.46	0.0024	0.38
4	0.157	29.92	0.00118	15.48	0.0066	0.52
5	0.19	21.03	0.00081	12.04	0.005	0.57
6	0.205	28.84	0.00112	14.19	0.0059	0.49
7	0.205	36.68	0.00144	22.57	0.0096	0.62
9	0.037	19.62	0.00094	4.06	0.0021	0.21
12	0.046	18.49	0.00082	1.78	0.0008	0.1
14	0.038	9.29	0.00034	-3.76	-0.0015	-0.4
16	0.036	5.69	0.0002	3.13	0.0012	0.55
18	0.034	-6.41	-0.0003	1.68	0.0008	-0.26

Table 3.2: Additional seafloor removal rates of ^{230}Th and ^{231}Pa. ^{230}Th removal (%) and ^{231}Pa removal (%) indicate the percentage of the additional removal of both nuclides caused by near-bottom scavenging relative to their production in the water column.

3.5.3 ^{232}Th-derived dust flux deposition

Unlike ^{230}Th produced in-situ through U decay in seawater, ^{232}Th (half-life 1.4×10^{10} yr) has a terrestrial source. Th-232 can therefore be used as a dust input tracer in the modern ocean, as first suggested by Hirose and Sugimura (1987) and applied by Hsieh et al. (2011). That study demonstrated that the distribution of ^{232}Th concentration in surface water is in good agreement with both modeled dust inputs and another potential dust tracer, Al, and that ^{232}Th has the advantage over Al that removal rates of the element can be assessed from ^{230}Th. In this study, we further test this method with our higher resolution data which allow extension of the coverage of ^{232}Th-derived dust fluxes to the south of the Hsieh et al. (2011) Atlantic data, and which span the dust plume emanating from the South American continent.

We use average dissolved ^{230}Th and ^{232}Th concentrations in the upper 250 m of the water column following equations adapted from Hsieh et al. (2011):

$$\tau_{^{230}\mathrm{Th}} = \frac{1/\lambda_{^{230}\mathrm{Th}}}{A_{^{234}\mathrm{U}}/A^{d}_{230\mathrm{Th}} - 1} \qquad (3.4)$$

$$F_{^{232}\mathrm{Th}} = \frac{A^{d}_{^{232}\mathrm{Th}} \times 250\ \mathrm{m}}{\tau_{^{230}\mathrm{Th}}} \qquad (3.5)$$

$$F_{\mathrm{dust}} = \frac{F_{^{232}\mathrm{Th}}}{[^{232}\mathrm{Th}]_{\mathrm{dust}} \times S_{\mathrm{Th}}} \qquad (3.6)$$

where $\tau_{^{230}\mathrm{Th}}$ is the ^{230}Th-derived residence time in years; $F_{^{232}\mathrm{Th}}$ is the removal flux of dissolved ^{232}Th in seawater, μg/m^2/yr; F_{dust} is the dust flux, g/m^2/yr; $\lambda_{^{230}\mathrm{Th}}$ is the decay constant of ^{230}Th,

y^{-1}; $A_{^{234}U}$ is the activity of ^{234}U in seawater, 2900 dpm/1000 l; $A^{d}_{^{230}Th}$ and $A^{d}_{^{232}Th}$ are average activities of dissolved ^{230}Th and ^{232}Th in the upper 250 m water column, dpm/1000 l; $[^{232}Th]_{dust}$ is the concentration of ^{232}Th dust; and S_{Th} is the soluble fraction of Th. Averages of ^{232}Th and ^{230}Th concentrations for the upper 250 m were calculated and adopted in the above equations to obtain dust flux. For stations where surface 25 m Th measurements are missing, a linear fit to ^{232}Th and ^{230}Th concentrations with depth in the upper 250 m was made, and the 25 m value was taken from this fit before averaging. This approach differs slightly from Hsieh et al. (2011) who calculated fluxes based on the upper 25 m, but our approach is not biased by the absence of measurements for some depths at some stations in our dataset. We follow Hsieh et al. (2011) in assuming a ^{232}Th concentration in dust of 13 ppm. We used 15% as the soluble fraction of dust Th in our calculations based on expected dust flux magnitudes; this value is within the range of observations for Fe solubility observed in previous studies (2.4-20%, Baker et al., 2013). The soluble fraction of dust Th, however, remains the biggest uncertainty in these calculations.

Calculated dust fluxes range from 0.41- 2.64 g/m^2/yr, which is within the range of dust fluxes modelled by Mahowald et al. (2005) (Table 3.3 and Figure 3.7). The high dust flux observed at the equatorial station is consistent with both Hsieh et al. (2011) and modelled dust deposition, which can be attributed to the high dust input from the Sahara. In regions between 32^o and 45^{o}S, our calculation yields high dust deposition, while models indicate a narrower South American dust plume around 45^{o}S. Our observations may give a more accurate measure of dust input from the Patagonia Desert, which covers an area spanning 36^{o}S-49^{o}S. Another possible explanation of the high ^{232}Th we observe at these latitudes, however, is that it reflects advection from the South American shelf within the Brazil-Malvinas confluence, and invalidates the steady-

state assumption used in the calculation in this region. Such transport has been suggested previously to explain high Al concentrations observed at the same stations as those of this study (Rob Middag, Per Com). No salinity anomaly is associated with the high ^{232}Th, but this does not preclude on-shelf modification of the ^{232}Th concentration during proximity to sediments on the shelf. Better assessment of the role of lateral advection in controlling open-ocean ^{232}Th will be required before Th isotopes can reliably be used as a dust input tracer. It is also important to note that the shifting feature observed for ^{230}Th residence time at ~40°S (Figure 3.7a) suggests that it is essential to check the validity of the steady-state assumption in further study.

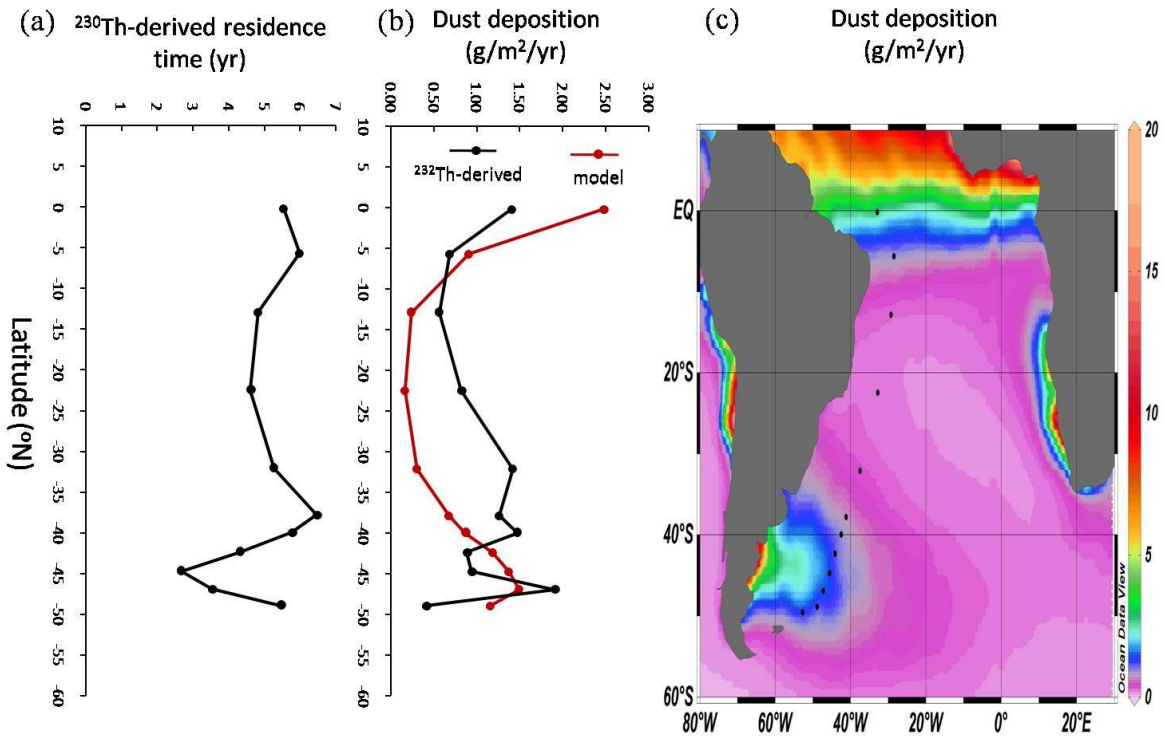


Figure 3.7: Comparison of ^{230}Th-^{232}Th-derived dust flux and modeled dust deposition. (a) ^{230}Th-derived residence time in the upper 250m of the water column; **(b)** Dust flux based on average ^{232}Th and ^{230}Th concentrations in the upper 250m of the water column and assuming 15% ^{232}Th solubility from dust, compared to model of dust deposition; **(c)** map of modelled dust deposition (Mahowald et al., 2005).

Station Number	^{230}Th-derived residence time (yr)	^{232}Th-derived dust flux (g/m^2/yr)	Modeled dust flux (g/m^2/yr)
JC057-1	4.53	2.64	1.33
JC057-2	5.46	0.41	1.16
JC057-3	3.53	1.90	1.49
JC057-4	2.68	0.94	1.37
JC057-5	4.32	0.89	1.18
JC057-6	5.77	1.47	0.86
JC057-7	6.46	1.26	0.68
JC057-9	5.27	1.42	0.31
JC057-12	4.61	0.82	0.16
JC057-14	4.82	0.56	0.24
JC057-16	5.98	0.69	0.91
JC057-18	5.54	1.41	2.47

Table 3.3: Results of ^{230}Th-derived residence time and ^{232}Th-derived dust flux. Model results of dust deposition by Mahowald et al. (2005) are also listed.

3.5.4 Controls on ^{230}Th, ^{231}Pa, and ^{231}Pa/^{230}Th in the water column

The ^{231}Pa/^{230}Th ratio of seawater is expected to be captured by equilibration at the seafloor between surface sediments and the deepest water mass (Thomas et al., 2006), so that sediments from different water depths may allow reconstruction of past vertical distributions of water-column ^{231}Pa/^{230}Th (Gherardi et al., 2009; Lippold et al., 2011). For this sedimentary information to be useful in reconstruction of past patterns and rates of ocean circulation requires that water-column ^{231}Pa/^{230}Th profiles reflect that flow. In the Southwest Atlantic, that flow is characterized by overlying water masses including the northward flowing AABW and the southward flowing NADW. These water masses might be expected to have characteristic ^{231}Pa/^{230}Th ratios, and to demonstrate systematic increase along their flow path as the waters age.

In our study, high values of ^{231}Pa/^{230}Th are observed between ~1000-2000 m broadly coincident with UCDW (Figure 3.3c). To further assess the presence or absence of this possible

water-mass control on ^{231}Pa/^{230}Th, we combine data from along the section to derive an average water-column profile against density (Figure 3.8). The relationship between ^{231}Pa/^{230}Th and UCDW is not clear in this analysis and so we consider the relationship suggestive (based on Figure 3.3) but not yet certain. Below 2000 m, there is, however, no indication of water-mass control on ^{231}Pa/^{230}Th ratios in the data of this study. Contours of phosphate in Figure 3.3c indicate the location of NADW and the underlying AABW, and there is no specific ^{231}Pa/^{230}Th ratio for either water mass (Figure 3.8).

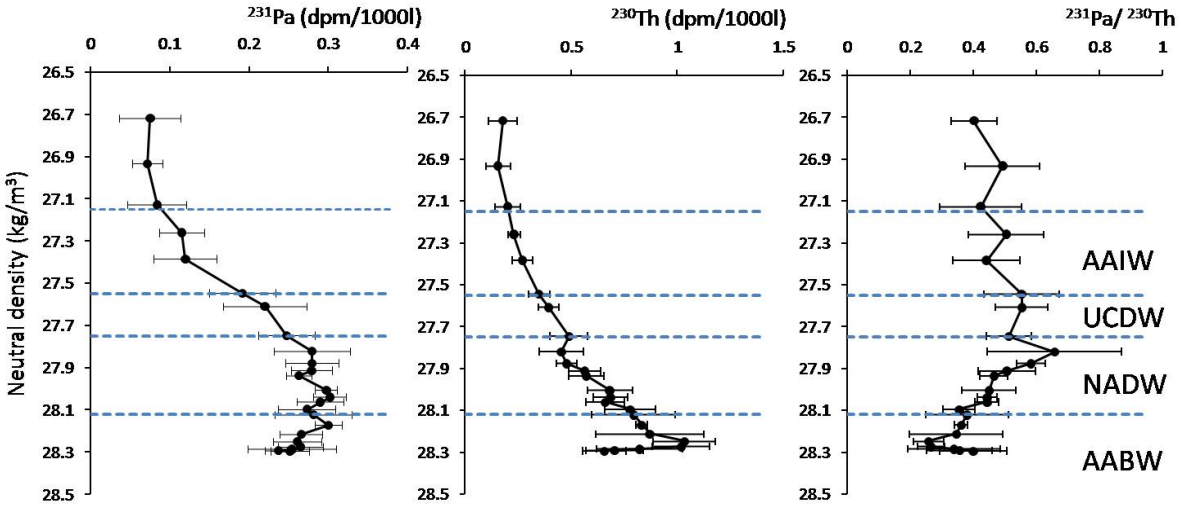


Figure 3.8: Water-column profile of ^{230}Th, ^{231}Pa, ^{231}Pa/^{230}Th averaged from measurements in this study. Data from all stations was sorted by water density and averages for density and ^{231}Pa/^{230}Th were taken for each successive 5 data points. Error bars indicate 2 standard errors. Dashed lines separate major water masses as defined by neutral density following Vanicek and Siedler (2002).

There is also no indication in the data of a systematic change of ^{231}Pa/^{230}Th along flow in either NADW or AABW (Figure 3.3c). 2D models of ^{231}Pa/^{230}Th (Luo et al., 2010; Lippold et al., 2012) suggest changes of ≈0.1 for NADW, and a steady northward increase of ≈0.15 for AABW.

No such changes can be observed in the data, suggesting that previous models do not fully capture the behaviour of ^{231}Pa and/or ^{230}Th in the water column.

A notable feature of the average ^{231}Pa concentration profile is a peak at ≈2km (Figure 3.8). Such a peak cannot be produced by 1D scavenging models without an unrealistic change in adsorption/desorption behaviour in mid-water column. The peak must, instead, be caused by lateral transport of a concentration signal, or by removal of ^{231}Pa at depth. Lateral transport might be from the margin, at which preferential release of ^{231}Pa could be caused by dissolution of opal at that depth. Pa is known to have a particular chemical affinity to opal (e.g. Chase et al., 2002) and opal plays a critical role in removal of Pa to ocean sediments (e.g. Bradtmiller et al., 2007). Opal dissolution profiles are poorly constrained (Ragueneau et al., 2000), but the dissolved Si concentration profile in seawater requires a significant dissolution of opal at mid depths. Such dissolution in marginal sediments might release ^{231}Pa which is then transported along isopynals to the open ocean. An alternative scenario is that bottom scavenging of ^{231}Pa, as indicated in this study for the South Atlantic, is widespread and causes ^{231}Pa to be preferentially removed from the deep-ocean, with this signal being transported upwards by mixing, and sideways from margins.

The lack of a water-mass control on ^{231}Pa/^{230}Th, and the inability of simple 1D scavenging models to explain observed ^{231}Pa profiles, challenges the use of sedimentary ^{231}Pa/^{230}Th data to reconstruct past flow conditions, particularly in situations where more than one water-mass is present such as the modern South Atlantic. Reconstruction of flow in different water masses appears unlikely to be successful. Relying instead on overall advection of ^{231}Pa from a basin (as first pursued by Yu et al., 1996) may be more successful but may be complicated where significant changes of water-mass flow have occurred in the past, such as in the North Atlantic.

3.6 Conclusions

Water column ^{230}Th and ^{231}Pa data in the Southwest Atlantic confirm the horizontal transport and fractionation of ^{231}Pa from ^{230}Th by deep ocean circulation out of the modern Atlantic. ^{231}Pa (and to a lesser extent, ^{230}Th) are removed from the North Atlantic, but are in equilibrium in the South Atlantic so that scavenging equals production. Pronounced decreases of ^{230}Th and ^{231}Pa in near-bottom water indicate enhanced sea-floor removal, particularly in regions where nepheloid layers are present. This enhanced scavenging in nepheloid layers preferentially removes ^{231}Pa and is likely to cause an increase in sediment ^{231}Pa/^{230}Th ratio. High ^{232}Th concentrations in surface waters of equatorial area and possibly at 32^{o}S-45^{o}S, indicate high dust input from the continent.

Although we demonstrate horizontal transport of ^{230}Th and ^{231}Pa, there is no clear indication of control on ^{231}Pa/^{230}Th ratios by water-mass age in the Southwest Atlantic, challenging the use of sedimentary ^{231}Pa/^{230}Th to assess past flow in this region. An observed mid-water-column peak in ^{231}Pa concentrations is difficult to explain with 1D models, and suggests the importance of opal dissolution or lateral transport in controlling seawater ^{231}Pa profiles.

Acknowledgements

We thank H.M. van Aken and E. van Weerlee for provision of hydrographic data, and the Captain, crew, and scientific party from cruise JC057. Yves Plancheral is thanked for calculating volumes for the North and whole Atlantic. This work was funded by NERC Grant NE/F017316/1. We

thank three reviewers, Robert Anderson, Michiel M. Rutgers van der Loeff, and Roger Francois, and the editor, Jean Lynch-Stieglitz, for their constructive comments on the manuscript.

Chapter 4

Assessing the use of $^{230}Th_{xs}$ to quantify sediment dissolution and its effect on sedimentary $(^{231}Pa/^{230}Th)_{xs}$

Abstract

Dissolution of marine sediment at the seafloor takes place in all ocean basins. It is considered to be an important process controlling the release of chemicals from sediment back to seawater, and in setting the composition of marine particulates buried in sediment. Assessing the rate and extent of this dissolution is critical for understanding of internal cycling of many chemical species in the ocean. In this study, I test the use of $^{230}Th_{xs}$, whose flux to the seafloor is assumed constant and well known, to assess sediment dissolution. High-resolution $^{230}Th_{xs}$ measurements were obtained from intact core-top sediment samples spanning a range of water depths on the slope of the Cape Basin and the South Atlantic Mid-Ocean Ridge. Sedimentary $^{230}Th_{xs}$ concentrations increase with depth in the upper ~3 cm of sediment and are constant below this depth. These observations can be best explained as a result of sediment dissolution in the upper centimetres of the sediment. Core-top ^{230}Th measurements thus provide a tool to quantify the rate of sediment dissolution at the seafloor and assess the magnitude of this process in various ocean settings. Dissolution rates derived in this study vary from 0.11 to 0.24 g/cm^2/kyr, with a strong increase in rate with depth. Combining ^{230}Th with sediment composition measurements provides an assessment of which constituents are dissolving from the sediment. In the core with the most unambiguous dissolution, situated a kilometer below the modern carbonate saturation horizon, there is suprising lack of observed carbonate dissolution, while opal does appear to be dissolving. Results also suggest dissolution of the detrital fraction of sediments, indicating the ^{230}Th may enable quantification of submarine weathering fluxes. Despite significant dissolution, sedimentary $(^{231}Pa/^{230}Th)_{xs}$ is largely unaffected, indicating the robustness of sedimentary $(^{231}Pa/^{230}Th)_{xs}$ ratios to dissolution.

4.1 Introduction

Sediment is generally a sink for elements dissolved in the ocean because these elements are incorporated or adsorbed onto sinking marine particles and subsequently buried in marine sediment. Most of these sinking particles are synthesized by marine organisms in the upper layers of the ocean, and are of three mineralogical forms: carbonates ($CaCO_3$), opal ($SiO_2 \cdot nH_2O$), and organic matter. Lithogenic particles derive from the continental lithosphere constitute a relatively minor fraction of sinking particles away from coastal settings (Honjo et al., 1982).

Once settled to the seafloor, these particles, especially biogenic particles, undergo dissolution processes, which affect the composition of the sediment and releases chemical components back to the overlying water. The dissolution of carbonate particles in sediments is controlled by the solubility and kinetic characteristics intrinsic to the mineral and by external processes that control the saturation state of the surrounding fluids (Jahnke and Jahnke, 2004). The dissolution of calcite, specifically, increases with decreasing temperature and increasing pressure, leading to increasing solubility with depth in the water column. The water depth at which calcite becomes undersaturated is defined as the $CaCO_3$ saturation horizon (Berner and Wilde, 1972) and also depends on the alkalinity and total carbon content of the water. In the Atlantic, for example, this depth is normally ≈4500 m (Li et al., 1969). The dissolution of opal, on the other hand, occurs more rapidly in warm water, because it is primarily a temperature-controlled process (Dixit et al., 2001; Hurd, 1973). Other processes, such as the aluminum concentration of biogenic silica, also influence the dissolution rate of opal at the sea floor (Dixit et al., 2001; Hurd, 1973; Van Bennekom et al., 1988; Van Cappellen and Qiu, 1997). Most organic matter dissolves at the

seafloor, with <10% of the organic matter that falls to the seafloor being preserved due to the highly efficient sedimentary organic matter oxidation (Hedges and Keil, 1995), except in regions of very low bottom-water oxygen. Lithogenic particles may also dissolve, in a process sometimes referred to as submarine weathering (Boggs, 1995), but such dissolution is generally expected to be slower than for the biogenic particles.

Dissolution of these marine particles at the seafloor is an important process not only to the biogeochemical cycling of elements associated with them, but also to attempts to interpret the sedimentary record for information regarding the past ocean environment. The dissolution of $CaCO_3$ at the sea-floor, for example, has been proposed to influence atmospheric CO_2 concentrations on glacial to interglacial time scales (Archer and Maier-Reimer, 1994; Broecker, et al., 2001; Farrell and Prell, 1989) and will neutralize the anthropogenic CO_2 currently accumulating through surface ocean-gas exchange or potentially intentionally injected into the deep ocean in the future. The dissolution of biogenic silica affects not only the return of nutrient silicic acid ($Si(OH)_4$) to the overlying water column, but also the integrity of the fossil diatom record. The latter is an important consideration when using silica accumulation rates and diatom assemblages preserved in sediment cores to reconstruct past changes in surface water productivity and paleoenvironmental conditions (e.g., Bareille et al., 1991; Charles et al., 1991; Lyle et al., 1988).

Understanding the dissolution of marine particles at the seafloor is therefore an important question for marine geochemistry. Such understanding remains elusive, however, and requires reliable approaches to provide quantification of these processes. In this study, I attempt to quantify dissolution fraction and dissolution rates based on $^{230}Th_{xs}$ concentrations in marine sediments. I

also assess the impact of this dissolution on sedimentary $^{231}Pa/^{230}Th$ ratios, in an effort to assess the preservation of this paleoceanographic proxy during early sediment burial.

4.2 Principles underlying the use of ^{230}Th as an indicator of sediment dissolution

Th-230 (half-life: 75,584 yr; Cheng et al., 2013) is produced in-situ in the ocean through the alpha decay of ^{234}U (half-life: 245,620 yr; Cheng et al., 2013). Because uranium has a residence time in the ocean of 200,000 to 400,000 years (Ku et al., 1977), its uniform concentration leads to production of ^{230}Th in the water column at a known constant rate at all locations. ^{230}Th, however, is highly particle-reactive with a short residence time of 20 years in the water column (Henderson and Anderson, 2003). Once produced, it is readily removed from seawater by adsorption onto sinking particle with subsequent burial in sediment. As a result, the flux of scavenged ^{230}Th reaching the seafloor is expected to be close to its known rate of production by ^{234}U decay in the overlying water column. Based on this assumption, early studies, e.g. Bacon (1984), Bacon and Rosholt (1982), and Francois et al. (1990), have proposed and developed the ^{230}Th-normlization method. This method suggests that the scavenged ^{230}Th activities in sediment can be used as a reference against which the flux of other sedimentary components can be estimated as (Bacon, 1984):

$$F_i = f_i \times \beta \times z / {}^{230}Th_{xs} \quad (4.1)$$

where F_i is the flux of component i in the sediment, g/m^2/yr; f_i is the weight fraction of component i in the sediment, %; β is the constant production rate of ^{230}Th in the water column, estimated as the product of the activity of ^{234}U in the water column (2894 dpm/m^3) and the decay constant of ^{230}Th; z is the water depth, m; $^{230}Th_{xs}$ is the activity of scavenged ^{230}Th in sediment, dpm/g.

In support of the ^{230}Th-normalization method, studies have evaluated fluxes of particulate ^{230}Th using sediment traps (e.g. Anderson et al., 1983a; Scholten et al., 2001; Yu et al., 2001) and models (Henderson et al., 1999), and justified the assumption that scavenged ^{230}Th fluxes are broadly equal to production in the overlying water column.

The constant Th flux to sediment for a given location means that, when sedimentation rates are low, sediment ^{230}Th concentrations are high, and vice versa. Sediment dissolution is also expected to change the concentration of ^{230}Th in sediment, as long as ^{230}Th remains in the sediment, as might be expected given its very high particle affinity. Sediment dissolution effectively lowers sedimentation rate, and is therefore expected to increase sediment ^{230}Th concentrations. The expected result of sediment dissolution on ^{230}Th concentrations is shown schematically in Figure 4.1. This study assesses whether these expected changes in ^{230}Th concentrations in sediment close to the seafloor are observed, and can provide an assessment of the rate and amount of sediment dissolution.

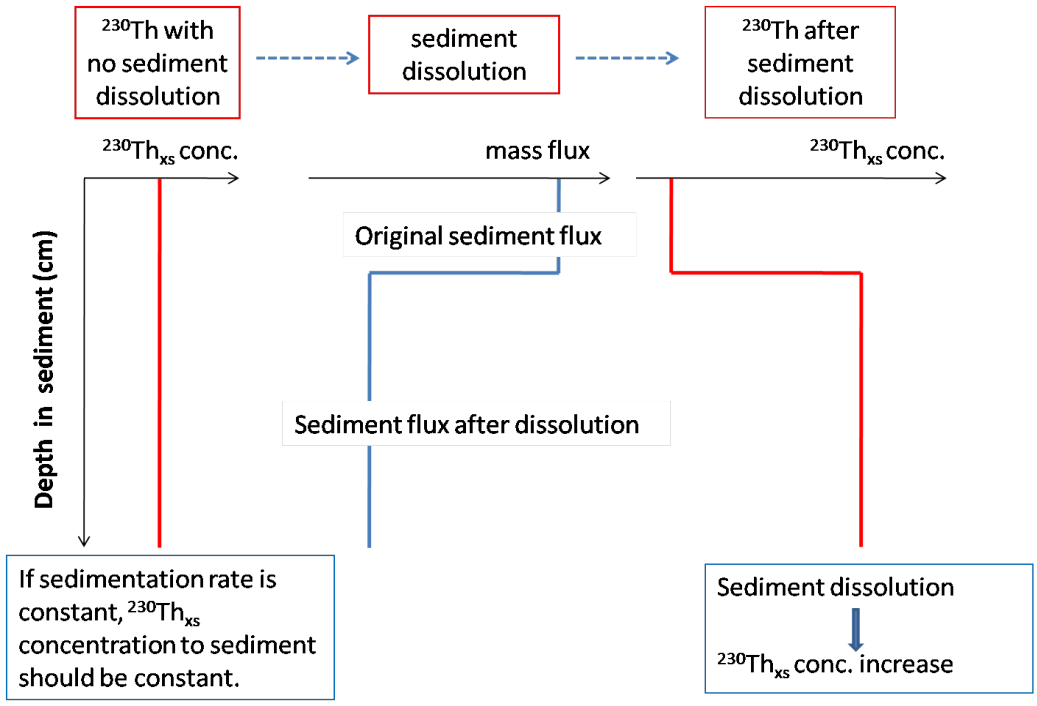


Figure 4.1: Schematic of principles underlying the use of ^{230}Th as an indicator of sediment dissolution.

4.3 Locations and samples

Surface sediment samples investigated in this study were collected on a down-slope transect on the continental margin of Cape Basin in the eastern South Atlantic (Figure 4.2; Table 4.1) during UK-GEOTRACES Cruise GA10E (D357). The Cape Basin is bounded to the north by the Subtropical Gyre and the Benguela Current (Peterson and Stramma, 1991; Orsi et al., 1995), and is influenced by the distal filaments of the Agulhas Current retroflection (Lutjeharms, 1996). In the upper water column (0-800 m), the surface waters represent a combination of at least three major water masses: Subtropical Water derived from the west and the southwest, upwelled South Atlantic

Central Water (most likely a mixture of Antarctic Intermediate Water and Subtropical Water), and Agulhas Water advected around the Cape of Good Hope (Darbyshire, 1966).

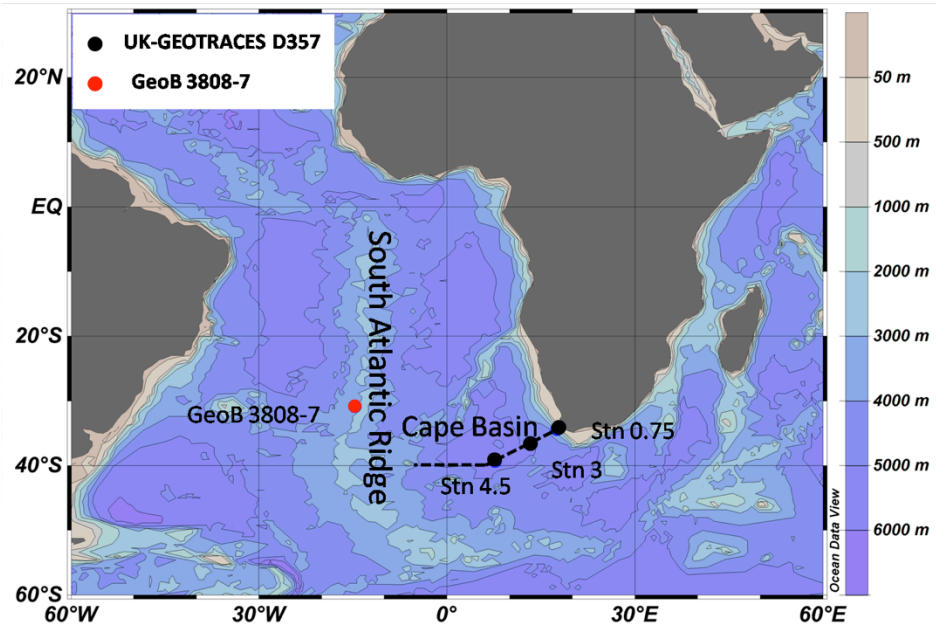


Figure 4.2: South Atlantic area showing sediment sample locations. Black dots indicate sample locations on the continental margin of Cape Basin investigated during the UK-GEOTRACES cruise D357 in 2011. Red dot indicates a sediment core retrieved from South Atlantic Mid-Ocean Ridge during Meteor cruise M34/3 in 1996.

Station	Longitude (°E)	Latitude (°N)	Water depth (m)
D357-0.75	17.57	-34.39	1168
GeoB3808-7	-14.71	-30.81	3213
D357-3	13.31	-36.47	4887
D357-4.5	7.67	-39.29	5269

Table 4.1: Locations and water depths of sediment samples in this study

Recovered cores were sampled from water depths between 1168 m to 5269 m, and show distinct color variation with depth, presumably reflecting different sediment composition due to productivity and dissolution at that setting (Figure 4.3). D357 cores were taken with a Megacorer,

which captures intact sediment-water interfaces with minimum sediment disturbance. Core D357-0.75 was positioned at a water depth of 1168 m, where the oxygen minimum (due to the presence of upper-circumpolar water) impinges on the continental slope (Figure 4.4). Cores D357-3 and D357-4.5 were recovered in the southern Cape Basin close to the northern flank of the Agulhas Ridge in ~ 4887 m and 5269 m of water, respectively. To fill in the gap in depth between these Cape Basin cores, sediment samples were retrieved from core GeoB3808-7 located in the South Atlantic Mid-Ocean Ridge in ~3213 m of water.

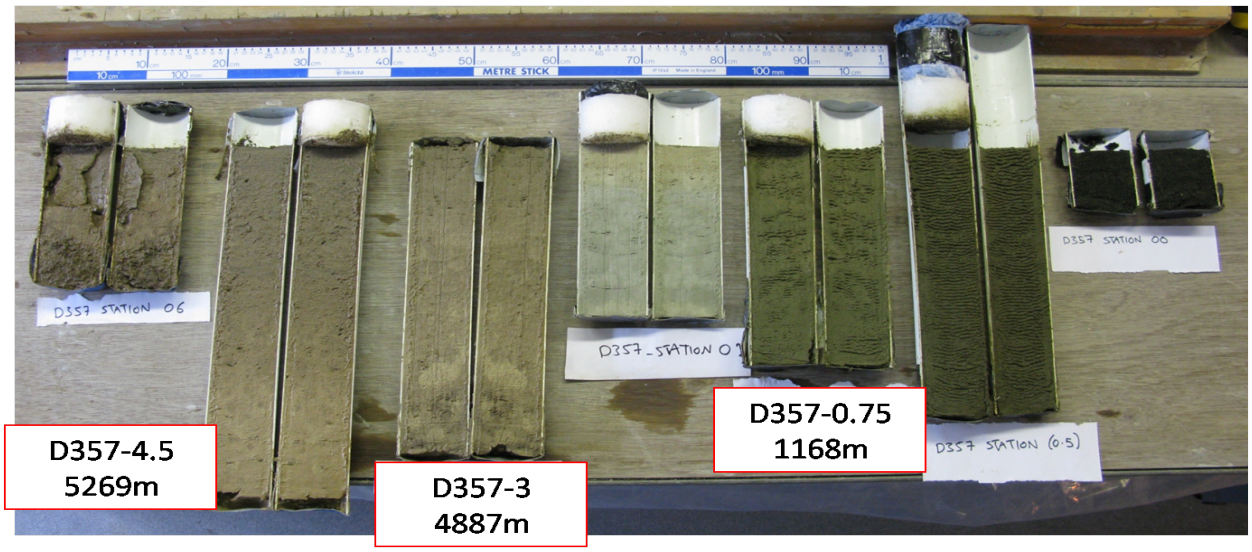


Figure 4.3: Sediment cores retrieved from the continental margin of Cape Basin in the eastern South Atlantic. Three cores in this study are labeled in red-outline boxes. The shallowest core (D357-0.75), is a dark green color, and was bathed in the Oxygen Minimum Zone (OMZ), indicating the presence of Fe^{2+} in a reducing environment.

Carbonate saturation decreases with depth in the southern Cape Basin. The depth of the $CaCO_3$ saturation horizon can be assessed using alkalinity and dissolved inorganic carbon (DIC) data collected on the same cruise by Matthew Humphries. The $CaCO_3$ horizon is at a depth of ~3700 m. Cores D357-3 and 4.5 are located below the saturation horizon, whereas cores D357-0.75 and GeoB3808-7 are located above (Figure 4.4).

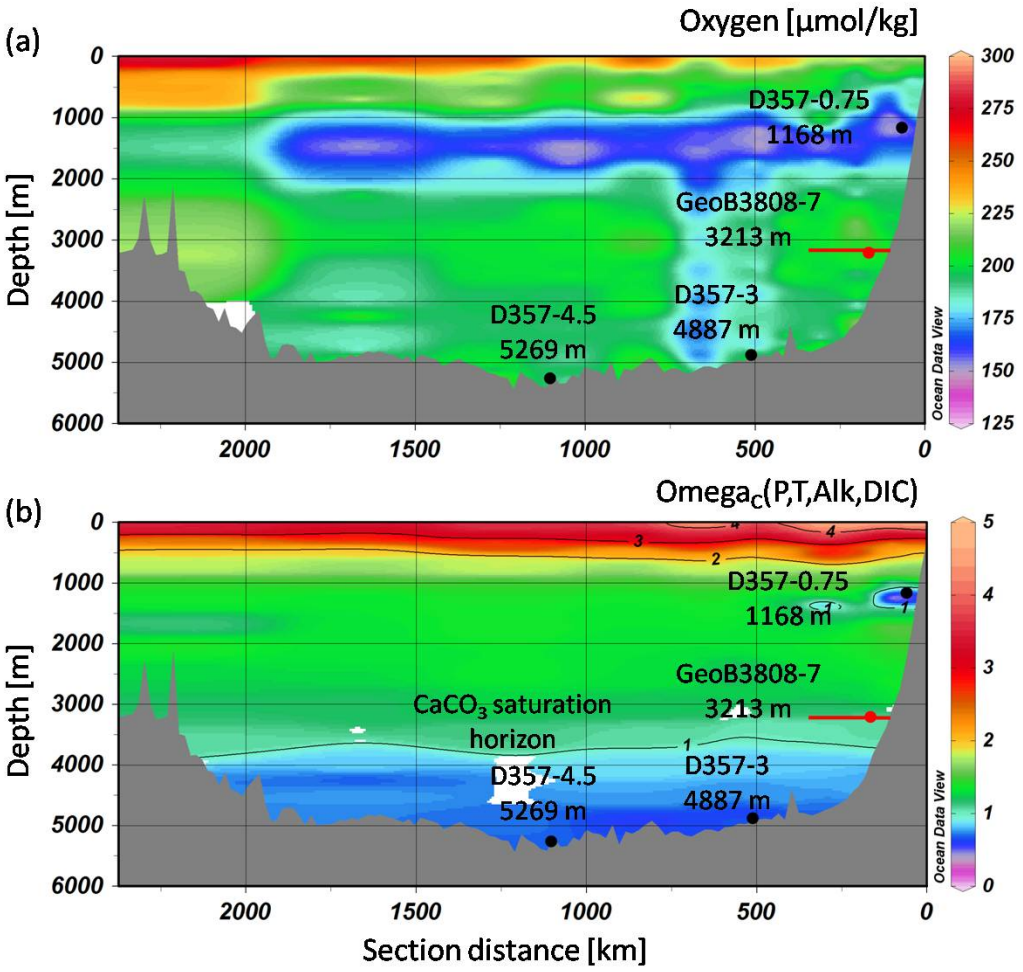


Figure 4.4: Section figures of a) oxygen concentrations; b) omega values derived from measurements of alkalinity (ALK) and dissolved inorganic carbon (DIC). Low oxygen concentrations are observed in the water column at ~1000-1500 m, overlying the shallowest core (D357-0.75). The $CaCO_3$ saturation horizon is at ~3700 m in the Cape Basin.

4.4 Analytical techniques

4.4.1 U-series analyses

D357 cores were sliced into 1 cm or 2 cm slices on the ship and each slice was bagged separately. Back on shore, an aliquot of sediment was taken from bags spanning the top 0.5 to 24 cm of each core, freeze-dried, homogenized by agate pestle and mortar, and subjected to total digestion using HCl, HNO_3, $HClO_4$ and HF acids. Subsampling and digestion of D357 sediment samples were conducted by Will Homoky at National Oceanography Center, Southampton (NOCS), and GeoB3808-7 by Lukas Jonkers. More details were given in Homoky et al., (2013). In the clean laboratory at Oxford, an aliquot of digested sediment solution, containing approximately 0.05-0.1 g of sediment, was spiked with a mixed ^{229}Th-^{236}U spike (Robinson et al., 2004), and a ^{233}Pa tracer solution (prepared from ^{237}Np following Regelous et al. (2004)) (see Chapter 2). Separation of U, Th and Pa was by anion exchange chromatography (Biorad AG 1×8 resin, 100-200 mesh), and measurement for U, Th and Pa isotopes was by a Nu Instruments MC-ICP-MS (Thomas et al. 2009; Negre et al., 2009; see Chapter 2). Mass discrimination and ion-counter gain were assessed by bracketing each sample analysis with measurement of CRM-145 U. Measurements were also made 0.5 amu either side of masses of interest to allow accurate correction for the effect of abundance sensitivity on small ^{231}Pa and ^{230}Th beams, and a correction for ^{232}ThH interference on the mass-233 beam is made from assessment of the hydride formation rate from a ^{232}Th standard. Further analytical details are given in Chapter 2.

Chemistry blanks were determined by performing a complete chemical procedure on Milli-Q water with each batch of samples. Blanks for ^{231}Pa, ^{230}Th, ^{232}Th and ^{238}U are 0.77±1.39 fg, 1.36±3.36 fg, and 128.5±95.2 pg, 132.8±109.3 pg, respectively, and are always less than 1 % of the mass in analysed samples.

4.4.2 Sediment composition

Sediment samples collected from Cape Basin margin were also analyzed for their sediment composition by Will Homoky at NOCS. Total carbon (TC) and total inorganic carbon (TIC) were determined by coulometry on dry homogenized sediments. Aluminum was determined by inductively coupled plasma atomic emission spectroscopy (ICP-AES) on an aliquot of the same solution obtained for U-series elements. Detailed procedures were described in Homoky et al. (2013). Weight percentages of the four major particulate components in sediment (lithogenic; carbonate; organic matter; opal) were calculated as follows. Using a crustal Al content of 8.15% (Rudnick and Gao, 2003), the percent of lithogenics is given by f_{litho} (wt%) = Al/8.15×100 (where Al is the weight fraction of Al (wt%)). The carbonate fraction was determined from TIC as follows: f_{CaCO_3}(wt%) =TIC/12×100 by assuming that all TIC is contained in $CaCO_3$. With TOC calculated as the difference between TC and TIC, and assuming that organic matter contains 58% organic carbon, organic matter was calculated by f_{OM} (wt%)= TOC/0.58 (Nelson and Sommers, 1996). Biogenic opal (bSi) was assumed to make up the remainder of the sediment and was not independently measured.

4.4.3 Salt-correction

Salt, originally dissolved in the pore fluid, remains as solid in the sediment after drying. This salt is included in dry weight measurement of sediment samples, and thus needs to be corrected to give the mass of sediment without salt. An aliquot of wet sediment was weighed before and after it was freeze-dried. The calculation of residue salt mass per dry sample mass is given by,

$$F = M_s / M_d = (M_w - M_d) \times S / M_d \quad (4.2)$$

where F is the residue salt mass per dry sample mass, g/g; M_s is the residue salt mass, g; M_d is the mass of dry sample, g; M_w is the mass of the wet sample, g; S is salinity, expressed as a decimal; i.e., 35 ppt= 0.035, Noorany (1984).

Salt-corrected sample mass can then be obtained by subtracting the weight of the remaining salt from the measured weight of the dry sample, given by

$$M_{corr} = M_{sam} - M_{sam} \times F \quad (4.3)$$

where M_{corr} is the salt-corrected sample mass, g; M_{sam} is the measured weight of the dry sample, g.

4.5 Results

4.5.1 ^{232}Th and ^{238}U

Th-232 concentrations range between 0.202 and 2.971 dpm/g, with low values observed in core-top sediment and relatively constant higher values at depth (see Appendix Table 4.1). Th-232 is expected to be entirely within the lithogenic fraction of marine particulate matter, and can thus be used to estimate the lithogenic fraction of the sediment as an alternative approach to Al. Assuming a uniform ^{232}Th concentration in lithogenics of 13 ppm gives lithogenic fractions for the sediments as shown on Figure 4.5. With few exceptions, down-core lithogenic fractions estimated by ^{232}Th and Al agree well with each other. The relatively lower estimates of lithogenic fractions observed in cores D357-3 and D357-4.5 are most likely due to the poor recovery of Al during sample digestion (Per. Comm. William Homoky). In the deepest core (D357-4.5), however, the lower value of core-top lithogenic fraction estimated by ^{232}Th is an artifact due to improper handling of the ^{232}Th sample during sample digestion, and will be reanalyzed in the future.

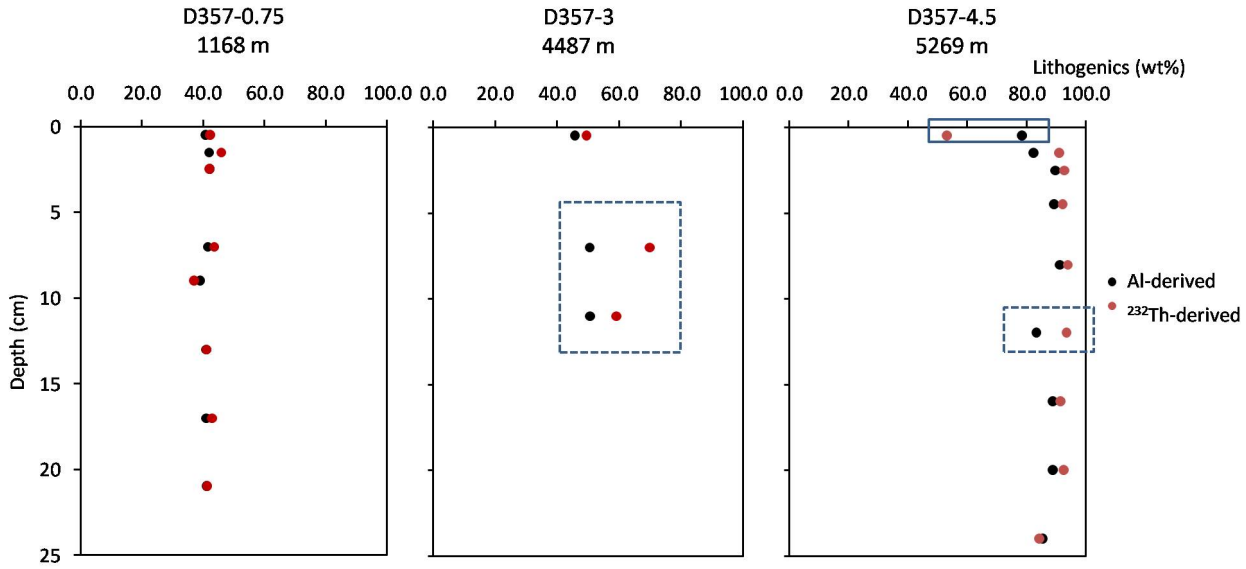


Figure 4.5: Lithogenic fractions in the Cape Basin sediment estimated by concentrations of Al (black dots) and of ^{232}Th (red dots). Lithogenics fractions estimated by Al and ^{232}Th are generally in good agreement with each other. Exceptions are however seen in cores D357-3 and D357-4.5 (highlighted by blue boxes). The relatively lower estimates by Al (blue dashed boxes) are most likely due to the poor recovery of Al during sample digestion, while the lower core-top estimate by ^{232}Th in core D357-4.5 (blue box) is an artifact caused by improper handling of ^{232}Th sample during sediment digestion.

U concentrations were also measured as a by-product of the analysis. ^{238}U concentrations in the sediment range between 0.172 and 3.315 dpm/g (See Appendix Table 4.1). This measured ^{238}U content consists of authigenic and detrital components. Using the detrital fractions calculated from ^{232}Th allows these components to be separated. Anderson et al. (1983b) estimated a detrital $^{238}U/^{232}Th$ ratio (expressed as activity ratios) of 0.8±0.4 for the Panama and Guatemala basins. Chase et al. (2003) estimated a $^{238}U/^{232}Th$ ratio of 0.5±0.1 for detrital phases in the Southwest Pacific sector of the Southern Ocean. Considering the geographical variation of detrital $^{238}U/^{232}Th$, localized detrital $^{238}U/^{232}Th$ values are estimated in this study using the end-member method described in Bourne et al. (2012b). Estimates of detrital $^{238}U/^{232}Th$ values are 1.22±0.09 (D357-0.75), 0.54±0.02 (D357-4.5), 0.87±0.08 (D357-3) and 0.51±0.02 (GeoB3808-7). The relatively

higher detrital $^{238}U/^{232}Th$ value from the shallowest sediment core (D357-0.75) probably reflects a different source of detrital material on the slope of Cape Basin Margin from those offshore.

Separating detrital fraction from measured U actvities, Authigenic U is estimated from:

$$^{238}U_{auth} = ^{238}U_{meas} - (^{238}U/^{232}Th)_{det} \times ^{232}Th_{meas} \qquad (4.4)$$

where $^{238}U_{meas}$ and $^{232}Th_{meas}$ are measured ^{238}U, ^{232}Th activities in dpm/g, and $(^{238}U/^{232}Th)_{det}$ is the local value of detrital $^{238}U/^{232}Th$, estimated by the end-member method discussed above.

Concentrations of authigenic U vary significantly from shallow cores to deep cores (Figure 4.6). The deepest core (D357-4.5) and the core from 3213 m (GeoB3808-7) have rather low authigenic U, ranging from 0.02 to 0.07 dpm/g in the upper sediment core and dropping to almost zero at depth. The core from 4887 m (D357-3) has slightly higher authigenic U in the top two sediment, reaching 0.38 dpm/g, and authigenic U concentrations close to zero below. In the shallowest core (D357-0.75), authigenic U is clearly present, ranging from 0.11 to 1.73 dpm/g. $\delta^{234}U$ values in this core are also relatively higher than other cores, with an average value of 41 (See Appendix Table 4.1). This suggests that a large fraction of the uranium found in this core cannot be detrital, but instead must have been added to the sediment as a result of reducing conditions either in the sediment or in microenvironments within settling particles (Anderson, 1982). This explanation is consistent with the fact that this core was located at a water depth where O_2 concentrations are relatively low (Figure 4.4a).

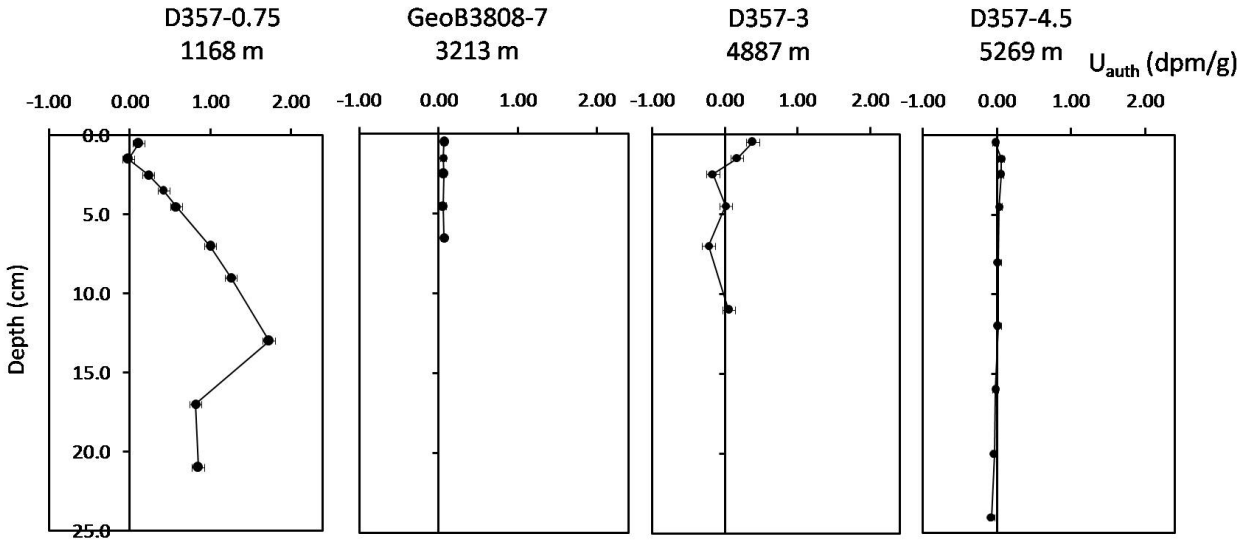


Figure 4.6: Vertical profiles of authigenic U measured in the Cape Basin Margin cores (D357-0.75, D357-3, D357-4.5) and the South Atlantic Mid-Ocean Ridge core (GeoB3808-7).

4.5.2 $^{230}Th_{xs}$

Measured concentrations of ^{230}Th in marine sediments consist of three components: that scavenged from seawater; that supported by U contained within detrital minerals; and that supported by radioactive decay of authigenic U (e.g. Henderson and Anderson, 2003). To obtain ^{230}Th scavenged from seawater, measured ^{230}Th concentrations must therefore be corrected for the presence of the other two components. To make this correction, it is generally assumed that the U decay series are in secular equilibrium in detrital phases, and that the formation of authigenic U is contemporary with the deposition of the sediments. Authigenic U is assumed to have an initial $^{234}U/^{238}U$ ratio equivalent to that of U dissolved in seawater (=1.146). Accepting those assumptions, unsupported (scavenged from seawater) ^{230}Th ($^{230}Th_{xs}$) is calculated from its measured values as:

$$^{230}Th_{xs} = {}^{230}Th_{meas} - [\ (^{238}U/^{232}Th)_{det} \times {}^{232}Th_{meas}] - [\ (^{238}U_{meas} - (\ ^{238}U/^{232}Th\ )_{det} \times {}^{232}Th_{meas}\ ) \times (\ (\ 1 - e^{-\lambda_{230Th}t}) + (\lambda_{230Th} / (\ \lambda_{230Th} - \lambda_{234U})) \times (\ e^{-\lambda_{234U}t} - e^{-\lambda_{230Th}t}) \times (\ (^{234}U/^{238}U)_{init} - 1)) \ ] \quad (4.5)$$

where ^{230}Th is the measured activity of ^{230}Th, dpm/g; λ_{230Th} and λ_{234U} are decay constants for ^{230}Th and ^{234}U, respectively, yr^{-1}; and t is time since deposition, yr.

The first term in square brackets corrects for ^{230}Th supported by U in detrital material, assuming detrital ^{234}U is in secular equilibrium with ^{238}U, and using local $(^{238}U/^{232}Th)_{det}$ values as discussed above. The second term in square brackets corrects for ^{230}Th ingrowth from authigenic U. This requires an estimate of the age of the sediment, t. All samples analyzed in this study were, however, from core-top or near-surface sediments. The age of these samples can realistically be considered as zero, negating the need for a correction to measured ^{230}Th for the ingrowth from authigenic U. For the same reason, generally required correction for the decay of ^{230}Th since the time of deposition is not applied. Measured total ^{230}Th activities and detritus-corrected $^{230}Th_{xs}$ activities based on the above assumptions are listed in Appendix Table 4.1 and shown in Figure 4.7a.

$^{230}Th_{xs}$ concentrations range between 1.28 and 50.55 dpm/g, with the highest $^{230}Th_{xs}$ concentrations observed in the deepest core (D357-4.5). All profiles, except the shallowest core (D357-0.75), exhibit similar pattern for $^{230}Th_{xs}$ variations throughout the sediment core. $^{230}Th_{xs}$ concentrations increase from low values in core-top sediment to a higher value at about 3 cm (D357-4.5, 1.5 cm; D357-3, 2.5 cm; GeoB3808-7, 1.5 cm). Below this depth, $^{230}Th_{xs}$ concentrations are relatively constant at depth. Such features of $^{230}Th_{xs}$ profiles however are not observed for the shallowest core (D357-0.75), which has relatively constant $^{230}Th_{xs}$ concentrations at all depths.

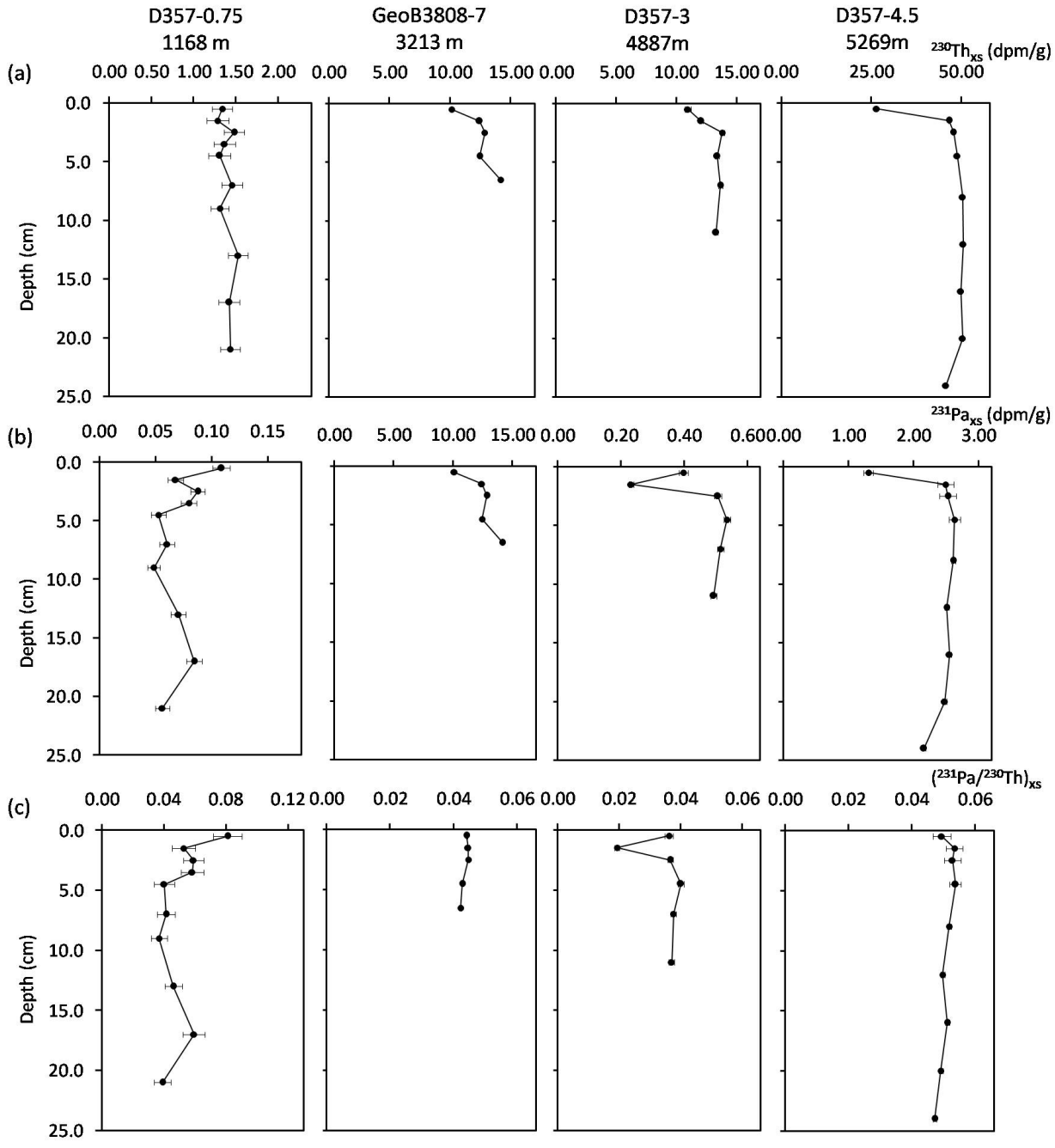


Figure 4.7: Vertical profiles of sediment (a) $^{230}Th_{xs}$ concentrations; (b) $^{231}Pa_{xs}$ concentrations; and (c) $(^{231}Pa/^{230}Th)_{xs}$ ratios measured in the Cape Basin Margin cores (D357-0.75, D357-3, D357-4.5) and the South Atlantic Mid-Ocean Ridge core (GeoB3808-7).

4.5.3 $^{231}Pa_{xs}$ and $(^{231}Pa/^{230}Th)_{xs}$

Measured $^{231}Pa_{xs}$ were corrected for the presence of detrital component in a similar manner as ^{230}Th, following the equation (Henderson and Anderson, 2003):

$$^{231}Pa_{xs} = {}^{231}Pa_{meas} - (0.046 \times (^{238}U/^{232}Th)_{det} \times {}^{232}Th_{meas}) \qquad (4.6)$$

where $^{231}Pa_{meas}$ and $^{232}Th_{meas}$ are measured activities of ^{231}Pa and ^{232}Th, dpm/g; $(^{238}U/^{232}Th)_{det}$ is the local value of $^{238}U/^{232}Th$ in detrital materials, as discussed above for $^{230}Th_{xs}$.

$^{231}Pa_{xs}$ concentrations range between 0.05 and 2.63 dpm/g (See Appendix Table 4.1). Similarly, $^{231}Pa_{xs}$ profiles in cores GeoB3808-7, D357-3, and D357-4.5 show increases in the upper sediment core, followed by fairly constant values at depth (Figure 4.7b). The depth at which $^{231}Pa_{xs}$ reached its maximum is however relatively deeper than that of $^{230}Th_{xs}$ in deep cores D357-3 and D357-4.5 (4.5 cm for both). $^{231}Pa_{xs}$ concentrations for the shallowest core (D357-0.75) are relatively constant throughout the core, except for a high value in core-top sediment (Figure 4.7b).

Ratios of $(^{231}Pa/^{230}Th)_{xs}$ range from 0.02 to 0.08, smaller than their production ratio in the water column, 0.093 (See Appendix Table 4.1). Given the measuring uncertainties, $(^{231}Pa/^{230}Th)_{xs}$ are generally constant throughout the sediment core, except for those in the shallowest core (D357-0.75) (Figure 4.7c), in which somewhat high values of $(^{231}Pa/^{230}Th)_{xs}$ were observed in the core-top sediment, reflecting the high core-top $^{231}Pa_{xs}$ concentration in this core.

4.5.4 Sediment composition

Sediment compositions in weight percentage (%) were measured for sediment cores on the Cape Basin margin (See Appendix Table 4.2; Figure 4.8). In all three cores, lithogenics are the most abundant constituent, ranging from 38.9% to 91.4%. The highest lithogenic contents (wt%) were observed in the deepest core (D357-4.5). Organic matter accounts for only 0.27% to 4.1% of the sediment in these cores. The highest values were observed in the shallowest core D357-0.75, indicating higher organic matter supply from the continental margin. In deep cores, D357-3 and D357-4.5, opal content accounts for 36.9% and 10.2% of the sediment, respectively, while $CaCO_3$ account for 13.8% and 2.0% of the sediment, respectively. In the shallowest core (D357-0.75), however, opal content, 23.7%, is only slightly lower than $CaCO_3$ content, 31.4%, reflecting a better preservation of $CaCO_3$ in sediment of a shallower water depth.

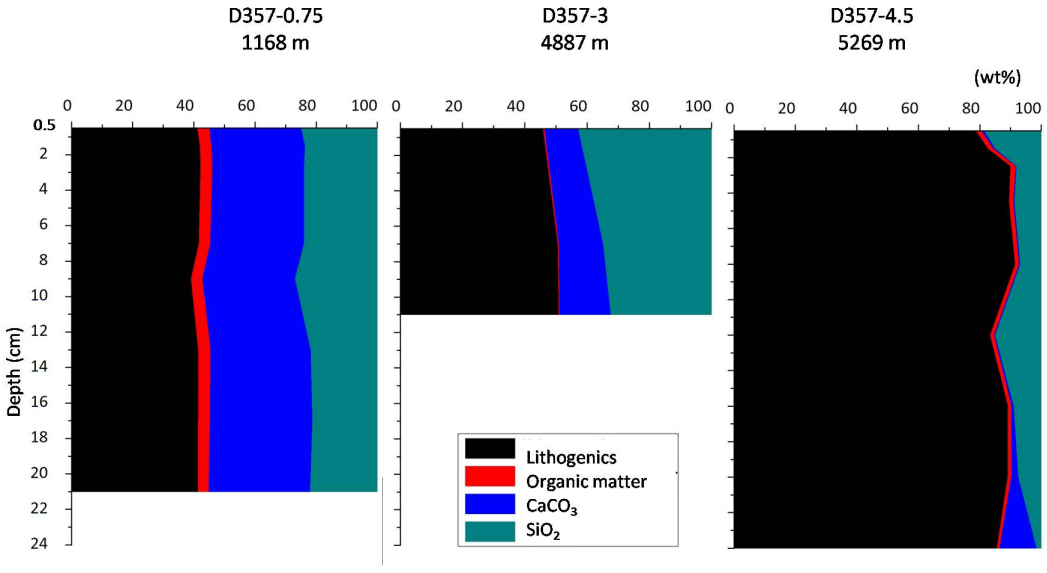


Figure 4.8: Vertical profiles of sediment content measured for sediment on the Cape Basin Margin in weight percentage (wt%).

4.6 Discussion

4.6.1 $^{230}Th_{xs}$ as an indicator of sediment dissolution

The striking feature observed in $^{230}Th_{xs}$ profiles is the increase of $^{230}Th_{xs}$ concentrations from low values in core-top sediment to higher values at 3 cm in sediment cores deeper than 3000 m, i.e. D357-3, D357-4.5, and GeoB3808-7. This structure of $^{230}Th_{xs}$ profile is consistent with the expectation of down-core ^{230}Th profiles if dissolution of sediment takes place in the upper section of core. Although sediment redistribution, caused by lateral bottom currents close to the seafloor, can also cause the loss of a fraction of sediment mass flux from its original site, ^{230}Th would be carried with the sediment during such transport so that this process would not lead to a change in ^{230}Th concentration. Assuming that there is no fractionation between the four particulate sediment components during the redistribution process, the variations of $^{230}Th_{xs}$ concentrations in the upper sediment core can therefore not be caused by such sediment redistribution.

If the flux of sediment from the water column has remained constant for the analysed portion of each core, the increase in ^{230}Th concentration observed with depth in the cores can only be generated by dissolution of sediment. The flux might reasonably be assumed to be constant if all sediments are deposited during the relative climate stability of the Holocene. The ^{230}Th concentrations can be used to assess the sedimentation rate and therefore the ages of sediment sampled in these cores. Assuming that the density of sediment is $1 g/cm^3$, sedimentation rate can be estimated as:

$$\text{Sedimentation rate} = \beta \times z / (^{230}Th_{xs} \times 1\ (g/cm^3)) \qquad (4.7)$$

The resulting sedimentation rates range from 0.53 to 2.31 cm/kyr, with the highest value in the shallowest core (D357-0.75). Based on these sedimentation rates, the estimated ages for the upper 5 cm of sediment in these cores range from 5.3 to 11.6 kyr. We can therefore consider these sediments as of Holocene age and the assumption that the flux of sediment from the water column has remained constant for the upper portion of each core is reasonable.

Based on $^{230}Th_{xs}$ data, sediment dissolution only takes place in the upper few centimeters of the sediment, typically down to 3 cm. Below this depth, sediment dissolution does not occur in the deep cores. In the shallow core (D357-0.75), however, a lack of ^{230}Th concentration change suggests little or no sediment dissolution at any depth. This core is significantly above the carbonate saturation horizon, which may explain its rather different dissolution history relative to the deeper cores.

4.6.2 Quantifying sediment dissolution rate with $^{230}Th_{xs}$

As discussed above, increases in $^{230}Th_{xs}$ concentrations observed in the upper centimeters of the sediment core are the result of sediment dissolution. We can therefore use down-core $^{230}Th_{xs}$ variations to indicate the presence of sediment dissolution and to estimate the rate of this process.

Sediment dissolution causes the loss of a fraction of sediment into the overlying seawater, which results in the observed increase of $^{230}Th_{xs}$ concentration with sediment depth. The fraction of sediment lost due to dissolution can be calculated from the difference between $^{230}Th_{xs}$

concentrations in the core-top sediment, where sediment dissolution has not yet occurred, and $^{230}Th_{xs}$ concentrations deeper in the sediment, where sediment dissolution is complete:

$$\text{Dissolved sediment fraction } (\%) = \frac{(^{230}\text{Th}_{xs})_{\text{core-top}} - (^{230}\text{Th}_{xs})_{\text{at-depth}}}{(^{230}\text{Th}_{xs})_{\text{at-depth}}} \qquad (4.8)$$

where $(^{230}Th_{xs})_{core\text{-}top}$ is the $^{230}Th_{xs}$ concentration in the core-top sediment, dpm/g; and $(^{230}Th_{xs})_{at\text{-}depth}$ is the average $^{230}Th_{xs}$ concentrations at depth where $^{230}Th_{xs}$ concentrations stay relatively constant in the core, dpm/g. This calculation assumes that the flux of sediment from the water column has remained constant for the upper portion of each core.

Sediment dissolution fractions calculated from the $^{230}Th_{xs}$ data range from 4.8% to 46.2% (Table 4.2, Figure 4.9). The shallowest core (D357-0.75) has very little dissolution, 4.8±0.5%, while, in the three cores deeper than 3000 m, dissolved sediment fraction range between 19.1 and 46.2%, suggesting a significant loss of sediment mass flux to the overlying water.

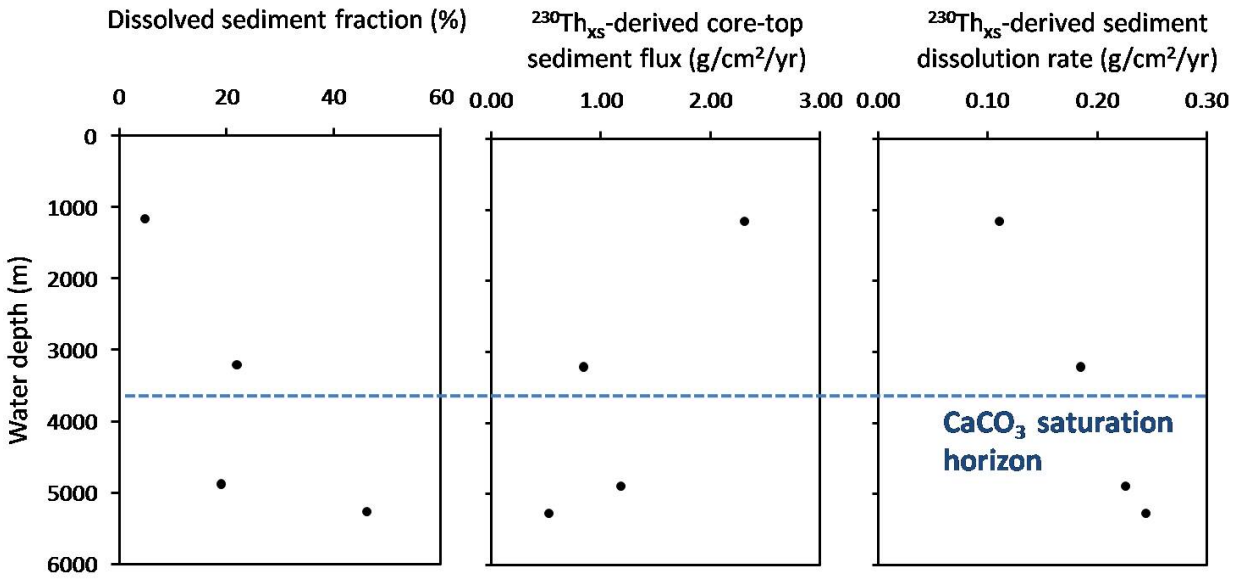


Figure 4.9: Dissolved sediment fraction (%), core-top $^{230}Th_{xs}$ flux (g/cm^2/kyr) and dissolution rate (g/cm^2/kyr) calculated from $(^{230}Th)_{xs}$ concentration. $CaCO_3$ saturation horizon is shown in the blue dashed line, at 3700 m in the Cape Basin.

Sample ID	Water depth (m)	Dissolved sediment fraction (%)	Core-top $^{230}Th_{xs}$ flux (g/cm^2/kyr)	Sediment dissolution rate (g/cm^2/kyr)
D357-0.75	1168	4.8±0.5	2.31±0.21	0.11±0.01
GeoB3808-7	3213	22.0±0.1	0.84±0.01	0.18±0.01
D357-3	4887	19.1±0.4	1.18±0.03	0.23±0.01
D357-4.5	5269	46.2±0.2	0.53±0.01	0.24±0.01

Table 4.2: Calculated estimates of dissolved sediment fraction (%), core-top $^{230}Th_{xs}$ flux (g/cm^2/kyr) and sediment dissolution rate (g/cm^2/kyr).

In addition to the fraction of sediment lost by dissolution, the rate of this dissolution can be calculated from the $^{230}Th_{xs}$ measurements. Th-230 can provide a measure of the flux of sediment to the core-top, given by (e.g. Henderson and Anderson, 2003):

$$F\ (g/cm^2/kyr) = \frac{\beta \times z}{^{230}Th_{xs}} \qquad (4.9)$$

The product of this sediment flux and the fraction of sediment that subsequently dissolves thus provides an estimate of a rate of sediment dissolution:

Sediment dissolution rate ($g/cm^2/kyr$) = Dissolved sediment fraction (%) × F ($g/cm^2/kyr$) (4.10)

Resulting rates of sediment dissolution range between 0.11 and 0.24 $g/cm^2/kyr$ (Table 4.2, Figure 4.9). A nearly linear increase in sediment dissolution rate with water depth can be observed (Figure 4.9), with the greatest sediment dissolution rate observed in the deepest core (D357-4.5).

4.6.3 Dissolution of sedimentary components and water-depth dependence

The ^{230}Th-normalization method can be used to assess the dissolution of each mineralogical component of the sediments at the seafloor. Following equation (4.1) the product of total sediment mass-flux (derived from $^{230}Th_{xs}$) and the measured weight fraction of each component in the sediment provides a flux of that component. By comparing these fluxes at the core-top with those deeper in the core, $^{230}Th_{xs}$-normalized sedimentary fluxes of lithogenics, OM, $CaCO_3$ and opal for D357 sediment are derived (Appendix Table 4.3 and Figure 4.10). If the assumption is made that

initial fluxes to the core-top are constant during the period of deposition of these cores, then changes in these component fluxes with depth in the sediment must reflect post-depositional dissolution.

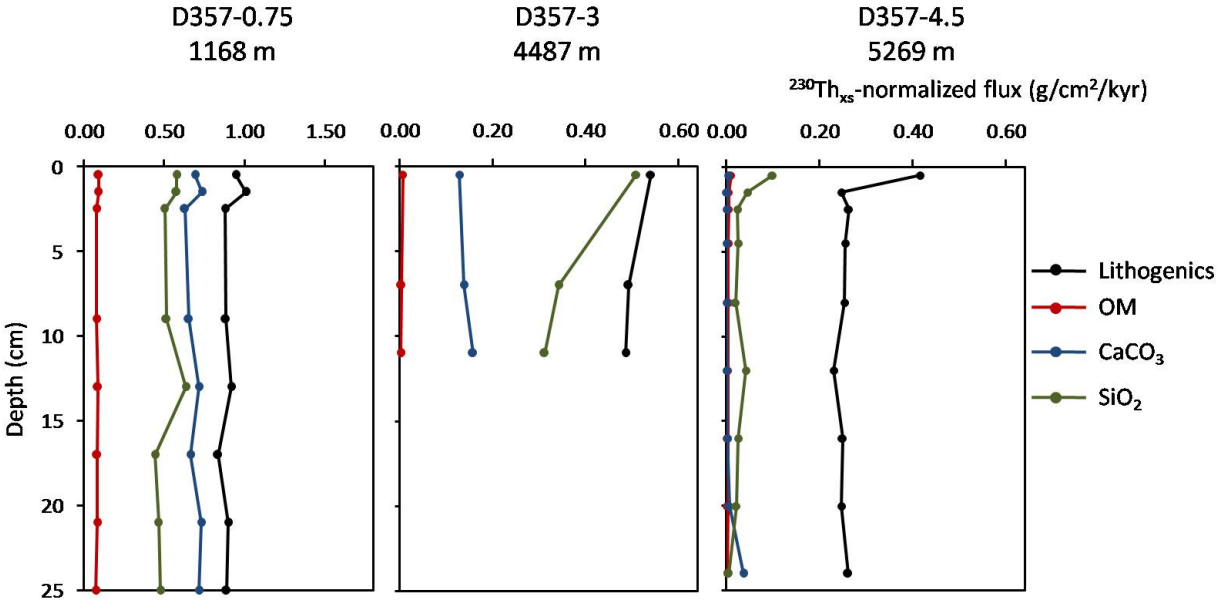


Figure 4.10: Vertical profiles of $^{230}Th_{xs}$-normalized fluxes of sediment content, i.e. lithogenics, organic matter (OM), $CaCO_3$, and SiO_2, for sediment on the Cape Basin Margin.

Downcore fluxes of sedimentary components are shown in Figure 4.10, but to simplify discussion, I focus here on a comparison of the core-top fluxes with those at 3 cm, below which sediment dissolution is complete as observed by $^{230}Th_{xs}$ profiles (Figure 4.11). For core D357-3 where sedimentary component data are not available at 3 cm, sediment fluxes at 7 cm were used for this comparison.

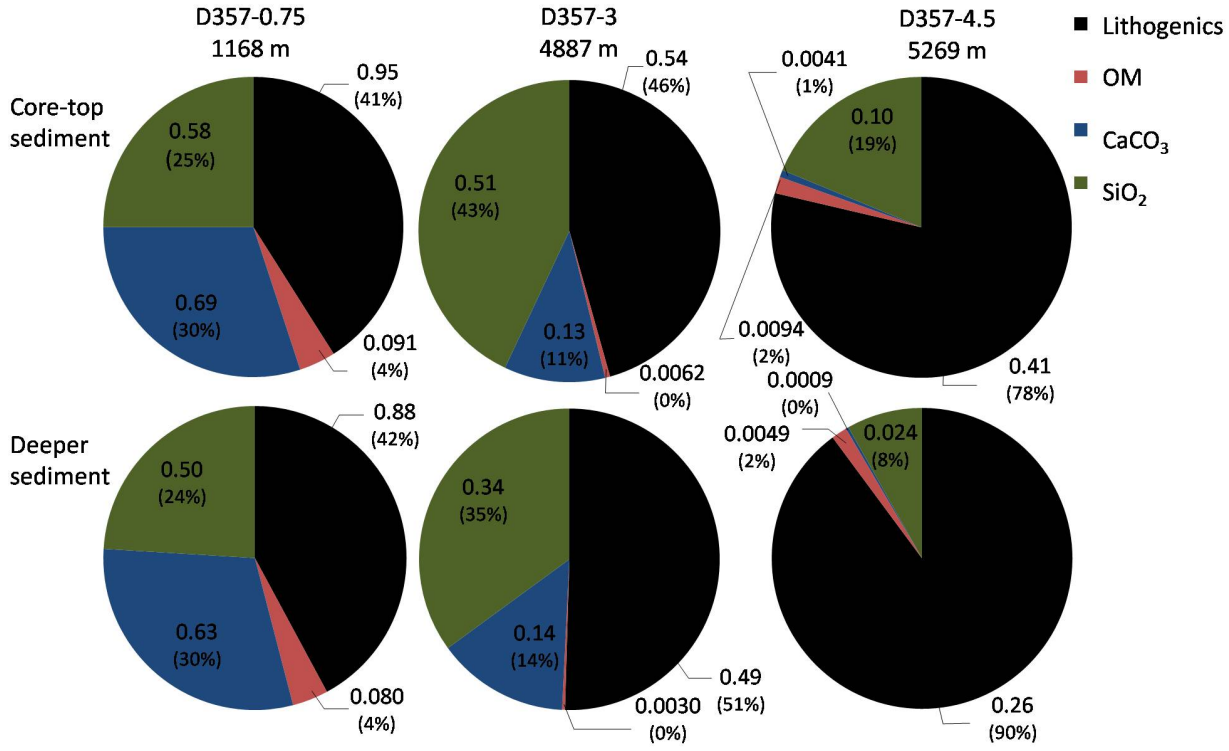


Figure 4.11: $^{230}Th_{xs}$-normalized fluxes of sediment content, e.g. lithogenics, organic matter (OM), $CaCO_3$, and opal, in g/m^2/yr, and their relative percentages to the total, in %, for the core-top sediment and the lower sediment in Cape Basin Margin.

I first discuss core D357-3, situated at 4487 m and therefore below the carbonate saturation horizon. This core has experienced significant dissolution as indicated by the $^{230}Th_{xs}$ profile, with the opal flux decreases from 0.51 g/cm^2/kyr in the core-top sediment to 0.34 g/cm^2/kyr in the deeper sediment. $CaCO_3$ fluxes, on the other hand, stay nearly constant from core-top sediment to the deeper sediment, being 0.13 g/cm^2/kyr and 0.14 g/cm^2/kyr, respectively. This indicates that opal dissolution is more significant than $CaCO_3$ deposition at this site. There is also a significant decrease of about 50% in OM flux due to dissolution, but the initial OM flux to the sediment is so small (about 100 times lower than fluxes of other components), that this does not contribute significantly to overall dissolution of sediment by mass at this site. Lithogenic fluxes also decrease, by ~9% in this core. Dissolution of opal, however, is therefore the major

contribution to the increases of $^{230}Th_{xs}$ observed in the upper centimeters of this sediment core. This finding is surprising, suggesting that, although the bottom water is undersaturated with respect to $CaCO_3$, dissolution of $CaCO_3$ at the seafloor is slow compared to that of opal.

Mechanisms other than the saturation state of the overlying water may be the major influence on dissolution within sediment at this site. The degradation of organic matter in sediments has been proposed as an important mechanism driving *in situ* $CaCO_3$ dissolution (e.g. Chen, 2002; Jahnke and Jahnke, 2004; Milliman et al., 1999). If this mechanism is the major driver of $CaCO_3$ dissolution in core D357-3, $CaCO_3$ dissolution may be reduced by the lack of significant OM flux at this site.

In the deepest core (D357-4.5), initial sedimentary fluxes of $CaCO_3$ and opal are about 5 times lower than those in core D357-3. This may reflect the greater water depth, allowing more time for dissolution during settling through the water, and the greater distance from the continental margin, leading to decreased productivity. Th-230-derived sedimentary fluxes indicate opal fluxes which decrease from 0.10 to 0.02 g/cm^2/kyr due to dissolution, and much small $CaCO_3$ and OM fluxes, decreasing from 0.004 to 0.001 g/cm^2/kyr, and from 0.009 to 0.005 g/cm^2/kyr, respectively. Lithogenics appear to experience appreciable dissolution in this core, decreasing from 0.41 g/cm^2/kyr in the core-top sediment to 0.26 g/cm^2/kyr in the lower sediment. Given the dominance of lithogenics to the overall sediment composition at this site, this change dominates the overall mass loss. Some caution is required with this interpretation, which rests on a single low ^{230}Th measurement at the core-top of D357-4.5, and requires replication. Taken at face value, however, and supported by evidence for lithogenic dissolution in core (D357-3), the ^{230}Th approach provides evidence for "submarine weathering" of continental silicates, and quantifies its flux. This process of silicate weathering could play an important role in long-term surface-earth chemical budgets,

but has been difficult to constrain with direct observations. The use of sedimentary $^{230}Th_{xs}$ may provide a powerful new tool to assess the significance of this process in global chemical cycles. Bathed in waters with low oxygen concentrations, the shallowest core (D357-0.75) has significantly higher fluxes of OM than the other two cores. Fluxes of lithogenics and $CaCO_3$ are also higher, presumably reflecting proximity to the continent. Little variation in fluxes of sediment components is observed with depth in this core, with all the major components varying by only ~10%. This indicates little or no sediment dissolution takes place at this site.

4.6.4 Influence of sediment dissolution on sedimentary $(^{231}Pa/^{230}Th)_{xs}$

Substantial sediment dissolution might be expected to lead to a change in the $^{231}Pa/^{230}Th$ ratio captured in sediment. This ratio is considered a possible proxy for the rate of ocean circulation (e.g. McManus et al., 2004; Negre et al., 2010) or for biological productivity, particularly of opal (e.g. Bradtmiller et al., 2007; Chase et al., 2003), but its use as a proxy would clearly be negatively impacted if the ratio changes during sediment burial. A change in the ratio might be expected if the sediment composition changes dramatically, because different particle types are known to have particular affinities for the scavenging of ^{230}Th and, particularly, ^{231}Pa (e.g. Chase et al., 2002; Luo and Ku, 1999).

Despite dissolution fractions of up to 50% in the cores we have investigated, we see no indication of a change in the $(^{231}Pa/^{230}Th)_{xs}$ ratios. Downcore records exhibit little structure that might be the result of sediment dissolution (Figure 4.7c). Sediment dissolution therefore does not

seem to significantly affect sedimentary $(^{231}Pa/^{230}Th)_{xs}$ ratios; a reassuring result for the use of this sediment proxy.

4.7 Conclusions

High-resolution measurements of U-series isotopes were obtained from the sediment collected on the Cape Basin Margin and the South Atlantic Mid-Ocean Ridge. Vertical profiles of $^{230}Th_{xs}$ concentrations exhibit a striking feature of increase of $^{230}Th_{xs}$ in the upper sediment followed by relatively constant values at depth. This study has demonstrated that such features can be used to indicate the presence of sediment dissolution in the upper centimeters of these cores, assuming that ^{230}Th flux to the seafloor is constant with time. $^{230}Th_{xs}$ measurements can therefore provide a tool to quantify the rate of sediment dissolution at the seafloor and assess the magnitude of this process in various ocean settings. Based on $^{230}Th_{xs}$ data in this study, the estimates of sediment dissolution rate range between 0.11 and 0.24 g/cm^2/kyr, and exhibit a nearly linear increase with water depth. Combining $^{230}Th_{xs}$ with sediment composition measurements provides an assessment of the dissolution rates of individual mineralogical components in the sediment. In the core with the most unambiguous dissolution, situated a kilometer below the modern carbonate saturation horizon, there is surprising lack of observed carbonate dissolution, while opal does appear to be dissolving. Results also suggest dissolution of the lithogenic fraction of sediments in two of the cores. If confirmed, this suggests the use of ^{230}Th to assess the process of submarine weathering, a process which is presently difficult to quantify. Measurements of ^{231}Pa enable and assessment of

the impact of sediment dissolution on $(^{231}Pa/^{230}Th)_{xs}$ ratios. Despite significant sediment dissolution, $(^{231}Pa/^{230}Th)_{xs}$ ratios stay relatively constant in the upper sediment core and do not appear to be affected by sediment dissolution, suggesting the robustness of sedimentary $(^{231}Pa/^{230}Th)_{xs}$ as a proxy for paleoceanographic studies.

Chapter 5

Assessing the use of water-column ^{232}Th-^{230}Th to assess dust deposition to the ocean with coupled water and aerosol measurements in the tropical Atlantic

Abstract

Water-column ^{230}Th and ^{232}Th were measured for five sites in the tropical Atlantic ocean between 7^{o}S and 19^{o}N during the UK-GEOTRACES cruise GA06 (D361). Dissolved ^{230}Th profiles exhibit a broadly linear increase with water depth in the upper water column, which can be explained by the reversible scavenging model. Dissolved ^{232}Th profiles exhibit variability between sites in the surface water and relatively constant values at depth. The distinct difference between ^{230}Th and ^{232}Th profiles reflects their different sources to the ocean, ^{230}Th being supplied by constant decay of uniformly-distributed ^{234}U, and ^{232}Th being supplied by dissolution from atmospheric dust falling on the surface. In this study, we assess the use of ^{232}Th to assess dust flux to the surface ocean, using coupled water-column and aerosol measurement. ^{230}Th-derived residence times enable ^{232}Th concentrations to be converted into flux values. These were calculated using mixed layer depth because deeper integration depths are complicated by differences in residence time for ^{232}Th relative to ^{230}Th. Using respective Th solubility obtained from aerosol measurement for each site, an estimation of dust flux was made from the ^{232}Th fluxes, and found to increase northward from 0.46 g/m^2/yr at 7^{o}S to 3.43 g/m^2/yr at 19^{o}N. A comparison between ^{232}Th-derived dust flux and dust fluxes from a widely used dust model shows agreement in the general northward increasing trend, but disagrees in the absolute values, with higher dust flux estimated by the model. With a relative solubility ratio of Fe and Th at 0.16, Fe flux was also estimated from ^{232}Th flux, lying in the range between 0.35 and 2.26 mg/m^2/yr.

5.1 Introduction

Eolian deposition plays an important role in supplying the ocean with terrestrial elements essential to the ocean ecosystem and ocean biogeochemical cycles. Iron, for instance, is supplied to the remote ocean by mineral dust deposition, and has been thought of as a limiting factor to the growth of phytoplankton in High-Nutrient Low-Chlorophyll (HNLC) ocean areas (e.g. Martin and Fitzwater, 1988). Kumar (1995) argued that iron was supplied in glacial periods by wind-blown dust, resulting in an increase in ocean productivity, which could have contributed to the lower concentrations of CO_2 in the glacial atmosphere. However, the flux and distribution of dust deposition even to the modern surface ocean remains poorly quantified. Direct measurements of dust deposition provided by measurement at dust collection sites are restricted to a few island or coastal locations (Duce and Tindale, 1991; Prospero, 1996; Ginoux et al., 2001). Current dust models (e.g. Mahowald et al., 2006) provide a wider coverage of dust deposition, but still need to be tested with more observations. Ship-board measurement of atmospheric dust loading provide some such observational constraints, but are discrete observations for the day of collection rather than a longer-term average, and are limited by assumptions about the settling rate of particles from the atmosphere and knowledge of the wet-to-dry deposition ratio (Baker et al., 2013). Chemical tracers of dust deposition in seawater have been proposed as a potential approach to provide better constraint on dust deposition. Dissolved Al in surface water has been used as such a tracer (e.g. Measures and Brown, 1996; Measured and Vink, 2000). More recent studies proposed the use of long-lived ^{232}Th (half-life 1.40×10^{10} yr; Holden, 1990) to estimate dust deposition, and suggested the advantages of this approach over Al (e.g. Hayes et al., 2013a; Hsieh et al., 2011).

The principals underlying use of ^{232}Th as a dust tracer is that dissolution of ^{232}Th from wind-blow dust is the dominant supply of ^{232}Th to the open ocean, and that the rate of its subsequent removal from seawater by adsorption onto sinking particles can be constrained by measurement of another Th isotope; ^{230}Th (half-life 75.58 kyr; Cheng et al., 2013). Hsieh et al. (2011) demonstrated that high ^{232}Th concentrations observed in the surface water of the Atlantic Ocean reflected the influence of Saharan dust plume. By using ^{230}Th-derived residence time, these authors gave an estimate of dust flux based on ^{232}Th concentrations in the surface water (~25 m). Hayes et al. (2013a) adopted a similar method to estimate dust flux in the Pacific Ocean, but suggested the integration of Th isotopes in the upper 500 m of the water column for the estimation of dust flux. Deng et al. (2014) also considered the use of Th isotopes to assess dust fluxes in a meridional transect of the western South Atlantic (Chapter 3). All three studies yielded dust fluxes comparable to a frequently used dust model (Mahowald et al., 2006) with an assumed fractional solubility of Th in dust. This assumed Th solubility however remains a major uncertainty for the use of ^{232}Th to quantify dust deposition.

This study assesses the use of Th isotopes to quantify dust deposition to the ocean with new data collected along a subtropical-tropical Atlantic transect. This transect covers an area under the influence of the Saharan dust plume; one of the most important sources of terrestrial elements to the ocean due to the huge production of dust from the Sahara Desert (e.g. Schutz, 1980; Marticorena and Bergametti, 1996). The investigated area contains a strong gradient in dust supply and is ideal for assessment of the overall validity of the ^{232}Th approach to quantify dust deposition to the remote ocean. For the first time, this study also directly combines measurements of water column ^{232}Th and ^{230}Th, with measurements of Th content and solubility of dust collected on

atmospheric filters during the same cruise. This enables a more complete characterisation of the use of this potential dust proxy than has previously been possible.

5.2 Sampling strategies and settings

Samples were collected from the Tropical-Subtropical Atlantic during UK-GEOTRACES cruise GA06 (D361) (Figure 5.1a). This cruise sailed from Tenerife, Canary Islands, Spain (7th February, 2011) back to Tenerife (19th March 2011) aboard the *RRS Discovery*. The study region is in the east of the North Atlantic subtropical gyre, and contains a number of well-marked water masses. The subtropical salinity maximum water forms the boundary of the North Atlantic Central Water (NACW) at a water depth of ~ 200-500 m. Below this layer is the northward-flowing Antarctic Intermediate Water (AAIW) at ~500-1200 m, characterized by high concentrations of nutrients. Below this, most of the water column is occupied by North Atlantic Deep Water (NADW), which extends to the seafloor north of the equator, and to a water depth of ~3500 m south of the equator. This water mass is characterized by high oxygen contents and increasing silicate concentrations. In the bottom water south of the equator a nutrient-rich water mass is observed, Antarctic Bottom Water (AABW), which flows northward beneath the NADW at ~ 4000 m.

Dust input to the investigated area estimated by model study (Mahowald et al., 2006) is shown in Figure 5.1b. Examples of 4-day air mass back trajectories encountered during the cruise are shown in Figure 5.2. In the tropical North Atlantic, aerosol samples were characterized by surface-level air mass arrivals from the north-east and upper level (> 500m) trajectory arrivals from West Africa (air mass type: Sahara). North of the Equator in the eastern South Atlantic, air

mass arrivals were predominantly southeasterly in origin, and were shielded from desert dust by the InterTropical Convergence Zone (ITCZ), which had its core at ~1°N during the cruise period (Scholsser et al., 2014).

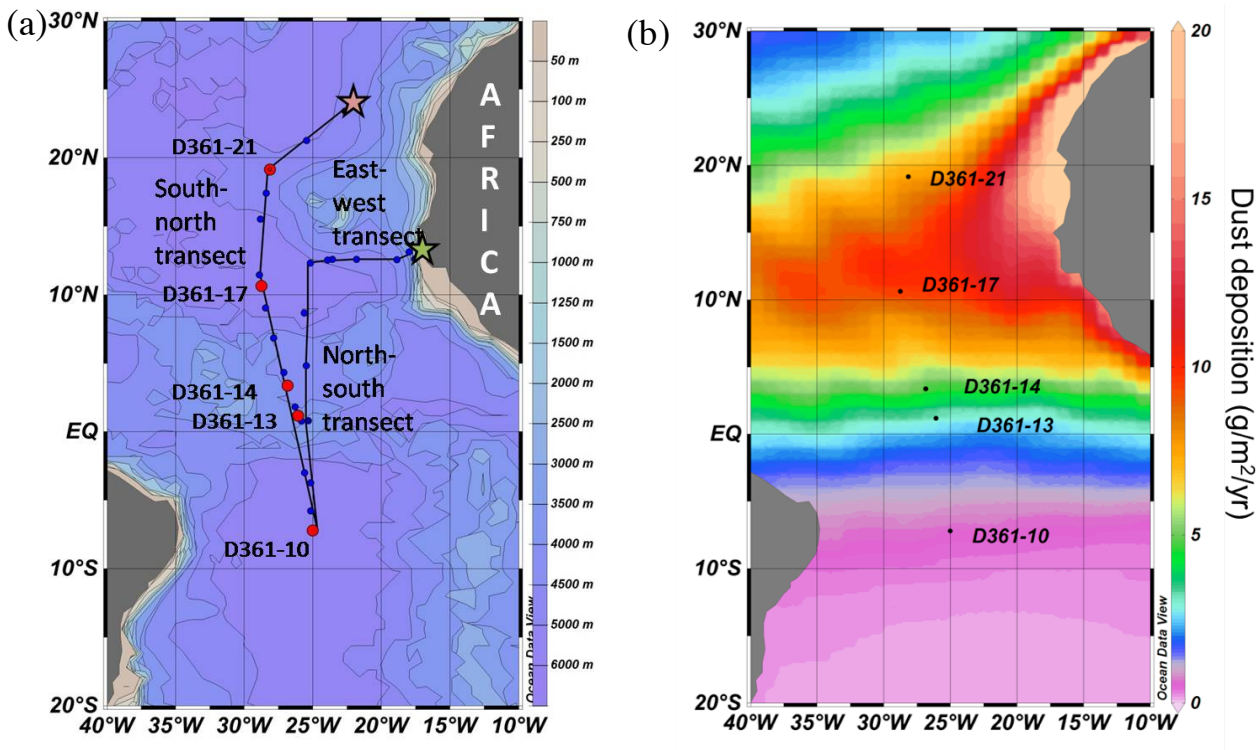


Figure 5.1: Sampling settings of GEOTRACES cruise GA06 (D361). (a) Cruise track and sampling locations of GEOTRACES cruise GA06 (D361). Red dots indicate locations for seawater sampling for this study. Blue dots indicate points at which aerosol filters were changed. Green and pink stars indicate the start and finish of the cruise, respectively. (b) dust deposition to the surface water of the investigated area modeled by Mahowald et al. (2006).

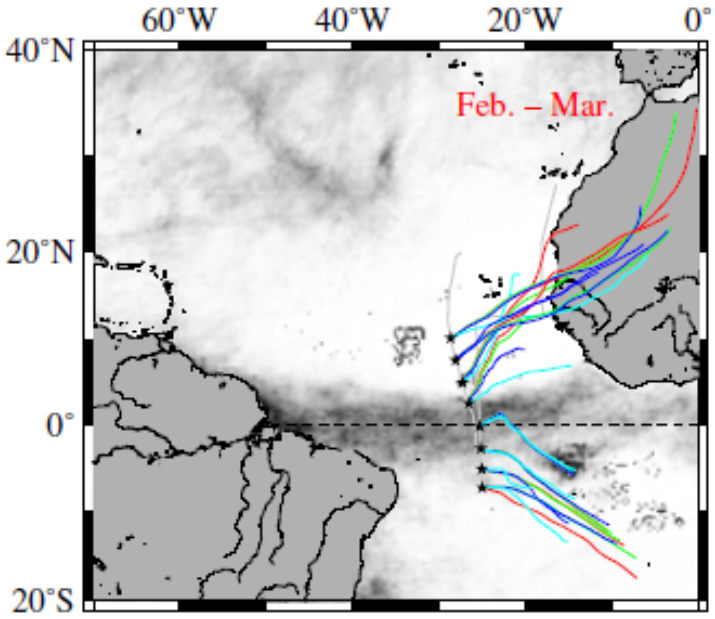


Figure 5.2: Airmass trajectories, over the 4 d before occupation, at certain points in the tropical Atlantic Ocean along the cruise track of D361, using the Hybrid Single-Particle Lagrangian Integrated Trajectory (HySPLIT) algorithm, at 100 m (red), 300 m (green), 500 m (dark blue), and 1, 000 m (sky blue). (Scholsser et al., 2014)

Seawater sampling protocols followed those described in GEOTRACES inter-calibration work (Anderson et al., 2012). Five litres of seawater were sub-sampled directly from Niskin bottles, mounted on a stainless steel CTD rosette, with online filtration through a 0.45µm AcroPak Supor® filter, and collected into acid-cleaned polyethylene sample bottles. A total of 46 samples were collected in this way from five stations (Figure 5.1a). Filtered seawater samples were stored until arrival in the home laboratory at the University of Oxford.

Sample ID	Start position Latitude (^{o}N)	Start position Longitude (^{o}E)	End position Latitude (^{o}N)	End position Longitude (^{o}E)
TM05.all	13.13	-17.97	12.60	-17.57
TM06.all	12.61	-17.57	12.54	-18.84
TM07.all	12.55	-18.87	12.57	-21.81
TM08.all	12.57	-21.82	12.58	-23.56
TM09.all	12.59	-23.56	12.57	-23.76
TM10.all	12.54	-23.92	12.30	-25.15
TM11.all	12.30	-25.17	9.46	-25.66
TM12.all	8.67	-25.62	5.02	-25.48
TM13.all	4.81	-25.48	1.02	-25.33
TM14.all	0.80	-25.31	-3.56	-25.15
TM15.all	-3.74	-25.14	-7.00	-25.00
TM16.all	-7.15	-25.00	-5.95	-25.12
TM17.all	-5.80	-25.14	-3.25	-25.54
TM19.all	-3.00	-25.60	-0.87	-25.81
TM20.all	0.76	-25.82	1.68	-26.25
TM21.all	1.81	-26.29	4.16	-27.07
TM22.all	4.32	-27.11	6.74	-27.80
TM23.all	6.84	-27.84	8.93	-28.43
TM24.all	9.02	-28.44	11.31	-28.86
TM25.all	11.45	-28.89	15.50	-28.80
TM26.all	15.51	-28.80	17.42	-28.38
TM27.all	17.42	-28.38	19.17	-28.12
TM28.all	19.18	-28.13	21.19	-25.55
TM29.all	21.27	-25.45	23.40	-22.66

Table 5.1: Details of aerosol sample collection on D361 cruise

Aerosol samples were collected on the same cruise by Rosie Chance (Table 5.1), using high-volume aerosol collectors. Power supply to the motors was automatically controlled such that sampling only took place when the relative wind direction was between -80 and 145 degrees relative to the bow of the ship. This avoided sampling being contaminated by air from the ship's funnel or other major sources of ship-board contamination. Bulk aerosol for the analysis of Th was sampled onto Whatman 41 paper filters for between 12 and 36 hours. Exposed filters were transferred to individual zip-lock bags immediately after collection, sealed, and stored frozen at -

20^{o}C until analysis at University of East Anglia. During the cruise, one set of filters was also mounted in the aerosol collectors for 24 h without the collector pump in operation to give an indication of the operational blank associated with the sampling procedure, i.e. filter blanks; cassette blank; exposure blank; and motor blank.

5.3 Analytical techniques

5.3.1 Thorium and protactinium isotopes analysis

Seawater samples were returned to the laboratory in Oxford and weighed in preparation for measurement of Th isotopes. Protactinium-231 was also analysed for completeness, though these data are not the main focus of this study. To desorb Pa and Th from the walls of the sample bottle, each sample was acidified with distilled HCl to pH <1.7, shaken and left for at least 48 hours. A mixed ^{229}Th-^{236}U spike and a ^{233}Pa spike were added to each sample. Pre-concentration of Th, Pa and U in samples by co-precipitation with Fe-oxyhydroxides and their chemical separation by anion exchange chromatography followed the procedures previously described in Chapter 2. Determination of Th and Pa was conducted on a Nu instruments MC-ICP-MS (Multi Collector Inductively Coupled Plasma Mass Spectrometry) (see Chapter 2).

Chemistry blanks for dissolved ^{230}Th, ^{232}Th and ^{231}Pa are 0.5 ± 1.3 fg, 29.8 ± 14.0 pg, 0.8 ± 0.9 fg, respectively (2 s.d., n = 4). Blank contributions account for 1-4%, 3-26% and 5-56% of the

dissolved ^{230}Th, ^{232}Th and ^{231}Pa, respectively (with the higher values for ^{230}Th and ^{231}Pa being for surface samples due to their low concentrations).

All uncertainties are 2 standard errors (2se) and include the contribution from sample weighing, spike calibration, impurities in the spikes, blank corrections, and mass spectrometric measurement. Average total uncertainties for ^{230}Th, ^{232}Th and ^{231}Pa are ±0.08 dpm/1000 l, ±0.001 dpm/1000 l, and ±0.02 dpm/1000 l, respectively.

5.3.2 Aerosol Th and Fe solubilities

Aerosol samples collected for analysis of metals were processed at the University of East Anglia by Rosie Chance, using techniques described by Baker et al. (2006). Soluble fractions of both Th and Fe were extracted from the aerosol filter using an ammonium acetate leach at pH ~4.7 for 1-2 h. The pH was chosen as a mimic for release of trace metals from aerosol in rainwater. Baker et al. (2006) suggested that the lower than seawater pH would be expected to enhance trace metal solubility relative to seawater conditions. With the internal consistency of the data considered, this leaching method, however, still reflects the relative changes in the inherent differences that are most probably reflected in the 'true' solubility of aerosol trace metal in seawater. Total fraction was determined adopting a strong acid digestion procedure with HNO_3 and HF to destroy organic matter (including the cellulose filter) and the aluminosilicate matrix of the mineral component of the aerosol. Analysis for soluble fractions was by quadrupole inductively-coupled-plasma mass spectrometry (ICP-MS) for Th and inductively-coupled-plasma optical emission spectroscopy (ICP-OES) for Fe. Total fraction was determined by instrumental neutron activation analysis

(INAA) of all size fractions for each sample combined. Procedural blanks were determined in every batch of analyses by carrying out identical extraction procedures in sample vessels that did not contain aerosol samples. These procedural blanks have been subtracted from the results for each batch. Aerosol collection operational blanks were assessed by analyzing filters that had been treated as samples. Concentrations in extracts were converted into atmospheric concentrations by calculating the total quantity of analyte on each filter, after appropriate (procedural and operational) blank correction, and dividing by the known volume of air filtered for each sample. Uncertainties quoted for atmospheric concentrations have been calculated from standard deviations of replicate analyses and propagated for each stage of data analysis by standard error propagation methods. The percentage solubility of the metal was calculated as:

$$\text{Solubility (\%)} = C_{sol} / C_{total} \times 100 \qquad (5.1)$$

where C_{sol} and C_{total} are the soluble and total atmospheric concentrations of the metal.

5.4 Results

5.4.1 Water-column ^{230}Th, ^{232}Th and ^{231}Pa

Measured ^{230}Th and ^{231}Pa concentrations were corrected for, 1) ingrowth from radioactive parents in seawater since the time of collection, and 2) detrital, U-supported ^{230}Th and ^{231}Pa concentrations

(see details in Chapter 3). Measured and corrected activities of ^{230}Th, ^{232}Th and ^{231}Pa are reported in dpm/1000 l with 2 standard errors (2se), and presented in Appendix Table 5.1.

Th-230 concentrations range from 0.05 to 0.87 dpm/1000 l throughout the water column (Figure 5.3a). Vertical profiles of ^{230}Th exhibit nearly linear increases with water depth from the surface to ~1500 m, which is consistent with ^{230}Th profiles observed in other ocean basins (e.g. Bacon and Anderson, 1982; Nozaki et al., 1981; Deng et al., 2014; Moran et al., 2001; Okubo et al., 2012; Thomas et al., 2006). Below 1500 m, ^{230}Th profiles deviate from the linear relationship with depth, increasing less rapidly with water depth. A decrease in ^{230}Th concentrations towards the bottom was observed at 11^{o}N (D361-17). Horizontally, surface-water ^{230}Th concentrations increase northward from south of the equator to higher latitudes in the North Atlantic. Low ^{230}Th observed in the equatorial area is likely due to an enhanced scavenging of ^{230}Th by higher concentrations of biogenic particles in the equatorial upwelling system. A northward increase of ^{230}Th was also observed in deep and bottom water.

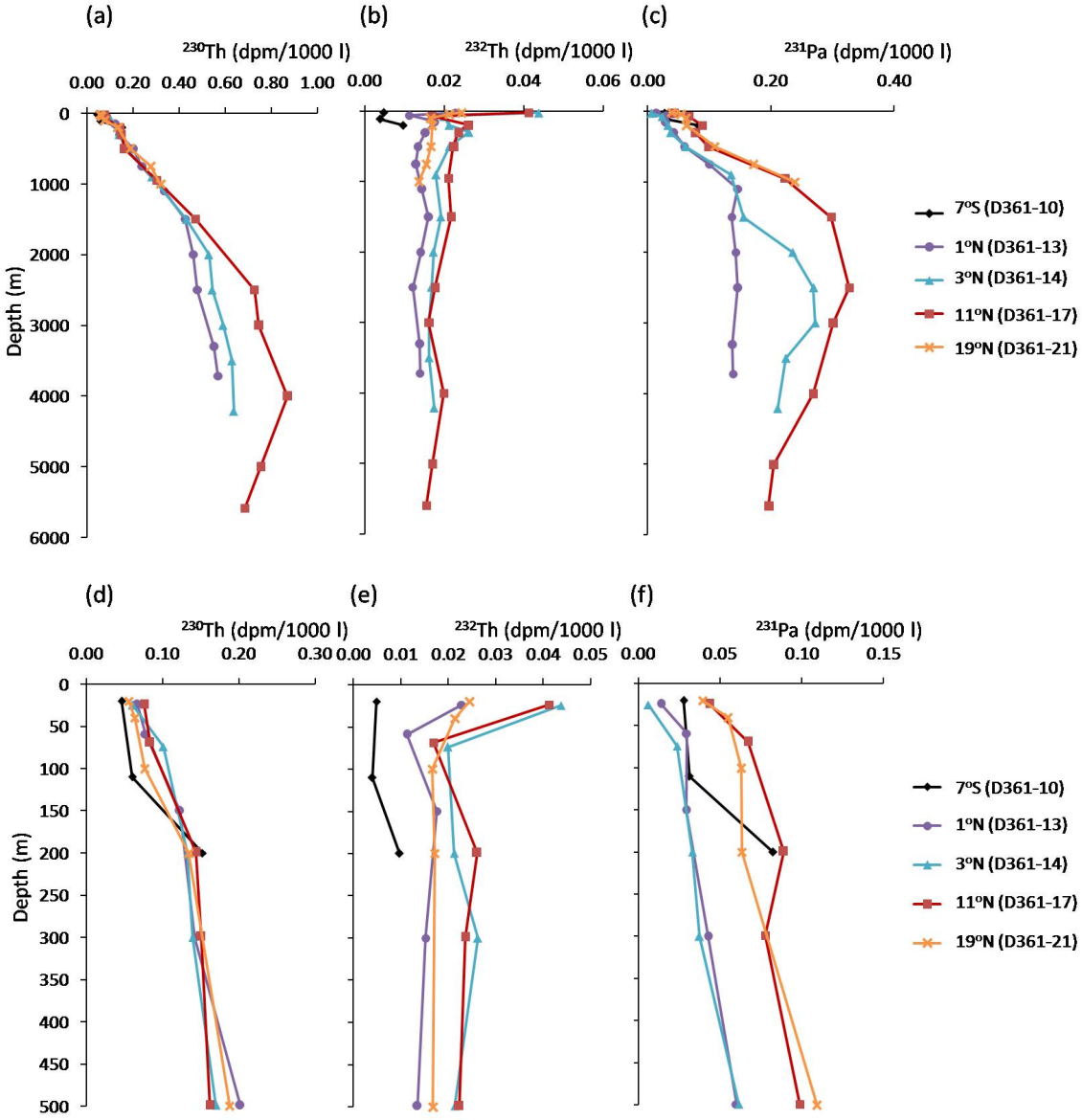


Figure 5.3: Vertical profiles of full-depth water-column (a) ^{230}Th, (b) ^{232}Th, and (c) ^{231}Pa; and shallow-depth (upper 500 m) water-column (d) ^{230}Th, (e) ^{232}Th, and (f) ^{231}Pa. Uncertainties (2 standard error) for ^{230}Th, ^{232}Th and ^{231}Pa are, ±0.08 dpm/1000 l, and ±0.001 dpm/1000 l, and ±0.02 dpm/1000 l, respectively.

Th-232 concentrations range from 0.004 to 0.044 dpm/1000 l throughout the water column (Figure 5.3b). ^{232}Th maxima were observed in the surface water (~25 m) for all stations except the most southern station at 7°S (D361-10), and the values vary greatly from one station to another (Figure 5.2e). The highest ^{232}Th concentrations, observed between 3°N (D361-14) and

11^{o}N (D361-17) are about a factor of two higher than those at 1^{o}N (D361-13) and 19^{o}N (D361-21), suggesting a source of high ^{232}Th concentrations supplied to the surface water in this region. Below 25 m, ^{232}Th concentrations exhibit less variability between sites with a convergence of ^{232}Th concentration at depth towards a uniform value of ~ 0.02 dpm/ 1000 l.

Pa-231 concentrations range from 0.01 to 0.33 dpm/1000 l (Figure 5.3c) throughout the water column. Pa-231 concentrations increase from low values in surface water to a maximum at ~1200 m. Below this depth, ^{231}Pa concentrations stay relatively constant followed by decreasing concentrations towards the bottom, suggesting a role for lateral advection in controlling the ^{231}Pa concentration of deep water masses. Horizontally, ^{231}Pa concentrations increase northward, as is observed for ^{230}Th. Dissolved ^{231}Pa/^{230}Th ratios range from 0.10 to 0.87, all exceeding the production ratio of ^{231}Pa and ^{230}Th in the water column (0.093) (Figure 5.4). In the upper water-column (~ 2000 m), ^{231}Pa/^{230}Th ratios exhibit greater variation than at depth, and are characterized by relatively higher values. In the surface water between 1^{o}N-3^{o}N, ^{231}Pa/^{230}Th ratios are significantly lower than at other stations, indicating an enhanced scavenging of ^{231}Pa and ^{230}Th with a preference for ^{231}Pa in this area. At depth, ^{231}Pa/^{230}Th ratios generally stay relatively constant or decrease towards the seafloor.

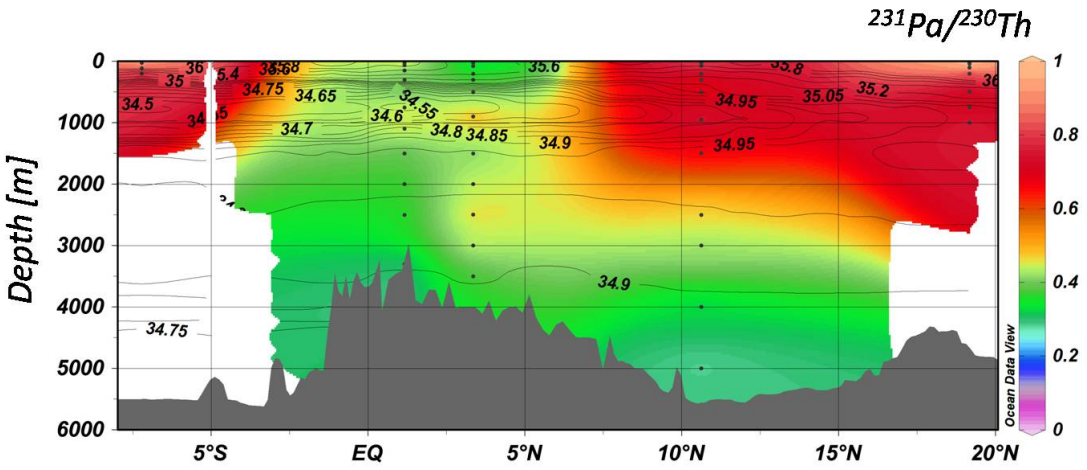


Figure 5.4: Distribution of water-column ^{231}Pa/^{230}Th ratios along the transect in the tropical Atlantic Ocean. Salinity contours give an indication of the water masses in this area.

5.4.2 Aerosol Th and Fe solubilities

Aerosol solubility values of Th and Fe were derived from total and soluble concentrations of Th and Fe measured in aerosol samples and presented in Appendix Table 5.2. Excluding values that are under detection limit, available data indicate Th and Fe solubilites of dust ranging from 5.4-11.0%, and 0.4-1.4%, respectively. Relative standard deviations associated with the measurement are 20% for Th, and 10% for Fe. Slightly higher Th and Fe solubilities are found in areas more remote from the continental dust source. For these Saharan samples, Th solubility exhibits an inverse function to its total loading, increasing from 5.4 to 11.0% as the total Th decreases from 6.9 to 0.6 pmol/m^3 (Figure 5.5). The same relationship is also found for Fe in this study, and has been previously observed and discussed elsewhere (e.g. Baker et al., 2006). This inverse relationship potentially smooths out the strong gradients in atmospheric iron supply to the ocean by delivering less soluble Fe to areas close to the dust sources (e.g. Baker and Jickells, 2006).

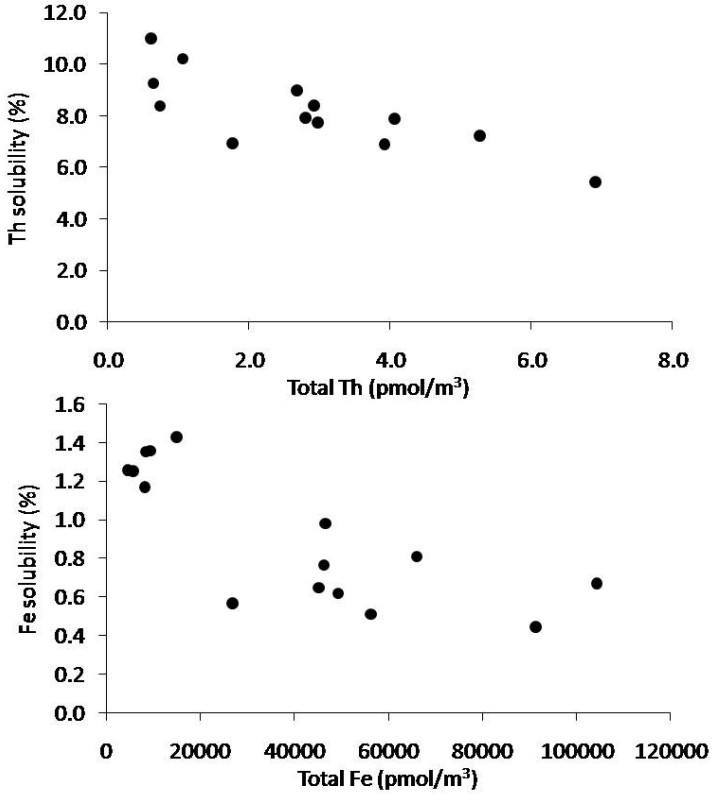


Figure 5.5: Relationship between Th and Fe solubilities (%) and their respective total concentrations in aerosol samples.

5.5 Discussion

5.5.1 Th residence times and optimal depth of integration for dust flux assessment

Th-230 is constantly produced in the ocean through the α-decay of uniformly distributed ^{234}U, and is removed from seawater by adsorption onto sinking particles with subsequent burial in the

sediment. Its removal from seawater is depicted by the reversible scavenging model which allows an exchange between the dissolved and particulate phases of ^{230}Th, and therefore predicts a linear increase of ^{230}Th concentrations with water depth (e.g. Bacon and Anderson, 1982). Th-232 has similar chemical behavior to that of ^{230}Th. Its removal from seawater is expected to also be by reversible scavenging and the removal rate to be the same as that of ^{230}Th. However, unlike ^{230}Th, ^{232}Th is mainly supplied by dust dissolution after its deposition in the surface water. Assuming that there are no other sources of ^{232}Th, that dust flux remains constant, and in the absence of lateral advection, dissolved ^{232}Th is expected to be constant with depth in the water-column, dependent only on the dust flux to the surface water. Based on these conceptual models, the downward ^{232}Th flux can be estimated by combining ^{232}Th concentrations with residence times derived from ^{230}Th concentrations. Following Hayes et al. (2013a), assuming steady-state, ^{230}Th residence time and ^{232}Th flux are given by:

$$\tau_{^{230}\mathrm{Th}} = \frac{\int_0^z {}^{230}\mathrm{Th}\,dz}{\int_0^z {}^{234}\mathrm{U} \times \lambda_{^{230}\mathrm{Th}}\,dz} \qquad (5.2)$$

$$\mathrm{F}_{^{232}\mathrm{Th}} = \frac{\int_0^z {}^{232}\mathrm{Th}\,dz}{\tau_{^{230}\mathrm{Th}}} \qquad (5.3)$$

where $\tau_{^{230}\mathrm{Th}}$ is the residence time of ^{230}Th with respect to removal, yr; ^{230}Th is the dissolved ^{230}Th activity, dpm/1000 l; ^{234}U is the dissolved ^{234}U activity, 2900 dpm/1000 l; $\lambda_{^{230}\mathrm{Th}}$ is the decay constant of ^{230}Th, yr^{-1}; z is the water depth, m; $\mathrm{F}_{^{232}\mathrm{Th}}$ is the flux of ^{232}Th, ug/m^2/yr; ^{232}Th is the dissolved ^{232}Th activity, dpm/1000 l.

To obtain a ^{232}Th flux that reflects its source, dust input to the surface ocean, an integration depth must be selected. Hsieh et al. (2011) adopted a constant mixed layer depth of 25 m, whereas Hayes et al. (2013a) chose 500 m taking into account the rapid Th cycling in the upper water column suggested by ^{232}Th profiles. More recently, Deng et al. (2014) integrated through the upper 250 m of water column. Considering the disagreement of the integration depth among these authors, a reasonable integration depth needs to be determined before calculation of dust inputs in this study. Th-230 residence time and ^{232}Th flux were therefore calculated with integration from the surface to all measured water depths, and shown in Figure 5.6.

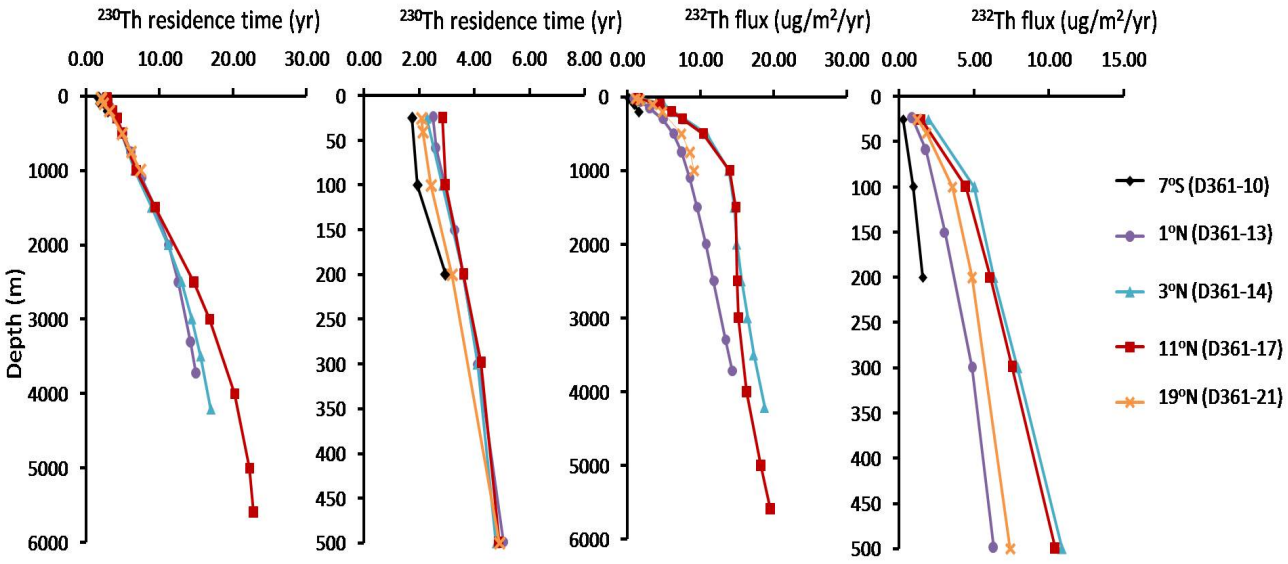


Figure 5.6: Full-depth and shallow-depth (upper 500 m) ^{230}Th residence time and ^{232}Th flux calculated from water-column ^{230}Th and ^{232}Th concentrations integrated at all water depths.

Th-230 residence times exhibit an increase with water depth, ranging between 1.25 and 22.59 years. Such an increase is expected given the increasing thickness of ocean layer considered with depth, which requires more time for Th to be removed downward from that layer. Th-232

fluxes calculated using these ^{230}Th-derived residence times (equations (5.2) and (5.3)) vary from 0.29 to 19.55 μg/m^2/yr, increasing rapidly from low values in surface waters to ~500 m, with relatively constant values at depth. This increase of ^{232}Th flux with depth does not agree with our conceptual models in which a constant ^{232}Th flux is predicted throughout the water column. It is very unlikely that this observation can be explained by a steady decrease in dust supply at the surface over the last two decades, as would be suggested if dust settles in a conservative 1D manner through the water column. A similar increase in apparent ^{232}Th flux with depth was previously observed by Hayes et al. (2013a) in the Pacific Ocean. That study argued that this feature might be caused by the difference in dissolved speciation of ^{230}Th and ^{232}Th, with ^{230}Th being more soluble and ^{232}Th more colloidal. The conversion of colloidal ^{232}Th into dissolved ^{232}Th adds a fraction of dissolved ^{232}Th to the dissolve phase at depth, and is unaccounted for by the removal of ^{230}Th. This would lead to an underestimation of ^{232}Th residence time. Hayes et al. (2013a) adopted ^{232}Th fluxes integrated to a water depth of 500 m as representative of the dust flux to the ocean, but there is a lack of evidence to support this particular depth, which makes the use of a 500 m integration depth somewhat questionable.

In this study, I suggest that the use of ^{230}Th residence time as an estimate of ^{232}Th residence time is not always appropriate and that this is the cause of the apparent increase in ^{232}Th flux with depth. One of the principals underlying the use of ^{232}Th to estimate dust flux is that ^{232}Th and ^{230}Th are both removed from seawater through reversible scavenging by downward settling of particles. Under steady state conditions the mean residence times of total ^{230}Th and ^{232}Th with respect to removal from a water layer of interest are given by,

$$\tau_{^{230}\mathrm{Th}} = \frac{[^{230}\mathrm{Th}]_{\mathrm{diss}} \times z}{[F_{^{230}\mathrm{Th}}]_{\mathrm{in}}} = \frac{[^{230}\mathrm{Th}]_{\mathrm{diss}} \times z}{[F_{^{230}\mathrm{Th}}]_{\mathrm{out}}} \quad (5.4)$$

$$\tau_{^{232}\mathrm{Th}} = \frac{[^{232}\mathrm{Th}]_{\mathrm{diss}} \times z}{[F_{^{232}\mathrm{Th}}]_{\mathrm{in}}} = \frac{[^{232}\mathrm{Th}]_{\mathrm{diss}} \times z}{[F_{^{232}\mathrm{Th}}]_{\mathrm{out}}} \quad (5.5)$$

where $[^{230}\mathrm{Th}]_{\mathrm{diss}}$ and $[^{232}\mathrm{Th}]_{\mathrm{diss}}$ are the dissolved ^{230}Th and ^{232}Th activities averaged within a water layer of interest; z is the depth of the water layer; $[F_{^{230}\mathrm{Th}}]_{\mathrm{in}}$ and $[F_{^{232}\mathrm{Th}}]_{\mathrm{in}}$ are the fluxes of ^{230}Th and ^{232}Th into this water layer; $[F_{^{230}\mathrm{Th}}]_{\mathrm{out}}$ and $[F_{^{232}\mathrm{Th}}]_{\mathrm{out}}$ are the fluxes of ^{230}Th and ^{232}Th out of this water layer.

Since fluxes of ^{230}Th and ^{232}Th out of the water layer are in effect activities of particulate ^{230}Th and ^{232}Th scavenged from the water column at the bottom of the water layer, the ratio of residence times of ^{230}Th and ^{232}Th is,

$$\frac{\tau_{^{230}\mathrm{Th}}}{\tau_{^{232}\mathrm{Th}}} = \frac{([^{230}\mathrm{Th}]_{\mathrm{diss}} / [^{232}\mathrm{Th}]_{\mathrm{diss}})_{\mathrm{mean}}}{([F_{^{230}\mathrm{Th}}]_{\mathrm{out}} / [F_{^{232}\mathrm{Th}}]_{\mathrm{out}})_{\mathrm{bottom}}} = \frac{([^{230}\mathrm{Th}]_{\mathrm{diss}} / [^{232}\mathrm{Th}]_{\mathrm{diss}})_{\mathrm{mean}}}{([^{230}\mathrm{Th}]_{\mathrm{part}} / [^{232}\mathrm{Th}]_{\mathrm{part}})_{\mathrm{bottom}}} \quad (5.6)$$

where $[^{230}\mathrm{Th}]_{\mathrm{part}}$ and $[^{232}\mathrm{Th}]_{\mathrm{part}}$ are activities of particulate ^{230}Th and ^{232}Th scavenged from the water column; subscripts ‘mean’ and ‘bottom’ denote the mean activity ratio averaged within the water layer and the activity ratio at the bottom of the water layer, respectively.

Further assuming a pseudo-equilibrium between dissolved and particulate phases gives:

$$([^{230}\mathrm{Th}]_{\mathrm{part}}/[^{232}\mathrm{Th}]_{\mathrm{part}})_{\mathrm{bottom}} = ([^{230}\mathrm{Th}]_{\mathrm{diss}}/[^{232}\mathrm{Th}]_{\mathrm{diss}})_{\mathrm{bottom}} \quad (5.7)$$

If the water layer of interest is the mixed layer, where everything is well mixed so that ^{230}Th and ^{232}Th are homogeneously distributed, the mean activity ratio of dissolved ^{230}Th and ^{232}Th equals to the activity ratio of dissolved ^{230}Th and ^{232}Th at the bottom of the mixed layer,

$$([^{230}\mathrm{Th}]_{\mathrm{diss}}/[^{232}\mathrm{Th}]_{\mathrm{diss}})_{\mathrm{mean}} = ([^{230}\mathrm{Th}]_{\mathrm{diss}}/[^{232}\mathrm{Th}]_{\mathrm{diss}})_{\mathrm{bottom}} \qquad (5.8)$$

The ratio of residence times of ^{230}Th and ^{232}Th is therefore,

$$\frac{\tau_{^{230}\mathrm{Th}}}{\tau_{^{232}\mathrm{Th}}} = \frac{([^{230}\mathrm{Th}]_{\mathrm{diss}}/[^{232}\mathrm{Th}]_{\mathrm{diss}})_{\mathrm{mean}}}{([^{230}\mathrm{Th}]_{\mathrm{part}}/[^{232}\mathrm{Th}]_{\mathrm{part}})_{\mathrm{bottom}}} = \frac{([^{230}\mathrm{Th}]_{\mathrm{diss}}/[^{232}\mathrm{Th}]_{\mathrm{diss}})_{\mathrm{mean}}}{([^{230}\mathrm{Th}]_{\mathrm{diss}}/[^{232}\mathrm{Th}]_{\mathrm{diss}})_{\mathrm{bottom}}} = \frac{([^{230}\mathrm{Th}]_{\mathrm{diss}}/[^{232}\mathrm{Th}]_{\mathrm{diss}})_{\mathrm{bottom}}}{([^{230}\mathrm{Th}]_{\mathrm{diss}}/[^{232}\mathrm{Th}]_{\mathrm{diss}})_{\mathrm{bottom}}} = 1 \qquad (5.9)$$

That is, within the mixed layer, ^{230}Th residence time equals to ^{232}Th residence time. Out of the mixed layer, however, ^{230}Th and ^{232}Th are not homogeneously distributed, as can be observed from their water-column profiles (Figure 5.3(a) and (b)). Using ^{230}Th residence time as ^{232}Th residence time to calculate ^{232}Th flux therefore leads to the deviation of ^{232}Th profile from the constant flux profile as is predicted by conceptual models. The relationship between residence times of ^{230}Th and ^{232}Th out of the mixed layer needs to be formulated to facilitate the use of ^{230}Th residence time to estimate ^{232}Th flux. In the further discussion, I use the ^{230}Th residence time as equivalent of ^{232}Th residence time to estimate ^{232}Th flux within the mixed layer, and consider this flux to be representative of the dust flux to the surface ocean.

Instead of a constant mixed layer depth assumed by Hsieh et al. (2011), this study obtained mixed-layer depth from *in-situ* CTD measurements at one-meter resolution during the cruise. Following Kara et al. (2000), mixed-layer depth was determined adopting the definition of mixed-layer depth as the depth at which potential temperature has decreased by ΔT, equal to 0.2 ^{o}C, from the surface value. Th-230 residence time and ^{232}Th-flux are then calculated with the integration of

^{230}Th and ^{232}Th concentrations averaged within the mixed layer to the mixed-layer depth following equations (5.2) and (5.3). Results are presented in Table 5.2. Mixed-layer depths in the investigated area are everywhere deeper than 25 m assumed by Hsieh et al. (2011), ranging from 40 to 124 m. Adopting individual mixed-layer depths, the calculation yields ^{232}Th flux that varies from 0.67 to 4.33 μg/m^2/yr. Th-232 flux shows a northward increasing trend from 7^{o}S (D361-10) to 19^{o}N (D361-21). This pattern well reflects higher ^{232}Th concentrations within the mixed layer observed at northerly latitudes.

Station number	Mixed layer depth (m)	^{230}Th residence time (yr)	^{232}Th flux (μg/m^2/yr)
D361-10	59	1.75	0.67
D361-13	46	2.50	1.72
D361-14	40	2.28	3.13
D361-17	53	2.85	3.17
D361-21	124	2.44	4.33

Table 5.2: Th-230 residence time and ^{232}Th flux within the mixed layer

5.5.2 Assessing Th solubility and ^{232}Th-derived dust flux

Like other elements that are supplied to the ocean through the partial dissolution of dust, the solubility of dust ^{232}Th in seawater is critical to the conversion of ^{232}Th flux into dust flux. Hsieh et al. (2011) suggested a range of 1-16% for ^{232}Th dust solubility by comparing calculated ^{232}Th flux with modelled dust deposition by Mahowald et al. (2006). That study showed that a good agreement between ^{232}Th-derived dust flux and dust model could be achieved using Th solubility of 1-5% for areas of high dust input and 5-10% for areas of low dust input. Hayes et al. (2013a) adopted a solubility of 20±5% obtained by comparing the eolian-^{232}Th sediment fluxes with the

500-m dissolved ^{232}Th fluxes. In this study, measurement of Th in both soluble and total fractions of aerosol samples collected on the same cruise provide a direct measurement of Th solubility and allow a more robust assessment of dust flux.

Based on the aerosol Th measurement, Th solubility varies from places of low dust loading to places of high dust loading. Individual Th solubility, instead of a mean value, is therefore adopted to estimate dust flux. For the most southern and northern stations, Th solubility data are not available, and a constant value of (9.7±0.3) %, averaged along the south-north transect of the investigated area (discounting Th solubility under detection limit), is adopted.

Assuming a Th concentration of 13 ppm in lithogenic material (Hsieh et al., 2011), dust flux can be estimated from ^{232}Th flux by:

$$F_{dust} = \frac{F_{^{232}Th}}{S_{Th} \times 13\ ppm} \quad (5.10)$$

where F_{dust} is the flux of dust, g/m^2/yr; S_{Th} is the fractional solubility of Th in dust, %.

Calculated dust fluxes, F_{dust}, are listed in Table 5.3. Dust fluxes range between 0.53 and 3.43 g/m^2/yr, increasing northward from low latitude in South Atlantic to high latitude in North Atlantic. High dust fluxes are observed north of 3^{o}N, with a mean value of 2.81 g/m^2/yr, up to three times higher than the mean value in lower latitude area. This pattern reflects the influence of high dust input between 3-19^{o}N, from deserts on the African continent.

Station number	Latitude (^{o}N)	^{232}Th-derived dust flux in this study (g/m^2/yr)	Modelled dust flux (g/m^2/yr)
D361-10	-7.22	0.53 (0.49)	0.43
D361-13	1.16	1.32	2.10
D361-14	3.35	2.59	4.34
D361-17	10.62	2.71	8.26
D361-21	19.15	3.43 (4.04)	10.70

Table 5.3: Th-232-derived dust flux in this study and modelled dust flux by Mahowald et al. (2005). Bracketed ^{232}Th-derived dust fluxes are estimates with Th solubilites estimated from Th solubility-dust flux relationship, and are used in further discussion.

Using these calculated dust fluxes and the measured Th solubilities, I propose an approach to derive dust flux from ^{232}Th with more robust Th solubility in ocean basins where such aerosol Th solubility data are not available. Based on the data available in this study, an inverse relationship is found between ^{232}Th-derived dust flux and Th solubility (Figure 5.7). This relationship has also been observed for aerosol Fe and Al, whose principal source in the surface water of the ocean is also atmospheric dust (e.g. Baker and Jickells, 2006). This relationship generates a function that allows Th solubility to be obtained from ^{232}Th-derived dust flux, which can be initially estimated with an assumed Th solubility. Dust flux can then be recalculated with the Th solubility derived from the function. This iterative process is repeated until a stable dust flux is achieved. I test this approach for the most southern and northern stations in this study, for which aerosol data are not available.

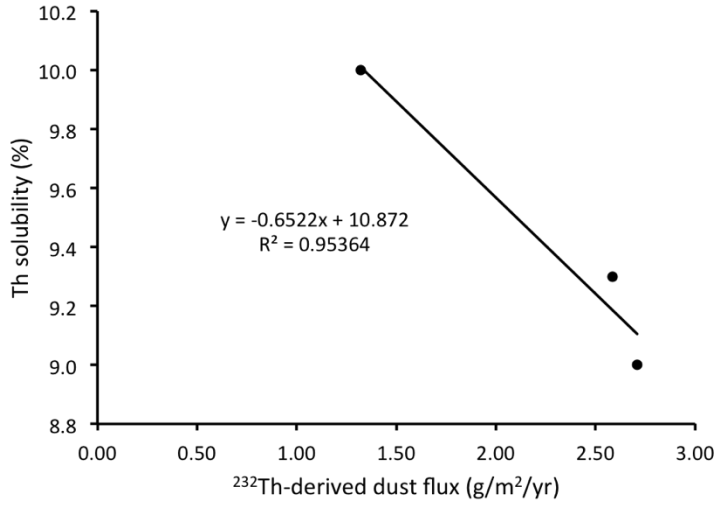


Figure 5.7: Relationship between Th solubility (%) obtained from aerosol analysis and ^{232}Th-derived dust flux (g/m^2/yr). The linear fit (blank line) gives the function from which Th solubility can be derived with a known dust flux.

A linear fit of the available Th solubility and ^{232}Th-derived dust flux data (Figure 5.7) gives a function:

$$\text{Th solubility (\%)} = \text{dust flux (g/m}^2\text{/yr)} \times (-0.65) + 10.87 \qquad (5.11)$$

Using dust fluxes of 0.53 g/m^2/yr and 3.43 g/m^2/yr at 7^{o}S and 19^{o}N, respectively (calculated with an initial assumed Th solubility of 9.7%), function (5.11) gives estimates of Th solubility of 10.5% and 8.6% at 7^{o}S and 19^{o}N, respectively. With these newly-generated Th solubilities, dust fluxes were re-calculated, being 0.49 g/m^2/yr at 7^{o}S, and 3.86 g/m^2/yr at 19^{o}N. This process was repeated until a stable dust flux was achieved. The final dust fluxes obtained are 0.49 g/m^2/yr and 4.04 g/m^2/yr at 7^{o}S and 19^{o}N, respectively. Corresponding Th solubilities are 10.6% and 8.2% at 7^{o}S and 19^{o}N, respectively. These values give better estimates of dust flux at these sites, and are used for further discussion. This iterative approach is suggested for other

ocean settings where associated aerosol measurements of solubility are not available. Further calibration of the technique would be desirable, however, given the sparse data (Figure 5.7) used to pursue the approach in this chapter.

5.5.3 Comparison with dust model

In this study, dust flux is estimated using the ^{232}Th approach first proposed by Hirose and Sugimura (1987), and applied by Hsieh et al. (2011). Compared with Hsieh et al. (2011), adjustment is made in two aspects, 1) more accurately determined the mixed-layer depths for each location; 2) directly measuring Th solubility from aerosol samples on the same cruise. Here I compare results with model-generated dust fluxes by Mahowald et al. (2006). The model is a composite of three published modelling results that match satellite optical depth, *in situ* dust concentrations, and deposition observations (Ginoux et al., 2001; Mahowald and Luo, 2003; Tegen et al., 2004). The composite overcomes the weaknesses of individual models and matches well with the observations available. Shown in Figure 5.8 is a comparison of ^{232}Th-derived dust flux in this study and model-simulated dust flux.

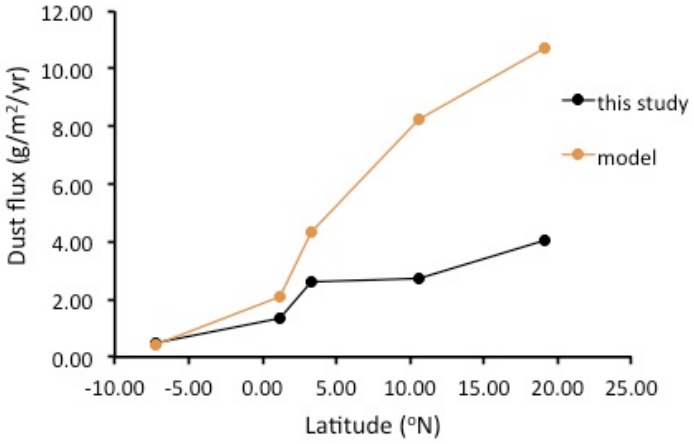


Figure 5.8: Th-232-derived dust flux in this study (black) and modelled dust flux by Mahowald et al. (2005) (yellow).

Both results show a northward increasing trend of dust flux from the South Atlantic to high latitude in the North Atlantic, which reflects the variation of dust input from the African continent to this area. Modelled dust flux is however generally higher than ^{232}Th-derived dust flux, ranging from 0.43 to 10.70 g/m^2/yr. At the two most northern stations (D361-17 and D361-21), the modelled dust flux is about 3 times higher than ^{232}Th-derived dust flux. This disagreement of absolute values between two results indicates either an underestimation of the ^{232}Th-approach or an overestimation of the model. One factor that might cause the underestimation of ^{232}Th-derived dust would be incorrect Th solubility, because estimates of dust flux are rather sensitive to the Th solubility. A decrease of Th solubility from ≈10% to ≈3% would explain the model-data discrepancy, but such an error seems very unlikely here given the direct measurements of Th solubility from collected aerosols. Another factor that might contribute to the underestimate of dust flux is the advection of low Th surface water into the investigated area from higher latitudes, as is suggested by Measures and Vink (2000) for the explanation of low Al concentrations in tropical Atlantic. However, it is less likely that the advection of surface water might be the major

contribution due to the relatively shorter residence time of Th in surface water (~2 yr) than Al (~5 yr) (Measures and Vink, 2000). Taken at face value, and supported by interpretation of surface-water Al data, the Th reconstruction of dust fluxes in this study appears to indicate that the model over-estimates dust fluxes to the surface Atlantic under the dust plume. This has important implications for the supply of elements to the ocean from this source.

5.5.4 Using Th to assess inputs of Fe to seawater

In principal, ^{232}Th fluxes also can be used to estimate Fe flux, supplied by dust, to the surface water. Such estimation is however difficult due to a lack of knowledge of the relative solubility of ^{232}Th and Fe, which controls the total amount of these metals that enters the dissolved phase in the ocean (e.g. Measures and Vink, 1999). With solubilities of Th and Fe obtained from coeval aerosol analysis, we are able to assess the relative solubility of Th and Fe and, therefore Fe flux to seawater.

A correlation is found between Th and Fe solubility ($r^2 = 0.467$) (Figure 5.9). A linear fit of these data gives a relative solubility ratio of Fe to Th of 0.16 (%/%). With this ratio, dissolved Fe flux can be calculated as:

$$\text{Dissolved Fe flux} = (\text{Fe}/^{232}\text{Th})_{\text{litho}} \times (S_{\text{Fe}}/S_{\text{Th}}) \times \text{dissolved } ^{232}\text{Th flux} \qquad (5.12)$$

where $(\text{Fe}/^{232}\text{Th})_{\text{litho}}$ is the average ratio of Fe/Th ratio in upper continental crust, 3262 g/g (Taylor and McLennan, 1985); $S_{\text{Fe}}/S_{\text{Th}}$ is the relative solubility ratio of Fe and Th, 0.16 (%/%).

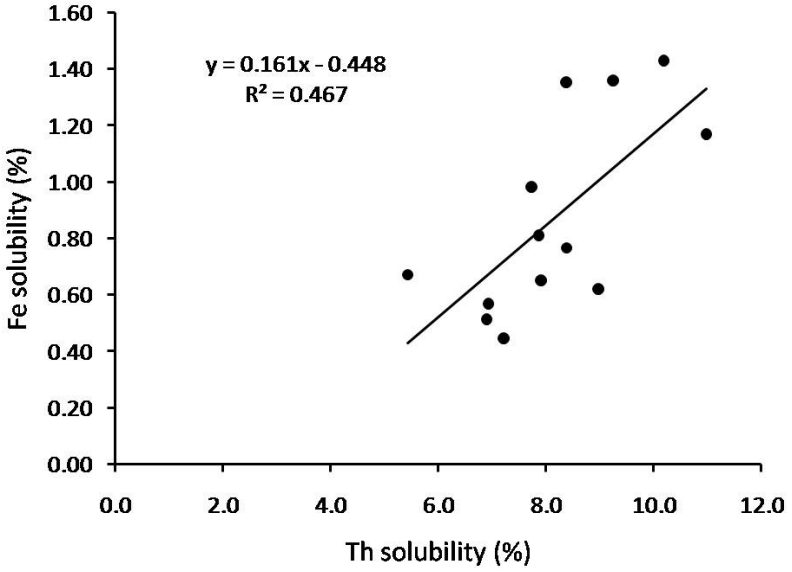


Figure 5.9: Relationship between Fe solubility (%) and Th solubility (%) obtained from aerosol analysis along the transect in the tropical Atlantic (discounting values that are under detection limit).

Estimated Fe fluxes lie in the range between 0.35 and 2.26 mg/m^2/yr, increasing from 7^{o}S to 19^{o}N in the north Atlantic. Using the C:Fe ratio of 94,100 (Fitsimmons et al., 2014), this would be enough Fe to produce productivity ranging between 32.9 and 212.7 g C /m^2/yr. Estimates of primary productivity rate in the investigated area range between 106 and 130 g C /m^2/yr (Longhurst et al., 1995). This suggests that partial dissolution from atmospheric dust is the major source supplying most Fe to the ocean in this region.

5.6 Conclusions

Measurements of ^{230}Th and ^{232}Th were made for five sites in the tropical Atlantic Ocean along a transect under the influence of Saharan dust plume. Surface ^{232}Th concentrations exhibit variability, reflecting its source from dust supply. Paired with ^{230}Th-derived residence times, ^{232}Th

concentrations were used to estimate dust flux to the surface seawater. Differences in expected residence times for ^{230}Th and ^{232}Th in thick layers suggest the use of the mixed layer as the optimal depth for calculation of ^{232}Th fluxes. Fractional solubilities of Th were obtained from aerosol measurements of total and soluble Th fractions on the same cruise. An approach to estimate Th solubility in areas where such data are not available is proposed based on the inverse relationship between Th solubility and dust flux observed in this study. Assessment of dust flux, improved with accurate mixed-layer depths and Th solubilities, were compared with model-generated dust fluxes. Both dust fluxes exhibit an increase of dust flux from 7^{o}S in the South Atlantic to 19^{o}N in the North Atlantic. Absolute values however show disagreement between the two results, with higher dust flux estimated by the model, suggesting that modeled dust fluxes may be too high in this important ocean region. Th-232 flux was also used to calculate Fe flux supplied to the ocean by partial dissolution of atmospheric dust. With a relative fractional solubility of Fe to Th of 0.16, the Fe flux was estimated in a range between 0.35 and 2.26 mg/m^2/yr. This would supply enough Fe to produce productivity ranging between 32.9 and 212.7 g C /m^2/yr, which is in the range of estimates of primary productivity rate in the investigated, indicating that partial dissolution from atmospheric dust is the major source supplying most Fe to the ocean in this region.

.

Chapter 6

Conclusions and outlook

Recent decades have seen an increasing interest in employing ^{230}Th, ^{232}Th and ^{231}Pa in the ocean settings to reconstruct past ocean environment and understand processes in the modern ocean. A better understanding of the behavior and distribution in the ocean is therefore required for robust application of these isotopes in the past and modern ocean. Under the framework of GEOTRACES program, seawater and sediment samples for ^{231}Pa, ^{230}Th, and ^{232}Th were collected and measured in this work. These datasets have expanded the data coverage of these isotopes in the Atlantic Ocean and have provided new information for potential application of these isotopes to study past ocean circulation, dissolution of marine sediment, and modern dust input to the oceans. The main findings of this thesis were summarized in this short chapter, together with some indications of possible areas for further work.

6.1 Water-column ^{230}Th, ^{231}Pa and ^{232}Th in the Southwest Atlantic

Measurements of dissolved ^{230}Th, ^{231}Pa and ^{232}Th were made for twelve full-depth profiles along a Southwest Atlantic section during GEOTRACES cruise GA02S to study the controls of the water-column distribution of these nuclides. This ocean basin has been the focus of down-core ^{231}Pa/^{230}Th records (e.g. Negre et al., 2010), but lacks a thorough understanding of the distribution of these nuclides due to its more complex pattern of deep-water circulation than the North Atlantic, with multiple water masses flowing in different directions. This dataset captures all the main Atlantic deep-water masses along their meridional flow paths and allows insight into the control on Th and Pa in a setting where waters are flowing in opposing directions. It is confirmed in this work that ^{231}Pa and ^{230}Th are transported by deep ocean circulation out of the modern Atlantic, and that this horizontal transport fractionates ^{231}Pa from ^{230}Th. The expected progressive change of ^{231}Pa and ^{230}Th within a water mass is however not observed, suggesting that ^{231}Pa (and to a lesser extent, ^{230}Th) are removed from the North Atlantic, but are in equilibrium in the South Atlantic so that scavenging equals production. Pronounced decreases of ^{230}Th and ^{231}Pa were observed in near-bottom water, indicating enhanced sea-floor removal, particularly in regions where nepheloid layers are present. This enhanced scavenging in nepheloid layers preferentially removes ^{231}Pa and is likely to cause a small increase in sediment ^{231}Pa/^{230}Th ratio. High ^{232}Th concentrations in surface waters of equatorial area, and possibly at 32^{o}S-45^{o}S, indicate high dust input from the continent.

Although I have demonstrated the horizontal transport of ^{230}Th and ^{231}Pa, there is no clear indication of a control on ^{231}Pa/^{230}Th ratios by water-mass age in the Southwest Atlantic, challenging the use of sedimentary ^{231}Pa/^{230}Th to assess past flow in this region. An observed mid-water-column peak in ^{231}Pa concentrations is difficult to explain with 1D models, and suggests the importance of opal dissolution or lateral transport in controlling seawater ^{231}Pa profiles.

The lack of water mass control in the Southwest Atlantic suggests that it is essential to look into the vertical control of ^{231}Pa and ^{230}Th by particle scavenging. Although particulate ^{231}Pa and ^{230}Th account for only a small portion of their total water-column concentrations, coupled with water-column measurement, they would give an insight into the exchange processes between the particulate and dissolved phases of the nuclides, which would also help us understand the cycling of other particle-reactive elements in the ocean. Understanding the puzzling mid-water-column peak observed in ^{231}Pa profile would also benefit from high-resolution dissolved and particulate profiles of ^{231}Pa not only in the deep water but also in the upper water column where particle cycling is most active.

6.2 ^{230}Th, ^{232}Th and ^{231}Pa in surface sediment of Southeast Atlantic

High-resolution measurements of U-series isotopes were obtained from sediment collected on the Cape Basin Margin (UK-GEOTRACES cruise D357) and the South Atlantic Mid-Ocean Ridge (Meteor cruise M34/3) to assess the use of ^{230}Th$_{xs}$ as a tool to quantify sediment dissolution and its

effect on sedimentary $(^{231}Pa/^{230}Th)_{xs}$. Vertical profiles of $^{230}Th_{xs}$ concentrations exhibit a striking increase of $^{230}Th_{xs}$ in the upper sediment followed by relatively constant values at depth. This study has demonstrated that such features can be used to indicate the presence of sediment dissolution in the upper centimeters of these cores, assuming that ^{230}Th flux to the seafloor is constant with time. $^{230}Th_{xs}$ measurements can therefore provide a tool to quantify the rate of sediment dissolution at the seafloor and assess the magnitude of this process in various ocean settings. Based on $^{230}Th_{xs}$ data in this study, estimates of sediment dissolution rate range between 0.11 and 0.24 g/cm^2/kyr, and exhibit a nearly linear increase with water depth. Combining $^{230}Th_{xs}$ with sediment composition measurements provides an assessment of the dissolution rates of individual mineralogical components in the sediment. In the core with the most unambiguous dissolution, situated a kilometer below the modern carbonate saturation horizon, there is surprising lack of observed carbonate dissolution, while opal does appear to be dissolving. Results also suggest dissolution of the lithogenic fraction of sediments in two of the cores. If confirmed, this suggests the use of ^{230}Th to assess the process of submarine weathering, a process which is presently difficult to quantify. Measurements of ^{231}Pa enable the assessment of the impact of sediment dissolution on $(^{231}Pa/^{230}Th)_{xs}$ ratios. Despite significant sediment dissolution, $(^{231}Pa/^{230}Th)_{xs}$ ratios stay relatively constant in the upper sediment core and do not appear to be affected by sediment dissolution, suggesting the robustness of sedimentary $(^{231}Pa/^{230}Th)_{xs}$ as a proxy for paleoceanographic studies.

The conclusions in this thesis regarding sediment dissolution are based on a relatively small dataset, with key data points not yet duplicated. Further work should confirm and extent the testing of the use of ^{230}Th to study sediment dissolution. A more complete measurement of the major components, such as opal, in sediments would also enable a more precise assessment of the

contribution of each component to the sediment dissolution by using $^{230}Th_{xs}$ approach. While encouraging, applying $^{230}Th_{xs}$ approach to quantify sediment dissolution requires the assumption that the flux of sediment from the water column has remained constant to be examined. This can be better assessed with sediment age derived from the measurement of a second chronometer, such as ^{201}Pb or ^{14}C, in the same sediments.

6.3 Water-column ^{230}Th and ^{232}Th in the tropical Atlantic Ocean

Measurements of ^{230}Th and ^{232}Th were made for five sites in the tropical Atlantic Ocean along a transect under the influence of Saharan dust plume (UK-GEOTRACES cruise GA06 (D361)). This setting is ideal to test ^{232}Th, paired with ^{230}Th-derived residence times, as a tool to quantify dust flux to the surface ocean as proposed by previous studies (e.g. Hayes et al., 2013, Hsieh et al., 2011). In particular, two aspects of this approach were assessed, 1) the optimal integration depth for yielding a ^{232}Th flux representative of the dust flux. Mixed layer depth was chosen because, at greater depths, the input of ^{232}Th and ^{230}Th is not identical leading to different residence times for the two nuclides; 2) fractional solubility of dust Th. This was made possible by aerosol measurement of total and soluble Th fractions on the same cruise. An approach to estimate Th solubility in areas where such data are not available was proposed based on the inverse relationship between Th solubility and dust flux estimated from ^{232}Th in this study. Estimates of dust flux improved with more accurate mixed layer depth and Th solubility were compared with model-generated dust flux. Both estimates exhibit an increase of dust flux from 7^{o}S in the South

Atlantic to 19^{o}N in the North Atlantic. Absolute values however show disagreement between the two results, with higher dust flux estimated by the model. Th-232 flux was also used to calculate Fe flux supplied to the ocean by partial dissolution of atmospheric dust. Using a relative fractional solubility of Fe and Th at 0.16 (based on direct measurements of coeval aerosols), Fe flux was estimated to be in a range between 0.35 and 2.26 mg/m^2/yr. This would supply enough Fe to produce productivity ranging between 32.9 and 212.7 g C /m^2/yr, which is in the range of estimates of primary productivity rate in the investigated, indicating that partial dissolution from atmospheric dust is the major source supplying most Fe to the ocean in this region.

This dataset of water-column ^{230}Th and ^{232}Th, coupled with aerosol measurement of Th and Fe, allows us to test ^{232}Th as a potential tool to quantify dust input to the surface ocean, and ultimately to estimate Fe flux supplied by the atmospheric deposition to the ocean. Assessing the robustness of this tool is, however, still limited by a lack of reliable water-column and aerosol measurements. A more complete dataset of metals in aerosol samples, particularly at low dust loading, would be helpful to better constrain the Th solubility and dust flux relationship, which can expand the application of ^{232}Th approach in areas where the direct measurement of Th solubility is not available. Also, a larger dataset of water-column and aerosol measurement of thorium and iron would help to establish a relationship between Th flux and Fe flux, so that we can estimate Fe flux from Th flux which has less complicated cycling and can be more easily quantified in the ocean. A better knowledge of applying ^{232}Th approach to derive dust flux also provides an alternative to constrain dust models that can generate a more accurate global map of dust deposition. Sources of ^{232}Th other than dust input, such as possible advection of ^{232}Th from ocean margins, would complicate the use of ^{232}Th. Off-shore measurements or ocean modelling is therefore recommended for future studies to better assess potential sources of ^{232}Th.

Bibliography

Adkins, J., deMenocal, P., Eshel, G., 2006. The "African humid period" and the record of marine upwelling from excess ^{230}Th in Ocean Drilling Program Hole 658C. Paleoceanography 21, PA4203.

Anderson, R.F., 1982. Concentration, vertical flux, and remineralization of particulate uranium in seawater. Geochim. Cosmochim. Acta 46, 1293-1299.

Anderson, R.F., Bacon, M.P., Brewer, P.G., 1983a. Removal of ^{230}Th and ^{231}Pa from the open ocean. Earth and Planetary Science Letters 62, 7-23.

Anderson, R.F., Bacon, M.P., Brewer, P.G., 1983b. Removal of ^{230}Th and ^{231}Pa at ocean margins. Earth and Planetary Science Letters 66, 73-90.

Anderson, R.F., Fleer, A.P., 1982. Determination of natural actinides and plutonium in marine particulate material. Analytical Chemistry 54, 1142-1147.

Anderson, R.F., Fleisher, M.Q., Robinson, L.F., Edwards, R.L., Hoff, J.A., Moran, S.B., Rutgers van der Loeff, M., Thomas, A.L., Roy-Barman, M., Francois, R., 2012. GEOTRACES intercalibration of ^{230}Th, ^{232}Th, ^{231}Pa, and prospects for ^{10}Be. Limnology and oceanography: methods 10, 179-213.

Andersson, P.S., Wasserburg, G.J., Chen, J.H., Papanastassiou, D.A., Ingri, J., 1995. ^{238}U-^{234}U and ^{232}Th-^{230}Th in the Baltic Sea and in river water. Earth and Planetary Science Letters 130, 217-234.

Archer, D., Maier-Reimer, E., 1994. Effect of deep-sea sedimentary calcite preservation on atmospheric CO_2 concentration. Nature 367, 260-263.

Baker, A.R., Adams, C., Bell, T.G., Jickells, T.D., Ganzeveld, L., 2013. Estimation of atmospheric nutrient inputs to the Atlantic Ocean from 50°N to 50°S based on large-scale field sampling: Iron and other dust-associated elements. Global Biogeochemical Cycles 27, 755-767.

Baker, A.R., Jickells, T.D., 2006. Mineral particle size as a control on aerosol iron solubility. Geophysical Research Letters 33, L17608.

Baker, A.R., Jickells, T.D., Witt, M., Linge, K.L., 2006. Trends in the solubility of iron, aluminium, manganese and phosphorus in aerosol collected over the Atlantic Ocean. Marine Chemistry 98, 43-58.

Bacon, M.P., 1984. Glacial to interglacial changes in carbonate and clay sedimentation in the Atlantic Ocean estimated from ^{230}Th measurements. Chem Geol 46, 97-111.

Bacon, M.P., Anderson, R.F., 1982. Distribution of thorium isotopes between dissolved and particulate forms in the deep sea. Journal of Geophysical Research: Oceans 87, 2045-2056.

Bacon, M.P., Rosholt, J.N., 1982. Accumulation rates of Th-230, Pa-231, and some transition metals on the Bermuda Rise. Geochim. Cosmochim. Acta 46, 651-666.

Bareille, G., Labracherie, M., Labeyrie, L., Pichon, J.-J., Turon, J.-L., 1991. Biogenic silica accumulation rate during the Holocene in the southeastern Indian Ocean. Marine Chemistry 35, 537-551.

Barnes, C.E., Cochran, J.K., 1990. Uranium removal in oceanic sediments and the oceanic U balance. Earth and Planetary Science Letters 97, 94-101.

Belshaw, N.S., Freedman, P.A., O'Nions, R.K., Frank, M., Guo, Y., 1998. A new variable dispersion double-focusing plasma mass spectrometer with performance illustrated for Pb isotopes. International Journal of Mass Spectrometry 181, 51-58.

Berner, R.A., Wilde, P., 1972. Dissolution kinetics of calcium carbonate in sea water; I, Saturation state parameters for kinetic calculations. American Journal of Science 272, 826-839.

Boggs, S., 1995. Weathering processese and products and sediment transport, in: Robert A. M. (Ed.), Principles of sedimentology and stratigraphy. Pretice-Hall, Inc., New Jersey, pp. 17-32.

Bourne, M., Mac Niocaill, C., Thomas, A.L., Knudsen, M.F., Henderson, G.M., 2012a. Rapid directional changes associated with a 6.5kyr-long Blake geomagnetic excursion at the Blake–Bahama Outer Ridge. Earth and Planetary Science Letters 333–334, 21-34.

Bourne, M.D., Thomas, A.L., Mac Niocaill, C., Henderson, G.M., 2012b. Improved determination of marine sedimentation rates using $^{230}Th_{xs}$. Geochemistry, Geophysics, Geosystems 13, Q09017.

Boyle, E.A., 1988. Cadmium: Chemical tracer of deepwater paleoceanography. Paleoceanography 3, 471-489.

Boyle, E.A., Keigwin, L.D, 1982. Deep circulation of the North Atlantic over the last 200,000 years: Geochemical evidence. Science 218, 784-787.

Bradtmiller, L.I., Anderson, R.F., Fleisher, M.Q., Burckle, L.H., 2007. Opal burial in the equatorial Atlantic Ocean over the last 30 ka: Implications for glacial-interglacial changes in the ocean silicon cycle. Paleoceanography 22, PA4216.

Broecker, W.S., Anderson, R., Clark, E., Fleisher, M., 2001. Record of seafloor $CaCO_3$ dissolution in the central equatorial Pacific. Geochemistry, Geophysics, Geosystems 2, 1050.

Broecker, W. S., and Peng, T. H., 1982. Tracers in the Sea, Lamont-Doherty Earth Obs., Palisades, N. Y.

Buesseler, K.O., Cochran, J.K., Bacon, M.P., Livingston, H.D., Casso, S.A., Hirschberg, D., Hartman, M.C., Fleer, A.P., 1992. Determination of thorium isotopes in seawater by nondestructive and radiochemical procedures. Deep Sea Research Part A. Oceanographic Research Papers 39, 1103-1114.

Charles, C.D., Froelich, P.N., Zibello, M.A., Mortlock, R.A., Morley, J.J., 1991. Biogenic opal in Southern Ocean sediments over the last 450,000 years: Implications for surface water chemistry and circulation. Paleoceanography 6, 697-728.

Chase, Z., Anderson, R.F., Fleisher, M.Q., Kubik, P.W., 2002. The influence of particle composition and particle flux on scavenging of Th, Pa and Be in the ocean. Earth and Planetary Science Letters 204, 215-229.

Chase, Z., Anderson, R.F., Fleisher, M.Q., Kubik, P.W., 2003. Accumulation of biogenic and lithogenic material in the Pacific sector of the Southern Ocean during the past 40,000 years. Deep Sea Research Part II: Topical Studies in Oceanography 50, 799-832.

Chen, C.-T.A., 2002. Shelf-vs. dissolution-generated alkalinity above the chemical lysocline. Deep Sea Research Part II: Topical Studies in Oceanography 49, 5365-5375.

Chen, J.H., Lawrence Edwards, R., Wasserburg, G.J., 1986. ^{238}U, ^{234}U and ^{232}Th in seawater. Earth and Planetary Science Letters 80, 241-251.

Cheng, H., Edwards, R.L., Hoff, J., Gallup, C.D., Richards, D.A., Asmerom, Y., 2000. The half-lives of uranium-234 and thorium-230. Chem Geol 169, 17-33.

Cheng, H., Lawrence Edwards, R., Shen, C.-C., Polyak, V.J., Asmerom, Y., Woodhead, J., Hellstrom, J., Wang, Y., Kong, X., Spötl, C., Wang, X., Calvin Alexander Jr, E., 2013. Improvements in ^{230}Th dating, ^{230}Th and ^{234}U half-life values, and U–Th isotopic measurements by multi-collector inductively coupled plasma mass spectrometry. Earth and Planetary Science Letters 371–372, 82-91.

Choi, M.S., Francois, R., Sims, K., Bacon, M.P., Brown-Leger, S., Fleer, A.P., Ball, L., Schneider, D., Pichat, S., 2001. Rapid determination of ^{230}Th and ^{231}Pa in seawater by desolvated micro-nebulization Inductively Coupled Plasma magnetic sector mass spectrometry. Marine Chemistry 76, 99-112.

Clegg, S.L., Whitfield, M., 1991. A generalized model for the scavenging of trace metals in the open ocean—II. Thorium scavenging. Deep Sea Research Part A. Oceanographic Research Papers 38, 91-120.

Coale, K.H., Bruland, K.W., 1985. Oceanic stratified euphotic zone as elucidated by ^{234}Th : ^{238}U disequilibria. Limnology and oceanography 30, 22-33.

Cochran J. K., 1992. The oceanic chemistry of the uranium- and thorium-series nuclides. In: Uranium-series disequilibrium: Applications to Earth, Marine, and Environmental Sciences (eds. M. Ivanovich and R. S. Harmon). Oxford, Clarendon Press.

Cochran, J.K., Livingston, H.D., Hirschberg, D.J., Surprenant, L.D., 1987. Natural and anthropogenic radionuclide distributions in the northwest Atlantic Ocean. Earth and Planetary Science Letters 84, 135-152.

Craig, H., Krishnaswami, S., Somayajulu, B.L.K., 1973. ^{210}Pb-^{226}Ra: Radioactive disequilibrium in the deep sea. Earth and Planetary Science Letters 17, 295-305.

Crain, J.S., Alvarado, J., 1994. Hydride interference on the determination of minor actinide isotopes by inductively coupled plasma mass spectrometry. Journal of Analytical Atomic Spectrometry 9, 1223-1227.

Curry, W.B., Duplessy, J.C., Labeyrie, L.D., Shackleton, N.J., 1988. Changes in the distribution of $\delta^{13}C$ of deep water ΣCO_2 between the Last Glaciation and the Holocene. Paleoceanography 3, 317-341.

Darbyshire, M., 1966. The surface waters near the coasts of Southern Africa. Deep Sea Research and Oceanographic Abstracts 13, 57-81.

Deng, F., Thomas, A.L., Rijkenberg, M.J.A., Henderson, G.M., 2014. Controls on seawater ^{231}Pa, ^{230}Th and ^{232}Th concentrations along the flow paths of deep waters in the Southwest Atlantic. Earth and Planetary Science Letters 390, 93-102.

Dixit, S., Van Cappellen, P., van Bennekom, A.J., 2001. Processes controlling solubility of biogenic silica and pore water build-up of silicic acid in marine sediments. Marine Chemistry 73, 333-352.

Duce, R.A. and Tindale, N.W., 1991. Atmospheric transport of iron and its deposition in the ocean. Limnology and Oceanography., 36*(8),* 1 715-1726

Edmonds, H.N., Moran, S.B., Hoff, J.A., Smith, J.N., Edwards, R.L., 1998. Protactinium-231 and Thorium-230 Abundances and High Scavenging Rates in the Western Arctic Ocean. Science 280, 405-407.

Farrell, J.W., Prell, W.L., 1989. Climatic change and $CaCO_3$ preservation: An 800,000 year bathymetric Reconstruction from the central equatorial Pacific Ocean. Paleoceanography 4, 447-466.

Fitzsimmons, J.N., Zhang, R., Boyle, E.A., 2013. Dissolved iron in the tropical North Atlantic Ocean. Marine Chemistry 154, 87-99.

Francois, R., Bacon, M.P., Suman, D.O., 1990. Thorium-230 profiling in deep-sea sediments: High-resolution records of flux and dissolution of carbonate in the equatorial Atlantic during the last 24,000 years. Paleoceanography 5, 761-787.

Francois, R., Frank, M., Rutgers van der Loeff, M.M., Bacon, M.P., 2004. ^{230}Th normalization: An essential tool for interpreting sedimentary fluxes during the late Quaternary. Paleoceanography 19, PA1018.

Gherardi, J.M., Labeyrie, L., Nave, S., Francois, R., McManus, J.F., Cortijo, E., 2009. Glacial-interglacial circulation changes inferred from ^{231}Pa/^{230}Th sedimentary record in the North Atlantic region. Paleoceanography 24, PA2204.

Ginoux, P., Chin, M., Tegen, I., Prospero, J.M., Holben, B., Dubovik, O., Lin, S.-J., 2001. Sources and distributions of dust aerosols simulated with the GOCART model. Journal of Geophysical Research: Atmospheres 106, 20255-20273.

Goldberg, E. D., Marine geochemistry, 1, Chemical scavengers of the sea, J. Geol., 62,249-265, 1954.

Hall, I.R., Moran, S.B., Zahn, R., Knutz, P.C., Shen, C.C., Edwards, R.L., 2006. Accelerated drawdown of meridional overturning in the late-glacial Atlantic triggered by transient pre-H event freshwater perturbation. Geophysical Research Letters 33, L16616.

Hayes, C.T., Anderson, R.F., Fleisher, M.Q., Serno, S., Winckler, G., Gersonde, R., 2013a. Quantifying lithogenic inputs to the North Pacific Ocean using the long-lived thorium isotopes. Earth and Planetary Science Letters 383, 16-25.

Hayes, C.T., Anderson, R.F., Jaccard, S.L., François, R., Fleisher, M.Q., Soon, M., Gersonde, R., 2013b. A new perspective on boundary scavenging in the North Pacific Ocean. Earth and Planetary Science Letters 369–370, 86-97.

Hedges, J.I., Keil, R.G., 1995. Sedimentary organic matter preservation: an assessment and speculative synthesis. Marine Chemistry 49, 81-115.

Henderson, G.M., 2002. New oceanic proxies for paleoclimate. Earth and Planetary Science Letters 203, 1-13.

Henderson, G.M., Anderson, R.F., 2003. The U-series Toolbox for Paleoceanography. Reviews in Mineralogy and Geochemistry 52, 493-531.

Henderson, G.M., Heinze, C., Anderson, R.F., Winguth, A.M.E., 1999. Global distribution of the ^{230}Th flux to ocean sediments constrained by GCM modelling. Deep Sea Research Part I: Oceanographic Research Papers 46, 1861-1893.

Hirose, K., and Sugimura, Y., 1987. Chemical speciation of particulate ^{238}U, ^{239,240}Pu and Th isotopes in seawater. The Science of the Total Environment 130/131, 517-524.

Hoffmann,S.S., McManus, J.F., Curry, W.B., Brown-Leger, L.S., 2013. Persistent export of ^{231}Pa from the deep central Arctic Ocean over the past 35,000 years. Nature 497, 603-606.

Holden, N.E., 1990. Total half-lives for selected nuclides. Pure and Applied Chemistry 62, 941-958.

Homoky, W.B., John, S.G., Conway, T.M., Mills, R.A., 2013. Distinct iron isotopic signatures and supply from marine sediment dissolution. Nat Commun 4.

Honjo, S., Manganini, S.J., Cole, J.J., 1982. Sedimentation of biogenic matter in the deep ocean. Deep Sea Research Part A. Oceanographic Research Papers 29, 609-625.

Hsieh, Y.-T., Henderson, G.M., Thomas, A.L., 2011. Combining seawater ^{232}Th and ^{230}Th concentrations to determine dust fluxes to the surface ocean. Earth and Planetary Science Letters 312, 280-290.

Huh, C.A., Bacon, M.P., 1985. Thorium-232 in the eastern Caribbean Sea. Nature 316, 718-721.

Hurd, D.C., 1973. Interactions of biogenic opal, sediment and seawater in the Central Equatorial Pacific. Geochim. Cosmochim. Acta 37, 2257-2282.

Jahnke, R.A., Jahnke, D.B., 2004. Calcium carbonate dissolution in deep sea sediments: reconciling microelectrode, pore water and benthic flux chamber results. Geochim. Cosmochim. Acta 68, 47-59.

Kara, A.B., Rochford, P.A., Hurlburt, H.E., 2000. An optimal definition for ocean mixed layer depth. Journal of Geophysical Research: Oceans 105, 16803-16821.

Klinkhammer, G.P., Palmer, M.R., 1991. Uranium in the oceans: Where it goes and why. Geochim. Cosmochim. Acta 55, 1799-1806.

Knudsen, M.F., Henderson, G.M., Mac Niocaill, C., West, A.J., 2007. Seven thousand year duration for a geomagnetic excursion constrained by $^{230}Th_{xs}$. Geophysical Research Letters 34, L22302.

Krishnaswami, S., Lal, D., Somayajulu, B.L.K., Weiss, R.F., Craig, H., 1976. Large-volume in-situ filtration of deep Pacific waters: Mineralogical and radioisotope studies. Earth and Planetary Science Letters 32, 420-429.

Ku, T.-L., Knauss, K.G., Mathieu, G.G., 1977. Uranium in open ocean: concentration and isotopic composition. Deep Sea Research 24, 1005-1017.

Kumar, N., Anderson, R.F., Mortlock, R.A., Froelich, P.N., Kubik, P., Dittrich-Hannen, B., Suter, M., 1995. Increased biological productivity and export production in the glacial Southern Ocean. Nature 378, 675-680.

Larqué, L., Maamaatuaiahutapu, K., Garçon, V., 1997. On the intermediate and deep water flows in the South Atlantic Ocean. Journal of Geophysical Research: Oceans 102, 12425-12440.

Li, Y.-H., Takahashi, T., Broecker, W.S., 1969. Degree of saturation of $CaCO_3$ in the oceans. Journal of Geophysical Research 74, 5507-5525.

Lippold, J., Gherardi, J.-M., Luo, Y., 2011. Testing the $^{231}Pa/^{230}Th$ paleocirculation proxy: A data versus 2D model comparison. Geophysical Research Letters 38, L20603.

Lippold, J., Luo, Y., Francois, R., Allen, S.E., Gherardi, J., Pichat, S., Hickey, B., Schulz, H., 2012. Strength and geometry of the glacial Atlantic Meridional Overturning Circulation. Nature Geosci 5, 813-816.

Longhurst, A., Sathyendranath, S., Platt, T., Caverhill, C., 1995. An estimate of global primary production in the ocean from satellite radiometer data. Journal of Plankton Research 17, 1245-1271.

Luo, S., Ku, T.-L., 1999. Oceanic $^{231}Pa/^{230}Th$ ratio influenced by particle composition and remineralization. Earth and Planetary Science Letters 167, 183-195.

Luo, Y., Francois, R., Allen, S.E., 2010. Sediment $^{231}Pa/^{230}Th$ as a recorder of the rate of the Atlantic meridional overturning circulation: insights from a 2-D model. Ocean Science 6, 381-400.

Lutjeharms, J. R. E., The exchange of water between the south Indian and south Atlantic oceans, The South Atlantic: Present and Past Circulation, G. Wefer, *et al.,* 125–162, Springer Verlag, New York, 1996.

Lyle, M., Murray, D.W., Finney, B.P., Dymond, J., Robbins, J.M., Brooksforce, K., 1988. The record of Late Pleistocene biogenic sedimentation in the eastern tropical Pacific Ocean. Paleoceanography 3, 39-59.

Lynch-Stieglitz, J., Adkins, J.F., Curry, W.B., Dokken, T., Hall, I.R., Herguera, J.C., Hirschi, J.J.-M., Ivanova, E.V., Kissel, C., Marchal, O., Marchitto, T.M., McCave, I.N., McManus, J.F., Mulitza, S., Ninnemann, U., Peeters, F., Yu, E.-F., Zahn, R., 2007. Atlantic Meridional Overturning Circulation During the Last Glacial Maximum. Science 316, 66-69.

Mahowald, N.M., Baker, A.R., Bergametti, G., Brooks, N., Duce, R.A., Jickells, T.D., Kubilay, N., Prospero, J.M., Tegen, I., 2005. Atmospheric global dust cycle and iron inputs to the ocean. Global Biogeochemical Cycles 19, GB4025.

Mahowald, N.M., Luo, C., 2003. A less dusty future? Geophysical Research Letters 30, 1903.

Mahowald, N.M., Muhs, D.R., Levis, S., Rasch, P.J., Yoshioka, M., Zender, C.S., Luo, C., 2006. Change in atmospheric mineral aerosols in response to climate: Last glacial period,

preindustrial, modern, and doubled carbon dioxide climates. Journal of Geophysical Research: Atmospheres 111, D10202.

Mangini, A., Key, R.M., 1983. A ^{230}Th profile in the Atlantic Ocean. Earth and Planetary Science Letters 62, 377-384.

Marticorena, B., Bergametti, G., 1996. Two-year simulations of seasonal and interannual changes of the Saharan dust emissions. Geophysical Research Letters 23, 1921-1924.

Martin, J.H., Fitzwater, S.E., 1988. Iron deficiency limits phytoplankton growth in the north-east Pacific subarctic. Nature 331, 341-343.

McManus, J.F., Francois, R., Gherardi, J.-M., Keigwin, L.D., Brown-Leger, S., 2004 Collapse and rapid resumption of Atlantic meridional circulation linked to deglacial climate changes. Nature 428, 834-837.

Measures, C.I., Brown, E.T., 1996. Estimating dust input to the Atlantic Ocean using surface water Al concentrations. In: Guerzoni, S., Chester R., (Eds.), The impact of African Dust across the Mediterranean, Kluwer, Dordrecht, 389pp.

Measures, C.I., Vink, S., 1999. Seasonal variations in the distribution of Fe and Al in the surface waters of the Arabian Sea. Deep Sea Research Part II: Topical Studies in Oceanography 46, 1597-1622.

Measures, C.I., Vink, S., 2000. On the use of dissolved aluminum in surface waters to estimate dust deposition to the ocean. Global Biogeochemical Cycles 14, 317-327.

Milliman, J.D., Troy, P.J., Balch, W.M., Adams, A.K., Li, Y.H., Mackenzie, F.T., 1999. Biologically mediated dissolution of calcium carbonate above the chemical lysocline? Deep Sea Research Part I: Oceanographic Research Papers 46, 1653-1669.

Moran, S.B., Charette, M.A., Hoff, J.A., Edwards, R.L., Landing, W.M., 1997. Distribution of ^{230}Th in the Labrador Sea and its relation to ventilation. Earth and Planetary Science Letters 150, 151-160.

Moran, S.B., Hoff, J.A., Buesseler, K.O., Edwards, R.L., 1995. High precision ^{230}Th and ^{232}Th in the Norwegian Sea and Denmark by thermal ionization mass spectrometry. Geophysical Research Letters 22, 2589-2592.

Moran, S.B., Shen, C.-C., Edmonds, H.N., Weistein, S.E., Smith, J.N., Edwards, R.L., 2002. Dissolved and particulate ^{231}Pa and ^{230}Th in the Atlantic Ocean: Constraints on intermediate/deep water age, boundary scavenging, and ^{231}Pa/^{230}Th fractionation. Earth and Planetary Science Letters 203, 999-1014.

Moran, S.B., Shen, C.C., Weinstein, S.E., Hettinger, L.H., Hoff, J.H., Edmonds, H.N., Edwards, R.L., 2001. Constraints on deep water age and particle flux in the equatorial and South

Atlantic Ocean based on seawater ^{231}Pa and ^{230}Th data. Geophysical Research Letters 28, 3437-3440.

Morel, F.M.M. and Hudson, R.J.M., 1985. The geobiological cycle of trace elements in aquatic systems: Redfield revisited. In: *Chemical progress in lakes*, Stumm, W., editor, Wiley, New York, pp. 251-281.

Morozov, E.G., Demidov, A.N., Tarakanov, R.Y., Zenk, W., 2010. Deep water masses of the South and North Atlantic, in: Abyssal Channels in the Atlantic Ocean. Springer, pp.25-50.

Nozaki, Y., Horibe, Y., Tsubota, H., 1981. The water column distributions of thorium isotopes in the western North Pacific. Earth and Planetary Science Letters 54, 203-216.

Nozaki, Y., Nakanishi, T., 1985. ^{231}Pa and ^{230}Th profiles in the open ocean water column. Deep Sea Research Part A. Oceanographic Research Papers 32, 1209-1220.

Nozaki, Y., Yang, H.-S., Yamada, M., 1987. Scavenging of thorium in the ocean. Journal of Geophysical Research: Oceans 92, 772-778.

Nozaki, Y., Yamada, M., 1987. Thorium and protactinum isotope distribution in waters of the Japan Sea. Deep Sea Research Part A. Oceanographic Research Papers 34, 1417-1430.

Negre, C., Thomas, A.L., Mas, J.L., Garcia-Orellana, J., Henderson, G.M., Masqué, P., Zahn, R., 2009. Separation and Measurement of Pa, Th, and U Isotopes in Marine Sediments by Microwave-Assisted Digestion and Multiple Collector Inductively Coupled Plasma Mass Spectrometry. Analytical Chemistry 81, 1914-1919.

Negre, C., Zahn, R., Thomas, A.L., Masque, P., Henderson, G.M., Martinez-Mendez, G., Hall, I.R., Mas, J.L., 2010. Reversed flow of Atlantic deep water during the Last Glacial Maximum. Nature 468, 84-88.

Nelson, D.W. and L.E. Sommers. 1996. Total carbon, organic carbon, and organic matter. In: Methods of Soil Analysis, Part 2, 2nd ed., A.L. Page et al., Ed. Agronomy. 9:961-1010. Am. Soc. of Agron., Inc. Madison, WI.

Noorany, I., 1984. Phase Relations in Marine Soils. Journal of Geotechnical Engineering 110, 539-543.

Okubo, A., Obata, H., Gamo, T., Yamada, M., 2012. ^{230}Th and ^{232}Th distributions in mid-latitudes of the North Pacific Ocean: Effect of bottom scavenging. Earth and Planetary Science Letters 339–340, 139-150.

Orsi, A.H., Whitworth Iii, T., Nowlin Jr, W.D., 1995. On the meridional extent and fronts of the Antarctic Circumpolar Current. Deep Sea Research Part I: Oceanographic Research Papers 42, 641-673.

Peterson, R.G., Stramma, L., 1991. Upper-level circulation in the South Atlantic Ocean. Progress in Oceanography 26, 1-73.

Prospero, J. M., Saharan dust transport over the North Atlantic Ocean and Mediterranean: And overview, in The Impact of Desert Dust Across the Mediterranean, edited by S. Guerzoni and R. Chester, pp. 133 – 151, Kluwer Acad., Norwell, Mass., 1996.

Ragueneau, O., Tréguer, P., Leynaert, A., Anderson, R.F., Brzezinski, M.A., DeMaster, D.J., Dugdale, R.C., Dymond, J., Fischer, G., François, R., Heinze, C., Maier-Reimer, E., Martin-Jézéquel, V., Nelson, D.M., Quéguiner, B., 2000. A review of the Si cycle in the modern ocean: recent progress and missing gaps in the application of biogenic opal as a paleoproductivity proxy. Global and Planetary Change 26, 317-365.

Regelous, M., Turner, S.P., Elliott, T.R., Rostami, K., Hawkesworth, C.J., 2004. Measurement of Femtogram Quantities of Protactinium in Silicate Rock Samples by Multicollector Inductively Coupled Plasma Mass Spectrometry. Analytical Chemistry 76, 3584-3589.

Robert, J., Miranda, C.F. and Muxart, R., 1969. Mesure de la periode du protactinium-231 par microcalorimetrie. Radiochimica Acta 11, 104-108.

Robinson, L. F. (2003). Pleistocene climate chronology and ocean circulation in the Bahamas using U-series nuclides. D.Phil, Oxford University.

Robinson, L.F., Belshaw, N.S., Henderson, G.M., 2004. U and Th concentrations and isotope ratios in modern carbonates and waters from the Bahamas. Geochim. Cosmochim. Acta 68, 1777-1789.

Roy-Barman, M., Chen, J.H., Wasserburg, G.J., 1996. ^{230}Th-^{232}Th systematics in the central Pacific Ocean: The sources and the fates of thorium. Earth and Planetary Science Letters 139, 351-363.

Rudnick, R.L., Gao, S., 2003. 3.01 - Composition of the Continental Crust, in: Holland, H.D., Turekian, K.K. (Eds.), Treatise on Geochemistry. Pergamon, Oxford, pp. 1-64.

Rutgers van der Loeff, M.M., Berger, G.W., 1993. Scavenging of 230Th and 231Pa near the antarctic polar front in the South Atlantic. Deep Sea Research Part I: Oceanographic Research Papers 40, 339-357.

Scholten, J.C., Fietzke, J., Mangini, A., Garbe-Schönberg, C.D., Eisenhauer, A., Schneider, R., Stoffers, P., 2008. Advection and scavenging: Effects on ^{230}Th and ^{231}Pa distribution off Southwest Africa. Earth and Planetary Science Letters 271, 159-169.

Scholten, J.C., Fietzke, J., Vogler, S., Rutgers van der Loeff, M.M., Mangini, A., Koeve, W., Waniek, J., Stoffers, P., Antia, A., Kuss, J., 2001. Trapping efficiencies of sediment traps from the deep Eastern North Atlantic: the ^{230}Th calibration. Deep Sea Research Part II: Topical Studies in Oceanography 48, 2383-2408.

Schlosser, C., Klar, J.K., Wake, B.D., Snow, J.T., Honey, D.J., Woodward, E.M.S., Lohan, M.C., Achterberg, E.P., Moore, C.M., 2014. Seasonal ITCZ migration dynamically controls the location of the (sub)tropical Atlantic biogeochemical divide. Proceedings of the National Academy of Sciences 111, 1438-1442.

Schütz, L., 1980. LONG RANGE TRANSPORT OF DESERT DUST WITH SPECIAL EMPHASIS ON THE SAHARA*. Annals of the New York Academy of Sciences 338, 515-532.

Shen, C.-C., Lawrence Edwards, R., Cheng, H., Dorale, J.A., Thomas, R.B., Bradley Moran, S., Weinstein, S.E., Edmonds, H.N., 2002. Uranium and thorium isotopic and concentration measurements by magnetic sector inductively coupled plasma mass spectrometry. Chem Geol 185, 165-178.

Stramma, L., England, M., 1999. On the water masses and mean circulation of the South Atlantic Ocean. Journal of Geophysical Research: Oceans 104, 20863-20883.

Suman, D.O., Bacon, M.P., 1989. Variations in Holocene sedimentation in the North American Basin determined from ^{230}Th measurements. Deep Sea Research Part A. Oceanographic Research Papers 36, 869-878.

Taylor S. R. and McLennan S. M. (1985) The Continental Crust: Its Composition and Evolution. Blackwell, Oxford.

Tegen, I., Werner, M., Harrison, S.P., Kohfeld, K.E., 2004. Relative importance of climate and land use in determining present and future global soil dust emission. Geophysical Research Letters 31, L05105.

Thomas, A.L. (2006). Variations in Past and Present Ocean Circulation Assessed with U-Series Nuclides. D.Phil, Oxford University.

Thomas, A.L., Henderson, G.M., McCave, I.N., 2007. Constant bottom water flow into the Indian Ocean for the past 140 ka indicated by sediment ^{231}Pa/^{230}Th ratios. Paleoceanography 22, PA4210.

Thomas, A.L., Henderson, G.M., Robinson, L.F., 2006. Interpretation of the ^{231}Pa/^{230}Th paleocirculation proxy: New water-column measurements from the southwest Indian Ocean. Earth and Planetary Science Letters 241, 493-504.

Usman, K., MacMahon, T.D., 2000. Determination of the half-life of ^{233}Pa. Applied Radiation and Isotopes 52, 585-589.

Van Bennekom, A.J., Berger, G.W., Van der Gaast, S.J., de Vries, R.T.P., 1988. Primary productivity and the silica cycle in the Southern Ocean (Atlantic sector). Palaeogeography, Palaeoclimatology, Palaeoecology 67, 19-30.

Van Cappellen, P., Qiu, L., 1997. Biogenic silica dissolution in sediments of the Southern Ocean. I. Solubility. Deep Sea Research Part II: Topical Studies in Oceanography 44, 1109-1128.

Vanicek, M., Siedler, G., 2002. Zonal Fluxes in the Deep Water Layers of the Western South Atlantic Ocean*. Journal of Physical Oceanography 32, 2205-2235.

Venchiarutti, C., van der Loeff, M.R., Stimac, I., 2011. Scavenging of 231Pa and thorium isotopes based on dissolved and size-fractionated particulate distributions at Drake Passage (ANTXXIV-3). Deep Sea Research Part II: Topical Studies in Oceanography 58, 2767-2784.

Vogler, S., Scholten, J., Rutgers van der Loeff, M., Mangini, A., 1998. ^{230}Th in the eastern North Atlantic: the importance of water mass ventilation in the balance of ^{230}Th. Earth and Planetary Science Letters 156, 61-74.

Yu, E.F., Francois, R., Bacon, M.P., 1996. Similar rates of modern and last-glacial ocean thermohaline circulation inferred from radiochemical data. Nature 379, 689-694.

Yu, E.F., Francois, R., Bacon, M.P., Fleer, A.P., 2001. Fluxes of ^{230}Th and ^{231}Pa to the deep sea: implications for the interpretation of excess ^{230}Th and ^{231}Pa/^{230}Th profiles in sediments. Earth and Planetary Science Letters 191, 219-230.

Appendix: Data tables and figures

Table 2.1: A summary of blank measurements alongside both seawater and sediment samples.

Cruise ID	Batch number	^{231}Pa (fg)	2se	^{230}Th (fg)	2se	^{232}Th (pg)	2se	^{238}U (pg)	2se
D361	1	2.22	0.71	-0.30	1.58	20.78	0.72		
seawater	2	0.39	0.07	-0.18	1.54	24.20	0.89		
	3	0.07	0.20	1.66	0.96	30.84	1.01		
	4	0.62	0.41	0.72	1.02	43.26	1.53		
JC057	1	0.48	0.77	0.33	0.81	28.47	3.30		
seawater	2	0.49	0.26	-0.20	1.35	34.94	1.28		
	3	0.76	0.56	0.07	0.69	30.57	1.08		
	4	0.36	0.49	0.09	0.63	17.49	0.67		
	5	0.93	0.27	0.49	0.64	33.68	1.26		
	6	0.20	0.46	-0.29	0.63	7.39	1.22		
	7	0.09	0.38	-0.05	0.75	11.81	1.22		
	8	0.09	0.38	0.75	0.99	6.14	1.38		
	9	0.04	0.27	0.27	0.88	7.30	1.67		
D357	1	0.04	0.15	4.25	150.35	122.45	249.85	98.01	505.45
sediment	2	0.20	0.17	2.52	174.65	90.99	326.90	86.58	271.65
	3	1.73	0.96	0.77	166.25	120.60	475.39	84.17	136.49
GeoB3808-7	1	1.50	0.51	0.14	90.26	219.35	934.05	217.86	4156.45
sediment	2	0.42	0.35	-0.86	84.60	88.97	158.37	177.38	352.47

Table 3.1: Results of water-column ^{231}Pa, ^{230}Th and ^{232}Th concentrations, and $^{231}Pa/^{230}Th$ ratios in the Southwest Atlantic Ocean

Station	Depth	^{231}Pa	$^{231}Pa_{corr}$	$^{231}Pa_{corr}$	2se	^{230}Th	$^{230}Th_{corr}$	$^{230}Th_{corr}$	2se	^{232}Th	^{232}Th	2se	$(^{231}Pa/^{230}Th)_{corr}$	2se
	m	fg/kg	fg/kg	dpm/1000l		fg/kg	fg/kg	dpm/1000l		pg/kg	dpm/1000l			
JC057-1	2299	2.95	2.94	0.32	0.02	15.22	15.01	0.70	0.02	56.76	0.0142	0.0008	0.45	0.03
49.55°S	2243	2.85	2.85	0.31	0.02	15.4	15.22	0.71	0.02	47.87	0.0119	0.0008	0.43	0.03
52.69°W	2118	3.00	2.99	0.32	0.13	15.57	15.42	0.72	0.10	39.49	0.0099	0.0013	0.45	0.19
	1875	2.87	2.87	0.31	0.03	14.75	14.64	0.68	0.02	30.06	0.0075	0.0008	0.45	0.04
	1502	2.45	2.45	0.26	0.01	14.16	14.03	0.66	0.02	34.17	0.0085	0.0007	0.40	0.02
	999	2.09	2.09	0.22	0.02	10.06	9.93	0.46	0.02	35.29	0.0088	0.0008	0.48	0.05
	900	1.81	1.81	0.19	0.01	10.22	10.05	0.47	0.01	44.55	0.0111	0.0007	0.41	0.03
	702	1.55	1.55	0.17	0.02	6.93	6.87	0.32	0.01	16.27	0.0041	0.0007	0.52	0.06
	499	1.27	1.27	0.14	0.02	6.12	6.06	0.28	0.01	16.23	0.0041	0.0007	0.48	0.07
	250	0.83	0.83	0.09	0.02	4.18	4.12	0.19	0.01	15.97	0.004	0.0007	0.46	0.10
	99	0.45	0.43	0.05	0.01	3.62	2.82	0.13	0.01	215.28	0.0537	0.0012	0.35	0.10
	24	0.46	0.46	0.05	0.01	0.95	0.79	0.04	0.01	42.17	0.0105	0.0004	1.33	0.32
JC057-2	5801	2.58	2.57	0.28	0.05	22.16	21.85	1.02	0.03	80.7	0.0201	0.0004	0.27	0.05
48.94°S	5500	2.43	2.43	0.26	0.05	19.38	19.11	0.89	0.02	72.92	0.0182	0.0004	0.29	0.06
48.79°W	5001	2.66	2.66	0.29	0.05	20.05	19.82	0.93	0.03	63.58	0.0159	0.0003	0.31	0.06
	4001	2.90	2.90	0.31	0.06	18.95	18.78	0.88	0.02	44.95	0.0112	0.0002	0.35	0.06

(continued on next page)

Table 3.1 (continued from previous page)

Station	Depth	^{231}Pa	$^{231}Pa_{corr}$	$^{231}Pa_{corr}$	2se	^{230}Th	$^{230}Th_{corr}$	$^{230}Th_{corr}$	2se	^{232}Th	^{232}Th	2se	$(^{231}Pa/^{230}Th)_{corr}$	2se
	m	fg/kg	fg/kg	dpm/1000l		fg/kg	fg/kg	dpm/1000l		pg/kg	dpm/1000l			
	3003	2.97	2.96	0.32	0.06	15.92	15.82	0.74	0.02	27.71	0.0069	0.0002	0.43	0.08
	2001	2.70	2.70	0.29	0.05	14.47	14.35	0.67	0.02	31.1	0.0078	0.0002	0.43	0.08
	1502	2.49	2.48	0.27	0.05	11.93	11.84	0.55	0.02	24.32	0.0061	0.0002	0.48	0.09
	1002	2.11	2.10	0.23	0.04	9.54	9.44	0.44	0.01	25.92	0.0065	0.0002	0.51	0.10
	501	1.27	1.27	0.14	0.03	6.24	6.16	0.29	0.02	20.35	0.0051	0.0001	0.47	0.10
	250	0.82	0.82	0.09	0.02	4.88	4.81	0.23	0.01	19.03	0.0047	0.0001	0.39	0.09
	99	0.48	0.48	0.05	0.01	1.59	1.53	0.07	0.01	17.71	0.0044	0.0001	0.72	0.23
	25	0.47	0.47	0.05	0.01	3.02	2.97	0.14	0.01	13.89	0.0035	0.0001	0.36	0.09
JC057-3	5699	2.50	2.49	0.27	0.01	14.83	14.59	0.68	0.02	63.56	0.0159	0.0004	0.39	0.02
46.91°S	5498	2.48	2.48	0.27	0.01	14.91	14.68	0.69	0.02	62.86	0.0157	0.0003	0.39	0.02
47.18°W	5001	2.95	2.95	0.32	0.01	17.71	17.49	0.82	0.02	56.81	0.0142	0.0003	0.39	0.02
	4000	2.6	2.6	0.28	0.05	15.0	14.88	0.70	0.02	32.46	0.0081	0.0002	0.40	0.07
	3001	2.96	2.96	0.32	0.01	14.36	14.24	0.67	0.02	32.73	0.0082	0.0002	0.48	0.02
	2002	3.0	3.0	0.32	0.01	11.22	11.1	0.52	0.02	30.53	0.0076	0.0002	0.62	0.03
	1503	3.35	3.35	0.36	0.01	9.27	9.16	0.43	0.01	28.51	0.0071	0.0002	0.84	0.04
	1001	1.57	1.57	0.17	0.01	7.38	7.27	0.34	0.01	30.22	0.0075	0.0002	0.49	0.04
	250	0.72	0.72	0.08	0.02	3.15	2.92	0.14	0.01	60.12	0.0150	0.0003	0.56	0.12

(continued on next page)

Table 3.1 (continued from previous page)

Station	Depth	^{231}Pa	$^{231}Pa_{corr}$	$^{231}Pa_{corr}$	2se	^{230}Th	$^{230}Th_{corr}$	$^{230}Th_{corr}$	2se	^{232}Th	^{232}Th	2se	$(^{231}Pa/^{230}Th)_{corr}$	2se
	m	fg/kg	fg/kg	dpm/1000l		fg/kg	fg/kg	dpm/1000l		pg/kg	dpm/1000l			
	101	0.38	0.37	0.04	0.01	3.01	2.76	0.13	0.01	67.68	0.0169	0.0007	0.31	0.08
	25	0.37	0.37	0.04	0.01	0.44	0.34	0.02	0.01	25.92	0.0065	0.0001	2.48	0.80
JC057-4	5040	2.29	2.29	0.25	0.04	15.53	15.30	0.72	0.02	61.40	0.0153	0.0003	0.34	0.06
44.71°S	5001	2.22	2.21	0.24	0.04	16.29	16.04	0.75	0.02	67.37	0.0168	0.0003	0.32	0.06
45.53°W	4498	2.81	2.80	0.30	0.05	21.56	21.32	1.00	0.02	64.74	0.0162	0.0003	0.30	0.05
	3501	3.03	3.03	0.33	0.06	17.76	17.61	0.82	0.02	37.99	0.0095	0.0002	0.39	0.07
	2501	2.92	2.92	0.31	0.06	15.15	15.02	0.70	0.02	34.05	0.0085	0.0002	0.45	0.08
	1750	2.73	2.72	0.29	0.05	13.00	12.86	0.60	0.02	36.88	0.0092	0.0002	0.49	0.09
	1501	2.69	2.69	0.29	0.05	11.44	11.32	0.53	0.02	33.02	0.0082	0.0002	0.55	0.10
	1002	1.91	1.90	0.20	0.04	8.55	8.45	0.40	0.02	27.64	0.0069	0.0002	0.52	0.10
	500	1.07	1.07	0.12	0.02	6.52	6.40	0.30	0.02	31.09	0.0078	0.0002	0.38	0.08
	250	0.77	0.77	0.08	0.02	2.99	2.86	0.13	0.01	35.73	0.0089	0.0002	0.62	0.15
	99	0.47	0.47	0.05	0.01	1.68	1.62	0.08	0.01	16.50	0.0041	0.0001	0.66	0.21
	23	0.14	0.14	0.02	0.01	0.12	0.10	0.004	0.01	5.34	0.0013	0.0001	3.37	3.54
JC057-5	5153	1.96	1.96	0.21	0.01	15.09	14.85	0.70	0.02	61.92	0.0155	0.0007	0.30	0.02
42.36°S	4999	2.14	2.13	0.23	0.01	18.63	18.35	0.86	0.02	73.65	0.0184	0.0007	0.27	0.02
44.03°W	4499	2.44	2.44	0.26	0.01	19.77	19.54	0.91	0.02	60.11	0.015	0.0008	0.29	0.02

(continued on next page)

Table 3.1 (continued from previous page)

Station	Depth	^{231}Pa	$^{231}Pa_{corr}$	$^{231}Pa_{corr}$	2se	^{230}Th	$^{230}Th_{corr}$	$^{230}Th_{corr}$	2se	^{232}Th	^{232}Th	2se	$(^{231}Pa/^{230}Th)_{corr}$	2se
	m	fg/kg	fg/kg	dpm/1000l		fg/kg	fg/kg	dpm/1000l		pg/kg	dpm/1000l			
	3500	2.65	2.65	0.28	0.01	18.33	18.17	0.85	0.02	44.00	0.0110	0.0007	0.34	0.02
	2500	2.67	2.67	0.29	0.01	15.04	14.90	0.70	0.02	38.84	0.0097	0.0007	0.41	0.02
	1750	2.33	2.33	0.25	0.01	12.76	12.63	0.59	0.01	35.84	0.0089	0.0007	0.42	0.03
	1500	2.22	2.22	0.24	0.01	10.74	10.62	0.50	0.01	32.73	0.0082	0.0007	0.48	0.03
	1000	1.55	1.55	0.17	0.01	8.19	8.07	0.38	0.01	30.13	0.0075	0.0007	0.44	0.04
	501	0.86	0.86	0.09	0.01	5.92	5.80	0.27	0.02	32.95	0.0082	0.0008	0.34	0.05
	250	0.58	0.58	0.06	0.01	4.70	4.53	0.21	0.01	44.25	0.0110	0.0007	0.29	0.06
	102	0.54	0.53	0.06	0.01	2.84	2.70	0.13	0.01	37.03	0.0092	0.0007	0.45	0.10
	25	0.12	0.12	0.01	0.01	0.16	0.14	0.01	0.01	6.08	0.0015	0.0003	2.04	3.04
JC057-6	5119	1.97	1.96	0.21	0.04	14.32	14.10	0.66	0.02	60.54	0.0151	0.0002	0.32	0.06
39.96°S	4999	2.27	2.26	0.24	0.06	22.12	21.76	1.02	0.30	96.74	0.0241	0.0053	0.24	0.09
42.42°W	4498	2.53	2.52	0.27	0.05	22.10	21.84	1.02	0.04	68.78	0.0172	0.0003	0.27	0.05
	3501	2.88	2.88	0.31	0.06	17.70	17.54	0.82	0.03	44.88	0.0112	0.0002	0.38	0.07
	3002	2.81	2.81	0.3	0.05	16.23	16.10	0.75	0.03	34.37	0.0086	0.0002	0.40	0.07
	2001	2.43	2.42	0.26	0.05	10.49	10.37	0.49	0.02	32.83	0.0082	0.0001	0.54	0.10
	1396	2.68	2.68	0.29	0.05	14.01	13.84	0.65	0.02	46.20	0.0115	0.0002	0.44	0.08

(continued on next page)

Table 3.1 (continued from previous page)

Station	Depth	^{231}Pa	$^{231}Pa_{corr}$	$^{231}Pa_{corr}$	2se	^{230}Th	$^{230}Th_{corr}$	$^{230}Th_{corr}$	2se	^{232}Th	^{232}Th	2se	$(^{231}Pa/^{230}Th)_{corr}$	2se
	m	fg/kg	fg/kg	dpm/1000l		fg/kg	fg/kg	dpm/1000l		pg/kg	dpm/1000l			
	1000	1.63	1.63	0.18	0.03	8.11	7.99	0.37	0.02	33.03	0.0082	0.0002	0.47	0.09
	500	0.90	0.89	0.10	0.02	5.06	4.95	0.23	0.01	31.23	0.0078	0.0001	0.41	0.09
	250	0.70	0.70	0.07	0.02	5.31	5.13	0.24	0.02	48.47	0.0121	0.0002	0.31	0.07
	101	0.41	0.41	0.04	0.01	3.18	2.93	0.14	0.01	67.98	0.0170	0.0002	0.32	0.09
JC057-7	5023	2.23	2.23	0.24	0.04	17.59	17.29	0.81	0.02	80.90	0.0202	0.0004	0.30	0.05
37.83°S	5000	1.43	1.43	0.15	0.03	16.63	16.36	0.77	0.02	71.19	0.0178	0.0004	0.20	0.04
41.12°W	4499	2.73	2.72	0.29	0.05	21.53	21.29	1.00	0.05	64.97	0.0162	0.0006	0.29	0.05
	3500	2.82	2.82	0.30	0.05	18.65	18.47	0.86	0.02	48.17	0.0120	0.0003	0.35	0.06
	2501	2.92	2.92	0.31	0.06	15.29	15.12	0.71	0.02	46.78	0.0117	0.0002	0.44	0.08
	1748	2.56	2.56	0.27	0.05	6.07	5.93	0.28	0.02	37.93	0.0095	0.0002	0.99	0.19
	1500	2.27	2.27	0.24	0.04	9.50	9.38	0.44	0.02	32.74	0.0082	0.0002	0.55	0.10
	1000	0.68	0.68	0.07	0.02	6.07	5.83	0.27	0.01	64.31	0.0160	0.0003	0.27	0.06
	409	1.35	1.35	0.15	0.03	6.58	6.46	0.30	0.01	33.52	0.0084	0.0002	0.48	0.09
	249	0.60	0.59	0.06	0.02	6.61	6.28	0.29	0.01	88.32	0.0220	0.0004	0.22	0.06
	101	0.49	0.48	0.05	0.01	3.08	2.85	0.13	0.01	62.77	0.0157	0.0003	0.39	0.11
	24	0.29	0.28	0.03	0.01	2.02	1.89	0.09	0.01	34.80	0.0087	0.0002	0.34	0.13

(continued on next page)

Table 3.1 (continued from previous page)

Station	Depth	^{231}Pa	$^{231}Pa_{corr}$	$^{231}Pa_{corr}$	2se	^{230}Th	$^{230}Th_{corr}$	$^{230}Th_{corr}$	2se	^{232}Th	^{232}Th	2se	$(^{231}Pa/^{230}Th)_{corr}$	2se
	m	fg/kg	fg/kg	dpm/1000l		fg/kg	fg/kg	dpm/1000l		pg/kg	dpm/1000l			
JC057-9	4121	2.52	2.51	0.27	0.02	19.32	19.10	0.89	0.03	58.53	0.0146	0.0003	0.30	0.02
32.09°S	4075	2.70	2.70	0.29	0.01	19.66	19.45	0.91	0.03	56.04	0.0140	0.0003	0.32	0.02
37.46°W	3500	2.96	2.95	0.32	0.02	21.68	21.46	1.00	0.03	59.71	0.0149	0.0003	0.32	0.02
	3000	2.74	2.74	0.29	0.02	16.94	16.75	0.78	0.03	48.65	0.0121	0.0003	0.38	0.03
	2501	2.80	2.80	0.30	0.02	16.01	15.81	0.74	0.03	53.16	0.0133	0.0003	0.41	0.03
	1750	3.04	3.04	0.33	0.06	11.73	11.63	0.54	0.02	27.21	0.0068	0.0002	0.60	0.11
	1501	2.66	2.66	0.29	0.01	10.86	10.73	0.50	0.03	35.07	0.0088	0.0002	0.57	0.04
	1001	1.72	1.72	0.18	0.02	7.35	7.22	0.34	0.02	33.16	0.0083	0.0002	0.55	0.06
	250	0.87	0.86	0.09	0.02	4.73	4.48	0.21	0.01	67.07	0.0167	0.0003	0.44	0.10
	102	0.48	0.47	0.05	0.02	2.08	1.95	0.09	0.01	36.39	0.0091	0.0002	0.56	0.17
	26	0.46	0.46	0.05	0.01	2.81	2.56	0.12	0.01	67.18	0.0168	0.0003	0.41	0.07
JC057-12	4498	2.22	2.21	0.24	0.01	19.38	19.15	0.90	0.02	63.88	0.0159	0.0003	0.27	0.02
22.47°S	4000	2.59	2.59	0.28	0.01	17.04	16.88	0.79	0.02	43.20	0.0108	0.0002	0.35	0.02
32.75°W	3499	2.43	2.42	0.26	0.01	22.25	22.06	1.03	0.02	53.09	0.0132	0.0003	0.25	0.01
	2999	2.52	2.51	0.27	0.01	12.10	11.97	0.56	0.02	34.36	0.0086	0.0002	0.48	0.03
	2500	2.55	2.55	0.27	0.01	17.12	16.88	0.79	0.02	64.17	0.0160	0.0003	0.35	0.02

(continued on next page)

Table 3.1 (continued from previous page)

Station	Depth	^{231}Pa	$^{231}Pa_{corr}$	$^{231}Pa_{corr}$	2se	^{230}Th	$^{230}Th_{corr}$	$^{230}Th_{corr}$	2se	^{232}Th	^{232}Th	2se	$(^{231}Pa/^{230}Th)_{corr}$	2se
	m	fg/kg	fg/kg	dpm/1000l		fg/kg	fg/kg	dpm/1000l		pg/kg	dpm/1000l			
	1750	2.43	2.43	0.26	0.01	12.47	12.28	0.57	0.02	51.68	0.0129	0.0003	0.45	0.02
	1501	2.69	2.68	0.29	0.02	9.51	9.39	0.44	0.01	32.66	0.0082	0.0007	0.66	0.04
	1000	2.13	2.13	0.23	0.01	9.19	9.09	0.43	0.01	27.53	0.0069	0.0001	0.54	0.04
	500	0.75	0.74	0.08	0.01	5.28	5.15	0.24	0.01	33.94	0.0085	0.0002	0.33	0.05
	250	0.41	0.41	0.04	0.01	2.96	2.89	0.14	0.01	20.29	0.0051	0.0001	0.33	0.09
	99	0.37	0.37	0.04	0.01	3.16	3.04	0.14	0.01	31.77	0.0079	0.0002	0.28	0.08
	23	0.52	0.52	0.06	0.01	2.06	1.93	0.09	0.01	34.20	0.0085	0.0002	0.62	0.15
JC057-14	5391	2.16	2.16	0.23	0.07	27.36	27.11	1.27	0.03	65.68	0.0164	0.0004	0.18	0.05
12.90°S	4999	2.73	2.72	0.29	0.05	24.94	24.69	1.16	0.03	66.85	0.0167	0.0005	0.25	0.05
29.23°W	4501	2.24	2.24	0.24	0.04	25.73	25.46	1.19	0.02	72.14	0.018	0.0004	0.20	0.04
	3499	2.77	2.77	0.30	0.05	21.58	21.43	1.00	0.02	40.47	0.0101	0.0003	0.30	0.05
	2501	3.03	3.03	0.33	0.06	16.64	16.53	0.77	0.02	29.67	0.0074	0.0003	0.42	0.07
	1749	2.71	2.70	0.29	0.05	15.12	14.92	0.70	0.02	52.17	0.013	0.0003	0.42	0.07
	1499	2.80	2.80	0.30	0.05	12.93	12.75	0.60	0.02	49.14	0.0123	0.0003	0.50	0.09
	1001	2.73	2.73	0.29	0.05	10.15	10.05	0.47	0.01	27.02	0.0067	0.0003	0.62	0.11
	500	1.44	1.44	0.15	0.03	6.13	6.05	0.28	0.01	22.90	0.0057	0.0003	0.55	0.11

(continued on next page)

Table 3.1 (continued from previous page)

Station	Depth	^{231}Pa	$^{231}Pa_{corr}$	$^{231}Pa_{corr}$	2se	^{230}Th	$^{230}Th_{corr}$	$^{230}Th_{corr}$	2se	^{232}Th	^{232}Th	2se	$(^{231}Pa/^{230}Th)_{corr}$	2se
	m	fg/kg	fg/kg	dpm/1000l		fg/kg	fg/kg	dpm/1000l		pg/kg	dpm/1000l			
	250	0.64	0.63	0.07	0.02	3.56	3.48	0.16	0.01	20.00	0.0050	0.0003	0.42	0.10
	99	0.33	0.33	0.04	0.01	2.82	2.76	0.13	0.01	14.99	0.0037	0.0002	0.28	0.09
	24	0.39	0.39	0.04	0.01	2.08	1.98	0.09	0.01	26.97	0.0067	0.0002	0.45	0.10
JC057-16	5519	2.02	2.01	0.22	0.02	20.24	20.00	0.94	0.02	66.19	0.0165	0.0002	0.23	0.02
5.67°S	4999	2.20	2.19	0.24	0.02	27.18	26.85	1.26	0.02	88.87	0.0222	0.0002	0.19	0.01
28.46°W	4499	2.37	2.37	0.25	0.01	23.88	23.6	1.10	0.02	74.44	0.0186	0.0002	0.23	0.01
	3500	2.23	2.23	0.24	0.01	16.23	16.01	0.75	0.02	58.32	0.0146	0.0002	0.32	0.02
	2500	2.92	2.92	0.31	0.01	15.39	15.23	0.71	0.01	43.70	0.0109	0.0001	0.44	0.02
	1751	2.46	2.46	0.26	0.01	13.37	13.14	0.61	0.01	62.82	0.0157	0.0001	0.43	0.02
	1499	2.50	2.50	0.27	0.01	9.82	9.63	0.45	0.01	49.77	0.0124	0.0001	0.60	0.04
	999	2.51	2.51	0.27	0.01	8.69	8.54	0.40	0.01	39.82	0.0099	0.0001	0.67	0.04
	499	1.43	1.43	0.15	0.01	5.23	5.05	0.24	0.01	46.44	0.0116	0.0007	0.65	0.06
	250	0.95	0.94	0.10	0.01	4.32	4.16	0.19	0.01	43.03	0.0107	0.0001	0.52	0.08
	109	0.51	0.51	0.05	0.02	3.40	3.29	0.15	0.01	29.76	0.0074	0.0002	0.35	0.09
JC057-18	4318	2.26	2.26	0.24	0.04	18.14	17.89	0.84	0.02	67.01	0.0167	0.0004	0.29	0.05
0.19°S	3998	1.81	1.81	0.19	0.04	15.17	14.92	0.70	0.02	67.37	0.0168	0.0004	0.28	0.05
32.87°W	3498	2.05	2.05	0.22	0.04	14.37	14.11	0.66	0.03	68.27	0.0170	0.0005	0.33	0.06

(continued on next page)

Table 3.1 (continued from previous page)

Station	Depth	^{231}Pa	$^{231}Pa_{corr}$	$^{231}Pa_{corr}$	2se	^{230}Th	$^{230}Th_{corr}$	$^{230}Th_{corr}$	2se	^{232}Th	^{232}Th	2se	$(^{231}Pa/^{230}Th)_{corr}$	2se
	m	fg/kg	fg/kg	dpm/1000l		fg/kg	fg/kg	dpm/1000l		pg/kg	dpm/1000l			
	3000	2.28	2.27	0.24	0.04	12.06	11.87	0.56	0.02	49.74	0.0124	0.0003	0.44	0.08
	2500	2.51	2.50	0.27	0.05	11.60	11.40	0.53	0.02	55.12	0.0138	0.0004	0.50	0.09
	1749	2.23	2.22	0.24	0.04	10.53	10.28	0.48	0.01	65.97	0.0165	0.0004	0.50	0.09
	1500	2.09	2.08	0.22	0.04	9.36	9.11	0.43	0.01	65.98	0.0165	0.0004	0.53	0.10
	1000	2.34	2.33	0.25	0.05	6.97	6.78	0.32	0.02	50.74	0.0127	0.0002	0.79	0.15
	499	1.37	1.36	0.15	0.03	5.45	4.98	0.23	0.01	127.01	0.0317	0.0004	0.63	0.12
	245	0.84	0.83	0.09	0.02	4.50	4.25	0.20	0.01	68.50	0.0171	0.0002	0.45	0.09
	100	0.60	0.60	0.06	0.02	3.37	3.22	0.15	0.01	41.82	0.0104	0.0001	0.43	0.10
	24	0.39	0.39	0.04	0.01	2.25	1.98	0.09	0.01	71.61	0.0179	0.0002	0.45	0.10

^{230}Th and ^{231}Pa are dissolved ^{230}Th and ^{231}Pa activities corrected for the ingrowth from seawater ^{234}U and ^{235}U, respectively, since the time of collection following equations:

$$^{230}Th = {}^{230}Th_m - {}^{238}U \times (1-\exp(-\lambda_{230Th}\times t)+ \lambda_{230Th}/(\lambda_{230Th}- \lambda_{234U}) \times ({}^{234}U/{}^{238}U-1) \times (1-\exp(-(\lambda_{230Th}- \lambda_{234U}) \times t)) \quad (1)$$

$$^{231}Pa = {}^{231}Pa_m - {}^{235}U \times (1- \exp(-\lambda_{231Pa}\times t)) \quad (2)$$

^{230}Th and ^{231}Pa are further corrected for detrital, U-supported ^{230}Th and ^{231}Pa concentrations as follows:

$$^{231}Pa_{corr}={}^{231}Pa- 0.046\times (0.7\times {}^{232}Th_m) \quad (3)$$

$$^{230}Th_{corr}={}^{230}Th_m- (0.7\times {}^{232}Th_m) \quad (4)$$

where $^{230}Th_m$, $^{231}Pa_m$ and $^{232}Th_m$ are activities obtained from measurement; ^{235}U and ^{238}U are their average activities in seawater, 118dpm/1000l and 2500dpm/1000l, respectively; $^{234}U/^{238}U$ is the activity ratio of ^{234}U and ^{238}U in seawater, 1.146; λ_{230Th} and λ_{231Pa} are decay constants of ^{230}Th and ^{231}Pa; t is the time between sample collection and chemical separation of U from ^{231}Pa and ^{230}Th. 0.7 is the average $^{238}U/^{232}Th$ activity ratio in detrital material (Marcatonio et al., 2001) and 0.046 represents the $^{235}U/^{238}U$ activity (Anderson et al., 1990). Activities of ^{231}Pa, ^{230}Th and ^{232}Th have been converted to dpm/1000l assuming the density of seawater ρ= 1.025g/cm^3. Half lives for ^{231}Pa, ^{230}Th and ^{232}Th are 32,760yr, 75,584yr and 1.40×10^{10}yr.

All errors are two standard errors including the contribution from sample weighing, spike calibration, ^{231}Pa, ^{230}Th and ^{232}Th in the respective ^{233}Pa and ^{230}Th spikes, blank correction, internal precision and related corrections of mass spectrometric measurement.

Table 4.1: U, ^{232}Th, ^{230}Th and ^{231}Pa concentrations for Cape Basin Margin sediment and South Atlantic Mid-Ocean Ridge sediment.

Sediment core ID	Depth (cm)	$^{232}Th_{meas}$ (dpm/g)	2se	$^{238}U_{meas}$ (dpm/g)	2se	U_{auth} (dpm/g)	2se	$\delta^{234}U$	2se	$^{238}U/^{232}Th$	2se
D357-0.75	0.5	1.345	0.008	1.7505	0.0029	0.11	0.07	7.20	0.02	1.302	0.008
	1.5	1.452	0.010	1.7522	0.0027	-0.02	0.07	9.12	0.02	1.207	0.009
	2.5	1.337	0.008	1.8666	0.0039	0.24	0.07	10.16	0.03	1.396	0.008
	3.5	1.416	0.008	2.1468	0.0036	0.42	0.07	36.05	0.09	1.516	0.009
	4.5	1.460	0.006	2.3560	0.0031	0.58	0.07	45.83	0.11	1.614	0.007
	7	1.381	0.008	2.6849	0.0047	1.00	0.07	50.82	0.15	1.944	0.012
	9	1.177	0.008	2.6943	0.0085	1.26	0.07	70.79	0.25	2.288	0.017
	13	1.301	0.007	3.3152	0.0050	1.73	0.07	75.48	0.19	2.548	0.014
	17	1.364	0.008	2.4818	0.0032	0.82	0.07	49.65	0.11	1.820	0.011
	21	1.306	0.008	2.4429	0.0029	0.85	0.07	50.90	0.12	1.870	0.012
GeoB3808-7	0.5	0.202	0.001	0.172	0.0004	0.07	0.04	73.98	0.36	0.850	0.005
	1.5	0.244	0.001	0.186	0.0009	0.06	0.04	74.70	0.51	0.763	0.005
	2.5	0.253	0.001	0.193	0.0009	0.06	0.04	75.37	0.53	0.764	0.005
	4.5	0.285	0.002	0.204	0.0014	0.06	0.04	66.08	0.68	0.715	0.007
	6.5	0.306	0.002	0.224	0.0013	0.07	0.04	69.68	0.62	0.734	0.006

Subscripts ‘meas’ and ‘xs’ indicate measured and detrital-corrected activities; all uncertainties are two standard error (2se). (continued on next page)

Table 4.1 (continued from previous page)

Sediment core ID	Depth (cm)	$^{232}Th_{meas}$ (dpm/g)	2se	$^{238}U_{meas}$ (dpm/g)	2se	U_{auth} (dpm/g)	2se	$\delta^{234}U$	2se	$^{238}U/^{232}Th$	2se
D357-3	0.5	1.563	0.009	1.739	0.0034	0.38	0.09	-58.02	0.18	1.112	0.007
	1.5	1.931	0.013	1.844	0.0037	0.16	0.09	-53.85	0.17	0.955	0.006
	2.5	2.187	0.014	1.733	0.0029	-0.17	0.09	-55.88	0.16	0.793	0.005
	4.5	2.015	0.011	1.762	0.0022	0.01	0.09	-59.24	0.14	0.874	0.005
	7	2.215	0.012	1.698	0.0021	-0.23	0.09	-58.53	0.14	0.767	0.004
	11	1.876	0.011	1.678	0.0019	0.05	0.09	-64.27	0.15	0.895	0.005
D357-4.5	0.5	1.689	0.012	0.900	0.0016	-0.02	0.04	-69.12	0.19	0.533	0.004
	1.5	2.885	0.018	1.630	0.0036	0.06	0.04	-70.32	0.24	0.565	0.004
	2.5	2.941	0.021	1.652	0.0037	0.05	0.04	-69.33	0.24	0.562	0.004
	4.5	2.914	0.018	1.617	0.0024	0.03	0.04	-70.64	0.18	0.555	0.004
	8	2.971	0.017	1.631	0.0019	0.02	0.04	-72.27	0.17	0.549	0.003
	12	2.956	0.018	1.623	0.0028	0.02	0.04	-73.26	0.21	0.549	0.003
	16	2.899	0.017	1.556	0.0032	-0.02	0.04	-74.31	0.25	0.537	0.003
	20	2.933	0.016	1.562	0.0035	-0.03	0.04	-76.09	0.27	0.533	0.003
	24	2.673	0.018	1.381	0.0026	-0.07	0.04	-75.75	0.24	0.517	0.004

(continued on next page)

Table 4.1 (continued from previous page)

Sediment sample ID	Depth (cm)	$^{231}Pa_{meas}$ (dpm/g)	2se	$^{231}Pa_{xs}$ (dpm/g)_	2se	$^{230}Th_{meas}$ (dpm/g)	2se	$^{230}Th_{xs}$ (dpm/g)	2se	$(^{231}Pa/^{230}Th)_{xs}$	2se
D357-0.75	0.5	0.184	0.005	0.109	0.008	2.981	0.014	1.342	0.121	0.081	0.009
	1.5	0.149	0.003	0.068	0.007	3.054	0.013	1.284	0.130	0.053	0.008
	2.5	0.163	0.004	0.088	0.007	3.112	0.014	1.482	0.120	0.059	0.007
	3.5	0.159	0.004	0.080	0.007	3.093	0.014	1.366	0.127	0.058	0.007
	4.5	0.135	0.003	0.053	0.007	3.090	0.014	1.310	0.131	0.040	0.007
	7	0.138	0.003	0.060	0.007	3.139	0.013	1.455	0.124	0.041	0.006
	9	0.115	0.003	0.049	0.006	2.749	0.014	1.313	0.106	0.037	0.005
	13	0.143	0.004	0.070	0.007	3.115	0.011	1.528	0.117	0.046	0.006
	17	0.161	0.004	0.084	0.007	3.085	0.012	1.422	0.122	0.059	0.007
	21	0.129	0.003	0.056	0.006	3.028	0.014	1.435	0.117	0.039	0.005
GeoB3808-7	0.5	0.451	0.003	0.447	0.003	10.228	0.028	10.126	0.004	0.044	0.0003
	1.5	0.560	0.004	0.554	0.004	12.547	0.058	12.423	0.008	0.045	0.0003
	2.5	0.580	0.004	0.574	0.004	12.986	0.058	12.858	0.008	0.045	0.0003
	4.5	0.539	0.004	0.532	0.004	12.590	0.088	12.445	0.013	0.043	0.0003
	6.5	0.605	0.004	0.598	0.004	14.333	0.082	14.178	0.012	0.042	0.0003

(continued on next page)

Table 4.1 (continued from previous page)

Sediment sample ID	Depth (cm)	$^{231}Pa_{meas}$ (dpm/g)	2se	$^{231}Pa_{xs}$ (dpm/g)	2se	$^{230}Th_{meas}$ (dpm/g)	2se	$^{230}Th_{xs}$ (dpm/g)	2se	$(^{231}Pa/^{230}Th)_{xs}$	2se
D357-3	0.5	0.460	0.013	0.398	0.014	12.31	0.05	10.95	0.13	0.036	0.0014
	1.5	0.311	0.005	0.233	0.008	13.73	0.05	12.05	0.16	0.019	0.0007
	2.5	0.594	0.009	0.507	0.011	15.71	0.06	13.81	0.18	0.037	0.0010
	4.5	0.617	0.008	0.536	0.010	15.13	0.05	13.38	0.16	0.040	0.0009
	7	0.604	0.008	0.515	0.011	15.59	0.05	13.66	0.17	0.038	0.0009
	11	0.568	0.007	0.493	0.010	14.91	0.05	13.28	0.15	0.037	0.0008
D357-4.5	0.5	1.352	0.076	1.310	0.076	27.39	0.10	26.47	0.11	0.049	0.0029
	1.5	2.568	0.122	2.496	0.122	48.23	0.20	46.66	0.21	0.053	0.0026
	2.5	2.604	0.128	2.530	0.128	49.45	0.22	47.85	0.23	0.053	0.0027
	4.5	2.704	0.086	2.631	0.086	50.48	0.19	48.90	0.20	0.054	0.0018
	8	2.687	0.032	2.613	0.033	52.02	0.16	50.41	0.17	0.052	0.0007
	12	2.587	0.031	2.513	0.031	52.16	0.18	50.55	0.19	0.050	0.0006
	16	2.626	0.031	2.553	0.031	51.43	0.19	49.86	0.20	0.051	0.0007
	20	2.553	0.031	2.480	0.031	52.01	0.20	50.41	0.21	0.049	0.0006
	24	2.226	0.026	2.159	0.026	47.16	0.15	45.71	0.16	0.047	0.0006

Table 4.2: Sediment content measured for samples collected on the Cape Basin Margin in weight percentage (%)

Sediment core ID	Depth	Total C (TC)	1SD	Total Inorganic C (TIC)	1SD	Total $CaCO_3$	1SD	Total organic C (TOC)	1SD	Organic Matter (OM)	1SD	Al	Al-derived Lithogenics	Opal
	(cm)	(wt %)		(wt %)		(wt %)		(wt %)		(wt %)		(wt %)	(wt %)	(wt %)
D357-0.75	0.5	5.89	0.10	3.61	0.06	30.05	0.48	2.29	0.16	3.94	0.28	3.34	41.01	25.00
	1.5	5.84	0.07	3.66	0.04	30.53	0.37	2.18	0.11	3.76	0.20	3.41	41.87	23.84
	2.5	5.82	0.06	3.60	0.06	30.01	0.49	2.21	0.11	3.82	0.20	3.44	42.13	24.04
	3.5	6.09	0.06	3.71	0.04	30.91	0.37	2.38	0.10	4.10	0.17	-	-	-
	4.5	5.88	0.06	3.79	0.04	31.56	0.37	2.10	0.10	3.61	0.18	-	-	-
	7	5.87	0.03	3.68	0.02	30.65	0.15	2.20	0.05	3.79	0.08	3.38	41.46	24.10
	9	5.77	0.06	3.65	0.04	30.40	0.37	2.13	0.10	3.66	0.18	3.18	38.95	26.99
	13	6.31	0.06	3.94	0.04	32.80	0.37	2.38	0.10	4.10	0.18	3.36	41.22	21.89
	17	6.29	0.02	4.02	0.04	33.54	0.37	2.27	0.06	3.91	0.11	3.36	41.23	21.32
	21	6.03	0.06	3.99	0.04	33.26	0.37	2.04	0.10	3.52	0.18	3.35	41.09	22.13
D357_3	0.5	1.61	0.02	1.30	0.02	10.83	0.18	0.31	0.04	0.53	0.07	3.72	45.66	42.99
	1.5	1.71	0.01	1.34	0.07	11.20	0.55	0.36	0.08	0.63	0.13	-	-	-
	2.5	1.84	0.02	1.56	0.04	12.99	0.36	0.28	0.06	0.49	0.10	-	-	-
	4.5	1.82	0.02	1.62	0.04	13.49	0.36	0.20	0.06	0.35	0.11	-	-	-
	7	1.88	0.02	1.70	0.04	14.19	0.36	0.18	0.06	0.31	0.11	4.11	50.46	35.04

Uncertainties are one standard error (1SD). (continued on next page)

Table 4.2 (continued from previous page)

Sediment core ID	Depth	Total C (TC)	1SD	Total Inorganic C (TIC)	1SD	Total $CaCO_3$	1SD	Total organic C (TOC)	1SD	Organic Matter (OM)	1SD	Al	Al-derived Lithogenics	Opal
	(cm)	(wt %)		(wt%)		(wt %)		(wt %)		(wt %)		(wt %)	(wt %)	(wt %)
	11	2.13	0.02	1.97	0.04	16.42	0.36	0.16	0.06	0.27	0.10	4.14	50.78	32.53
D357-4.5	0.5	1.13	0.01	0.09	0.01	0.77	0.06	1.04	0.02	1.79	0.04	6.41	78.65	18.79
	1.5	1.06	0.01	0.07	0.01	0.60	0.05	0.99	0.01	1.70	0.02	6.73	82.54	15.16
	2.5	1.01	0.02	0.04	0.01	0.29	0.05	0.98	0.02	1.69	0.04	7.33	89.86	8.16
	4.5	0.86	0.02	0.04	0.01	0.30	0.05	0.82	0.03	1.42	0.04	7.28	89.35	8.93
	8	0.79	0.02	0.03	0.01	0.25	0.05	0.76	0.03	1.30	0.04	7.45	91.37	7.07
	12	0.75	0.02	0.05	0.01	0.40	0.05	0.71	0.03	1.22	0.04	6.79	83.23	15.15
	16	0.76	0.01	0.09	0.00	0.76	0.03	0.66	0.02	1.14	0.03	7.26	89.02	9.07
	20	0.91	0.02	0.28	0.01	2.37	0.05	0.63	0.03	1.08	0.04	7.25	88.97	7.58
	24	1.95	0.02	1.45	0.01	12.07	0.05	0.50	0.03	0.87	0.04	6.96	85.40	1.67

Table 4.3: $^{230}Th_{xs}$-normalized fluxes of lithogenics, Organic Matter (OM), $CaCO_3$ and opal ($bSiO_2$) for Cape Basin Margin sediment

Sediment core ID	Depth (cm)	Lithogenic ($g/cm^2/kyr$)	Organic Matter (OM) ($g/cm^2/kyr$)	$CaCO_3$ ($g/cm^2/kyr$)	$bSiO_2$ ($g/cm^2/kyr$)
D357-0.75	0.5	0.95	0.091	0.69	0.58
	1.5	1.01	0.091	0.74	0.57
	2.5	0.88	0.080	0.63	0.50
	3.5	-	-	-	-
	4.5	-	-	-	-
	7	0.88	0.081	0.65	0.51
	9	0.92	0.086	0.72	0.64
	13	0.83	0.083	0.66	0.44
	17	0.90	0.085	0.73	0.46
	21	0.89	0.076	0.72	0.48
D357_3	0.5	0.54	0.0062	0.13	0.51
	1.5	-	-	-	-
	2.5	-	-	-	-
	4.5	-	-	-	-
	7	0.49	0.0030	0.14	0.34
	11	0.49	0.0026	0.16	0.31
D357-4.5	0.5	0.41	0.0094	0.0041	0.10
	1.5	0.25	0.0051	0.0018	0.05
	2.5	0.26	0.0049	0.0009	0.02
	4.5	0.26	0.0041	0.0009	0.03
	8	0.25	0.0036	0.0007	0.02
	12	0.23	0.0034	0.0011	0.04
	16	0.25	0.0032	0.0021	0.03
	20	0.25	0.0030	0.0066	0.02
	24	0.26	0.0027	0.0369	0.01

Table 5.1: Results of water-column ^{230}Th, ^{232}Th and ^{231}Pa concentrations, and ^{231}Pa/^{230}Th ratios in the tropical Atlantic Ocean

Station	Depth	^{230}Th	^{230}Th$_{corr}$	^{230}Th$_{corr}$	2se	^{232}Th	^{232}Th	2se	^{231}Pa	^{231}Pa$_{corr}$	^{231}Pa$_{corr}$	2se	(^{231}Pa/^{230}Th)$_{corr}$	2se
	m	fg/kg	fg/kg	dpm/1000l		pg/kg	dpm/1000l		fg/kg	fg/kg	dpm/1000l			
D361-10	200	3.40	3.25	0.15	0.02	39.04	0.0097	0.0018	0.77	0.20	0.082	0.022	0.54	0.15
7.22°S	110	1.34	1.28	0.06	0.02	15.93	0.0040	0.0017	0.29	0.20	0.031	0.021	0.52	0.39
25.00°W	20	1.07	0.99	0.05	0.02	19.60	0.0049	0.0017	0.26	0.19	0.028	0.021	0.60	0.50
D361-13	3720	12.38	12.17	0.57	0.16	56.10	0.0140	0.0008	1.30	1.29	0.139	0.023	0.24	0.08
1.16°N	3300	12.00	11.79	0.55	0.16	55.64	0.0139	0.0008	1.28	1.28	0.137	0.023	0.25	0.08
26.05°W	2499	10.42	10.24	0.48	0.16	48.68	0.0121	0.0008	1.36	1.36	0.146	0.022	0.31	0.11
	2000	10.08	9.87	0.46	0.16	56.49	0.0141	0.0008	1.34	1.33	0.143	0.022	0.31	0.12
	1499	9.35	9.11	0.43	0.15	64.36	0.0161	0.0008	1.28	1.27	0.137	0.023	0.32	0.13
	1099	7.40	7.18	0.34	0.16	57.64	0.0144	0.0008	1.36	1.36	0.146	0.023	0.43	0.21
	749	5.28	5.08	0.24	0.16	51.62	0.0129	0.0008	0.94	0.93	0.100	0.023	0.42	0.29
	499	4.51	4.31	0.20	0.15	53.99	0.0135	0.0008	0.56	0.56	0.060	0.022	0.30	0.25
	300	3.26	3.04	0.14	0.16	61.18	0.0153	0.0008	0.40	0.40	0.043	0.023	0.30	0.37
	150	2.88	2.62	0.12	0.15	70.60	0.0176	0.0008	0.28	0.27	0.029	0.021	0.24	0.33
	59	1.82	1.65	0.08	0.15	45.38	0.0113	0.0007	0.14	0.28	0.030	0.021	0.38	0.81
	24	1.76	1.42	0.07	0.15	91.50	0.0228	0.0009	0.11	0.13	0.014	0.022	0.21	0.58

All errors are two standard errors including the contribution from sample weighing, spike calibration, ^{231}Pa, ^{230}Th and ^{232}Th in the respective ^{233}Pa and ^{230}Th spikes, blank correction, internal precision and related corrections of mass spectrometric measurement. (continued on next page)

Table 5.1 (continued from previous page)

Station	Depth	^{230}Th	$^{230}Th_{corr}$	$^{230}Th_{corr}$	2se	^{232}Th	^{232}Th	2se	^{231}Pa	$^{231}Pa_{corr}$	$^{231}Pa_{corr}$	2se	$(^{231}Pa/^{230}Th)_{corr}$	2se
	m	fg/kg	fg/kg	dpm/1000l		pg/kg	dpm/1000l		fg/kg	fg/kg	dpm/1000l			
D361-14	4212	13.87	13.61	0.64	0.02	70.00	0.0175	0.0019	1.97	1.97	0.211	0.024	0.33	0.04
3.35°N	3498	13.69	13.45	0.63	0.02	64.94	0.0162	0.0019	2.09	2.09	0.225	0.024	0.36	0.04
26.82°W	2997	12.87	12.62	0.59	0.02	64.86	0.0162	0.0019	2.54	2.53	0.272	0.024	0.46	0.04
	2497	11.87	11.62	0.54	0.02	67.42	0.0168	0.0019	2.51	2.51	0.270	0.024	0.50	0.05
	1999	11.56	11.30	0.53	0.02	69.25	0.0173	0.0019	2.20	2.19	0.236	0.024	0.45	0.05
	1499	9.53	9.24	0.43	0.16	76.80	0.0192	0.0008	1.46	1.45	0.156	0.022	0.36	0.14
	900	6.29	6.02	0.28	0.15	71.87	0.0179	0.0008	1.27	1.26	0.136	0.022	0.48	0.27
	499	3.95	3.63	0.17	0.15	85.60	0.0214	0.0008	0.58	0.57	0.062	0.022	0.36	0.35
	300	3.37	2.98	0.14	0.15	105.09	0.0262	0.0009	0.36	0.35	0.037	0.021	0.27	0.33
	200	3.14	2.83	0.13	0.15	85.16	0.0213	0.0008	0.31	0.31	0.033	0.022	0.25	0.33
	74	2.45	2.15	0.10	0.16	79.91	0.0199	0.0008	0.23	0.22	0.024	0.022	0.24	0.42
	25	1.95	1.30	0.06	0.15	175.36	0.0438	0.0011	0.07	0.06	0.006	0.021	0.10	0.42
D361-17	5590	14.89	14.65	0.69	0.03	62.47	0.0156	0.0003	1.84	1.83	0.197	0.021	0.29	0.03
10.62°N	4999	16.40	16.14	0.76	0.03	68.54	0.0171	0.0004	1.91	1.90	0.205	0.021	0.27	0.03
28.73°W	3999	18.89	18.59	0.87	0.03	79.99	0.0200	0.0004	2.51	2.50	0.269	0.021	0.31	0.03
	2998	16.15	15.91	0.74	0.03	64.67	0.0161	0.0004	2.81	2.80	0.301	0.021	0.40	0.03

(continued on next page)

Table 5.1 (continued from previous page)

Station	Depth	^{230}Th	$^{230}Th_{corr}$	$^{230}Th_{corr}$	2se	^{232}Th	^{232}Th	2se	^{231}Pa	$^{231}Pa_{corr}$	$^{231}Pa_{corr}$	2se	$(^{231}Pa/^{230}Th)_{corr}$	2se
	m	fg/kg	fg/kg	dpm/1000l		pg/kg	dpm/1000l		fg/kg	fg/kg	dpm/1000l			
D361-17	2498	15.80	15.53	0.73	0.03	71.00	0.0177	0.0004	3.05	3.05	0.327	0.021	0.45	0.03
	1497	10.41	10.09	0.47	0.03	87.29	0.0218	0.0006	2.78	2.78	0.298	0.021	0.63	0.06
	949	6.80	6.49	0.30	0.02	84.74	0.0211	0.0005	2.08	2.08	0.223	0.021	0.74	0.09
	499	3.80	3.47	0.16	0.02	89.48	0.0223	0.0005	0.93	0.92	0.099	0.020	0.61	0.15
	299	3.57	3.22	0.15	0.03	94.75	0.0236	0.0006	0.73	0.72	0.078	0.021	0.52	0.17
	199	3.47	3.08	0.14	0.02	104.40	0.0261	0.0008	0.84	0.83	0.089	0.021	0.62	0.17
	69	2.04	1.78	0.08	0.02	67.80	0.0169	0.0004	0.63	0.63	0.067	0.020	0.81	0.31
	24	2.24	1.62	0.08	0.02	165.34	0.0413	0.0008	0.42	0.41	0.044	0.020	0.58	0.31
D361-21	1000	7.04	6.84	0.32	0.02	54.96	0.0137	0.0003	2.23	2.22	0.239	0.021	0.75	0.08
19.15°N	750	6.12	5.89	0.28	0.03	62.10	0.0155	0.0003	1.61	1.60	0.172	0.020	0.63	0.09
28.12°W	500	4.27	4.02	0.19	0.02	67.13	0.0168	0.0004	1.02	1.02	0.109	0.021	0.58	0.13
	200	3.12	2.87	0.13	0.02	68.50	0.0171	0.0005	0.59	0.59	0.063	0.021	0.47	0.17
	100	1.88	1.63	0.08	0.02	66.77	0.0167	0.0004	0.59	0.59	0.063	0.020	0.82	0.34
	40	1.67	1.35	0.06	0.02	85.63	0.0214	0.0005	0.52	0.51	0.055	0.020	0.87	0.46
	20	1.55	1.18	0.06	0.02	98.02	0.0245	0.0005	0.37	0.37	0.039	0.021	0.71	0.44

Table 5.2: Concentrations of total and soluble Th, and Th solubility in aerosol samples collected on D361 cruise

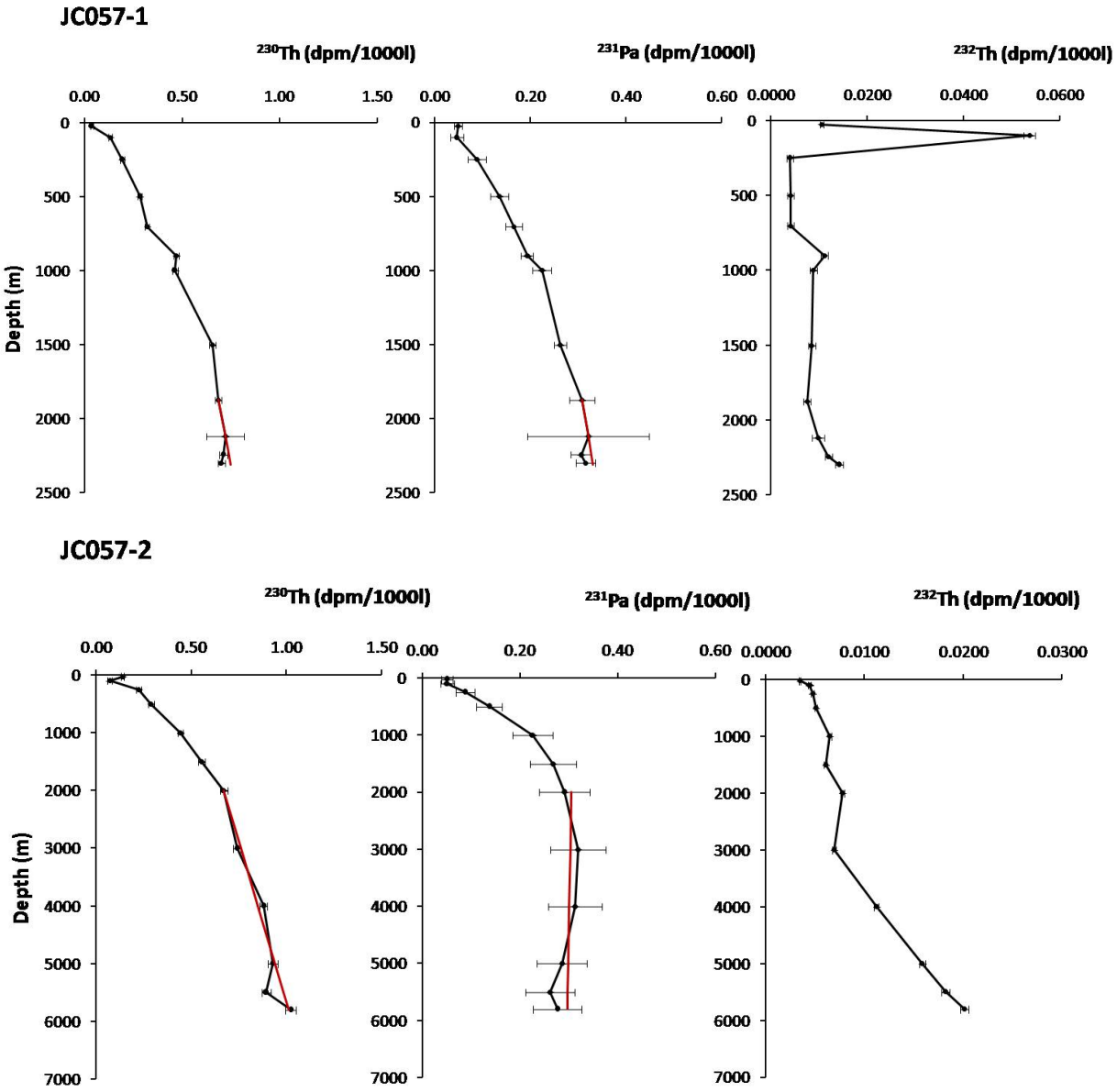
Sample ID	Total Th	s.d.	Total Fe	s.d.	Sol Th	s.d.	Sol Fe	Th solubility	s.d.	Fe solubility	s.d.
	pmol/m^3		pmol/m^3		pmol/m^3		pmol/m^3	%		%	
TM05.all	2.7	0.3	49312	2681	0.241	0.012	306.1	9.0	1.0	0.62	0.06
TM06.all	3.0	0.3	46568	2528	0.231	0.019	457.3	7.7	0.9	0.98	0.07
TM07.all	2.9	0.3	46287	2639	0.245	0.017	354.8	8.4	1.1	0.77	0.19
TM08.all	6.9	0.4	104320	5325	0.376	0.008	701.4	5.4	0.3	0.67	0.04
TM09.all	5.3	0.4	91351	4873	0.381	0.036	407.6	7.2	0.9	0.45	0.04
TM10.all	3.9	0.4	56299	3199	0.271	0.011	289.5	6.9	0.7	0.51	0.06
TM11.all	4.1	0.6	66047	4032	0.320	0.033	535.9	7.9	1.4	0.81	0.09
TM12.all	2.8	0.3	45137	2584	0.222	0.009	294.0	7.9	0.9	0.65	0.07
TM13.all	1.8	0.4	26842	1994	0.123	0.013	152.8	6.9	1.6	0.57	0.05
TM14.all	0.3	DL	1084	DL2	0.012	0.000	33.7	4.3	min	3.11	min
TM15.all	0.4	DL	1382	DL2	0.003	0.000	9.5	0.7	min	0.69	min
TM16.all	0.3	DL	1277	DL2	0.001	DL	5.8	0.4	max	0.46	max?
TM17.all	0.4	DL	1415	DL2	0.005	0.001	19.3	1.4	min	1.37	min
TM19.all	0.7	0.2	8431	933	0.062	0.001	114.1	8.4	2.4	1.35	0.15
TM20.all	0.4	DL	5664	739	0.039	0.006	70.9	10.0	min	1.25	0.17
TM21.all	0.6	0.2	9266	763	0.060	0.010	125.9	9.3	2.7	1.36	0.15

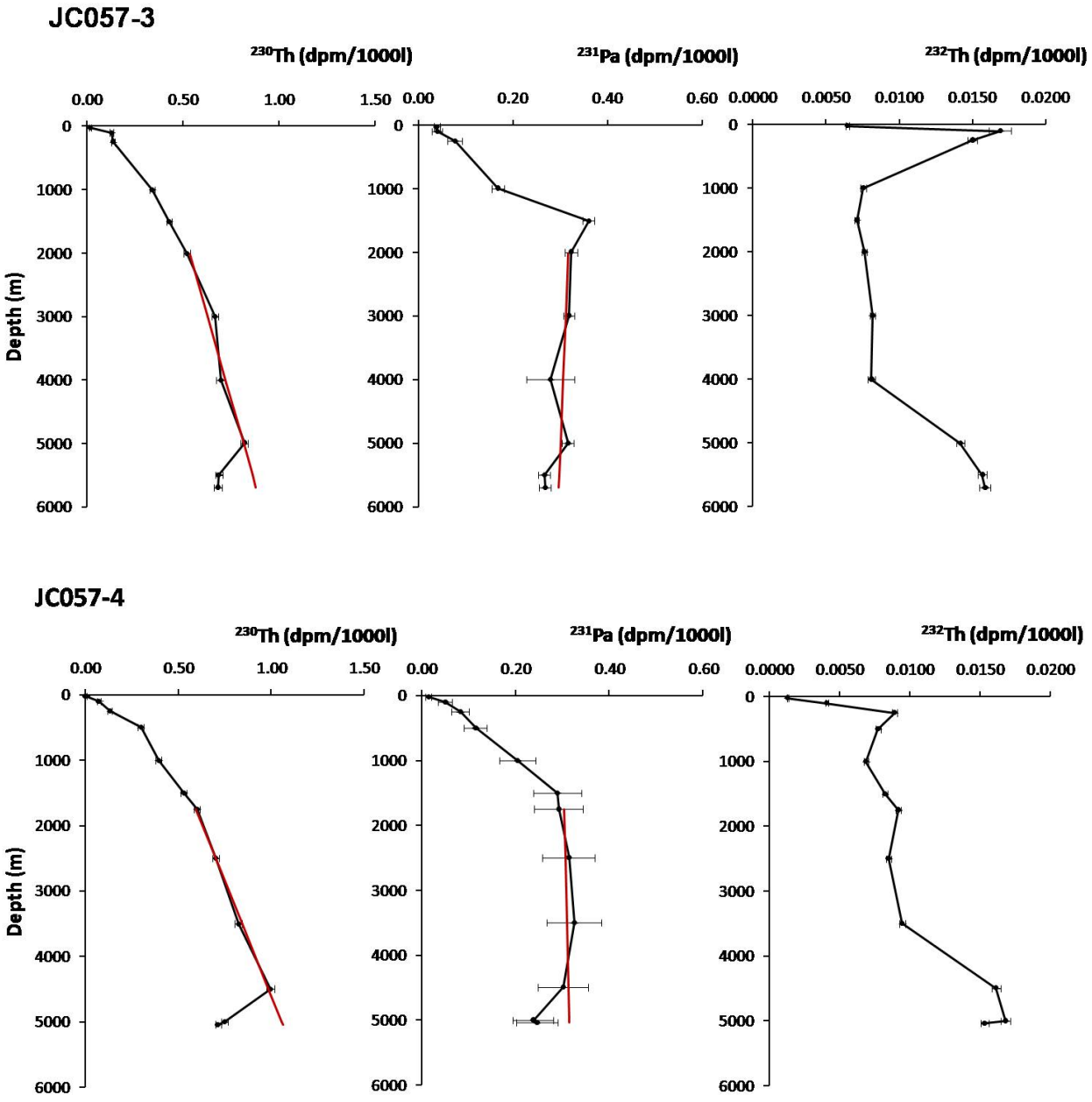
All errors are one standard error. ‘DL’ indicates measurement under detection limit. ‘min’ and ‘max’ indicate that solubility values in the preceding column are minimum or maximum estimates. (continued on next page)

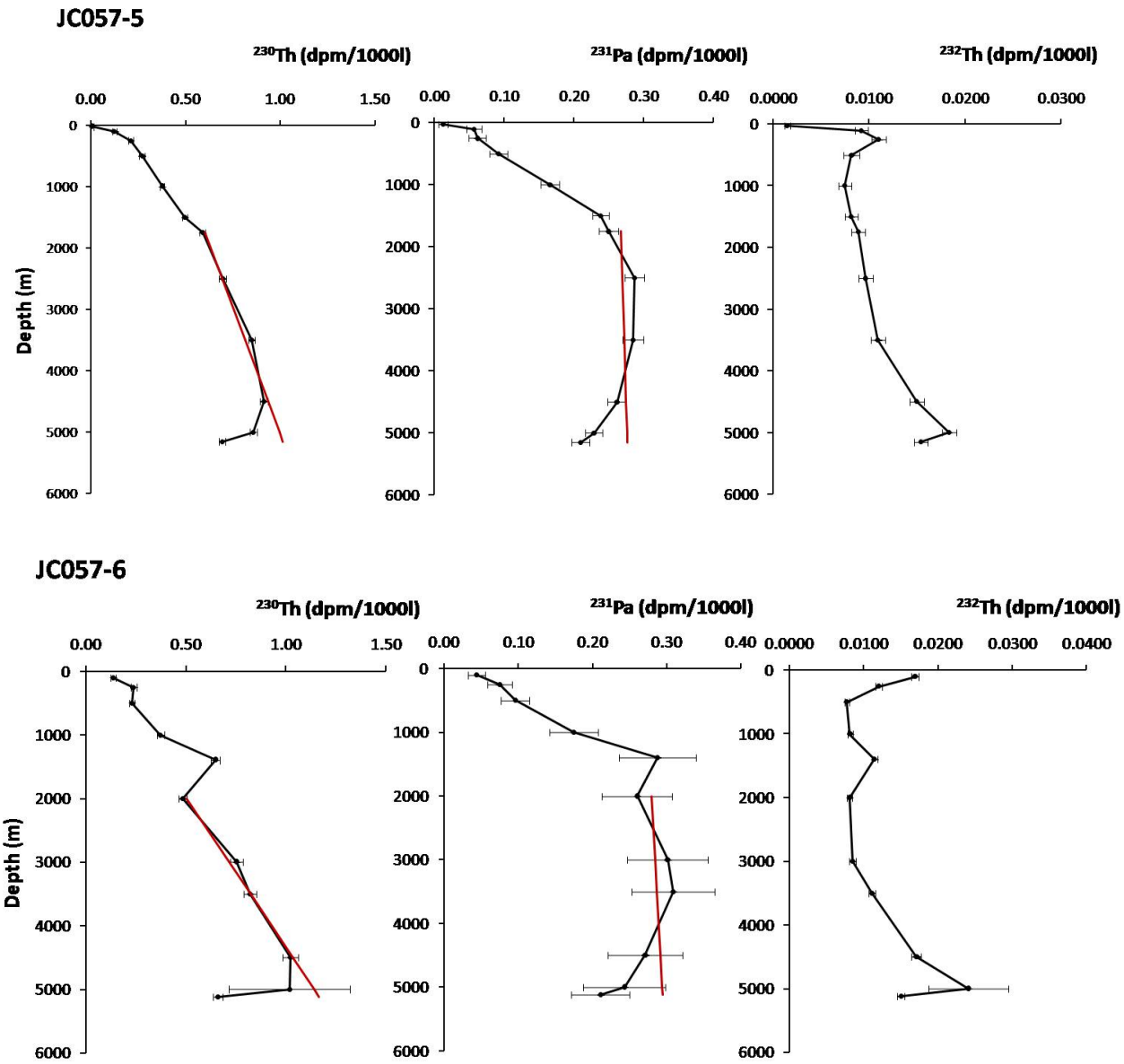
Table 5.2. (continued from previous page)

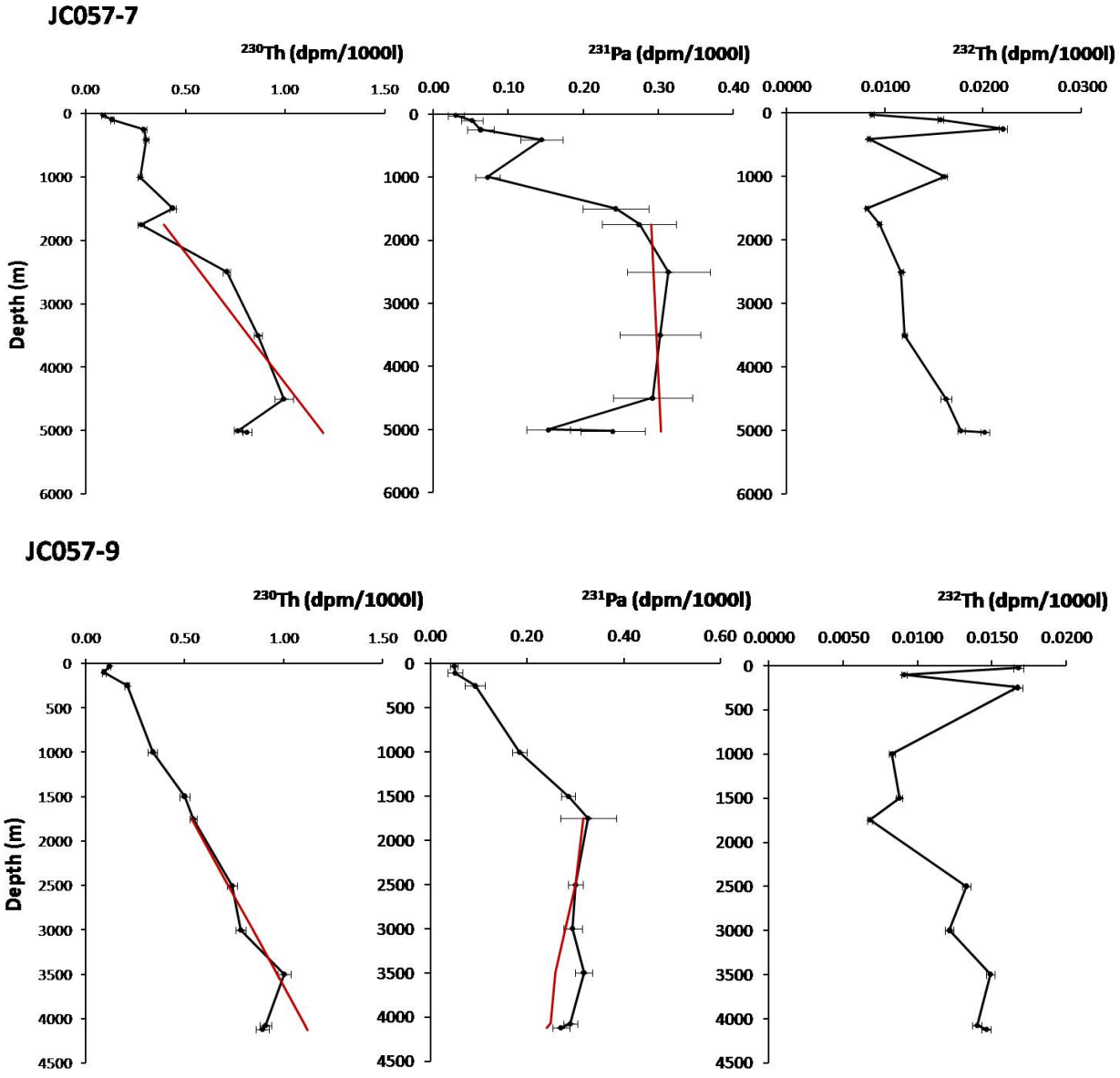
Sample ID	Total Th	s.d.	Total Fe	s.d.	Sol Th	s.d.	Sol Fe	Th solubility	s.d.	Fe solubility	s.d.
	pmol/m^3		pmol/m^3		pmol/m^3		pmol/m^3	%		%	
TM22.all	1.1	0.2	14935	982	0.109	0.005	213.6	10.2	1.6	1.43	0.14
TM23.all	0.6	0.2	8147	727	0.067	0.009	95.3	11.0	3.1	1.17	0.11
TM24.all	0.3	DL2	4598	628	0.030	0.004	57.8	9.0	min	1.26	0.18
TM25.all	0.2	DL2	763	DL	0.004	DL	16.8	2.2	max	2.20	max?
TM26.all	0.3	DL2	1270	DL	0.005	DL	20.0	1.5	max	1.57	max?
TM27.all	0.3	DL2	1278	DL	0.001	DL	7.1	0.4	max	0.55	min
TM28.all	0.3	DL2	1189	DL	0.001	DL	5.4	0.4	max	0.46	max?
TM29.all	0.3	DL2	1272	DL	0.001	DL	5.8	0.4	max	0.46	max?

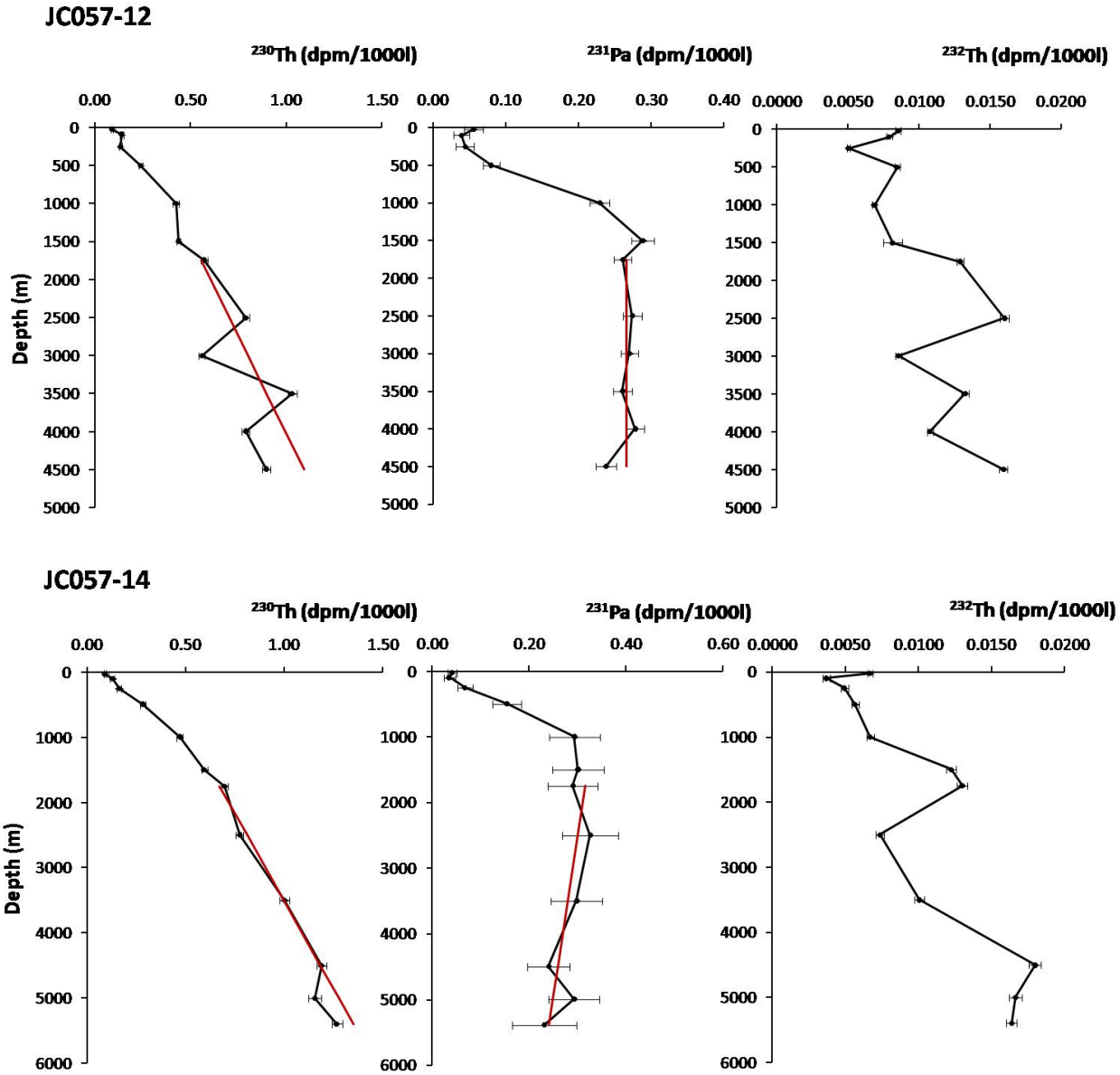
Figure 3.1: Vertical profiles of water-column ^{230}Th, ^{231}Pa and ^{232}Th along a transect in the Southwest Atlantic Ocean. Black lines are JC057 data, red lines are linear extrapolation line used to cauculation additional removal rates in Chapter 3, section 3.5.2.

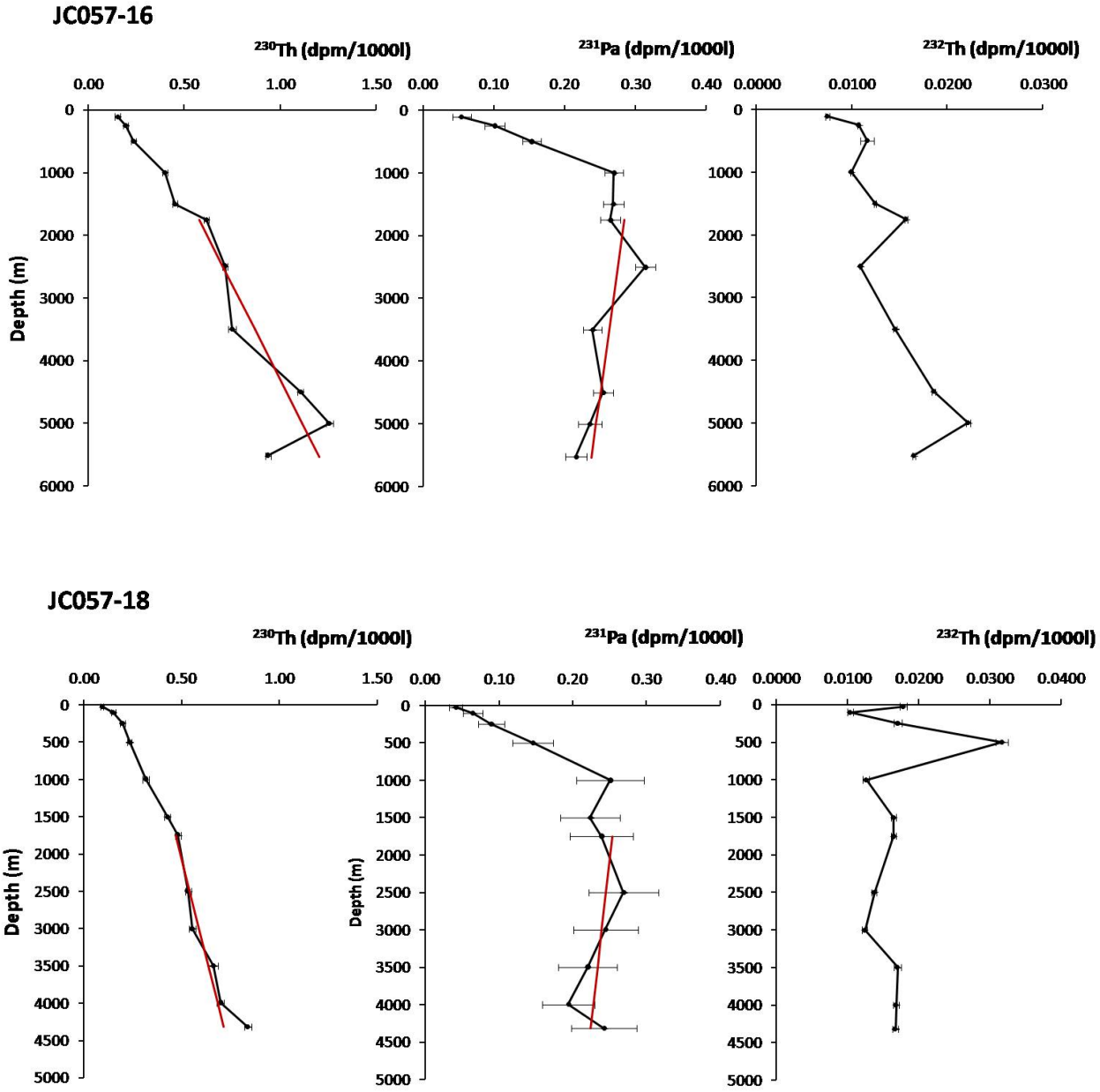



JC057-3
230Th (dpm/1000l)
231Pa (dpm/1000l)
232Th (dpm/1000l)
Depth (m)
JC057-4
230Th (dpm/1000l)
231Pa (dpm/1000l)
232Th (dpm/1000l)
Depth (m)


JC057-5
230Th (dpm/1000l)
231Pa (dpm/1000l)
232Th (dpm/1000l)
Depth (m)
JC057-6
230Th (dpm/1000l)
231Pa (dpm/1000l)
232Th (dpm/1000l)
Depth (m)


JC057-7
230Th (dpm/1000l)
231Pa (dpm/1000l)
232Th (dpm/1000l)
Depth (m)
JC057-9
230Th (dpm/1000l)
231Pa (dpm/1000l)
232Th (dpm/1000l)
Depth (m)


JC057-12
230Th (dpm/1000l)
231Pa (dpm/1000l)
232Th (dpm/1000l)
Depth (m)
JC057-14
230Th (dpm/1000l)
231Pa (dpm/1000l)
232Th (dpm/1000l)
Depth (m)


JC057-16
230Th (dpm/1000l)
231Pa (dpm/1000l)
232Th (dpm/1000l)
Depth (m)
JC057-18
230Th (dpm/1000l)
231Pa (dpm/1000l)
232Th (dpm/1000l)
Depth (m)